Propriétés magnétiques d'hétérostructures à base d'oxydes pour la réfrigération magnétique et la spintronique

Magnetic properties of oxide heterostructures for magnetic cooling systems and spintronics

par

Mohammad Abbasi Eskandari

Thesis présentée au Département de physique

en vue de l'obtention du grade de Philosophiae Doctor (Ph.D.)

FACULTÉ des SCIENCES

UNIVERSITÉ de SHERBROOKE

Sherbrooke, Québec, Canada, 18 mai 2023

Le 18 mai 2023

le jury a accepté la thèse de Monsieur Mohammad Abbasi Eskandari dans sa version finale.

Membres du jury

Professeur Patrick Fournier
Directeur de recherche
Département de physique

Professeur René Côté
Membre interne
Département de physique

Professeur Louis Taillefer
Membre interne + Président rapporteur
Département de physique

Professeur Amlan Biswas
Membre externe
Département de physique
University of Florida

Sommaire

Motivée par leur grand potentiel d'applications technologiques dans plusieurs domaines, la recherche sur les matériaux et composants à base d'oxydes de type pérovskite comme les manganites et les doubles pérovskites demeure très active et d'actualité. Dans la présente thèse, la spintronique et la réfrigération magnétique sont les deux cibles principales. Le manganite semi-métallique ferromagnétique $La_{2/3}Sr_{1/3}MnO_3$ (LSMO) et le double pérovskite isolant ferromagnétique La_2NiMnO_6 (LNMO) sont d'intérêt puisqu'ils peuvent être utilisés en réfrigération magnétique et pour des jonctions à effet tunnel magnétiques grâce à leur grande température de transition magnétique, leur grande aimantation et leur grande polarisation magnétique.

Dans la première partie de cette thèse, nous étudions l'effet magnétocalorique (EMC) d'hétérostructure de LSMO et LNMO simulant des composites. Les buts de cette première étude sont d'étendre l'intervalle de température avec un effet magnétocalorique significatif et d'améliorer leurs performances en modifiant les propriétés magnétiques de multicouches grâce à des effets de contraintes structurales entre les couches et le substrat. Les propriétés magnétiques et magnétocaloriques des couches de LSMO et LNMO incluses dans les hétérostructures peuvent être contrôlées et même ajustées en les soumettant à différents champs de contraintes, tout particulièrement pour le double pérovskite LNMO pour lequel les propriétés magnétiques sont très sensibles au niveau d'ordre cationique sur les sites B/B'. Nous démontrons comment la proportion d'ordre cationique dans LNMO peut être ajusté dans les hétérostructures simplement en changeant l'ordre de succession des couches provoquant des effets différents des contraintes structurales. La présence de plusieurs transitions magnétiques dans le LNMO multi-domaine permet le de-

sign de structures artificielles présentant un EMC de type "table-top" (constant sur une large gamme de température). Cependant, la présence de plusieurs domaines avec différentes propriétés est parfois difficile à confirmer en utilisant seulement l'aimantation permettant d'évaluer l'EMC. D'autres approches, par exemple l'effet tunnel au travers LNMO, peut être une avenue intéressante pour les détecter.

Dans la deuxième partie de la thèse, nous exploitons la nature isolante du double pérovskite LNMO pour étudier l'effet d'une barrière ferromagnétique sur la magnétorésistance tunnel (TMR) d'une jonction à effet tunnel magnétique (MTJ). Nous montrons que la TMR ne dépend pas seulement de l'orientation relative de l'aimantation des deux électrodes métalliques, mais dépend aussi de l'orientation de l'aimantation de la barrière de LNMO par rapport à celles des électrodes. Il est proposé que la conduction au travers la barrière de LNMO se produit via des canaux pour électrons et pour des trous impliquant des états e_g vides ou pleins près du niveau de Fermi dans la barrière. Se basant sur l'observation de TMR jusqu'à la température de transition maximale observée pour le LNMO, on constate que ces composants MTJ peuvent être utilisés comme sondes très sensibles de la présence de phases magnétiques dans différents domaines, et ceci en très faible quantité.

Abstract

There has been an active, ongoing research on perovskite-structured oxides such as manganites and double perovskites due to their great potential for a wide range of technological applications in many fields. In the present thesis, spintronics and magnetic refrigeration are the main targets. Half-metallic ferromagnetic manganite $La_{2/3}Sr_{1/3}MnO_3$ (LSMO) and ferromagnetic insulating double perovskite La_2NiMnO_6 (LNMO) are of particular interest as they can be used in magnetic refrigeration and magnetic tunnel junctions due to their high and tunable transition temperature, large magnetization and large spin polarization.

In the first part of this thesis, we study the magnetocaloric effect (MCE) of composite-like heterostructures of LSMO and LNMO. The goal is to extend the MCE and improve its performance by altering the magnetic properties in multilayers using epitaxial strain. The magnetic and magnetocaloric properties of LSMO and LNMO layers can be controlled and tuned by subjecting them to different strain fields, especially for LNMO double perovskite where its magnetic properties are very sensitive to the level of cationic ordering at the B/B' sites. We demonstrate how the ratio of cation ordering in LNMO can be adjusted in heterostructures simply by changing the layout of the layers triggering contrasting strain effects. The presence of multiple transitions in a multi-domain LNMO allows the design of artificial structures with table-top-like MCE. The presence of several domains with different properties is often difficult to perceive using only magnetization. Other approaches, like tunneling through LNMO, may be an interesting avenue to explore its multi-domain aspect.

In the second part, we exploit the insulating nature of LNMO double perovskite to study the effect of a ferromagnetic barrier on the tunnel magnetoresis-

tance (TMR) of a magnetic tunnel junction (MTJ). We show that the TMR does not depend only on the relative orientation of the magnetization in the two metallic electrodes, but also depends on the orientation of magnetization in the LNMO barrier with respect to those of the two electrodes. It is proposed that the conduction occurs through the LNMO barrier via electron and hole channels involving empty and filled e_g states around the Fermi level in the barrier. Based on the observation of TMR up to the maximum transition temperature of LNMO, these MTJ devices can also be used as a sensitive probe to detect magnetic phases in the barrier coming from different domains in the same film.

Acknowledgments

This doctoral dissertation would not be possible with the help and support of kind individuals around me. I would like to thank everyone who directly or indirectly has been involved during the past five years leading to this thesis. First and foremost, I would like to express my sincere gratitude to my supervisor Prof. Patrick Fournier for giving me the opportunity to be a part of his research group. I have learned a lot from him from our numerous discussions where he always patiently explained the ideas, problems and mechanisms to me. I would like to thank him for his constant support, encouragement and guidance throughout my PhD. His support and understanding were not limited to research activities and also included personal circumstances. It was an honor to have him as my supervisor.

I would like to extend my gratitude and appreciation to the thesis committee members: Prof. René Côté, Prof. Louis Taillefer and Prof. Amlan Biswas from the University of Florida for their precious advice, useful discussion and constructive suggestions that helped me to improve the quality of this work. I am also grateful to Prof. André-Marie Tremblay and Prof. Ion Garate for all the valuable discussions we had.

I would like to thank the following organization for financial support during the years of my PhD: the Natural Sciences and Engineering Research Council of Canada (NSERC), the Canada Foundation for Innovation (CFI), the Fonds de Recherche du Québec - Nature et Technologies (FRQNT), the Canada First Research Excellence Fund (CFREF), Institut Quantique (IQ) and Université de Sherbrooke.

I would like to offer my special thanks to Prof. Mohamed Balli from Rabat Uni-

versity in Morocco, a former member of our team, for all the valuable discussions we had which greatly contributed towards the success of the first project. A very special thanks to Dr. Maxime Dion for all his help and technical assistance in the lab, and also for taking the time to train me on the instruments in the lab. I am also thankful to my colleagues Sara Ghotb, Guillaume Hardy, Naima Brahiti, Imad Hussain, Etienne Blais, François Naud, Prosper Reulet, Olivier Bernard and Priyanka Brojabasi for their help and collaboration during my study.

I would like to thank the faculty and staff in the physics department at UdeS. In particular, I am deeply grateful for technical assistance of Bobby Rivard and Stéphane Pelletier who were always there when we had a problem in the lab. I am thankful to the cryogenic team for providing liquid helium that we could run experiments. I also want to thank Patrick Vachon, the computer systems technician, for assisting me with IT problems. I would like to mention and thank Lise Charbonneau for helping me during the enrollment process and giving me invaluable tips and advice as a newcomer.

I would also like to thank all my friends at the department, especially, Sidhartha Shankar Dash, Arash Akbari Sharbaf, Redha Rouane, Bahman Pahlevanzadeh Garjani, Aimé Verrier, Arghyadip Ghosh and Lucas Désoppi for all the great times we have shared.

Last but most crucially, I am deeply grateful to my family, my parents, my father- and mother-in-law, my sisters, my niece (Mahsa) and my nephews (Abolfazl, Mahdi, Amir Hossein and Arshia) for their constant support, encouragement and persistent love throughout this journey. I would also like to thank my nephew Abolfazl Kariminejad for assisting me in drawing the schematic figures in the thesis and the papers. I have saved the last word of acknowledgment for my wife, Sara Ghotb, who has also been my best friend and colleague. I would like to thank her for being always by my side when times were hard. I am sure I could not have made it to where I am today without her constant love and support.

Dedication

To:

my wife

Contents

List of Figures

Introduction

Transition metal oxides are among the most studied materials experimentally and theoretically in condensed matter physics and material science. They have been under the spotlight due to their rich variety of physical properties such as magnetic, electrical and optical properties. Manganites, double perovskites (DPs), cuprates and vanadates are a few prominent examples. Among transition metal oxides, perovskite-structured manganites with general formula $R_{1-x}A_xMnO_3$ where R is a trivalent rare earth and A is a divalent alkaline earth element, have generated a great deal of interest due to their unique properties including colossal magnetoresistance (CMR) [1], large magnetocaloric effect (MCE) [2], multiferroicity and half-metallicity [3] close to room temperature. The mixed-valence $La_{1-x}Sr_xMnO_3$ (LSMO) compound is one of the most intriguing members of manganites family where half-metallicity is combined with a high magnetic transition at 370 K [4]. These properties make it a suitable candidate for a wide range of industrial and technological applications such as magnetic cooling systems and spintronics. Another family of perovskite-type materials is the double perovskites with general formula $A_2BB'O_6$ consisting of two interpenetrated simple perovskites, where B and B′ are transition metals. The large number of possible combinations of 3*d* ions at the B/B′-sites results in a wide variety of magnetic interactions in DPs. Some combinations of B and B′ can lead to ferromagnetic insulating compounds which are rarely seen in any other materials [5]. Furthermore, cation ordering can also occur at both A and B sites in DPs, which can strongly affect their structural and magnetic properties [6]. La_2NiMnO_6 (LNMO) is an example of DPs where it has a magnetic phase transition with a maximum transition temperature T_c of 285 K. Most noticeably, its T_c can depend on the level of B/B′ cationic ordering in the sample [5].

It has been shown that the magnetic and transport properties of manganites and DPs such as magnetic phase transition can be easily tuned to meet specific functional requirements. Chemical doping and changing the growth conditions are two widely used methods to adjust their properties [7–9]. Moreover, the epitaxial strain which originates from the lattice mismatch between the layer and a substrate is introduced as another way to control and affect the magnetic and electrical properties of perovskite oxides thin films [10, 11]. The substrate-induced strain can affect the lengths and the angles of $B-O-B'$ bonds between adjacent $BO_6/B'O_6$ octahedra and even the ratio of B/B'-site cation ordering in DPs. For instance, the level of cationic ordering as well as magnetic and structural properties in LNMO DPs have been altered using substrate-induced strain and varying growth conditions [7, 10].

Magnetic refrigeration based on the magnetocaloric effect (MCE) is defined as the heating or cooling of a magnetic material due to a varying external magnetic field. It originates from the changes in entropy of the system due to the coupling of magnetic moments and external magnetic field. In comparison with conventional gas-based cooling systems, magnetic refrigeration can be a more efficient and environmentally friendly technology. According to surveys [12], about 25 % of residential and 15 % of commercial power consumption is used in refrigeration and cooling systems. Additionally, the usage of some harmful greenhouse gases such as chlorofluorocarbons (CFCs), hydrochlorofluorocarbons (HCFCs) and hydrofluorocarbons (HFCs) in conventional gas compression refrigeration has raised many concerns due to their impact on the ozone layer and as green-house gases. These issues have impelled scientists to seek alternatives. Magnetic refrigeration is one of the best candidates due to its high efficiency and being a green technology. The cooling efficiency of Gadolinium-based magnetic refrigerators was shown to reach 60 % of the theoretical limit [13], whilst the best gas compression refrigerators only produce 40 % of the theoretical cooling limit.

Over the years, many families of magnetic materials have been introduced with a large MCE such as Gd and Gd-based alloy [14], $La(Fe,Si)_{13}$ compounds [15], Heusler alloys [16] and perovskite oxides [2]. Among these families, materials with a second-order magnetic phase transition (SOMT) are the ideal candidates for magnetic cooling systems due to their wide operating temperature range. Manganites and DPs have attracted much attention not only because they exhibit a SOMT,

but also due to their tunable transition temperature, large thermal conductivity, low thermal and magnetic hysteresis, high electrical resistivity, small lattice entropy, low cost of production and high chemical stability. As already mentioned, LSMO is one of the excellent candidates for magnetic refrigeration at room temperature [17]. On the other hand, LNMO DPs with tunable multiple magnetic phase transitions from 170 K to 285 K are considered a promising material for extending the temperature span of the MCE below room temperature [18]. The transition temperature can be adjusted in LNMO by varying the level of cationic ordering to meet specific purpose. It has been reported that a certain level of cationic ordering results in the coexistence of multiple magnetic phases in LNMO, allowing to spread the magnetic entropy change over a large range of temperature from 100 to 300 K [7].

In general, most of the magnetocaloric materials operate within a narrow temperature range close to their transition temperature. For the implementation in domestic cooling devices, one needs to have materials with a large operating temperature range including room temperature. Several approaches have been investigated to extend the working temperature of the MCE in magnetic materials including chemical manipulation and changing the growth conditions [7, 19]. The results indicated that broadening the MCE usually results in a loss of magnitude. Another approach to design a desirable magnetocaloric material where the magnetic entropy change is distributed over a wide temperature range while its value remains constant and temperature independent is to combine different materials in a composite structure. For this purpose, magnetic materials with different transition temperatures can be combined in form of powders or thin film heterostructures [20–22]. With this technique, the temperature range with significant entropy change in a varying field of such composites can be widened while preserving the magnitude of entropy value.

In the first part of this thesis, composite-like thin film heterostructures were chosen as the main route to tailor a table-top-like magnetic entropy variation over a large temperature range using LSMO and LNMO. We try to adjust the magnetocaloric properties by making bilayer and trilayer composites of these two materials in form of thin films. We prepared two bilayers with LSMO/LNMO and LNMO/LSMO layouts, and two trilayers with layouts of LSMO/LNMO/LSMO and

LNMO/LSMO/LNMO. We also take advantage of multiple magnetic transitions in LNMO and try to tune the T_c by controlling the ratio of cationic ordering in the sample. To accomplish this, the LNMO layers were exposed to different epitaxial strains by varying the layout of the layers in the bilayer and trilayer samples.

In the second part of the thesis, we focus on the transport properties of the LSMO/LNMO/LSMO trilayer sample where it can act as a magnetic tunnel junction (MTJ). This trilayer sample provides a unique opportunity to explore the tunnel magnetoresistance (TMR) through a ferromagnetic insulating barrier. The insulating nature of LNMO DP allows it to behave as a magnetic barrier in this MTJ. Moreover, as already mentioned, the presence of multiple magnetic phases in LNMO determines its magnetic properties. However, in some cases, one of these phases may exist in such a small fraction that is invisible in magnetization measurements. Nevertheless, it might still affect the magnetic properties of the sample. We intend to use these LNMO-based MTJs as a sensitive probe to detect all magnetic phases in a LNMO layer, and also explore their contribution in the magnetic and magnetocaloric properties of the heterostructures.

Spintronics is a rapidly emerging field of technology that uses the spin degrees of freedom of electrons to manipulate the electron transport or store information. As compared to the conventional charged based systems, spintronics devices offer non-volatile storage, ultra-fast switching, reduced energy consumption and increased integration density [23, 24]. Tunnel magnetoresistance is one of the most important phenomena in spintronics, occurring in magnetic tunnel junctions where two ferromagnetic electrodes are separated by a thin insulating barrier layer. It was first discovered by Jullière [25] in 1975 in Fe/Ge/Co junctions. The resistance of MTJs strongly depends on the relative orientation of the magnetic moments in the ferromagnetic electrodes, which can be controlled by an external magnetic field. Studies have shown that half-metallic ferromagnetic electrodes, where only one spin direction exists at the Fermi level can produce a giant TMR ratio due to their large spin polarization [26]. Perovskite manganites have gained immense attention in spintronics due to their large spin polarization (even at room temperature) and tunable transition temperature [27]. Optimally-doped $La_{2/3}Sr_{1/3}MnO_3$ manganite is considered to be one of the best electrodes in MTJs with nearly 100 % spin polarization and above room temperature magnetic transition. It has been demon-

strated that the TMR reaches a maximum value of 1850 % in a MTJ consisting of LSMO electrodes and $SrTiO_3$ barrier, which is the highest TMR ever reported [28]. Based on the Jullière formula, this giant TMR corresponds to a spin polarization of 95 %, indicating the half-metallic nature of LSMO.

Non-magnetic amorphous and crystalline barriers in MTJs have been extensively studied. In this thesis, we make use of LNMO to study the effect of a ferromagnetic insulating barrier in MTJs for the first time. The insulating nature of LNMO provides the tunneling conditions in the entire temperature range of operation, combined with a ferromagnetic phase that persists between 180 to 285 K depending on the level of cationic ordering in the sample. We investigate how magnetic order in LNMO and its relative orientation with respect to those of two ferromagnetic electrodes affect the tunneling process in MTJs.

Accordingly, this thesis is divided into four chapters. In Chapter 1, we provide a brief introduction to perovskite oxides and introduce LSMO and LNMO as the main compounds in this thesis. Chapter 2 focuses on the magnetocaloric effect in oxide heterostructures. This chapter starts with the theoretical concepts of the MCE. Then it is followed by the experimental techniques we used to fabricate and characterize the samples. Finally, the results are presented in form of a scientific paper. In Chapter 3, first we explain the theory of TMR in MTJs. The following section describes the method we used to fabricate our MTJ devices. The last section of this chapter contains the results obtained in this project. Finally, Chapter 4, summarizes the main outcomes of this thesis.

Chapter 1

Perovskite oxides

The present chapter introduces the basic information about the materials that are going to be used to build the heterostructures studied in this thesis. They are part of large families of materials with a wide variety of physical properties, some of them of great interest for applications.

1.1 Manganites

Manganese oxides or manganites are strongly correlated electron systems which have been the subject of a great deal of experimental and theoretical studies since they were introduced by Jonker and Van Santen in 1950 [29]. Manganites have attracted much interest due to their remarkable magnetic and transport properties such as colossal magnetoresistance (CMR) [30] and large magnetocaloric effect (MCE) [2]. The doped perovskite manganites have the general formula $R_{1-x}A_xMnO_3$, where R is a trivalent rare-earth element such as La, Pr, Nd and Sm and A is a divalent alkaline-earth element such as Sr, Ca, and Ba. The ideal perovskite structure of manganites is cubic, where the A site cations as trivalent rare-earth and divalent alkaline-earth are located in the dodecahedral sites surrounded by twelve oxygen anions, while the B site cations (Mn) occupy the center of the cell and are octahedrally coordinated by six oxygen atoms, as illustrated in Figure 1.1.

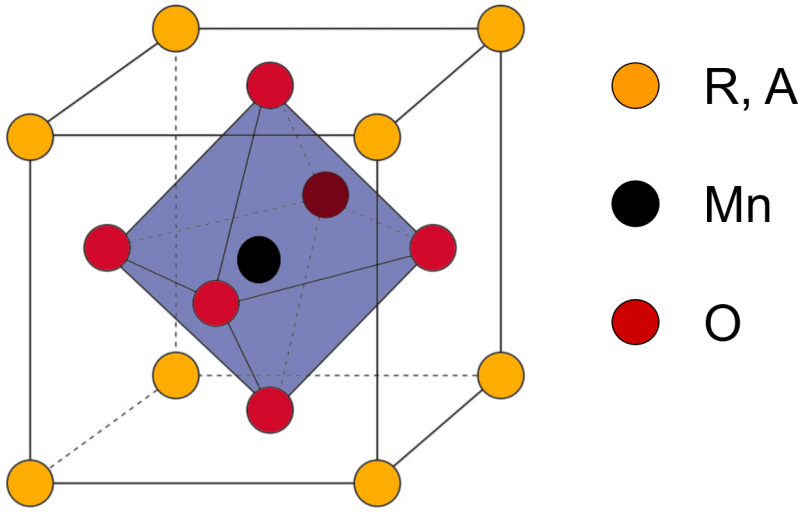

Figure 1.1: Schematic view of an ideal perovskite structure of manganites ($R_{1-x}A_xMnO_3$).

It has been shown that the ideal cubic perovskite structure is not very common as manganites are often slightly distorted due to the difference in ionic size of the cations at the A and B sites, or due to the Jahn-Teller effect which deforms the MnO_6 octahedron. The degree of distortion induced by the bond length mismatch in the unit cell can be calculated by the "Goldsmith tolerance factor" (t_G), which is defined in terms of the ionic radii [31] as follow:

$$t_G = \frac{(r_A + r_O)}{\sqrt{2}\,(r_B + r_O)} \tag{1.1}$$

where r_A, r_B are the average ionic radii of the A-site and B-site cations, respectively, and r_O denotes the ionic radius of oxygen ions. $t_G = 1$ corresponds to the perfect cubic closely packed structure. In practice, this is not the case and the quasi-cubic structure is stable for $0.89 < t < 1.02$. Deviations from this range cause a significant amount of stress, which results in a completely different crystal structures (hexagonal) [32].

Jahn-Teller effect [33] is another source of lattice distortions in manganites by reducing symmetry and lifting the double degeneracy of the e_g orbitals in Mn^{3+} ions. In manganites, Mn ions can exist in a number of ionic states, but Jahn-Teller effect only occurs for the Mn^{3+} ions with the electron configuration of $3d^4$ ($t_{2g}^3 e_g^1$)

where there is only one electron in the e_g orbital. In this configuration the interaction between the orbital state of the e_g electron and the crystal field of the surrounding oxygen octahedra causes a Jahn-Teller distortion which compresses the MnO_6 octahedra along *ab*-plane and elongates it along its *c*-axis or the reverse. This distortion orients the partially-filled e_g orbitals towards the oxygen sites and lifts the double degeneracy by lowering the energy of one e_g orbital and raising the energy of the other. Since there is no electron in the e_g orbital of the Mn^{4+} ions, Jahn-Teller effect does not occur. In doped manganites, both Mn^{3+} and Mn^{4+} ions are present leading to an interplay of lattice distortion and electron delocalization as electrons can hop from Mn^{3+} e_g orbitals to that of Mn^{4+}.

Crystal-field theory describes the effect of a local environment on the energy levels in an ion. The energy levels of a transition metal ion, such as Mn^{3+} or Mn^{4+}, has an active *d* shell with five degenerate levels. In the case of manganites, each Mn ion in the perovskite structure is surrounded by an octahedron of O^{2-} ions. These five degenerate levels get affected by the crystal field of the oxygen octahedra and split into twofold degenerate e_g ($d_{3z^2-r^2}$ and $d_{x^2-y^2}$) and threefold degenerate t_{2g} (d_{xy}, d_{yz}, and d_{zx}) orbitals. The e_g orbitals have higher energy level than the t_{2g} orbitals because the t_{2g} orbitals do not lie directly along the Mn−O bond (thus less overlap between d_{xy}, d_{yz}, d_{xz} orbitals and O_{2p} ones) while the e_g orbitals point along the directions where the negative oxygen ions are located. For the MnO_6 octahedra, the splitting between the lowest t_{2g} level and the highest e_g level is in the range of 1–2 eV. Further splitting of the e_g orbitals is possible if the MnO_6 octahedron undergoes a Jahn-teller distortion. As discussed earlier, under Jahn-Teller distortion, the e_g levels split and the mean energy of the level remains constant. The splitting of the degenerate *d* levels caused by crystal field and the Jahn-Teller effect is depicted in Figure 1.2.

1.1.1 Magnetic interaction

The magnetic properties of manganites are determined by the transfer of electrons between the B-site cations and the oxygen anions which is known as exchange interaction. An exchange interaction between two neighboring magnetic ions with spin $\mathbf{S}_i$ and $\mathbf{S}_j$ is described using the following hamiltonian:

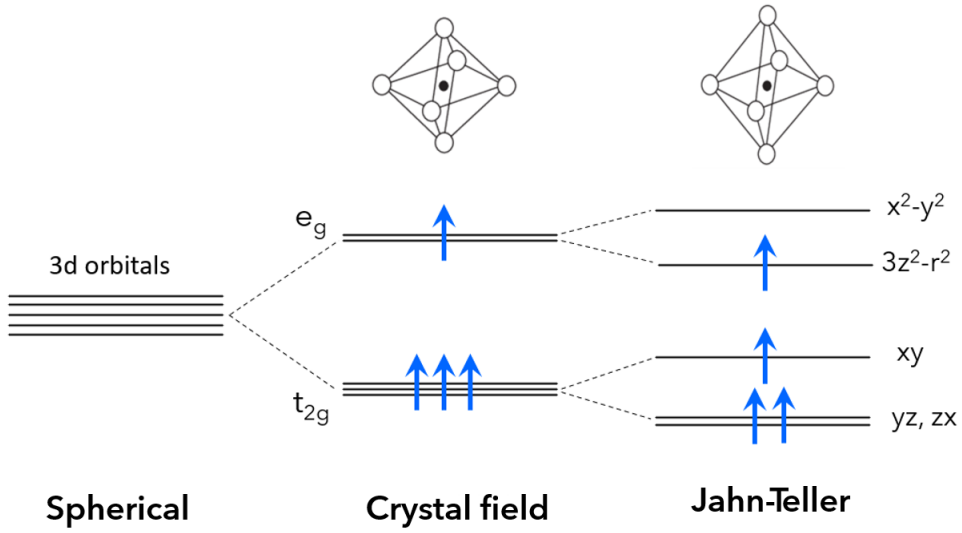

Figure 1.2: A schematic diagram of the crystal field splitting of the Mn 3*d* levels into e_g and t_{2g} levels. Further splitting of e_g levels due to Jahn-Teller distortion. The number of electrons shown here is that of Mn^{3+}.

$$\hat{H} = -\sum_{ij} J_{ij} \mathbf{S}_i . \mathbf{S}_j \tag{1.2}$$

where J_{ij} is the exchange constant between the i^{th} and j^{th} spins and it also represents the strength of the magnetic interaction. Furthermore, the sign of J_{ij} indicates whether the magnetic interaction between two spins is ferromagnetic ($J > 0$) or antiferromagnetic ($J < 0$).

Exchange interaction depends on the details of the overlap of the electronic wavefunctions between the ions. In perovskite oxides, there is very little direct overlap of the electronic wavefunctions of two nearest-neighbor Mn cations (direct exchange). However, the e_g orbitals strongly overlap with the oxygen $2p$ orbitals. Thus, the magnetic interactions in oxides are mediated by intervening oxygen (indirect exchange). There are two important magnetic interactions in oxides, namely superexchange and double exchange.

1.1.1.1 Superexchange

The superexchange interaction can be defined as an indirect exchange interaction between two neighboring magnetic ions separated by an intermediate nonmagnetic ion with a closed shell. This is a very common interaction in most of the oxides, especially in insulating magnetic oxides, where the intermediate ion is oxygen. If two orbitals on adjacent ions point towards each other, with one orbital fully occupied and the other orbital with a vacancy, then the electron will spend part of its time in the empty orbital of the other ion lowering the total kinetic energy by delocalizing over the bond. In the case of manganites, the electron is shared between an occupied O $2p$ orbital and a vacant Mn e_g orbital. This virtual transfer of the electron is at the origin of the "superexchange" interaction which can lead to either a ferromagnetic or an antiferromagnetic alignment of the spins, depending on the occupancy of the magnetic ions, as shown for example in Figure 1.3 for a Mn−O−Mn bond.

The occupancy as well as the orbital degeneracy of the $3d$ states are critical variables in determining superexchange strength and sign. There are many possible cases to consider and the results were summarized by the Goodenough-Kanamori rules [34, 35] which were formulated by Anderson [36]. In a simple way the rules state that:

i. When two half-filled e_g orbitals of identical ions point towards each other giving a strong overlap and large hopping integrals, it results in a strong antiferromagnetic ($J < 0$) interaction.

ii. When two t_{2g} orbitals point towards each other giving a poor overlap and small hopping integrals, it results in a weak antiferromagnetic ($J < 0$) interaction.

iii. When a half-filled e_g orbital points towards a t_{2g} orbital, it results in a ferromagnetic ($J > 0$) interaction.

The exchange constant is given by: $J \propto -t^2/U$, where t is the $p-d$ hopping integral and U is the on-site $3d$ Coulomb interaction. J depends on the interatomic

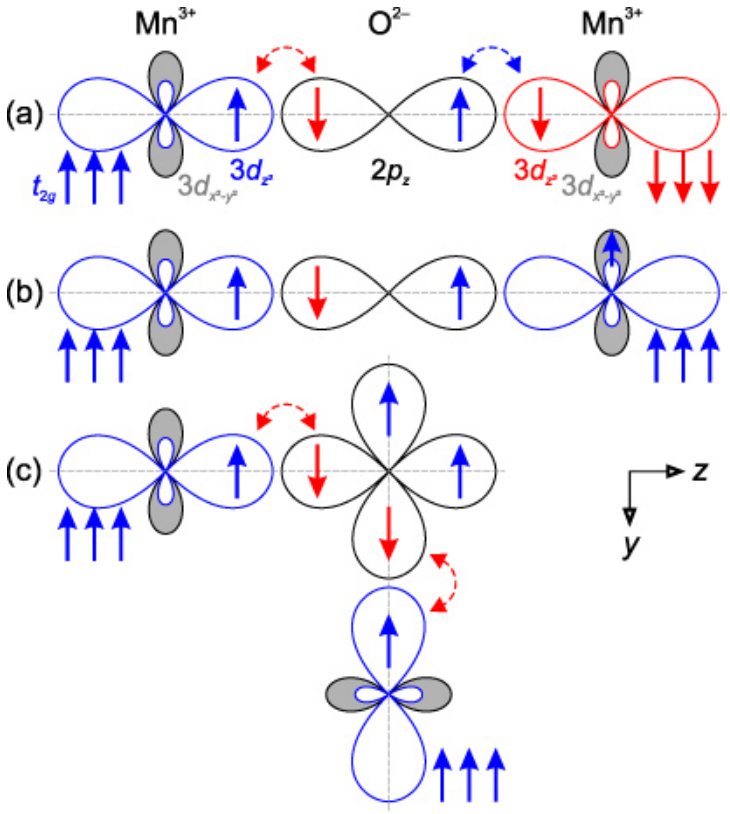

Figure 1.3: A diagram of the superexchange interaction for two Mn^{3+} ions separated by an O^{2-} ion. (a) The 180°-exchange interaction between two half-filled orbitals is relatively strong and antiferromagnetic. (b) In cases where an overlap between an occupied and an empty orbital occurs, the resulting 180°-exchange is ferromagnetic and relatively weak. (c) The 90°-exchange interaction between half-filled orbitals is ferromagnetic and relatively weak.

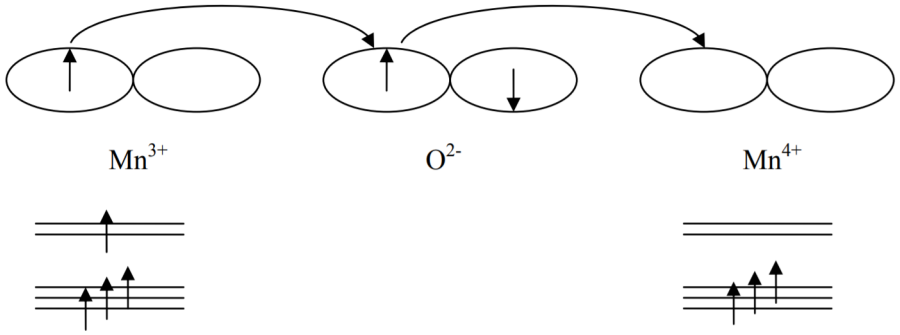

Figure 1.4: A schematic diagram of double exchange mechanism showing the virtual transfer of electrons between the adjacent Mn ions in the presence of an oxygen ion.

separation, but also on the Mn−O−Mn bond angle [37]. These rules need to be adjusted when, for example, the ions are not the same. In particular, it can lead to a strong ferromagnetic coupling if one ion has less than five electrons in the 3*d* orbitals while the other has more than five. This is at the origin of ferromagnetism in several double perovskites, like La_2NiMnO_6.

1.1.1.2 Double exchange

Double exchange interaction arises between 3*d* ions which have both localized and delocalized *d* electrons. It takes place in mixed valence materials, such as manganites that contain both Mn^{3+} and Mn^{4+} ions. The basic idea of double exchange mechanism was first proposed by Zener [38] to explain electrical resistivity in manganites. According to the Zener model, first an electron from the oxygen 2*p* orbital hops to the unoccupied e_g orbital of a Mn^{4+} ion and simultaneously a second electron with the same spin from the e_g orbital of the adjacent Mn^{3+} ion transfers to the same oxygen 2*p* orbital, as shown in Figure 1.4. In this mechanism, the e_g electrons can hop through the lattice from one Mn ion to another. In order for this hopping to take place, it must preserve the spin of the electron, imposing that the magnetic moments of adjacent Mn^{3+} and Mn^{4+} ions must be oriented ferromagnetically. In such a case, the onset of the ferromagnetic order coincides with the delocalization of the electrons.

This simple picture describes qualitatively the origin of the ferromagnetism in

the manganites and demonstrates the direct relation between hopping and FM ordering. Further theoretical work was performed by Anderson and Hasegawa [39] and de Gennes [40] to generalize the double-exchange mechanism by considering interaction between a pair of magnetic ions with general spin directions. They calculated the hopping amplitude of electrons in the Mn−O−Mn bonds which can be expressed as:

$$t_{ij} = t_0 \cos\left(\frac{\theta_{ij}}{2}\right) \tag{1.3}$$

where t_0 is the normal transfer integral and θ_{ij} is the angle between the core t_{2g} spins of neighboring Mn ions. This angle is intimately related to the Mn−O−Mn bond angle. It is clear that the hopping, t_{ij}, is the largest when $\theta_{ij} = 0$, while if $\theta_{ij} = \pi$, it corresponds to an antiferromagnetic background, and the transfer integral is zero.

1.1.2 $La_{1-x}Sr_xMnO_3$

Among perovskite manganites, mixed-valence $La_{1-x}Sr_xMnO_3$ (LSMO) compounds have been an optimal choice in different solid-state fields to test for various devices such as magnetic data storage, spintronic devices, high-sensitivity magnetic field sensors and magnetic cooling systems due to their high spin polarization and the highest transition temperature within the manganite family well above room temperature [4, 17, 41, 42]. The magnetic, transport, and structural properties of LSMO manganites depend on the amount of Sr dopant in the structure. The parent compound, $LaMnO_3$ is an A-type antiferromagnetic insulator with a magnetic phase transition at 140 K, which only contains Mn^{3+} ions. In order to preserve charge neutrality, mixed valent Mn^{3+} and Mn^{4+} ions start developing at the Mn-sites when trivalent rare-earth (La^{3+}) ions are substituted by divalent alkaline-earth elements such as Sr^{2+}.

The phase diagram of mixed-valence LSMO is shown in Figure 1.5. Once Sr-doping reaches $x \sim 0.1$ a low temperature ferromagnetic but insulating phase develops. By increasing the Sr^{2+} content (above $x > 0.17$), a ferromagnetic metallic ground state with a rhombohedral structure is stabilized where T_c reaches its maximum value at 370 K for $x \sim 0.3$ which represents the highest transition temperature for the manganite family. For $0.2 < x < 0.5$, the magnetic transition is followed by

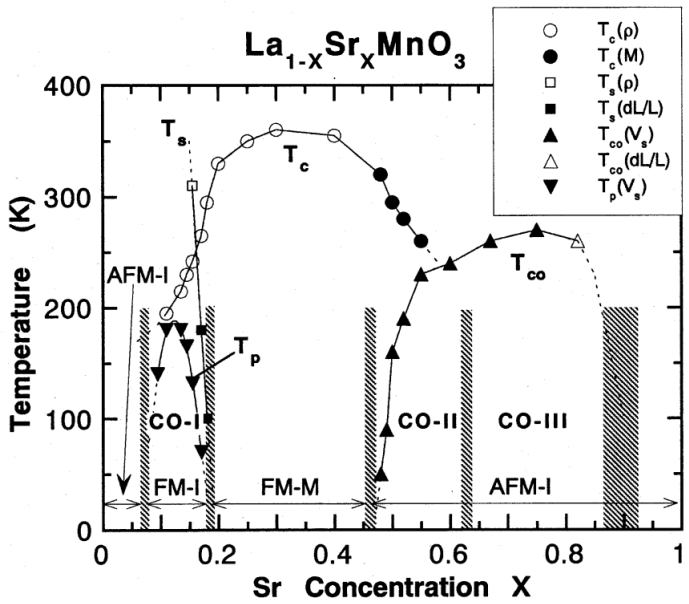

Figure 1.5: The phase diagram of $La_{1-x}Sr_xMnO_3$ for the entire doping regime [43]. T_c shows the Curie temperature which is determined from the $\rho(T)$ ($\circ$) and $M(T)$ ($\bullet$) values. T_s shows structural transition temperature which is determined from $\rho(T)$ ($\square$) and the dilatation $dL(T)/L$ ($\blacksquare$) values. T_{co} shows the charge-ordering temperature determined from the $v_s(T)$ ($\blacktriangle$) and the $dL(T)/L$ ($\triangle$) values. T_p shows the polaron-ordering temperature determined from the $v_s(T)$ minima ($\blacktriangledown$). The shaded regions correspond to the borders of the three types of charge ordering (CO-I, CO-II, and CO-III). AFM-I, FM-I, and FM-M imply antiferromagnetic insulator, ferromagnetic insulator, and ferromagnetic metal, respectively.

a metal-insulator transition which either can coincide or vary substantially with it depending on the structural defects and grain boundaries. For $x \gtrsim 0.5$, the crystal structure shifts from rhombohedral to tetragonal while the high-temperature magnetic phase remains FM metallic. With decreasing temperature, it undergoes a magnetic and structural transition into a monoclinic charge-ordered (CO-II) antiferromagnetic phase. Finally, for $x \gtrsim 0.6$, a purely insulating AFM phase with an almost cubic structure remains.

In general, the magnetic and transport properties of this type of correlated electrons system are governed by a competition between super-exchange and double exchange interaction. The properties of LSMO are mainly influenced by two parameters: the doping level of Sr which controls the Mn^{3+}/Mn^{4+} ratio, and the chang-

ing average size of the A-site cations, $\langle r_A \rangle$, which controls the tolerance factor, the average Mn−O bond length and the Mn−O−Mn bond angle of the MnO_6 octahedra. For hole-doped LSMO, the highest transition temperature ($T_c = 370\,K$) is obtained for $x = 0.33$ corresponding to an average A-site radius $\langle r_A \rangle \approx 1.24\,Å$ and the Mn−O−Mn bond angle of 166.3° [44].

Miller *et al* [45] have shown that double exchange alone cannot explain the transport properties in hole-doped LSMO. They proposed that there is a polaron effect due to a very strong electron-phonon coupling stemming from the Jahn-Teller splitting of the Mn^{3+} ion, which contributes to electronic transport. A strong electron-phonon coupling tends to localize carriers because the presence of an electron in the e_g orbital of a Mn^{3+} ion causes a local lattice distortion (often called "dynamical Jahn-Teller" effect), creating a potential minimum which prefers to trap the electron in that orbital. Electron-phonon coupling competes with the delocalizing tendency of electron hybridization. A dimensionless quantity λ is defined to parametrize the competition, where λ is the ratio of the energy E_{latt} gained from the electron-phonon coupling in the absence of hybridization to the bare electron kinetic energy t_{eff}, thus $\lambda \approx E_{latt}/t_{eff}$ [46]. In hole-doped manganites, variations of magnetic field and temperature as well as the doping concentration may change λ, since they affect spin correlation and tolerance factor, respectively. Several theoretical works [47, 48] have shown that the electron-phonon coupling governs the transport properties at high temperature, where t_{eff} is sufficiently small, so λ is large and the electron-phonon interaction localizes the electrons. By decreasing the temperature, the ferromagnetic order starts developing in the system which increases t_{eff}, leading to metallic behavior below the transition temperature.

1.1.2.1 Control of $La_{2/3}Sr_{1/3}MnO_3$ properties

The magnetic and electronic properties of LSMO strongly depend on lattice-charge-spin coupling, which is very sensitive to phase/structural transformations, oxygen stoichiometry, growth temperature, and lattice distortions induced by doping and substrate-induced strain. For instance, the effect of substrate-induced strain on the electrical transport and magnetic properties of epitaxial LSMO thin films has been extensively studied (see for example [49–51]). Over the years, thin films of LSMO

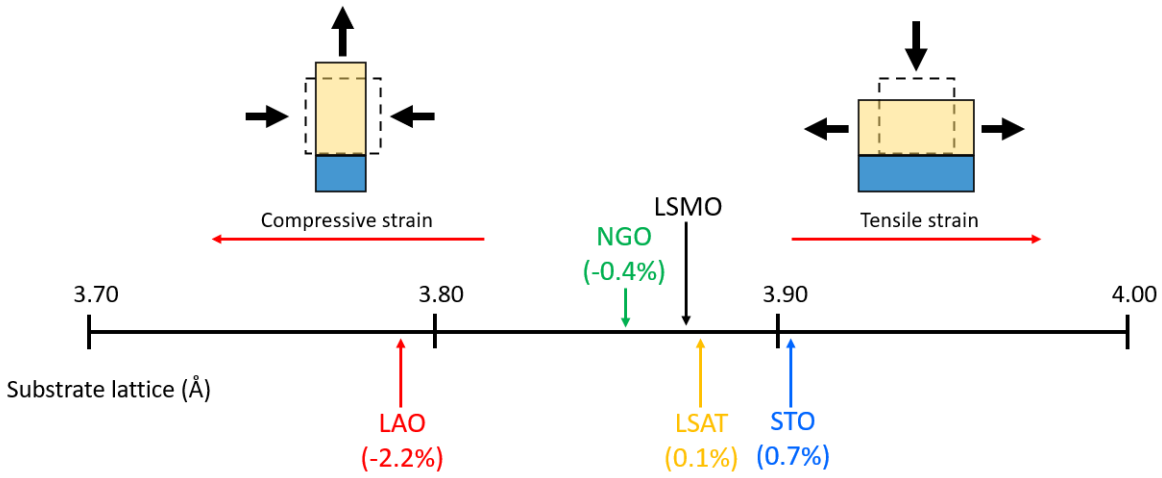

Figure 1.6: The lattice mismatch between LSMO manganite and LAO, NGO, LSAT, and STO substrates. Schematic of the LSMO unit cell distortion in a strained epitaxial film under tension and compression. Dashed line (square) is a schematic of the bulk (unstrained) lattice.

have been grown on various substrates with different lattice parameters such as (001)-oriented $SrTiO_3$ (STO), $La_{0.18}Sr_{0.82}Al_{0.59}Ta_{0.41}O_3$ (LSAT), $LaAlO_3$ (LAO), and $NdGaO_3$ (NGO) single crystals. Polycrystalline $La_{2/3}Sr_{1/3}MnO_3$ has rhombohedral crystal structure with a pseudocubic lattice parameter of 3.876 Å which results in the lattice mismatch of 0.1 %, 0.7 %, −0.4 %, and −2.2 % with LSAT, STO, NGO, and LAO substrates, respectively. It has been shown by Dho *et al* [52] that LSMO layer undergoes a uniaxial compressive strain on NGO and LAO substrates, whereas LSMO layers on STO substrates is under a biaxial tensile stress. As a result of the different types of stress, the easy magnetization direction changes from out-of-plane on LAO substrates to in-plane on STO substrates. Figure 1.6 presents the lattice mismatch between LSMO and different substrates, as well as the distortion of LSMO pseudocubic unit cell under compressive and tensile strains.

The substrate-induced lattice strain can be decomposed into a bulk strain $\epsilon_B = (\epsilon_{xx} + \epsilon_{yy} + \epsilon_{zz})$ and a Jahn-Teller strain $\epsilon_{JT} = \sqrt{1/6}(2\epsilon_{zz} - \epsilon_{xx} - \epsilon_{yy})$. Increasing the magnitude of the Jahn-Teller strain ϵ_{JT} leads to a decrease in the magnetic transition T_c, and the saturation magnetization as well as an increase in the resistivity due to the localization of charge carriers by MnO_6 octahedra distortions. It was shown that the T_c of $La_{2/3}Sr_{1/3}MnO_3$ layer shifts from 350 K on LSAT to 300 K on LAO substrate, indicating that large lattice mismatches

weaken the magnetic properties in thin films [51]. Moreover, in the case of LAO, Jahn-Teller strain is large enough ($\epsilon_{JT} = 3.59\,\%$) to bring insulating behavior even below T_c. This is a clear evidence of the localization of carriers due to Jahn-Teller strain.

Another important factor that affects remarkably the magnetic and transport properties of doped manganite perovskites is oxygen deficiency. Generally, manganites are influenced by oxygen deficiency in many different ways. First of all, each loss of oxygen leads to the conversion of two Mn^{4+} ions into Mn^{3+} ions in order to preserve the charge neutrality. It alters the ratio of Mn^{4+}/Mn^{3+} in the system, which is equivalent to changing the concentration of doping. Second, oxygen vacancies breakdown Mn−O−Mn bond chains and disrupt the long-range magnetic order in the structure, resulting in a significant decline in the bandwidth of the conduction band. Accordingly, the resistivity of samples increases and the metal-insulator transition shifts towards lower temperatures as the oxygen vacancy density increases. Third, lattice distortions and even phase transition are observed in oxygen-deficient LSMO and other doped manganites. These effects will cause significant changes in structural, transport and magnetic properties of manganites. There have been many studies about the effect of oxygen pressure during synthesis on magnetic and transport properties of LSMO films [53, 54]. Kumari *et al* have grown 30 nm-thick $La_{2/3}Sr_{1/3}MnO_3$ films using pulsed laser deposition at various oxygen partial pressures: 10, 30, 50, 100, 150, 200 and 250 mTorr [54]. It was found that the samples synthesized at 200 mTorr show the highest transition temperature at 345 K, while the highest magnetization with the lowest average roughness were observed in the samples grown at 150 mTorr. It has been concluded that these two samples might exhibit the lowest density of oxygen vacancies and defects due to the low roughness and high magnetization values. The 150–200 mTorr probably represents the optimal oxygen pressure range to grow LSMO. Temperature dependence of the magnetization for samples grown at different pressures is shown in Figure 1.7.

Finally, the deposition temperature is also a very important parameter which influences the film microstructure and consequently, the magnetic and transport properties. It has been shown that the LSMO thin films deposited at low tempera-

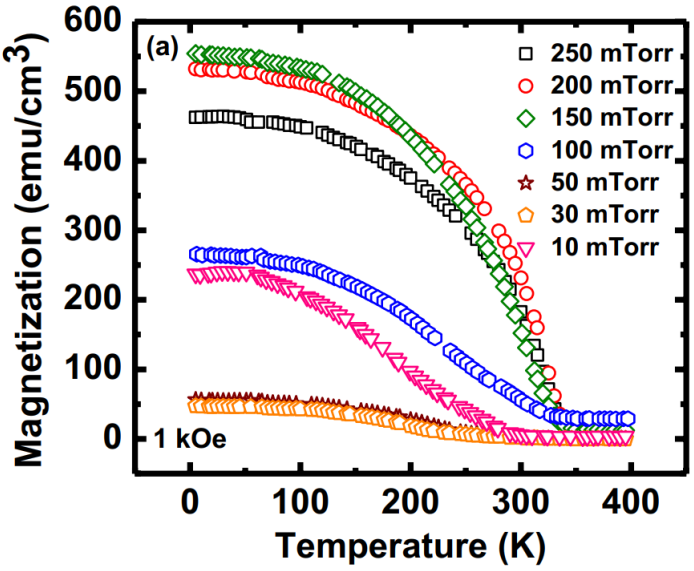

Figure 1.7: The magnetization versus temperature of the LSMO films grown at various deposition pressures [54].

ture, below 550 °C, are amorphous or mixed amorphous and crystalline phases, while those deposited at higher temperatures (above 600 °C) are epitaxial [55]. Generally, increasing the substrate temperature leads to a gradual evolution from the PM state to the FM state at the Curie temperature as well as transitioning from the insulating to the metallic state due to the increased structural order which stabilizes the ferromagnetic and metallic phases. In a study by Wang *et al* [53], LSMO thin films were deposited on STO single crystalline substrates using PLD at different substrate temperatures ranging from 650 to 850 °C. It was found that the smoothest films were grown at 750 °C, while the samples made at 800 °C show the maximum surface roughness, about 2.5 nm. It was concluded from this study that a high oxygen partial pressure and a relatively low substrate temperature ($T = 750\,^{\circ}\mathrm{C}$) is necessary to promote the layer-by-layer growth of LSMO films. However, for the films grown at higher substrate temperature ($T = 800\,^{\circ}\mathrm{C}$), the growth mode changes from layer-by-layer to island growth. Moreover, the T_c and saturation magnetization reach their maximum values for samples grown at 800 °C, and by increasing the substrate temperature the magnetic properties do not improve anymore, indicating that 800 °C might be the optimal temperature to grow LSMO.

1.2 Double perovskites

Another family of perovskite-type materials known as the double perovskites (DPs) has a similar crystallographic structure to simple perovskite materials (manganites). DPs with the general formula $AA'BB'O_6$ consist of two interpenetrating simple perovskite ABO_3 and $A'B'O_3$ structures, where A and A′ are generally alkaline-earth or lanthanoid ions and B and B′ are two distinct transition metal ions. The investigation of DPs dates back to 1961 when a ferromagnetic behavior was observed in rare-earth-based DP by Longo and Ward [56]. Afterwards, a slow progress was made until 1998 when a large room temperature magnetoresistive effect at low magnetic field was discovered in Sr_2FeMoO_6 by Kobayashi [57]. Regarding the fact that some DPs show metallic ferromagnetic behavior with high transition temperature up to 635 K and have a highly polarized conduction band make these materials interesting for spintronic devices such as magnetic tunnel junctions, low-field magnetoresistive sensors, and spin injection devices.

Figure 1.8 shows the crystal structure of DPs which, similarly to simple perovskites, is based on a pseudo-cubic sublattice and belongs to the $Fm\bar{3}m$ space group. The unit cell is doubled in each direction as compared to simple perovskites, and also two different atoms with the same coordination located on the B sites. The positions of the atoms in the pseudo-cubic DP sub-cell are $(0,0,0)$ and $(\frac{1}{2},\frac{1}{2},\frac{1}{2})$ for the two B site atoms and $(\frac{1}{4},\frac{1}{4},\frac{1}{4})$ for the A/A′ site atoms. The oxygen anions sit at $(x,0,0)$ where $x \approx \frac{1}{4}$.

1.2.1 Cation ordering in double perovskites

Cation ordering in DPs can occur on both the A and B sites and it is classified into three simple patterns, rock salt, columnar, and layered (Figure 1.9). The probability of the cation ordering either at the A or B sites strongly depends on the difference in ionic charges and ionic sizes between A and A′ ions, and B and B′ ions. In general, a charge difference of $\geq$2 e or a size difference of $\geq$10 % is needed to induce ordering [58]. B site ordering is more commonly observed in DPs [6].

Rock-salt ordering is the most favorable pattern in the case when one of the two

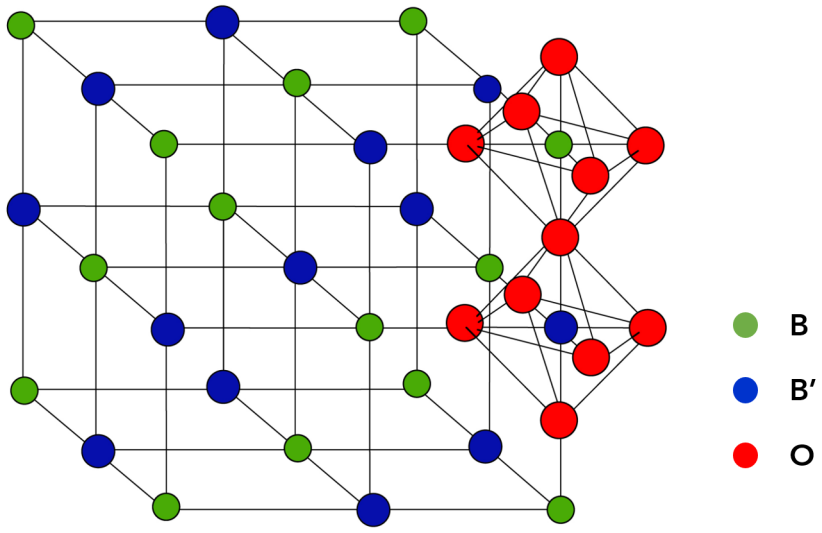

Figure 1.8: Schematic structure of $AA'BB'O_6$ double perovskite. The A / A′ site atoms are at the body-center positions of each cubic units but are not shown for clarity.

cations A or B is more highly charged than the other, A′ or B′. From an electrostatic point of view, the rock-salt pattern maximizes the separation of the more highly charged cations. In this configuration, each B (A) cation is surrounded by six B′ (A′) as its nearest neighbors. The next most favorable arrangement among DPs is columnar ordering where each B (A) cation has four B′ (A′) and two B (A) nearest neighbors. Layered ordering is the least favorable electrostatic arrangement where each B (A) cation has four B (A) and two B′ (A′) nearest neighbors. A summary of different types of ordering in DPs is given in Table. 1.1, together with materials known to adapt these different structures.

1.2.2 Magnetic order in double perovskites

The large number of possible combinations of B and B′ in DPs gives rise to different magnetic phases, such as ferromagnetic, antiferromagnetic and spin glass. In some DPs ($A_2BB'O_6$) where B has partially filled e_g orbitals, while B′ has empty e_g orbitals or vice versa, a unique opportunity is provided to promote multiferroic behaviors due to their ferromagnetic insulating behavior, owing to the 180°-superexchange interactions between B and B′ cations via the oxygen ions.

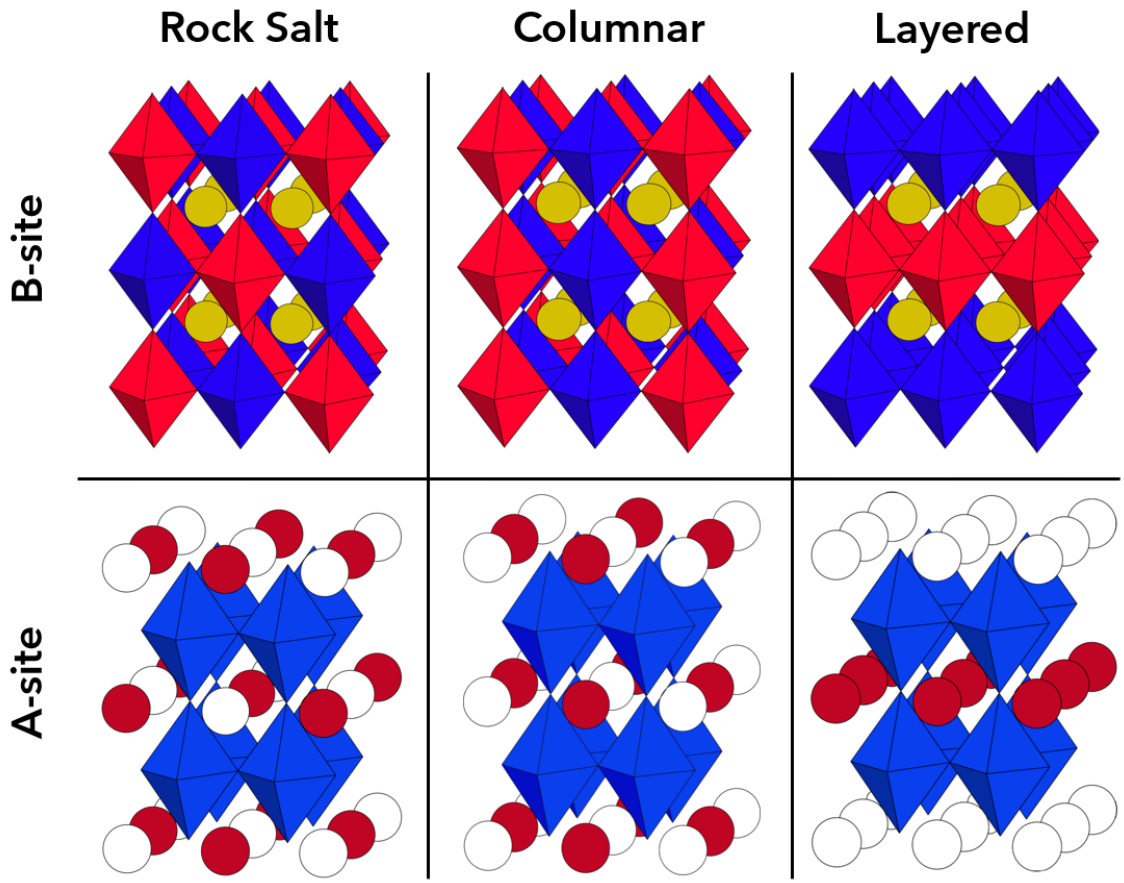

Figure 1.9: Illustration of the rock-salt, columnar, and layered ordering of A and B cations in double perovskites.

Table 1.1: A summary of the different types of cation ordering observed in double perovskites [6].

Ordering type		Space group	Example
B-site	Rock-salt	$Fm\bar{3}m$	La_2NiMnO_6
	Columnar	$P4/mmm$	$NdSrMn^{3+}Mn^{4+}O_6$
	Layered	$P4/mmm$	La_2CuSnO_6
A-site	Rock-salt	$Fm\bar{3}m$	$NaBaLiNiF_6$
	Columnar	$P4_2/nmc$	$CaFeTi_2O_6$
	Layered	$P4/mmm$	$NaLaMgWO_6$

La_2NiMnO_6 and La_2CoMnO_6 are examples of ferromagnetic insulating DPs that exhibit also magnetodielectric responses due to coupling between the magnetization and polarization order parameters [59].

Ferromagnetic metallic phase is also observed in DPs where either one of the B-site ions or both of them are intrinsically magnetic. Sr_2FeMoO_6 DP belongs to the first category where only Fe ions are magnetic, while Sr_2FeReO_6, Ca_2FeReO_6, and Sr_2CrReO_6 DPs would be in the second category.

For some combinations of B and B′, DPs exhibit antiferromagnetic insulating characteristics. Sr_2FeWO_6 is a member of this family with an antiferromagnetic transition at 40 K. In this case, the $3d$-element, Fe^{2+} ion, is in the high spin state ($S = 2$), and $5d$-element, W^{6+} ion, is in a non magnetic state ($5d^0$). Localized electrons at the Fe-site give rise to a large exchange splitting. Strong hybridization between the $5d$-orbitals of W and the $2p$-orbitals of O drives the hybridized states above the t_{2g} down level of Fe. The electron is transferred from the W−5 d O−2 p hybridized state to the Fe $3d$ level, leading to an insulating compound with formally W^{6+} and Fe^{2+} states [60].

The spin glass phase is generally caused either by a large B-site disorder or by a structural frustration. For instance, in Sr_2FeCoO_6, the B-site is randomly occupied by Fe and Co ions in the mixed valence states of Fe^{3+}/Fe^{4+} and Co^{3+}/Co^{4+}. The very similar ionic radii of the B-site cations (Fe and Co) results in a large B-disorder in the sample. This random distribution of B-site cations causes a competition between nearest-neighbor and next-nearest-neighbor superexchange interactions giving rise to local magnetic frustration in the lattice which can explain the spin glass behavior in Sr_2FeCoO_6 DPs [61]. On the other hand, in Ba_2YMoO_6 DPs, Mo is in its 5+ oxidation state (Mo^{5+}, S=$\frac{1}{2}$) with a singly occupied degenerate t_{2g} orbital in a cubic crystal field, while Y^{3+} ion does not carry any magnetic moment. The Mo^{5+} ions are located on an FCC sublattice and coupled antiferromagnetically. This arrangement is geometrically frustrated, which, in conjunction with quantum fluctuations, gives rise to spin glass behavior in Ba_2YMoO_6. It has been reported that AC and DC magnetic susceptibility, heat capacity and muon spin rotation experiments were not able to detect any magnetic order down to 2 K [62].

1.2.3 La_2NiMnO_6

Among DPs, La_2NiMnO_6 (LNMO) has been widely studied due to its ferromagnetic insulating nature, with a near room temperature phase transition as well as large magnetodielectricity [63] and large magnetocaloric effect [18, 64]. In particular, LNMO has attracted a great deal of attention because of its rich physics and potential applications in spintronics, such as magnetodielectric capacitors, spin based sensors, multiple state memory elements and spin tunneling junctions [65, 66]. The crystal structure of LNMO strongly depends on the B-site cationic ordering. In the case of disordered LNMO, where Mn^{4+} and Ni^{2+} cations are randomly distributed at the B and B′ sites, the crystal structure is orthorhombic in the *Pbnm* symmetry with the lattice parameters $a = 5.5035$ Å, $b = 5.4527$ Å, and $c = 7.7279$ Å [67]. In contrast, when Mn^{4+} and Ni^{2+} cations are alternatively occupying B/B′ sites known as ordered LNMO, it leads to a monoclinic crystal structure (space group: $P2_1/n$) with the lattice parameters $a = 5.467$ Å, $b = 5.510$ Å, and $c = 7.751$ Å [68]. Figure 1.10 shows the distribution of Mn^{4+} and Ni^{2+} cations in the crystal structure of ordered and disordered LNMO. There is an intermediate configuration where no long-range order is observed at B/B′ sites. In this case, B-site ordering is limited to a few unit cells or domains, resulting in an admixture phase which is thermodynamically stable.

As mentioned earlier, different combinations of B and B′ in DPs lead to a variety of magnetic states. For instance, cation ordering in LNMO leads to a ferromagnetic superexchange interaction between $Mn^{4+}(d^3 : t_{2g}^3\, e_g^0)$-$O^{2-}$-$Ni^{2+}(d^8 : t_{2g}^6\, e_g^2)$ resulting in a second-order magnetic phase transition at 285 K with a saturation magnetization of 5 μ_B/f.u. [5, 18, 63]. It was shown that there may be antiphase boundaries even in highly ordered LNMO DP [69]. The antiphase boundaries couple adjoining ferromagnetic domains antiferromagnetically at zero field, but a modest applied magnetic field is able to rotate the ferromagnetic domains with a 360° spin rotation across the antiphase boundaries, giving rise to small remanence in the hysteresis loop. In the case of disordered LNMO, anti-site disorder leads to superexchange antiferromagnetic coupling between $Mn^{4+}-O^{2-}-Mn^{4+}$ and $Ni^{2+}-O^{2-}-Ni^{2+}$ bonds in addition to the $Mn^{4+}-O^{2-}-Ni^{2+}$ bonds which drives the transition temperature of cation-disordered LNMO down to 170 K [5].

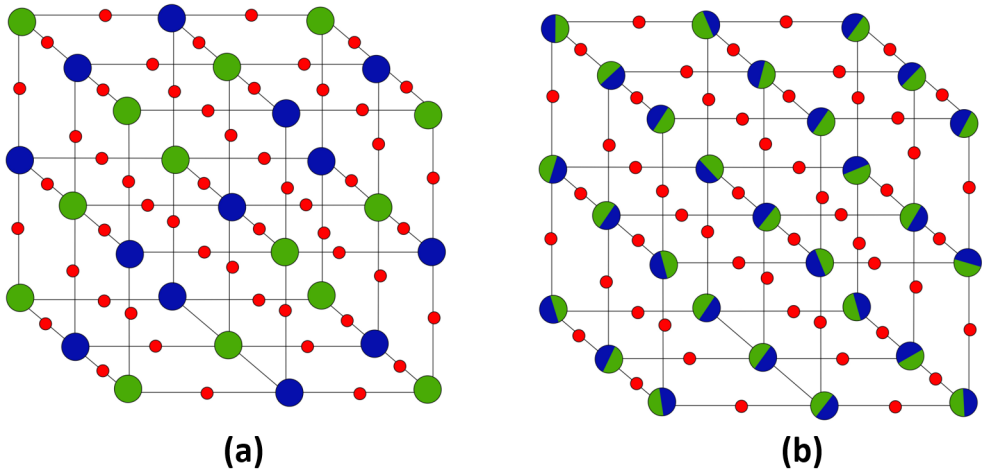

Figure 1.10: The distribution of Mn^{4+} (blue) and Ni^{2+} (green) cations in the pseudocubic LNMO leading to (a) ordered and (b) disordered phase. The red circles represent oxygen atoms. The La ions are not shown for clarity.

Furthermore, the saturation magnetization of disordered LNMO is found to be around $2\,\mu_B$/f.u. which is significantly lower than ordered LNMO. Sometimes another magnetic transition is seen at low temperature especially for biphase samples. This low temperature transition at 140 K is attributed to the superexchange interaction for $Mn^{3+}-O^{2-}-Ni^{3+}$ bonds [70]. Examples of the resulting temperature dependence of the magnetization of ordered LNMO, disordered LNMO, and admixture phase in thin films is shown in Figure 1.11. According to studies [10, 71], epitaxial strain can also affect the structural and magnetic properties in LNMO DPs. Wu *et al* [10] studied multiferroic thin films of double-perovskite LNMO epitaxially grown on $SrTiO_3$, $KTaO_3$, $LaAlO_3$ and $DyScO_3$ substrates by pulsed laser deposition. It is found that LNMO films under tensile strain exhibit a monoclinic structure, while under compressive strain the crystal structure of LNMO films is rhombohedral. In addition, by optimizing the film deposition conditions (in particular, pressure and temperature) a long-range ordering of B-site cations in LNMO films has been obtained in both monoclinic and rhombohedral phases [5].

The band gap of LNMO was calculated to be around 1.2 eV [72] explaining the semiconducting nature of LNMO. This semiconducting behavior is confirmed from the resistivity measurement in the whole temperature range up to 400 K (Figure 1.12) [73]. In contrast to other manganites, the temperature dependence of

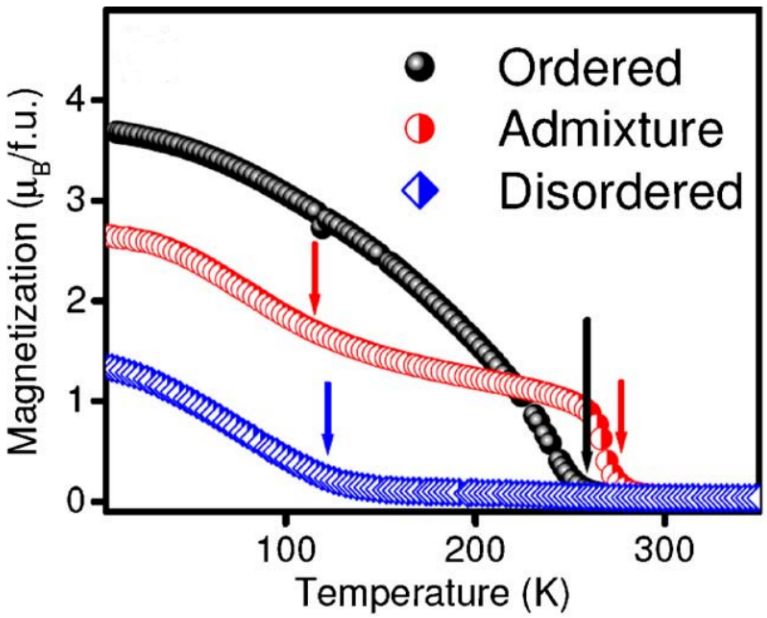

Figure 1.11: The magnetization as a function of temperature for ordered LNMO, disordered LNMO, and admixture phase [5].

resistivity for LNMO does not show any anomaly across the magnetic transition. Various types of conduction mechanisms such as thermally activated conduction, variable range hopping (VRH), small polaron hopping (SPH) and Schnakenberg's polaronic conduction have been proposed to understand the mechanism of conduction. Among these models, Schnakenberg's model has been found to fit satisfactorily in three magnetic regimes [74]. The deviation of this model for different magnetic regimes indicates a strong correlation between the transport and magnetic properties of LNMO. According to this model, the resistivity varies with temperature as follows:

$$\rho(T) = AT\left[\sinh\left(\frac{h\upsilon_o}{k_B T}\right)\right]^{\frac{-1}{2}} \exp\left[\left(\frac{4\omega_H}{h\upsilon_o}\right) \times \tanh\left(\frac{h\upsilon_o}{4k_B T}\right)\right] \exp\left(\frac{\omega_D}{k_B T}\right) \quad (1.4)$$

where A is a constant, ω_D is the disorder energy, ω_H is the polaron hopping energy, and υ_o is the phonon frequency (Debye). It was found that the activation energy of the polaron and the disorder energy decrease with the lowering of temperature which is consistent with the theory [74].

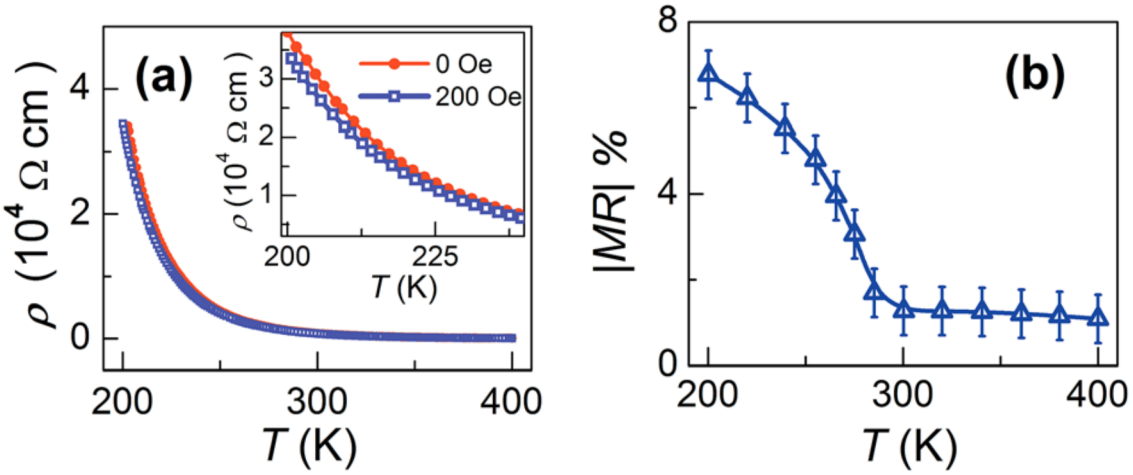

Figure 1.12: The temperature dependence of the resistivity ρ in 200 K$\leq$ T $\leq$ 400 K for LNMO both under zero and 200 Oe magnetic field. (b) Temperature dependence of the absolute value of MR under 200 Oe [73].

There is an inflection point around T_c on the MR versus temperature curve. Above this point, in the paramagnetic region, the value of MR is less than 1.5 % and remains almost unchanged with temperature. However, below T_c, the value of MR increases rapidly upon cooling. According to this observation, LNMO has a spin-dependent MR [73].

In this thesis, we present two studies of the properties of heterostructures made of LSMO and LNMO. First, in Chapter 2, we explore the magnetic and magnetocaloric properties of bilayer and trilayer samples. Then, in Chapter 3, we use one type of our trilayer samples to examine the tunnel magnetoresistance through a ferromagnetic insulating barrier in magnetic tunnel junctions.

Chapter 2

Magnetocaloric effect in oxide heterostructures

2.1 Theoretical concepts

The magnetocaloric effect (MCE) is defined as the temperature change produced by the adiabatic application of an external magnetic field, or the magnetic entropy change produced by the isothermal application of an external magnetic field to a magnetic substance. This phenomenon was first discovered by P. Weiss and A. Piccard in 1918 when they were studying the magnetic properties of nickel (Ni). They observed a reversible heating and cooling of the Ni sample near its transition temperature at 627 K observed as a change of its temperature when an applied magnetic field was varied [75]: they named it a "novel magnetocaloric phenomenon". In 1927 Debye and Giauque proposed that this effect can be used to reach ultra-low temperature, below 1 K [76]. The first prototype of magnetic cooling systems was made in 1933 using $Gd_2\,(SO_4)_3 \cdot 8\,H_2O$ paramagnetic salts as a magnetic coolant, which could reach 0.25 K in a process known as adiabatic demagnetization [77]. Afterwards, a slow progress in this field was made until the late 1970s when it was recognized that a much larger MCE can be obtained in ferromagnets in the vicinity of their Curie temperature.

The first breakthrough on magnetic refrigeration close to room temperature

was achieved by Brown [78] in 1976 when he demonstrated that a large MCE at around 294 K can be obtained with the use of gadolinium (Gd) as the working material. He showed that a continuously operating device could reach a temperature span of 47 K after 50 magnetic Stirling cycles using a fluid including 80 % water and 20 % alcohol as a regenerator. In 1978, the concept of active magnetic regenerator (AMR) was introduced by Steyert [79] where he proposed that the magnetocaloric material can simultaneously act as the refrigerant material and the regenerator. It has been demonstrated that a much larger temperature span than the adiabatic temperature change can be achieved by AMR cycles. Therefore, the AMR has proven to be the only type of magnetic cooling scheme which can compete with other modern cooling technologies.

2.1.1 Thermodynamic cycle

In order to explain the origin of the MCE, we use thermodynamics which relates the magnetic variables such as magnetization and magnetic field to entropy and temperature. The thermodynamic cycle of magnetic cooling systems is analogous to the Carnot refrigeration cycle. The only difference is that in magnetic cooling systems, the magnetic field is increased or decreased instead of pressure. The principle of a magnetic refrigeration cycle is depicted in Figure 2.1. This cycle includes four processes:

i. Adiabatic magnetization a $\rightarrow$ b: Initially the magnetic material is at the temperature T and magnetic moments are oriented randomly. An external external magnetic field is applied in adiabatic condition, and all the magnetic moments try to align themselves with the direction of the applied magnetic field. The decrease of magnetic entropy during the transformation causes an increase in lattice entropy and temperature $T + \Delta T_{\mathrm{ad}}$.

ii. Isofield heat extraction b $\rightarrow$ c: In this step, the extra heat ΔT_{ad} is removed from the material to the hot reservoir by an exchange liquid or gas. After the heat transfer the temperature is back at T.

iii. Adiabatic demagnetization c $\rightarrow$ d: Once the magnetic field is removed adiabatically, all the magnetic moments try to randomize themselves, this randomization needs energy which is provided by the system (by the lattice). So, as a result, the temperature of the system decreases to $T - \Delta T_{ad}$.

iv. Isofield heat absorption d $\rightarrow$ a: The reverse adiabatic temperature change $-\Delta T_{ad}$ is removed by a heat-transfer medium between the load (the volume being cooled) and the active material which leads to a temperature decrease of the cold reservoir. Once the sample and the cold reservoir reach a thermal equilibrium state, the refrigeration cycle resumes. Depending on the operating temperature, the heat-transfer medium can be water or air, and for very low temperatures, gas such as helium (depending on the temperature range of operation).

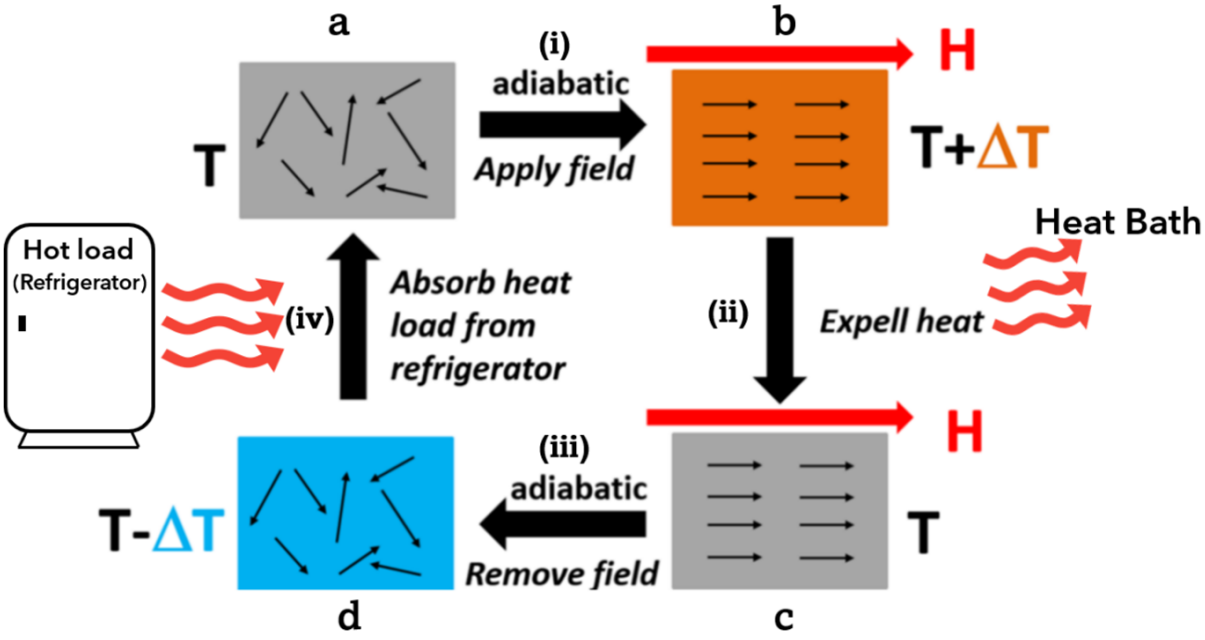

Figure 2.1: Schematic representation of a magnetic refrigeration cycle which transports heat from a heat load to its surroundings.

All magnetic materials intrinsically show MCE, however the intensity of the effect depends on the properties of each material. In a magnetic system, the origin

of MCE is the coupling of the magnetic moments and the external magnetic field which changes the magnetic entropy contribution to the total entropy. The total entropy $S(B,T)$ of a magnetic substance at a constant pressure is a function of both magnetic field (B) and temperature (T), and is represented by:

$$S\left(B,T\right) = S_{\mathrm{m}}\left(B,T\right) + S_{\mathrm{lat}}\left(B,T\right) + S_{\mathrm{el}}\left(B,T\right) \tag{2.1}$$

where S_{m}, S_{lat}, and S_{el} are the magnetic, lattice and electronic contributions to the total entropy, respectively. In general, the magnetic field dependence of S_{lat} and S_{el} can be neglected, while S_{m} is very sensitive to the external magnetic field. Figure 2.2 shows the total entropy of a ferromagnetic material as a function of temperature in the vicinity of T_{c}, under an external magnetic field $(\mu_0 H \neq 0)$ and zero field $(\mu_0 H = 0)$. Two reversible processes are depicted in Figure 2.2 which help to understand the thermodynamics of the MCE.

- **Isothermal condition:** in this process the magnetic field is varied in isothermal condition (temperature remains constant). When an external magnetic field is applied, it is aligning the magnetic moments along its direction. As a result, the magnetic entropy decreases and consequently, the total entropy decreases. Reversely, a decreasing applied magnetic field implies an increase in entropy. The total entropy change which is known as the isothermal entropy change, is defined as:

$$\Delta S_{\mathrm{m}}(T,\Delta B) = S_f(T,B_f) - S_i(T,B_i) \tag{2.2}$$

- **Adiabatic condition:** the total entropy is conserved in adiabatic condition. By varying the magnetic field, the magnetic entropy decreases but the total entropy does not change $\left(S_f(T_f,B_f) = S_i(T_i,B_i)\right)$. In order to keep the total entropy constant, the lattice and electronic entropy have to change in opposite ways to compensate the magnetic entropy loss. It means the temperature of the sample increases. This temperature change is called the adiabatic temperature change and it is given by:

$$\Delta T_{\mathrm{ad}}(T,\Delta B) = T_f(B_f) - T_i(B_i) \tag{2.3}$$

In a reversible process, once the magnetic field is removed the magnetic entropy increases and the lattice and electronic entropy decrease, therefore the material is forced to cool down.

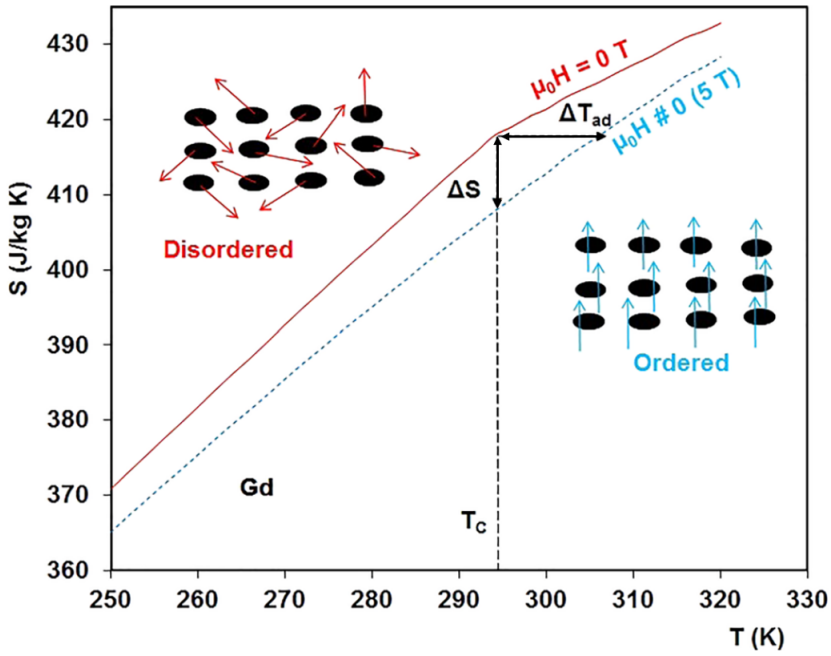

Figure 2.2: The total entropy of a ferromagnetic material (Gd) under zero and non-zero magnetic field near its transition temperature [13].

The adiabatic temperature change (ΔT_{ad}) and the isothermal magnetic entropy change (ΔS_m) are the most commonly used figures of merit to assess the potential of magnetocaloric materials. They will be discussed in detail in the following sections.

2.1.2 Thermodynamic principles

The origin of the MCE lies in the change of the internal energy U due to a change in an external magnetic field. In order to understand the MCE behavior, the description of Gibbs free energy (G) can be used. G is a function of the internal energy (U), intrinsic variables such as the total entropy (S), the volume (V) and the magnetization (M) and external parameters such as the temperature (T), the pressure (P) and the magnetic field (B):

$$G = U - TS + PV - MB \tag{2.4}$$

The total differential of G is given by:

$$\mathrm{d}G = \mathrm{d}U - T\,\mathrm{d}S - B\,\mathrm{d}M + P\,\mathrm{d}V - S\,\mathrm{d}T - M\,\mathrm{d}B + V\,\mathrm{d}P \tag{2.5}$$

The first law of thermodynamics ($\mathrm{d}U = T\,\mathrm{d}S + B\,\mathrm{d}M - P\,\mathrm{d}V$) can be used to simplify the equation as follows:

$$\mathrm{d}G = V\,\mathrm{d}P - S\,\mathrm{d}T - M\,\mathrm{d}B \tag{2.6}$$

The expression for S, M and V can then be derived from Eq. 2.6 as follows:

$$S(T,P,B) = -\left(\frac{\partial G}{\partial T}\right)_{P,B} \tag{2.7}$$

$$M(T,P,B) = -\left(\frac{\partial G}{\partial B}\right)_{P,T} \tag{2.8}$$

$$V(T,P,B) = \left(\frac{\partial G}{\partial P}\right)_{T,B} \tag{2.9}$$

Based on Eq. 2.7 and 2.8, the so-called Maxwell relation can be obtained which links the entropy change to the bulk magnetization, the temperature and the external magnetic field through the following equation:

$$\left(\frac{\partial S}{\partial B}\right)_{T,P} = \left(\frac{\partial M}{\partial T}\right)_{B,P} \tag{2.10}$$

The total differential of S depends on T, H and P. In the case of isobaric condition, $\mathrm{d}S$ is:

$$dS = \left(\frac{\partial S}{\partial T}\right)_B dT + \left(\frac{\partial S}{\partial B}\right)_T dB \tag{2.11}$$

Thus, the isothermal ($dT = 0$) entropy change ΔS_m can be calculated by integrating Eq. 2.11 under a magnetic field changing from B_1 to B_2, as follows:

$$\Delta S_m(T, \Delta B) = \int_{B_1}^{B_2} \left(\frac{\partial M}{\partial T}\right)_H dB \tag{2.12}$$

Eq. 2.12 indicates that the magnetic entropy change depends on the external magnetic field variation and the nature of the magnetic phase transition. Furthermore, the isothermal magnetic entropy change can be obtained directly from the second law of thermodynamics using the heat capacity which is defined as:

$$C_p = \left(\frac{\delta Q}{dT}\right)_P \tag{2.13}$$

from the second law of thermodynamics we have $dS = \frac{\delta Q}{T}$, so the heat capacity can be written as:

$$\frac{C_p}{T} = \left(\frac{\partial S}{\partial T}\right)_P \tag{2.14}$$

which allows us to calculate the isothermal magnetic entropy change from the heat capacity:

$$\Delta S_m(T, \Delta B) = \int_0^T \frac{C_p\left(T', B_f\right) - C_p\left(T', B_i\right)}{T'} dT' \tag{2.15}$$

Another important parameter which is used to characterize magnetocaloric materials is the adiabatic temperature change (ΔT_{ad}). It is the temperature change in a magnetic material during magnetization and demagnetization processes under

adiabatic and isobaric conditions. In order to calculate the adiabatic temperature change, we start with the total differential of the entropy in a closed system:

$$\mathrm{d}S\left(P,T,B\right)=\left(\frac{\partial S}{\partial P}\right)_{T,B}\mathrm{d}P+\left(\frac{\partial S}{\partial T}\right)_{P,B}\mathrm{d}T+\left(\frac{\partial S}{\partial B}\right)_{P,T}\mathrm{d}B \tag{2.16}$$

In adiabatic and isobaric conditions, it can be assumed that $\mathrm{d}S=0$ and $\mathrm{d}P=0$. Hence, Eq. 2.16 becomes:

$$\left(\frac{\mathrm{d}T}{\mathrm{d}B}\right)=-\left(\frac{\partial S}{\partial B}\right)_{T}\left(\frac{\partial T}{\partial S}\right)_{B} \tag{2.17}$$

By replacing the Maxwell relation (Eq. 2.10) and the specific heat relation (Eq. 2.14), Eq. 2.17 can be rewritten as follows:

$$\mathrm{d}T=-\left(\frac{T}{C_P\left(T,B\right)}\right)_{B}\left(\frac{\partial M}{\partial T}\right)_{B}\mathrm{d}B \tag{2.18}$$

The adiabatic temperature change (ΔT_{ad}) can be calculated by integrating Eq. 2.18 under a magnetic field changing from B_i to B_f

$$\Delta T_{\mathrm{ad}}\left(T,\Delta B\right)=-\int_{B_i}^{B_f}\left(\frac{T}{C_P\left(T,B'\right)}\right)_{B'}\left(\frac{\partial M\left(T,B'\right)}{\partial T}\right)_{B'}\mathrm{d}B' \tag{2.19}$$

According to Eq. 2.15 and 2.19, the isothermal entropy change (ΔS_{m}) and the adiabatic temperature change (ΔT_{ad}) are larger when $(\partial M/\partial T)_H$ is large and $C_p(T,H)$ is small. $(\partial M/\partial T)_H$ reaches its maximum value in the vicinity of the magnetic phase transition, and therefore ΔS_{m} and ΔT_{ad} show peaks at $T=T_{\mathrm{c}}$. The magnetization in ferromagnets and paramagnets decreases with increasing temperature, *i.e.*, $(\partial M/\partial T)_H<0$ which leads to a positive adiabatic temperature change $(\Delta T_{\mathrm{ad}}>0)$ and a negative isothermal entropy change $(\Delta S_{\mathrm{m}}<0)$. Contrary to that, antiferromagnets show an increase in magnetization with temperature $((\partial M/\partial T)_H>0)$, and hence, ΔT_{ad} is negative, while ΔS_{m} is positive.

2.1.3 Measurement of the MCE

The two characteristics of magnetocaloric materials, ΔS_m and ΔT_{ad}, can be measured either directly or indirectly. Direct isothermal measurement of the heat transfer and therefore, direct measurement of ΔS_m is very inconvenient and it is rarely performed in practice. However, for the measurement of ΔT_{ad}, both direct and indirect methods can be used.

2.1.3.1 Direct measurements

Direct measurement techniques involve the measurement of the initial and final temperatures of the magnetocaloric material when it is subjected to an external magnetic field. In this technique which only measures the adiabatic temperature change (ΔT_{ad}), the temperature sensor can be in direct thermal contact with the sample or not. The direct measurements can be carried out on a immobilized sample by changing the magnetic field rapidly or by moving the sample in and out of a uniform magnetic field region. The accuracy of the direct technique is in the range of 5–10 %, and it depends on the errors in thermometry, errors in field setting, the quality of thermal isolation of the sample and the effect of the magnetic field on the temperature sensor readings [80–82].

This method can be an alternative solution to determine the ΔT_{ad} of first-order magnetic transition materials, because their transitions are usually accompanied by thermal and magnetic hysteresis and this has raised many arguments in regards to the way to perform the isothermal magnetization measurements (see below) as well as the equations used for calculation of ΔS_m [83].

2.1.3.2 Indirect measurements

Indirect measurement techniques are based on heat capacity and/or magnetization measurements. Nowadays, the indirect measurement techniques are more popular than the direct methods among scientists due to the availability of magnetometers

and calorimeters in research laboratories and their potential to estimate very accurately both ΔS_m and ΔT_{ad}.

Magnetization route

The most commonly used technique for measuring MCE is isothermal magnetization. Based on this technique which only allows to determine ΔS_m, magnetization (M) must be measured as a function of magnetic field (H) and temperature (T). Each isothermal magnetization curve is measured at a fixed temperature as a function of field. Then, these isothermal magnetization curves are used to calculate ΔS_m using the Maxwell relation (Eq. 2.12). Since the magnetization measurements are usually performed at discrete magnetic fields and temperatures, ΔS_m can be written in the numerical form of the Maxwell relation as follow:

$$\Delta S_m(T, B) = \sum_i \frac{M_{i+1} - M_i}{T_{i+1} - T_i} \Delta B_i \tag{2.20}$$

where M_{i+1} and M_i represent the magnetization values in a magnetic field B at the temperatures T_{i+1} and T_i, respectively. An example of isothermal magnetization measurement in the temperature range of 5 to 355 K with a temperature interval of 10 K for a $Pr_{0.6}Sr_{0.4}MnO_3$ bulk sample is presented in Figure 2.3. As indicated by yellow, the isothermal entropy change (ΔS_m) is the area between two isotherms divided by the temperature interval.

Figure 2.4 shows the ΔS_m obtained from the magnetization measurements using the Maxwell relation. As it was mentioned before, the maximum of ΔS_m occurs around T_c.

Heat capacity route

The most complete measurement of MCE is provided by the heat capacity measurement which provides both ΔS_m and ΔT_{ad}. The heat capacity must be measured as a function of temperature in constant magnetic fields and pressure. ΔS_m and ΔT_{ad}

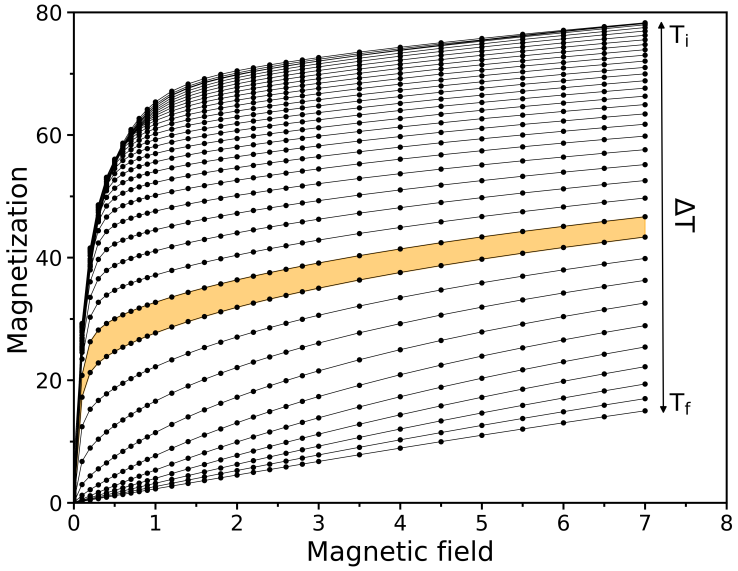

Figure 2.3: Isothermal magnetization curves of $Pr_{0.6}Sr_{0.4}MnO_3$ manganite. The yellow shaded area indicates the magnetic entropy change between two adjacent magnetic isotherms.

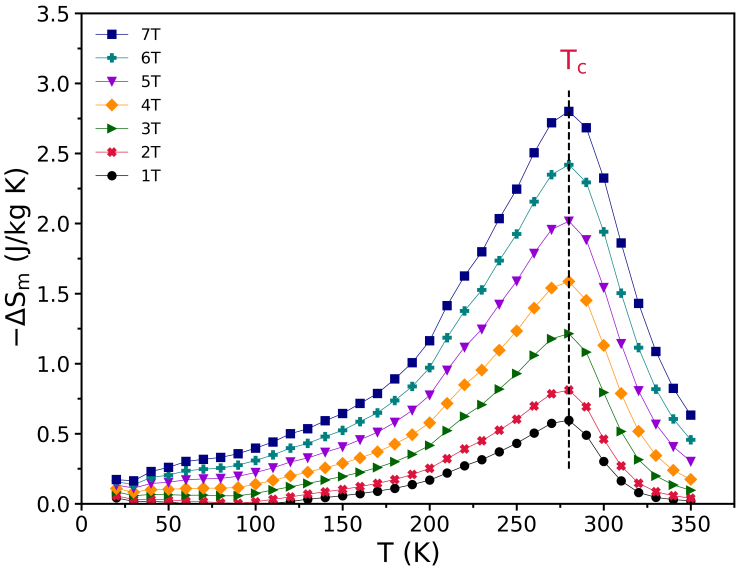

Figure 2.4: Isothermal magnetic entropy change (ΔS_m) as a function of temperature in various magnetic fields obtained from the magnetization measurement for $Pr_{0.6}Sr_{0.4}MnO_3$ manganite. The dashed line indicates the transition temperature.

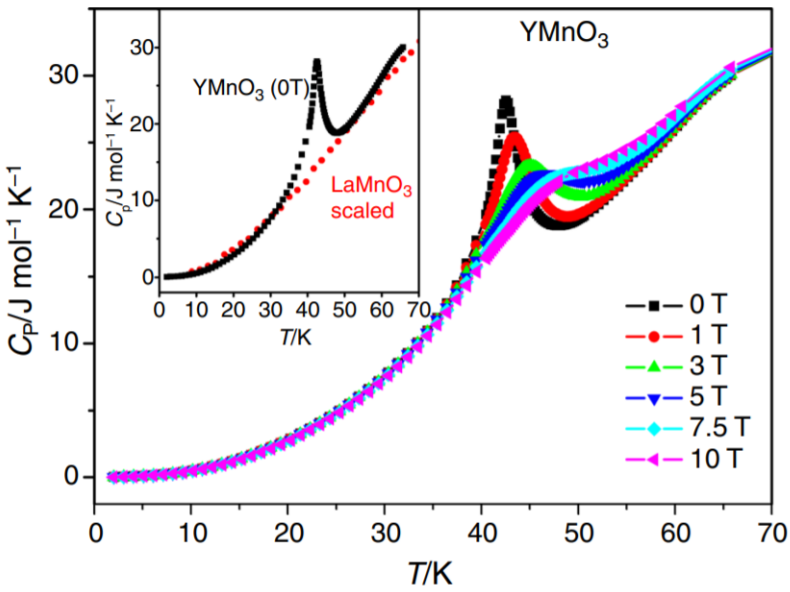

Figure 2.5: Specific heat measurement of $YMnO_3$ sample versus temperature under different magnetic fields [84].

can then be calculated using Eq. 2.14 and 2.19, respectively. Figure 2.5 shows an example of the heat capacity measurement as a function of temperature for $YMnO_3$ under different magnetic fields in order to calculate the isothermal entropy change and the adiabatic temperature change.

Figure 2.6 (a) and (b) display the magnetic entropy change and adiabatic temperature change as a function of temperature for $YMnO_3$ sample calculated using heat capacity measurements (Fig. 2.5).

2.1.4 The criteria for selecting the best magnetic refrigerant

In order to bring magnetic refrigerants to the commercial market, there are several important criteria that must be taken into account. Based on the theoretical analyses and the magnetocaloric nature of existing materials, the selection criteria of a magnetocaloric material as a refrigerant are defined as follows:

- Materials with a large magnetic entropy change (ΔS_m) and a high adiabatic temperature change (ΔT_{ad}).

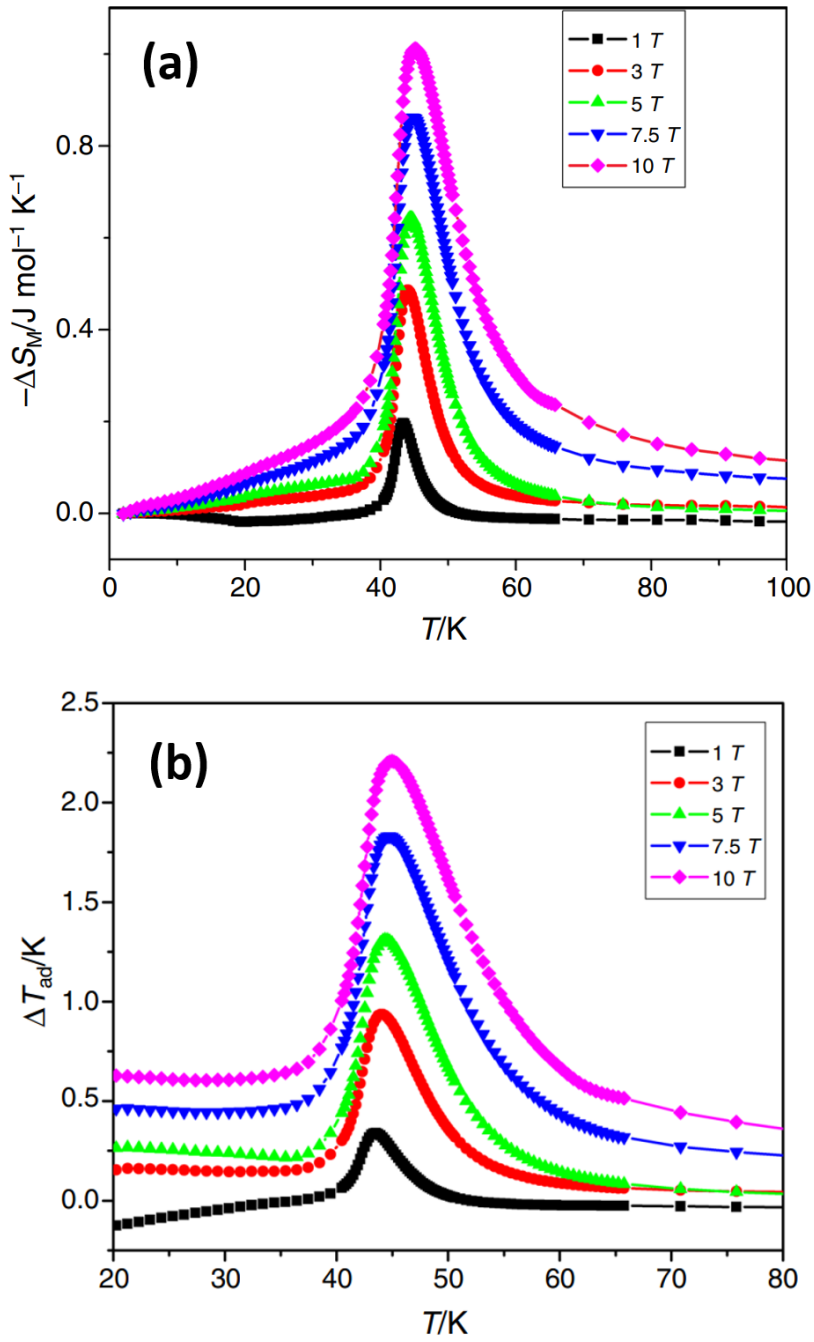

Figure 2.6: (a) ΔS_m and (b) ΔT_{ad} as a function of temperature for $YMnO_3$ sample obtained from heat capacity measurements [84].

- Materials with a large density of magnetic entropy: it is an important factor contributing to the working efficiency of materials.
- Materials with a small lattice entropy (i.e., a high Debye temperature) are great assets for magnetic refrigerants near room temperature.
- Materials with a nearly zero magnetic hysteresis: it is related to the working efficiency of magnetic refrigerant materials.
- Materials with a small thermal hysteresis: it is related to the reversibility of the MCE of magnetic refrigerant materials.
- Materials with low specific heat and high thermal conductivity, which are required for remarkable temperature change and fast heat exchange.
- Materials with high electrical resistance, which minimizes heating generated by eddy currents in a varying magnetic field.
- Materials with high chemical stability

The cost is an additional measure that controls a material's selection as a refrigerant. The natural abundance of the atoms in the active material is also important as rarity would drive the costs of such magnetic refrigerator out of range for commercial/domestic applications and sustainability.

2.1.5 Refrigerant capacity

Comparing the MCE in different magnetic materials requires a precise tool which considers both the height and the width of ΔS_m or ΔT_{ad} at the same time. Relative cooling power (RCP) is a very useful tool which considers not only the amplitude of the magnetic entropy change $\Delta S_m(\max)$, but it also takes into account the working temperature range δT_{FWHM} which is a key parameter in magnetic cooling systems. RCP is defined as the amount of heat transferred between the cold and hot reservoir in one refrigeration cycle. As shown in Figure 2.7 (b), it is determined by the product of the maximum of the ΔS_m (ΔT_{ad}) and the full-width at half maximum (δT_{FWHM}) of the peaks observed in Fig. 2.4 as:

$$RCP(S) = -\Delta S_{\mathrm{m}}(\mathrm{max}) \times \delta T_{\mathrm{FWHM}} \tag{2.21}$$

An equivalent quantity can be obtained using ΔT_{ad} as a function of the temperature:

$$RCP(T) = -\Delta T_{\mathrm{ad}}(\mathrm{max}) \times \delta T_{\mathrm{FWHM}} \tag{2.22}$$

RCP is mostly used for materials with a single transition which have a single fairly symmetric peak in $\Delta S_{\mathrm{m}}(T)$ curves similar to that in Fig. 2.4. However, in the case of composites and materials with more than one transition, refrigerant capacity ($\mathcal{RC}$) is usually employed [7, 85]. As shown in Fig. 2.7 (a), $\mathcal{RC}$ is specified as the area under the curve of ΔS_{m} (ΔT_{ad}) between the temperatures which corresponds to half maximum [86]:

$$\mathcal{RC}_S = -\int_{T_C}^{T_H} \Delta S_{\mathrm{m}}(T)\mathrm{d}T \tag{2.23}$$

Again, an equivalent relation can be written for $\Delta T_{\mathrm{ad}}(T)$:

$$\mathcal{RC}_T = -\int_{T_C}^{T_H} \Delta T_{\mathrm{ad}}(T)\mathrm{d}T \tag{2.24}$$

where T_H and T_C are the temperature of the hot and cold reservoirs, respectively. The value of $\mathcal{RC}_T$ has a K^2 dimension, and may be useful for comparing different magnetocaloric materials numerically.

Figure 2.7 compares these two different ways to characterize the performance of a magnetocaloric material in terms of the isothermal entropy change. In general,

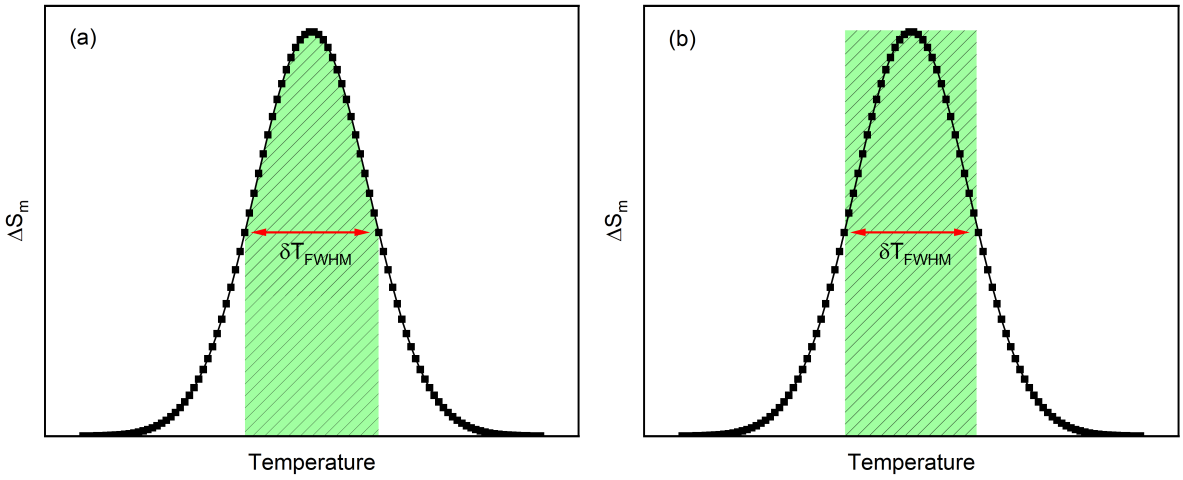

Figure 2.7: An example of the evaluation of refrigerant capacity based on the temperature dependence of magnetic entropy change under a fixed magnetic field. (a) shows the area corresponding to the refrigerant capacity $\mathcal{RC}$ (integrated area), (b) shows the area corresponding to the RCP.

for materials with a single symmetrical peak the value of $\mathcal{RC}$ is close to 75 % of RCP.

2.1.6 Magnetocaloric materials

The choice of magnetocaloric material is the most crucial component of a magnetic cooling system. Over the past few decades, researchers have performed a great deal of research on developing new materials as well as improving current magnetocaloric materials through alloying, doping and making composites. Because magnetic cooling systems will be used in a variety of applications, each with its own operating temperature range, selecting a material with suitable magnetocaloric properties within that temperature range is imperative. In this section, we briefly review the properties of some of the most common magnetocaloric materials.

2.1.6.1 Gd and its alloys

The discovery of the large MCE near room temperature in Gd in 1976 was a major breakthrough in magnetic refrigeration close to room temperature [78]. Gd under-

goes a second order magnetic phase transition from the paramagnetic to ferromagnetic state at 294 K. It shows a magnetic entropy change of ΔS_m =5.5 J kg^{-1} K^{-1} and adiabatic temperature change of ΔT_{ad} =6 K for a magnetic field change from 0 to 2 T [87]. The high cost and narrow working temperature range of Gd highly restricted its usage in magnetic cooling systems. However, it has been reported that the operating temperature span (ΔT_{span}) of Gd can be increased by doping with other rare earth such as Tb and Dy [88, 89]. Gd is often used as a benchmark material to evaluate the performance of other magnetic materials.

A family of Gd-based alloys with the general formula $Gd_5(Ge_{1-x}Si_x)_4$ have been discovered with a giant MCE near room temperature in 1997 [14]. These alloys have attracted a great deal of interest not only due to the large MCE, but also because of their colossal magnetostriction and their giant magnetoresistance. Based on the phase diagram of $Gd_5(Ge_{1-x}Si_x)_4$ in Figure 2.8, there are three different composition regions in the entire doping range. In both the intermediate region and the Ge-rich region, $Gd_5((Ge_{1-x}Si_x)_4$ alloys undergo a first-order magnetic phase transition from paramagnetic to ferromagnetic, while the magnetic transition in the intermediate region is accompanied by a structural transition from monoclinic to orthorhombic structure, yielding a giant magnetic entropy change, as large as 70 J kg^{-1} K^{-1} for $\Delta H = 5$ T, which is larger than any other prototype material in all temperature range [90]. A second-order magnetic transition without crystal structure change occurs for $x > 0.55$, resulting in a sharp reduction in ΔS_m.

The MCE of $Gd_5(Ge_{1-x}Si_x)_4$ alloys were investigated by Pecharsky and Gschneidner in the entire doping range [90]. They have observed that the ΔS_m increases by increasing the Si:Ge ratio and reaches its maximum at $x = 0.25$ which is the largest reported ΔS_m for any known magnetic refrigerant material. Moreover, it has also been revealed that the transition temperature can be tuned from 30 to 276 K by adjusting the Si:Ge ratio without losing the giant magnetic entropy change. They showed that the $Gd_5Ge_2Si_2$ compound with a $T_c = 276$ K exhibits a large magnetic entropy change of 14 J kg^{-1} K^{-1} for a field variation from 0 to 2 T, which makes it one of the best candidate for ambient magnetocaloric devices. A direct measurement of the adiabatic temperature change on $Gd_5Ge_2Si_2$ was conducted by Gschneidner et al [92] and it was found to be 16.5 K when the magnetic field changes from 0–2 T. The results was in close agreement with the ΔT_{ad} value

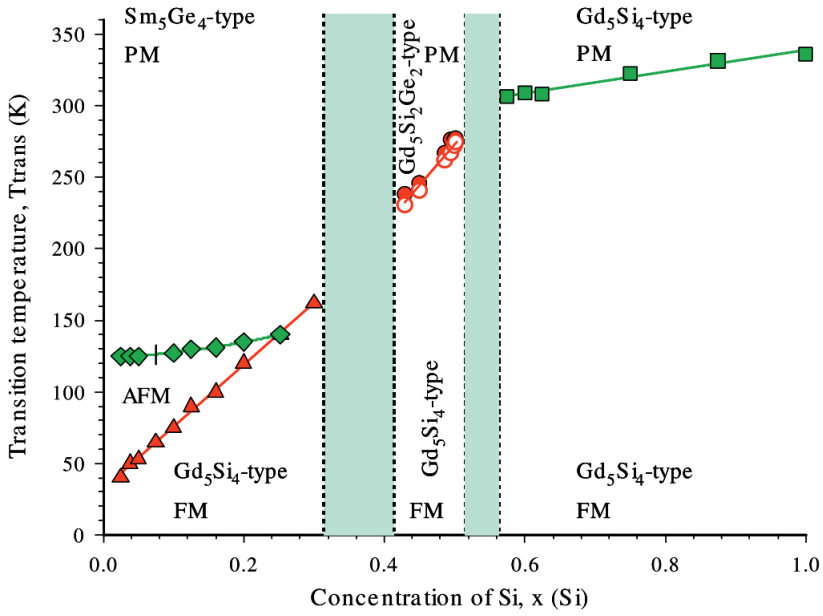

Figure 2.8: The magnetic phase diagram of $Gd_5(Ge_{1-x}Si_x)_4$ alloys at zero field. The vertical dotted lines indicate crystallographic phase boundaries and where the alloys are single phase materials (the compositions within shaded areas are two phase alloys). The solid red and green lines show the first-order and second-order magnetic phase transitions, respectively[90, 91].

of 16.8 K determined from heat capacity measurements.

2.1.6.2 $La(Fe, Si)_{13}$ compounds

The $LaFe_{13-x}Si_x$ alloys crystallizing in the cubic $NaZn_{13}$ structure have recently been attracting a lot of attention due to their potentials as magnetic refrigerants. They exhibit large MCE, they are made of low cost raw materials and they show small thermal hysteresis. The binary $LaFe_{13}$ does not exist, therefore, the addition of Si or Al is required to stabilize the $NaZn_{13}$-type phase [93]. Moreover, it has been reported that the magnetic ordering temperature can be tuned in $LaFe_{13-x}Si_x$ compounds by varying the concentration of Si [93–95]. For example, Palstra *et al* [93] reported that the transition temperature of $LaFe_{13-x}Si_x$ compounds increases from 198 to 262 K when Si concentration increases from $x = 1.5$ to $x = 2.5$, while the saturation magnetization decreases from 2.08 to 1.85 μ_B/Fe.

A giant MCE was found in the $LaFe_{13-x}Si_x$ alloys by Hu *et al* in 2000 [96]. They have reported that $LaFe_{11.4}Si_{1.6}$ compound exhibits a ΔS_m value of 10.5, 14.3 and 19.4 J kg^{-1} K^{-1} at 208 K for the magnetic field changes of 0–1 T, 0–2 T, and 0–5 T, respectively. This large MCE is ascribed to the sharp change of magnetization (first order transition), which is caused by a large negative lattice expansion at T_c.

For small concentrations of Si, $LaFe_{13-x}Si_x$ compounds undergo a first-order magnetic transition, which is accompanied by large thermal and magnetic hysteresis. It has been shown that for $x > 0.18$, the crystal structure of $LaFe_{13-x}Si_x$ compounds shifts toward the tetragonal symmetry and the magnetic transition type changes from first to second order with the disappearance of hysteresis [97]. As depicted in Figure 2.9, the change in the type of magnetic transition causes a dramatic drop in ΔS_m.

2.1.6.3 MnAs and similar compounds

MnAs-based family and its similar compounds such as $MnFeP_{1-x}As_x$ have shown very interesting MCE behaviors. The base material MnAs exhibits a first order

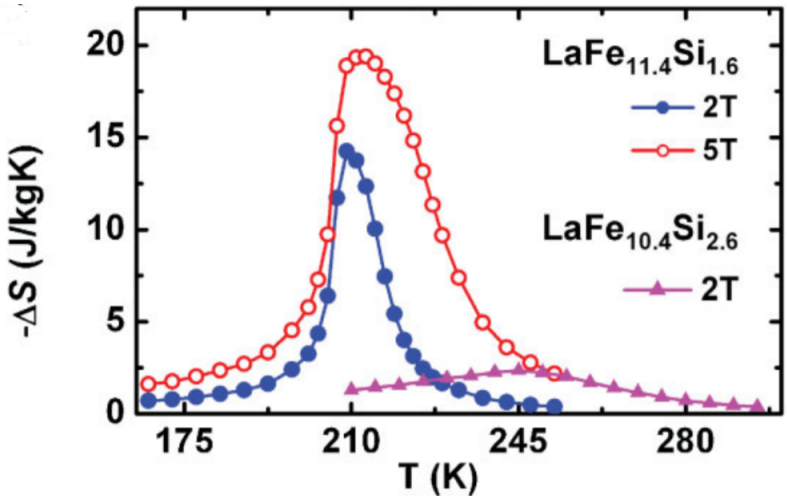

Figure 2.9: Magnetic entropy change (ΔS_m) as a function of temperature for $LaFe_{11.4}Si_{1.6}$ and $LaFe_{10.4}Si_{2.6}$ compounds [95].

magnetostructural transition at 318 K, where the ferromagnetic hexagonal NiAs-type structure transforms into the paramagnetic orthorhombic MnP-type structure upon heating or demagnetizing. Very large magnetic entropy changes are observed in this compound which are considered to be in the GMCE class of magnetic refrigerants. The ΔS_m reaches a maximum value of 40 J kg^{-1} K^{-1} for a magnetic field change of 0–2 T [98]. It was observed that the magnitude of ΔS_m does not change very much with magnetic field, whereas the width of the entropy change peak increases linearly with increasing ΔH [99]. In addition, substitution of Sb for Al can alter the magnetic and magnetocaloric properties of MnAs [100, 101]. As illustrated in Figure 2.10, both T_c and ΔS_m decrease by increasing the Sb concentration. The structural transformation and thermal hysteresis disappear for $x \geq 0.1$, resulting in the magnetic transition becoming second order which leads to a reduction of ΔS_m and ΔT_{ad}. The maximum value of ΔS_m does not change much in $0 \leq x \leq 0.3$, while the Curie temperature is decreased from 318 to 230 K. For $x = 0.4$, ΔS_m considerably decreases. These results indicate that the Curie temperature can be tuned between 230–318 K while retaining the giant ΔS_m in $MnAs_{1-x}Sb_x$. The magnetocaloric properties of $MnAs_{1-x}Sb_x$ compounds are outstanding and they are among the leading candidates for near room temperature magnetic refrigerants. One of the biggest issues with these compounds is the presence of a toxic element such as As with a high vapor pressure which makes it difficult to prepare in large

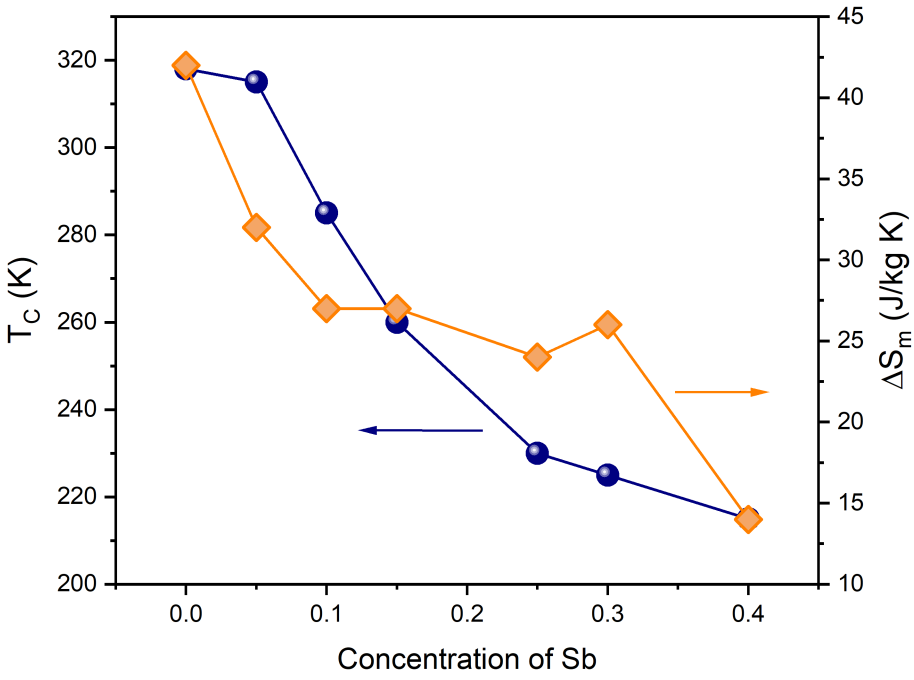

Figure 2.10: The Curie temperature and the magnetic entropy change ΔS_m versus concentration of Sb for $MnAs_{1-x}Sb_x$. Data obtained from [99–101]

quantities in an economical way. So far the toxicity of these compounds drastically restricts their utilization as refrigerants in commercial devices.

2.1.6.4 Manganites

Manganites nowadays are under the spotlight of attention not only as materials with a colossal magnetoresistance but also as materials with interesting magnetocaloric properties. The MCE in manganites is not as outstanding as Gd and intermetallic alloys due to their second-order magnetic transition. However, their exclusive properties such as high and tunable transition temperature, as well as their low cost of production compared to Gd-based alloys make them suitable candidates for magnetic cooling systems at room temperature.

The discovery of MCE in the La-based perovskite compounds ($La_{1-x}A_xMnO_3$) by Morelli *et al* in 1996 [102] has attracted much attention to this family, where they reported a total entropy change of 1.4, 1.6 and 2.1 J kg^{-1} K^{-1} under a magnetic field change of 5 T for $La_{2/3}A_{1/3}MnO_3$ compound doped by Ba, Sr and Ca, respec-

tively. More interestingly, a larger ΔS_m than Gd was found in $La_{1-x}Ca_xMnO_3$ for $0.20 \leq x \leq 0.33$ [103, 104]. It was shown that the ΔS_m reaches a maximum value of $5.5\,J\,kg^{-1}\,K^{-1}$ at 230 K, $4.7\,J\,kg^{-1}\,K^{-1}$ at 224 K and $4.3\,J\,kg^{-1}\,K^{-1}$ at 260 K under a magnetic field $H = 1.5\,T$ for $x = 0.20$, 0.25 and 0.33, respectively. These values are larger than that of Gd, $\Delta S_m = 4.2\,J\,kg^{-1}\,K^{-1}$, for the same magnetic field. It should be noted that Zhang *et al* [105] have found a much smaller ΔS_m value, $0.61\,J\,kg^{-1}\,K^{-1}$ for $\Delta H = 1\,T$, but a much wider peak, $\delta T_{FWHM} = 62\,K$, than what Guo reported [103] ($\delta T_{FWHM} = 11\,K$) for the same compound $La_{2/3}Ca_{1/3}MnO_3$. This discrepancy could be due to the differences in the sample preparation or slight differences in composition. $La_{2/3}Ca_{1/3}MnO_3$ shows the largest MCE among this family. In spite of the fact that their MCE are comparable to Gd, it remains significantly smaller than that observed in Gd-based and intermetallic alloys. The extraordinary large MCE in those alloys are attributed to the first-order magnetic phase transition, while magnetic transition in manganites is mostly second order. It is worth noting that, while the MCE decreases significantly, the MCE peak broadens as the magnetic transition changes from first to second order, which is beneficial for MR.

$La_{1-x}Sr_xMnO_3$ compounds have also been of much interest for its large MCE at room temperature. The magnetic and magnetocaloric properties of $La_{1-x}Sr_xMnO_3$ have been heavily studied in the entire doping regime. The MCE of polycrystalline $La_{1-x}Sr_xMnO_3$ where $0.13 \leq x \leq <0.16$ was investigated by Szewczyk *et al* [106]. They reported for $\Delta H = 1.5\,T$, ΔS_m that reaches their maximum values of $2.9\,J\,kg^{-1}\,K^{-1}$ at 196 K and $2.7\,J\,kg^{-1}\,K^{-1}$ at 243 K for $x = 0.13$ and 0.16, respectively. Afterwards, the direct and indirect measurements of MCE for $La_{0.845}Sr_{0.155}MnO_3$ near its $T_c = 234\,K$ showed ΔS_m and ΔT_{ad} under a change in magnetic field from 0 to 7 T reaching values of $6.6\,J\,kg^{-1}\,K^{-1}$ and 3.4 K, respectively, which are about 2 and 4 times smaller than Gd [81]. Later on, it was demonstrated that the MCE increases with increasing Sr content in $La_{1-x}Sr_xMnO_3$ for $x = 0.120$, 0.135, 0.155, 0.185 and 0.200 [107]. The ΔS_m and ΔT_{ad} reached the maximum values of $7.9\,J\,kg^{-1}\,K^{-1}$ and 4.15 K for $\Delta H = 7\,T$ for $x = 0.200$, respectively. The most attention in this family has been paid to the intermediate doping range where $0.20 \leq x \leq <0.35$ due to their potentials as magnetocaloric materials above room temperature. Jeong *et al* [108] investigated the MCE in polycrystalline LSMO in in-

termediate doping ($0.20 \leq x \leq <0.35$). They obtained the largest magnetic entropy change for $x = 0.20$, the value of ΔS_m reached $2.74\,J\,kg^{-1}\,K^{-1}$ under $\Delta H = 2.5\,T$. They also introduced $La_{0.65}Sr_{0.35}MnO_3$ as the best candidate for magnetic refrigeration at room temperature with a ΔS_m of $1.10\,J\,kg^{-1}\,K^{-1}$ and relative cooling power of $48.85\,J\,kg^{-1}$ under a magnetic field change of 1 T. Furthermore, Rostamnejadi *et al* [17] synthesized $La_{0.67}Sr_{0.33}MnO_3$ by sol-gel technique and reported that the change of magnetic entropy reaches the value of $5.15\,J\,kg^{-1}\,K^{-1}$ at 370 K for $\Delta H = 5\,T$. The corresponding adiabatic temperature change and RCP are 3.3 K and $252\,J\,kg^{-1}$, respectively, for the same magnetic field. Besides the large values of ΔS_m and ΔT_{ad} above room temperature, the chemical stability, simple preparation, low cost and tunable transition temperature are other important parameters which suggest LSMO could be considered as a good candidate for magnetic refrigeration at room and above room temperature at moderate magnetic fields. According to studies, both ΔS_m and ΔT_{ad} decrease upon increasing the doping level above, $x \geq 0.4$. It has been reported that the ΔS_m reaches values of 2.2 and $0.9\,J\,kg^{-1}\,K^{-1}$ for $\Delta H = 2\,T$ for $x = 0.4$ and 0.5, respectively [109, 110]. ΔT_{ad} was determined to be 1.2 K for $x = 0.4$ under the same magnetic field [109].

Most studies of MCE have taken place in bulk materials, but there have been some attempts to study MCE on thin films as well [114–116]. Most of the previous studies have shown that the intensity of ΔS_m decreases in thin films compared to the same material as a bulk, however the magnetic entropy change spreads over a wider temperature range. For example, the thickness dependence of the magnetic and magnetocaloric properties of $La_{0.88}Sr_{0.12}MnO_3$ thin films were investigated [117]. The results have shown that the maximum value of ΔS_m is about $1.8\,J\,kg^{-1}\,K^{-1}$ for $\Delta H = 3\,T$ which is 36 % of the bulk value. On the other hand, ΔS_m reveals a broad peak over a temperature range of 100 K, which is almost 3 times wider than what has been reported for the polycrystalline samples. As discussed earlier, the epitaxial strain is a very important parameter which influences the structural and magnetic properties of thin films. As a proof of concept, the strain dependence of the magnetocaloric properties of $La_{0.67}Sr_{0.33}MnO_3$ thin films deposited on three different substrates, LAO, STO and LSAT has been investigated under low magnetic field [11]. As a result of substrate induced strain, T_c decreases significantly in all the films compared to the bulk samples. The magnetic transition occurs at 321 and

Table 2.1: Summary of the magnetocaloric properties in $La_{1-x}Sr_xMO_3$ manganites.

Composition	T_c(K)	H(T)	ΔS_m(J/kg K)	ΔT_{ad}(K)	RCP(J/kg)	Ref
$La_{0.88}Sr_{0.12}MnO_3$	152	7	6.00	2.5	372	[107]
$La_{0.87}Sr_{0.13}MnO_3$	197	5	5.80	–	232	[106]
$La_{0.865}Sr_{0.135}MnO_3$	195	7	4.4	2.3	330	[107]
$La_{0.845}Sr_{0.155}MnO_3$	235	7	6.7	3.5	670	[107]
$La_{0.84}Sr_{0.16}MnO_3$	244	5	5.80	–	–	[106]
$La_{0.815}Sr_{0.185}MnO_3$	280	7	7.1	3.9	533	[107]
$La_{0.8}Sr_{0.2}MnO_3$	305	7	7.9	4.5	395	[107]
$La_{0.75}Sr_{0.25}MnO_3$	369	5	2.31	–	69	[111]
$La_{0.70}Sr_{0.30}MnO_3$	340	1.5	1.5	–	65	[112]
$La_{0.70}Sr_{0.30}MnO_3$	369	2	1.27	–	29	[111]
$La_{0.67}Sr_{0.33}MnO_3$	369	1.5	1.74	–	52	[113]
$La_{0.67}Sr_{0.33}MnO_3$	370	2	2.68	1.8	85	[17]
$La_{0.67}Sr_{0.33}MnO_3$	348	5	1.69	–	211	[102]
$La_{0.6}Sr_{0.4}MnO_3$	365	1.5	1	0.60	64	[109]
$La_{0.6}Sr_{0.4}MnO_3$	365	2	1.34	0.76	99	[109]
$La_{0.6}Sr_{0.4}MnO_3$	365	2.5	1.53	0.97	127	[109]
$La_{0.5}Sr_{0.5}MnO_3$	352	1	0.51	–	46	[110]
$La_{0.5}Sr_{0.5}MnO_3$	352	5	2.17	–	228	[110]

312 K for LSMO/LSAT and LSMO/STO samples which are lower than the reported values for bulk samples (370 K). Unlike those of LSMO on STO and LSAT with a sharp transition, the paramagnetic to ferromagnetic transition in LSMO/LAO sample spreads over a wide temperature range as a result of the large lattice mismatch between LSMO and the substrate lattice. Due to the broad transition, the magnetic entropy change distributes over a large temperature range. The maximum value of ΔS_m was determined to be 1.47 and 1.54 J kg^{-1} K^{-1} for $\Delta H = 1.5$ T, for LSMO/LSAT and LSMO/STO samples, respectively. The LSMO/STO sample shows a broader ΔS_m leading to a large RCP value of 50.16 J kg^{-1}, as high as the bulk samples [11]. Table. 2.1 summarizes the magnetocaloric properties of LSMO in the entire doping regime.

2.1.6.5 Double perovskites

Double perovskites (DPs) have been widely explored as other oxides in the hope of finding a wide range MCE covering room temperature. Some DPs show giant MCE at low temperature which are comparable with intermetallics. For instance, a giant anisotropic MCE was observed in Gd_2CoMnO_6 single crystal originating from the large magnetic moments of Gd^{3+} below $T_{Gd} = 21$ K [118]. The maximum values of magnetic entropy were found to be 12.1 and 25.4 J kg^{-1} K^{-1} below T_{Gd} for $\Delta H = 0$–9 T applied along and perpendicular to the c-axis, respectively. Moreover, a much smaller ΔS_m was observed at $T_c = 112$ K, ascribed to the ferromagnetic order of the Co^{2+} and Mn^{4+} moments. Yang *et al* have also reported [119] a giant MCE in distorted Gd_2ZnTiO_6 DP. They found that the antiferromagnetic interactions in the Gd−Gd sublattice produce a significantly large ΔS_m and relative cooling power of 53.5 J kg^{-1} K^{-1} and 620.6 J kg^{-1}, respectively, under a field change of 9 T at $T_c = 3.1$ K. The corresponding adiabatic temperature change was 23.7 K, far exceeding the commercial cryo-coolant $Gd_3Ga_3O_{12}$.

In addition, there has been considerable interest in ferromagnetic semiconducting DPs due to their chemical and mechanical stability as well as their insulating properties which prevents eddy currents. Two members of this rare family are La_2NiMnO_6 (LNMO) and La_2CoMnO_6 (LCMO) which had their magnetocaloric properties fully investigated. Balli *et al* [120] have studied the MCE in LCMO single

crystals. They reported that a maximum value of ΔS_m is 4.5 J kg^{-1} K^{-1} for $\Delta H = 7$ T at $T_c = 170$ K which is two times larger than that of polycrystalline samples. It also exhibits a large refrigerant capacity of 222 and 330 J kg^{-1} for $\Delta H = 5$ and 7 T, respectively. These values are comparable with those found in the reference materials with giant MCE. The study of MCE in LNMO single crystals has also shown that a large ΔS_m over a wide temperature range at T_c can be obtained regardless of the type of the B-site cation ordering in the system [18]. It was found that ΔS_m in both ordered and disordered phase reaches a maximum values of 2.65 and 3 J kg^{-1} K^{-1} for a magnetic field variation from 0–7 T, respectively. Matte *et al* [7] have demonstrated how the level of cationic disorder in LNMO thin films can be controlled by changing the growth parameters in order to tune the magnetic and magnetocaloric properties. They grew a sample in which both ordered and disordered phases coexisted resulting in a temperature-independent tabletop-like magnetic entropy change over an unusually large temperature range from 100 to 300 K. This broad ΔS_m leads to a large refrigerant capacity comparable with the reference magnetocaloric materials such as Gd and $Gd_5Ge_2Si_2$. The comparison of the magnetic entropy change obtained for LNMO films grown at various oxygen pressure, 100, 200, 300, 400 and 600 mTorr is illustrated in Figure 2.11.

These results demonstrate the advantages of oxides over many other materials families with the possibility to control the defect and impurity levels, or the structural disorder in the case of LNMO to tailor the magnetocaloric properties to meet specific application requirements, whether it is around room temperature or at low temperature.

2.1.6.6 Composites

In general, most of the magnetocaloric materials, including those with a giant MCE, operate within a limited temperature range around their magnetic phase transition. However, for practical application, it is strongly desirable that the magnetocaloric material exhibits a large ΔS_m over a sufficiently wide temperature range especially for AMR refrigeration cycle. In this regard, the idea of composites containing several magnetocaloric materials with different transition temperatures to expand the working temperature range was proposed for the first time by Hashimoto in

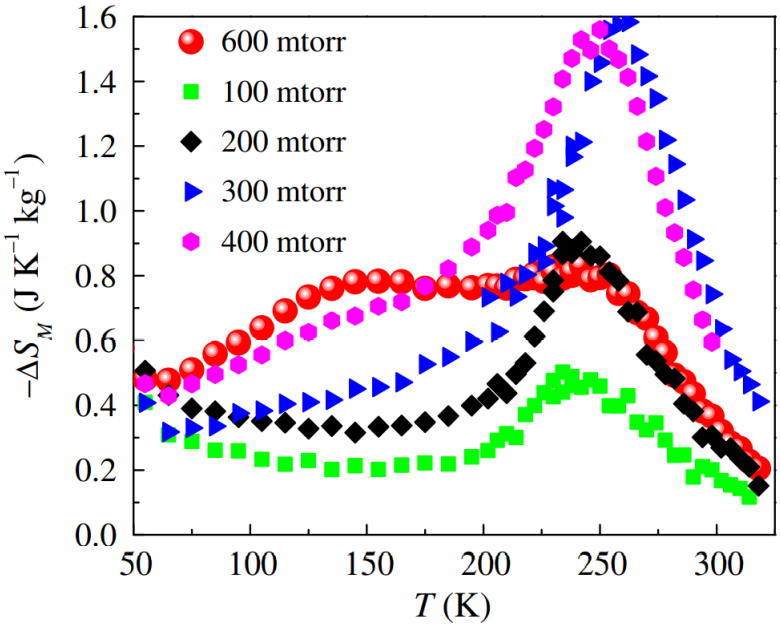

Figure 2.11: Magnetic entropy change as a function of temperature for a fixed field change from 0 to 5 T for LNMO films grown at different O_2 pressures [7].

1987 [121]. By designing a trilayer sample composed of $ErAl_{2.15}$, $HoAl_{2.15}$ and $(Ho_{0.5}Dy_{0.5})Al_{2.15}$ with $T_c = 11$, 26 and 33 K, he covered the temperature range from 10 to 40 K. Afterwards, several attempts have been made to study the MCE in bulk composites as well as thin films [89, 122–124]. For instance, composite magnetic refrigerants of $LaFe_{11.6}Si_{1.4}H_y$ with different Curie temperatures were prepared by physical mixing method [85]. It was specified that an optimal mixing ratio can make the composite magnetic refrigerant possess a table-top-like $\Delta S_m - T$ curve with a δT_{FWHM} and $\mathcal{RC}$ values of 48.7 K and 177.76 J kg^{-1} under a magnetic field change of 2 T, which is beneficial to magnetic Ericsson cycle. Compared with single $LaFe_{11.6}Si_{1.4}H_y$ alloys, the composite broadens the operating temperature range and enhances the refrigerant capacity of $LaFe_{11.6}Si_{1.4}H_y$ alloys.

This technique was also implemented with intermetallic compounds where composite materials of two single-phase Dy_2Cu_2Cd and Tm_2Cu_2Cd compounds have been fabricated [20]. A table-top-like MCE in a wide temperature range of 10–70 K and enhanced refrigerant capacity are achieved in 0.77 Dy_2Cu_2Cd – 0.23 Tm_2Cu_2Cd composite material (Figure 2.12). The maximum

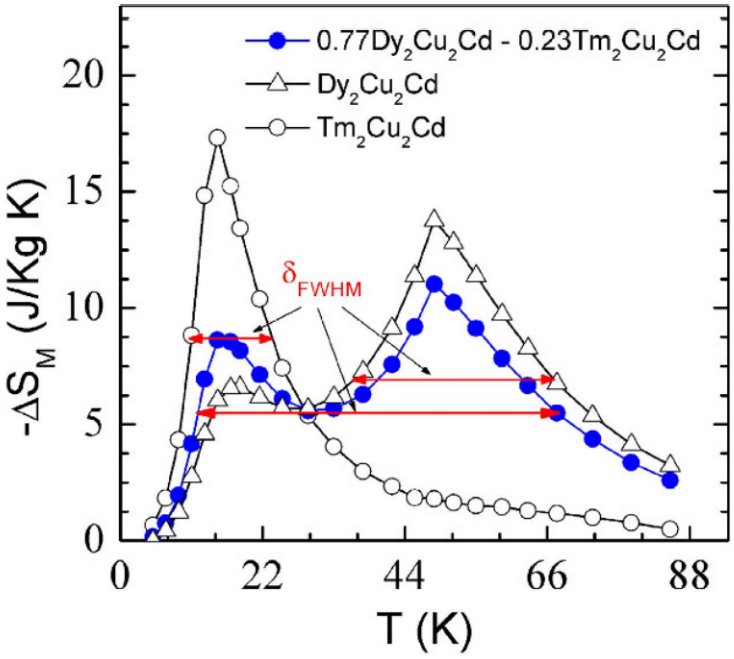

Figure 2.12: Temperature dependence of magnetic entropy change $-\Delta S_{\text{comp}}$ for the $0.77\,Dy_2Cu_2Cd - 0.23\,Tm_2Cu_2Cd$ composite material for the magnetic field change of 50 kOe [20].

value of $\mathcal{RC}$ reaches $417\,J\,kg^{-1}$ in the composite material for a magnetic field change of 50 kOe, which is larger than those for either Dy_2Cu_2Cd $(316\,J\,kg^{-1})$ or $Tm_2Cu_2Cd(165\,J\,kg^{-1})$ compounds.

In 2009, Mukherjee [125] have proposed that the magnetocaloric properties could be improved in nanostructural thin films with respect to corresponding polycrystalline systems. Contrary to the prediction, the study of the MCE in metallic Gd/W thin film heterostructures [126] has shown a decrease in the magnetic entropy change compared to bulk Gd, but the full width at half maximum of the entropy change was significantly increased. It is well known that the synthesis of smooth and sharp layer interfaces in perovskite oxide superlattices and heterostructures is the key to influence the magnetic properties and a successful tailoring of the magnetocaloric properties. For this purpose, Zhang *et al* [124] have examined the MCE in a series of $La_{0.7}Sr_{0.3}MnO_3/SrRuO_3$ superlattices, where the $SrRuO_3$ layer thickness is varying from 1 to 6 unit cells. They have reported that the transition from PM to FM states in all superlattices occurs in a wider temperature range, re-

sulting in an enlarged working temperature range. As shown in Figure 2.13, the maximum values of ΔS_m were found to be 4.45, 4.3 and 3.07 J kg^{-1} K^{-1} under a magnetic field change of 50 kOe, for n of 1, 3 and 6, respectively. These values are similar to those of polycrystalline $La_{0.7}Sr_{0.3}MnO_3$, but with larger δT_{FWHM}, resulting in higher RCP values compared to bulk LSMO.

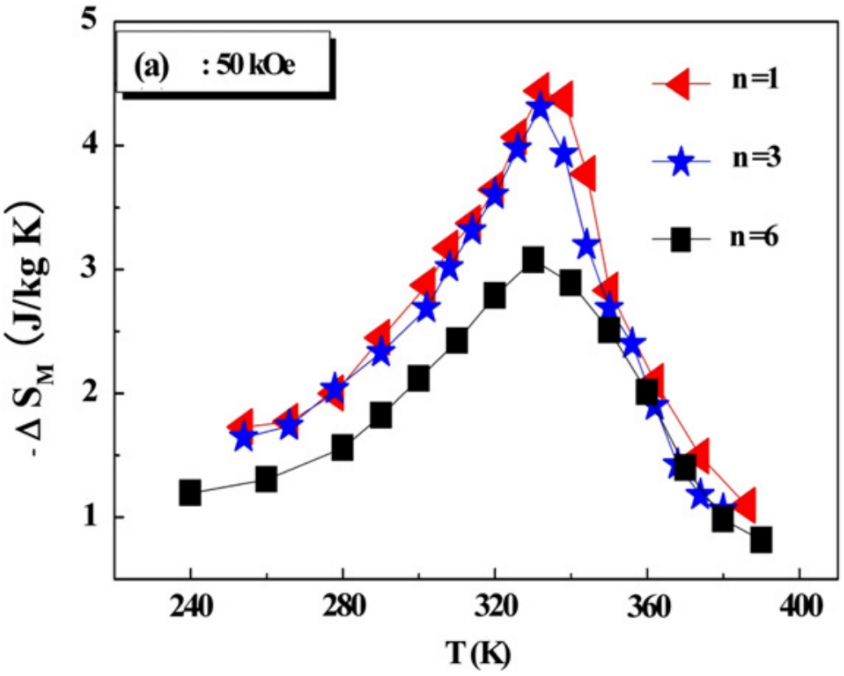

Figure 2.13: Temperature dependence of $-\Delta S_m$ in LSMO/SRO superlattices with different numbers (n) of $SrRuO_3$ unit cells for a magnetic-field change of 50 kOe (5 T) [124].

2.2 Experimental techniques

In this section, we provide specific descriptions of the equipment and techniques that we used to grow and characterize the multilayer samples for this project. The working principles of the devices are briefly explained with the focus on the practical performances.

2.2.1 Pulsed laser deposition

The pulsed laser deposition (PLD) method is a growth technique which was first used by Smith and Turner [127] in 1965 in order to prepare semiconductors and dielectric thin films. Then it was established in 1987 by Dijkkamp *et al.* [128] due to his work on high-temperature superconductors. Since then, this technique has been widely used among scientists to grow different types of materials such as oxides, nitrites, carbides, etc. This technique allows one to obtain high quality epitaxial thin films with atomic precision. The PLD technique has the advantage of easy control and tuning of the growth conditions during deposition as well as the ability to deposit several thin film layers consecutively without breaking the vacuum in order to make heterostructures.

2.2.1.1 PLD setup

In this work, we used Plasmionique's GLAZE Series PLD system with a target carousel to grow the bilayer and trilayer samples as well as the tunnel magnetic junction devices (see Chapter 3). The system includes substrate heating by a high-power diode laser which can reach up to 1500 °C, and also an infrared thermometer (pyrometer) used to measure the substrate temperature in the range of 385–1600 °C. Also, a krypton fluoride (KrF) excimer laser (Lambda-Physik LPX305) with a wavelength of 248 nm was used to ablate the materials and create the plume towards the substrate. Figure 2.14 shows a schematic drawing of the pulsed laser deposition system used in this project consisting of a laser beam, a vacuum chamber equipped with a mechanical and a turbopump, a multi-target carousel and a substrate heater. The PLD system is equipped with a set of optics including an aperture, mirrors and a lens to direct and focus the laser beam onto the target with the right energy density. The high power pulsed laser beam at an angle of 55° is focused on a selected target, resulting in the ablation of the atoms and ions from the target. The ablated species form a luminous plasma plume that expands quasi adiabatically away and perpendicular to the target and are deposited on a substrate. The substrate is attached with the surface parallel to the target surface at a distance of around 10 cm. In addition, this PLD system is equipped with gas inlets which

allow us to use different background pressures such as oxygen, argon or nitrogen, and mixtures during the deposition. The background gas plays a crucial role in the deposition process. It interacts with the plasma plume and controls the deposition rate, morphology and stoichiometry. The background gas can affect the film stoichiometry because the detailed scattering of each cation depends strongly on the gas composition and pressure. In addition, the background gas can significantly reduce the kinetic energy of ablated species arriving at the substrate which prevents resputtering from the substrate and controls the deposition rate. Moreover, the target carousel allows us to grow several different materials sequentially in a single vacuum run to fabricate heterostructures with minimum cross-contamination.

2.2.1.2 Targets

PLD is well known for making films whose stoichiometry fit the target very closely. Both La_2NiMnO_6 and $La_{2/3}Sr_{1/3}MnO_3$ targets used in this project were made by standard solid-state reaction. The right stoichiometry ratio of La_2O_3, $SrCO_3$ and MnO_2 as well as La_2O_3, NiO and MnO_2 precursors with purity better than 99.9 % were mixed in the stoichiometric proportions to prepare LSMO and LNMO targets, respectively. The mixtures were thoroughly grounded until homogeneous powders were obtained and then calcined in air at 900, 1000 and 1100 °C for 24 h with intermediate grindings. Finally, the resulting powders were pressed into solid pellets with a diameter of 2.5 cm followed by a sintering at 1350 °C for 24 h to make them robust and resistant.

2.2.1.3 Substrates

Generally, ablated target materials are deposited on single crystal substrates placed at a distance of 10 cm in front of the target. For this project, all depositions were made on $5 \times 5 \times 0.5$ mm^3, one side polished $La_{0.18}Sr_{0.82}Al_{0.59}Ta_{0.41}O_3$ (LSAT) and $SrTiO_3$ (STO) single crystal substrates with (001) orientation. LSAT and STO substrates were selected since they have minimal lattice mismatch with LSMO and LNMO compounds. The lattice constants of LSAT and STO as well as other commonly used substrates are listed in Table. 2.2.

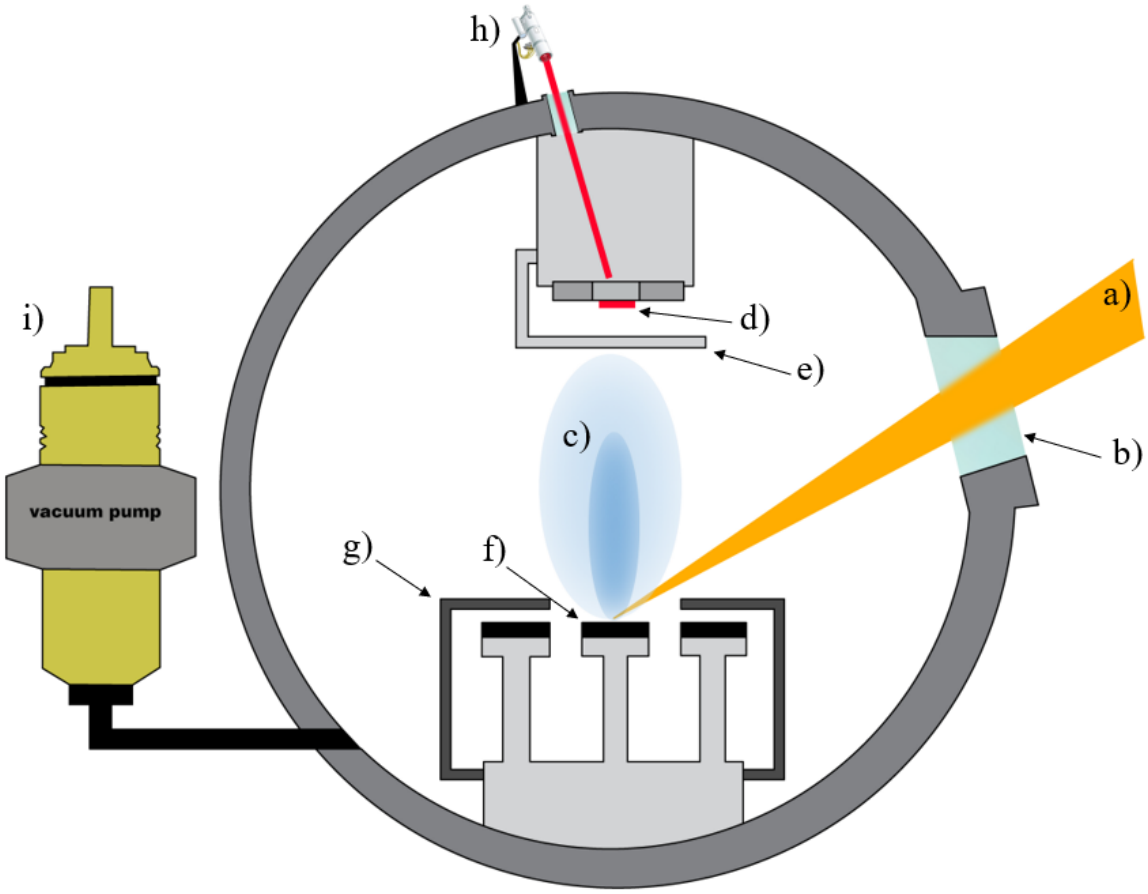

Figure 2.14: Schematic drawing of the PLD system used in this work, consisting of (a) laser beam, (b) quartz window, (c) plasma plume, (d) substrate, (e) shutter, (f) target, (g) cache, (h) substrate heater, and (i) vacuum pump.

Table 2.2: A list of some common single crystal oxide substrates along with their lattice constants and crystal structures.

Substrate/Compound	**Structure**	**Lattice constants** (Å)	**Cubic (pseudo) lattice constant** (Å)
$SrTiO_3$	Cubic	$a = 3.905$	3.905
$La_{0.18}Sr_{0.82}Al_{0.59}Ta_{0.41}O_3$	Cubic	$a = 3.87$	3.87
$NdGaO_3$	Orthorhombic	$a = 5.43$ $b = 5.50$ $c = 7.71$	∼3.86
$LaAlO_3$	Rhombohedral	$a = 3.78$	3.78

2.2.1.4 Deposition conditions

Prior to a deposition run, the energy of the laser is measured inside the chamber and is fixed at 110 mJ for our materials. The focus spot size of the beam on the target is approximately 1.5×2.5 mm, resulting in an average energy density of $2.9\,J/cm^2$. Substrates are glued on silicon plates using silver paste followed by a drying step on a hotplate at ∼100 °C for 20 min. After installing the substrate in the chamber, it is pumped down to a base pressure of $\sim 5 \times 10^{-6}$ Torr before raising the temperature. Then, the substrate temperature is increased to 800 °C with a rate of 10 °C/min. Once the temperature is stable, the gate valve is closed up to 99 % in order to increase the pressure inside the chamber. Then, the pressure is set to 200 mTorr using oxygen as the background gas in the chamber. Oxygen flows continuously in the chamber and controlled with a mass flow controller (MFC) throughout the deposition process while the pressure is kept at 200 mTorr using a feedback loop on the MFC. Before the deposition run, a preablation step is done in order to clean the targets and remove any contaminations that may have settled there. We clean the surface of the targets with 10 000 laser shots at a frequency of 10 Hz before every single deposition. Right after this step, the shutter is removed to begin the deposition of the thin layers. For the deposition run, the laser frequency is set to 5 Hz. After the deposition, the PLD chamber is filled with oxygen up to 200 Torr. This al-

lows in principle to cure the sample from oxygen vacancies that may have formed during the deposition. Then the films are cooled down to room temperature with a cooling rate of 5 °C/min.

In order to determine the deposition rate, the thickness of a monolayer, a bilayer and a trilayer sample is measured using a profilometer after etching a part of the sample down to the substrate. The thickness of the monolayer, bilayer and trilayer sample was found to be around 60, 120 and 180 nm, respectively for 10 000 laser shots for each layer. It gives us a deposition rate of 6 nm/1000 shot for both LSMO and LNMO. This deposition rate was used to estimate the thickness of the samples in this thesis.

2.2.2 X-ray diffraction

X-ray diffraction (XRD) is the most well-known technique to investigate structural properties of materials. This technique is especially informative in the study of crystalline solids that exhibit long-range structural order. X-rays were discovered for the first time by German physicist Wilhelm Conrad Röntgen in 1895. A few years later, Max von Laue realized that if X-rays have wavelengths similar to the interatomic distances in crystals, then they have to be diffracted by crystals. Finally, in 1912 he announced his discovery of X-ray diffraction in crystals and was awarded the Nobel prize in 1914. Then, two English researchers W. H. Bragg and his son W. L. Bragg used this discovery to determine the crystal structure of diamond and other crystals. They also initiated the first X-ray diffraction analysis of single crystals. As a result of their work, X-ray diffraction (XRD) became a common method for characterizing solids.

In this section, we briefly go through the theory of X-ray diffraction and then explain how diffractometers work and, at the end, the measurement of thin film samples will be discussed.

2.2.2.1 Theory of X-ray diffraction

The diffraction pattern of a crystal is mapping the reciprocal space associated with the crystal structure. The primitive vectors of direct lattice $(\vec{a}_1, \vec{a}_2, \vec{a}_3)$ are connected to the primitive vectors of reciprocal lattice $(\vec{b}_1, \vec{b}_2, \vec{b}_3)$ via the following relations:

$$\begin{aligned} \vec{b}_1 &= 2\pi \frac{\vec{a}_2 \times \vec{a}_3}{|\vec{a}_1 . (\vec{a}_2 \times \vec{a}_3)|} \\ \vec{b}_2 &= 2\pi \frac{\vec{a}_3 \times \vec{a}_1}{|\vec{a}_1 . (\vec{a}_2 \times \vec{a}_3)|} \\ \vec{b}_3 &= 2\pi \frac{\vec{a}_1 \times \vec{a}_2}{|\vec{a}_1 . (\vec{a}_2 \times \vec{a}_3)|} \end{aligned} \tag{2.25}$$

So, a reciprocal lattice vector $(\vec{G})$ can be written as a set of these three basis vectors:

$$\vec{G} = h\vec{b}_1 + k\vec{b}_2 + l\vec{b}_3 \tag{2.26}$$

where h, k and l are integers. The reciprocal lattice vector $\vec{G}$ is perpendicular to the corresponding plane defined by the Miller indices (h, k, l) in real space, with a length of $\left|\vec{G}\right| = 2\pi/d_{hkl}$, where d_{hkl} is an integer fraction of the distance between planes. Thus, every set of possible planes in the real-space crystal lattice is represented by a set of vectors in the reciprocal lattice which reveals the orientation of the planes. With that in mind, we can move to the diffraction of X-rays from crystal structures.

X-rays are high energy electromagnetic radiations with the wavelength on the order of 1 Å which is comparable with the inter atomic distances ($\backsim$ 1–4 Å) in solids. Let us assume a set of X-ray beams travelling parallel to each other under an angle θ toward a set of lattice planes with an inter-plane distance of d, as shown in Figure 2.15. The beams are scattered from different planes of atoms in all directions and leave the crystal. X-rays diffracted from different set of planes do not travel the same distance. Depending on the phase difference, they can interfere constructively or destructively. For instance, in Figure 2.15, the second X-ray beam which reflects from the second plane of atoms, travels an extra distance of $2d \sin\theta$ further

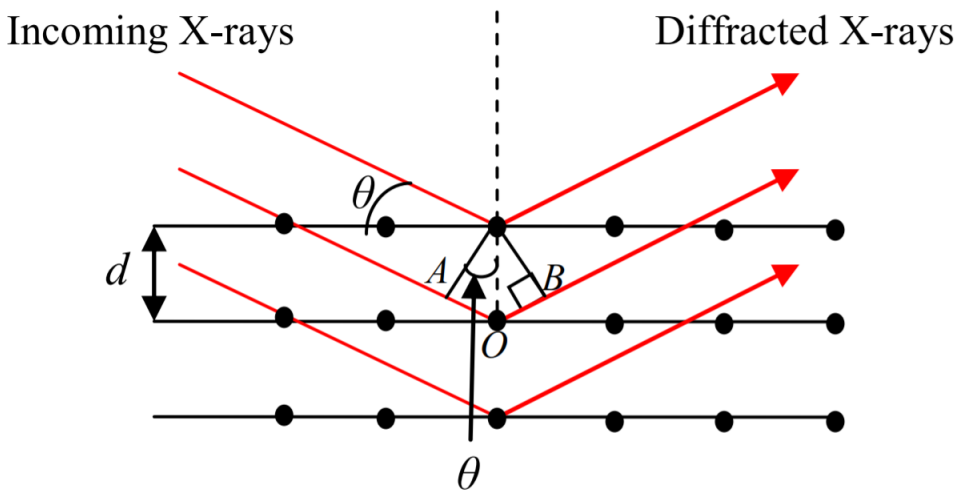

Figure 2.15: Diffraction of X-ray beams from crystallographic planes

than the first one. Constructive interference only occurs when the diffracted beams have the same phase such that the additional distance that the second beam travels $(2d \sin\theta)$ must be an integer multiple of λ. This leads to the famous relationship, which is known as Bragg's law [129]:

$$n\lambda = 2d \sin\theta \tag{2.27}$$

where n is an integer, λ is the wavelength of the X-rays, d is the interplanar spacing of the diffracting planes and θ is the diffraction angle.

Most measurements are conducted with a constant wavelength and the diffractometer records the interference of diffracted beams as a function of θ. For each θ at which Bragg's law is obeyed, a peak appears in the $\theta - 2\theta$ measurement. Various crystalline materials have different crystal symmetries, bond distances and space groups, resulting in different intensities at different positions in $\theta - 2\theta$ measurements which can be seen as a fingerprint of the materials.

2.2.2.2 XRD components

In general, an X-ray diffractometer consists of an X-ray source, a set of primary optics (Soller slit, divergence slit and monochromator), a set of secondary optics

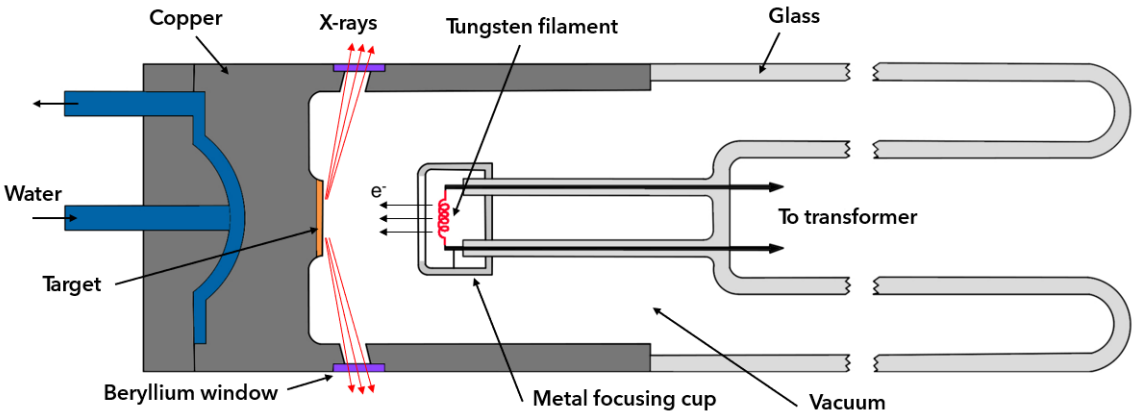

Figure 2.16: Schematic of a conventional X-ray tube, the electrons are emitted from the filament and collected at the target releasing X-ray radiation.

(anti-scatter slit, soller slit, receiving slit and monochromator), a sample holder and a detector. Following is a brief description of each part.

The source

X-ray tubes are often used as the source of a diffractometer. They are either a ceramic or a glass container that have a tungsten filament. The tungsten filament liberates electrons when it is heated electrically, and those electrons are accelerated towards a metal target using a high voltage power source (in the range of 20 to 220 kV). The accelerated free electrons hit the cloud electrons of the target and decelerate. When a high energy photon collides with a core electron, the core electron can be ejected, leaving an empty atomic state behind. This empty state is filled by an electron from an outer shell with higher energy, releasing energy in the form of X-ray equivalent to the difference in energy between the excited and the ground state. The type of radiation produced depends on which atomic shells are involved. Typically for a copper target the characteristic radiations are classified as $K_{\alpha 1}$, $K_{\alpha 2}$ and K_{β}. Figure 2.16 shows a typical X-ray tube used in diffractometers.

The primary optics

The primary optics are located between the source and the sample and can be broken down into two main parts:

i. **Divergence slit** is used to block X-rays that have too great a divergence. By reducing the spread of the beam, the output resolution significantly increases. Divergence slit comes in a variety of sizes which affect the peak intensity and the shape of the output. For example, a narrow divergence slit will reduce the intensity and the length of the X-ray beams, but it will produce sharper peaks resulting in greater angular (and momentum) resolution.

ii. **Monochromator** filters unwanted radiations in X-ray beams. It only allows $K_{\alpha 1}$ and $K_{\alpha 2}$ radiations to pass, and it filters out any of the white background and $K_{\beta 1}$ radiations. Moreover, monochromators much like divergence slit greatly increase the resolution of the output data. Some monochromators can be used to separate out $K_{\alpha 1}$ and $K_{\alpha 2}$, as in our high-resolution setup (see below).

The secondary optics

The secondary optics are on the receiving end of the X-ray diffractometer, between the sample and the detector. They can be divided into four main parts.

i. **Selection (detector) slit** which is known as an anti-scatter slit. It reduces the diffusion or scattering of the X-rays that occurs due to amorphous or air scattering.

ii. **Height-limiting slit** which is a type of soller slit. It reduces the axial divergence and limits the beam height.

iii. **Receiving slit** is the height divergence limiting slit that removes diffuse scattered X-rays that occur from previous elements in the secondary optics.

iv. **Monochromator**, the beams pass through another monochromator which acts just as it did in the primary optics. It deflects away K_β and white radiations while allowing only $K_{\alpha 1}$ and $K_{\alpha 2}$ to go through.

The detector

During the detection, the X-rays are absorbed by a compound and then this compound emits visible light. The process of converting X-rays to visible lights is called scintillation. The scintillating compound can be organic or inorganic crystals, or organic compound dissolved in a solvent of NaI activated with Tl. A photomultiplier is used to detect the visible light from the scintillation. The photomultiplier detects photons and then produces a proportional electrical voltage which is the actual source used by the computer to create an output proportional to the flux of incoming X-ray photons.

2.2.2.3 Thin film measurements

In this project, we used a high-resolution D8 Discover diffractometer with $CuK_{\alpha 1}$ radiation filtered by a double-bounce monochromator from Bruker AXS to carry out all our X-ray diffraction measurements. A wide range of measurements can be performed with this diffractometer, including $2\theta/\omega$, rocking curves and reciprocal space mapping (RSM). An interior view of the diffractometer is shown in Figure 2.17.

The most common diffraction scan that is used to characterize the crystal structure of thin films is the $2\theta/\omega$ scan. For this measurement, the ω angle is kept to half of 2θ and the scattering is plotted as a function of 2θ. Prior to performing a $2\theta/\omega$ scan, the thin film sample must be aligned to the correct height. Single crystal substrates are usually used for epitaxial film growth. These substrates are oriented and cut with a selected crystalline plane parallel to the polished surface. After the sample height alignment, these planes should then be aligned into the Bragg plane, resulting in the surface of the film being also aligned. During the $2\theta/\omega$ scan, the Bragg plane is always kept parallel to the surface of the substrate, so the Bragg condition is fulfilled only for *hkl* planes which are parallel to the sample surface. Since

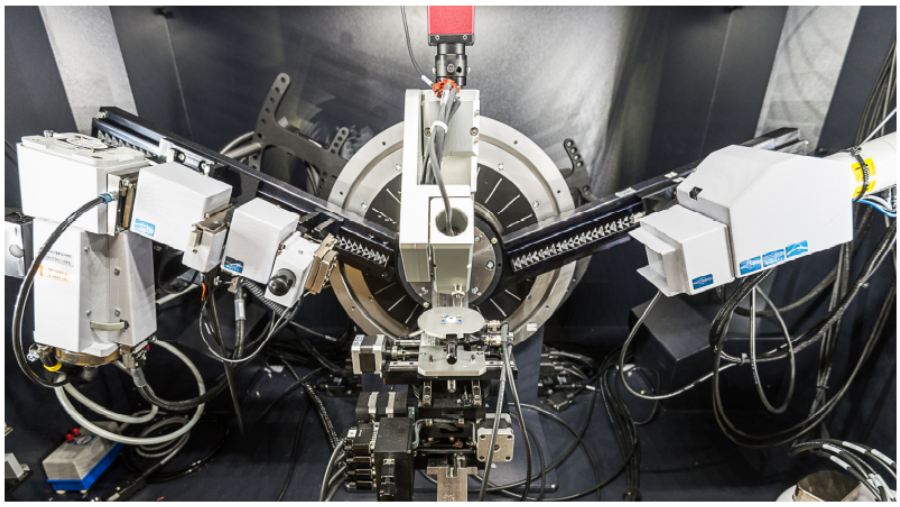

Figure 2.17: The interior view of the X-ray diffractometer used in this project.

epitaxial films are also single crystalline, one expect to see a single set of diffraction peaks in the XRD pattern according to a single orientation of the film. It should be noted that $2\theta/\omega$ scan detects only out-of-plane reflections. In order to access in-plane orientation, pole figures ϕ scans or reciprocal space mapping can be used. Due to the almost perfect nature of the single crystals, peaks from the substrate will often dominate the pattern, whereas peaks from the film may be very low in intensity due to the much lower film thickness. Accordingly, it is common to plot patterns from thin films on a logarithmic intensity scale [130].

2.2.3 Magnetization measurements

The magnetometry data for this thesis have been collected using a Quantum Design Magnetic Property Measurement System (MPMS) XL SQUID magnetometer using the Reciprocating Sample Option (RSO). Different types of measurements have been performed in order to probe different magnetic properties of the materials. In this work, we have carried out two types of magnetic measurements which will be explained in detail, namely magnetization as a function of temperature and magnetization as a function of magnetic field (also called isotherms). Isotherms will be used to evaluate the magnetic entropy changes.

2.2.3.1 RSO measurements

A so-called reciprocating sample option (RSO) measurement is often used for highly sensitive measurements where the volume of the sample is small, such as thin films, leading to very small magnetic moments. Unlike the usual DC transport option in which the sample is moved through the pickup coils in discrete steps, RSO measurements are performed using a servo motor that oscillates the sample rapidly. The position of the sample is tracked by a shaft encoder on the RSO motor. The sample is moved several times through the pickup coils and the measured values are averaged to lower the signal to noise ratio. The sensitivity of the RSO measurements is on the order of 10^{-8} emu, roughly a factor of 100 better than the DC transport option.

RSO measurements can be carried out in two modes: center trace and maximum slope. For the temperature scans at a fixed magnetic field, the center trace mode is employed where it uses large oscillations (1 to 4 cm) around the central point of the pickup coil. The magnetometer can then track the center as it tends to move with temperature due to the thermal expansion of the sample-holder assembly. On the other hand, for the field scans at a fixed temperature (isotherms), the maximum slope mode is used. In this type of scans, the sample is oscillated over a small region at the most linear part of the SQUID voltage response. Smaller amplitudes speed up measurements and prevent the sample from being subjected to significant magnetic field variations, but it may also result in less accurate measurements and be proned to drift in the sample position.

2.2.3.2 M vs T

Measurements of the magnetization as a function of temperature enable one to determine the transition temperature of magnetic materials. Additionally, it provides information about the strength of magnetic interactions in a system and the type of magnetic interactions at play (χ vs. T above T_c). There are two ways to perform this measurement. First, a relatively low magnetic field is applied at high temperature and then, the sample is cooled down to low temperature in the presence of a magnetic field. The sample is centered at low temperature and the measurement begins.

The sample is slowly brought to room temperature while the magnetization is being measured. This is known as field-cooled (FC) magnetization measurement. Zero-field-cooled (ZFC) measurement is another way to perform M vs T measurements in which the sample is cooled down to low temperature in zero applied magnetic field. Afterward, a low magnetic field is applied to the sample at low temperature, and the magnetization measurement starts while the sample warms up. It is important to note that the applied field for ZFC M vs T measurements must be higher than the coercive field (H_c) of the sample at low temperatures, otherwise the shape of the M vs T curve can be significantly altered, leading to misinterpretation of the results.

In this work, all M vs T measurements were done with the FC approach while the RSO was set in the center trace mode in the temperature range of 10–370 K at a fixed magnetic field of 200 Oe applied along the surface of the films. This mode allows us to track the gradual change of length of the sample-holder rod with temperature.

2.2.3.3 M vs H

Measurements of magnetization as a function of magnetic field allow one to define the hysteresis loop of a magnetic material and to determine the coercive field (H_c) and the saturation magnetization (M_s) at a fixed temperature. In order to obtain the maximum values of H_c and M_s, isothermal M vs H measurements were carried out at 10 K. During the measurements, the magnetic field changed from 7 T to -7 T by small increments, then returned back to 7 T again. Since the temperature is constant in these measurements, M vs H measurements were conducted using the RSO maximum slope mode. It should be mentioned that a large negative background is observed at high magnetic fields originating from the sample holder and the substrate. In order to define the saturation magnetization, this negative background must be subtracted from the magnetization of the samples. Similar M vs H measurements were carried out at other temperatures up to room temperature (300 K).

2.2.3.4 MCE

In this project the magnetic entropy change ΔS_m of all bilayer and trilayer samples have been calculated from the magnetization measurements using Maxwell relation (Eq. 2.20). For this purpose, the magnetic field dependence of the isothermal magnetization of the samples were measured in the temperature range of 50–370 K with a temperature interval of 10 K. Similar to M vs H measurements, the magnetization was recorded using the RSO maximum slope mode, but to avoid drifting of the sample position with respect to the center of the pickup coil due to thermal expansion of the straw, the sample was centered with a low magnetic field before every isothermal magnetization measurement. In addition, since the DC susceptibility of the sample holder and the straw varies very slowly with temperature compared to LSMO and LNMO films, the negative background does not have to be subtracted to evaluate the MCE.

2.3 Results and discussion

2.3.1 Motivation

Among many ways to improve the MCE, composites are considered as one of the most effective approaches to broaden the magnetic entropy variations while maintaining intensity uniformly throughout the temperature range. In this work, we simulate a composite approach using heterostructures to tailor an appropriate magnetocaloric material for magnetic refrigeration over a large temperature range. For this purpose, we chose $La_{2/3}Sr_{1/3}MnO_3$ (LSMO) manganite with a magnetic phase transition above room temperature, at 370 K, and also La_2NiMnO_6 (LNMO) double perovskite with two magnetic transitions at 170 K and 285 K. Combining these two materials and taking advantage of the potential presence of tunable multiple magnetic transitions in LNMO by varying the growth conditions and/or strain effects, the MCE can be adjusted over a wide range of temperature covering room temperature. As discussed in section 1.2.3, the magnetic phase transitions in LNMO can be tuned by changing the level of cationic ordering in the sample. In this project,

we try to control the level of cationic ordering in LNMO using epitaxial strain originating from the lattice mismatch between the layers and the substrate. We propose to tailor wide-range magnetocaloric materials with the combination of LSMO and LNMO in form of composite-like heterostructures. In order to do that, pulsed laser deposition technique is used to grow epitaxial bilayer and trilayer heterostructures of LSMO and LNMO with different layouts on (001)-oriented LSAT substrates. We prepared bilayer samples with LSMO/LNMO and LNMO/LSMO configurations as well as trilayer samples with LSMO/LNMO/LSMO and LNMO/LSMO/LNMO arrangements.

The results of our work are presented in the following paper and accompanying supplemental material submitted to the Journal of Magnetism and Magnetic Materials on Dec 18, 2022 . It should be noted that the results of monolayers of LSMO and LNMO are presented in appendix A.

The authors confirm contribution to the paper as follows: **M. Abbasi Eskandari:** Conceptualization, Samples preparation, Investigation, Visualization, Writing – original draft. **S. Ghotb:** Samples preparation, Investigation. **M. Balli:** Writing – review & editing. **P. Fournier:** Conceptualization, Writing – review & editing, Supervision, Project administration, Funding acquisition.

2.3.2 Paper

Impact of strain on the magnetocaloric effect of oxide heterostructures

M. Abbasi Eskandari,[1] S. Ghotb,[1] M. Balli,[2] and P. Fournier[1]

[1] *Institut quantique, Regroupement québécois sur les matériaux de pointe et Département de physique, Université de Sherbrooke, Sherbrooke, J1K 2R1, Québec, Canada*

[2] *LERMA, ECINE, International University of Rabat, Parc Technopolis, Rocade de Rabat-Salé, 11100, Morocco*

We report a detailed study of the magnetocaloric effect in heterostructures of La_2NiMnO_6 and $La_{2/3}Sr_{1/3}MnO_3$. The shape, width and magnitude of the temperature dependence of the magnetic entropy change (ΔS_m) for these multilayer samples are affected by their layout with a clear impact from epitaxial strains on each layer. A large ΔS_m over a wide temperature range which goes beyond room temperature is observed in all samples. We observe a temperature-independent table-top-like ΔS_m over a temperature range as large as 100 K in the trilayer samples. La_2NiMnO_6 double perovskite with multiple magnetic phase transitions sensitive to strain is the key to tuning and shaping the temperature dependence of the magnetic entropy changes to suit specific cooling cycle requirements.

I. INTRODUCTION

Magnetic refrigeration technology based on the magnetocaloric effect (MCE) has been under the spotlight due to its advantages over the conventional gas compression technology, such as higher energy efficiency and being eco-friendly [1, 2]. The MCE is an intrinsic property of magnetic materials and it is defined as the heating or cooling of a magnetic substance as it is magnetized or demagnetized, respectively. The MCE was first reported in 1917 by P. Weiss and A. Piccard in nickel close to its paramagnetic to ferromagnetic transition temperature. They noted that Ni would warm up or cool down when magnetized or demagnetized [3]. Isothermal magnetic entropy change (ΔS_m) and adiabatic temperature change (ΔT_{ad}) are two parameters that are mostly used in order to characterize the potential of a magnetocaloric material. ΔS_m and ΔT_{ad} indicate the amount of heat that can be moved during the refrigeration process and the temperature change that can be achieved, respectively. They can be measured using specific heat or magnetization. In the late 1970s, gadolinium was introduced as the first working material for magnetic refrigeration at room temperature taking advantage of its large MCE near its magnetic transition [4]. Gd shows a large isothermal entropy change of $-\Delta S_m = 5.5\,J\,kg^{-1}\,K^{-1}$ and an adiabatic temperature change of $\Delta T_{ad} = 6\,K$ near its transition temperature at 294 K under a magnetic field of 2 T, numbers still used as reference for comparison with novel competing materials. However, for an implementation in domestic cooling devices, one needs to find materials with a magnetic transition leading to a significant magnetic entropy change over a wide temperature range covering roughly from 20 °C to −20 °C. For some magnetic refrigeration cycles such as active magnetic regenerative (AMR) refrigeration, a so-called *table-top* temperature independence of the magnetic entropy change would be also a great asset [2].

A narrow working temperature range, the metallic behavior and the high cost of Gd restrict its utilization for domestic and large scale applications. Looking for alternative solutions, many families with significant magnetocaloric effect close to room temperature such as Gd-based alloys [5, 6], $LaFe_{13-x}Si_x$ intermetallic compounds [7, 8] and manganites of general formula $R_{1-x}A_xMnO_3$ (where R = Lanthanide and A = divalent alkaline earth) have received enormous attention due to their advantages such as tunable transition temperature using chemical manipulations and large MCE [9, 10]. For instance, magnetic and magnetocaloric properties of $La_{1-x}Sr_xMnO_3$ (LSMO) manganites have been widely explored. It shows a high transition temperature (T_c), as high as 370 K, with a maximum magnetic entropy change of $1.5\,J\,kg^{-1}\,K^{-1}$ at 1 T [11]. Despite the narrow operating temperature range related to ΔT_{ad} and its metallic nature driven by double exchange, a large ΔS_m makes $La_{1-x}Sr_xMnO_3$ a promising candidate for magnetic cooling systems at room temperature. Similarly, double perovskites with general formula $A_2BB'O_6$ (where A is a trivalent rare earth or divalent alkaline and B and B′ are transition metals) have also attracted interest for their large MCE [12–14]. The main advantage of double perovskites over manganites is their higher electrical resistivity [15, 16]. La_2NiMnO_6 (LNMO) as a near room-temperature ferromagnetic semiconductor is attracting because of its unique properties such as the existence of two magnetic phases with different transition temperatures controlled by the level of B/B′ site cationic ordering [17–19]. Cation-ordered LNMO exhibits a maximum magnetic phase transition at 285 K. In this ordered phase, only ferromagnetic $Ni^{2+}-O-Mn^{4+}$ bonds driven by superexchange exist. On the other hand, non-optimal growth conditions can lead to a mixture of ferromagnetic ($Ni^{2+}-O-Mn^{4+}$) and antiferromagnetic ($Ni^{2+}-O-Ni^{2+}$ and $Mn^{4+}-O-Mn^{4+}$) bonds in a so-called cation-disordered phase. The fully disordered LNMO still shows a magnetic transition at $T_c \sim 150$ K [17]. This transition temperature gradually increases with the level of cationic ordering as samples oftentimes show two magnetic transitions [20]. This unique feature allows one to control and tune the magnetic and

magnetocaloric properties in LNMO by changing the ratio of ordering in the system through variation of the growth conditions in hope of tailoring a proper MCE. For instance, Matte *et al*, [21] investigated the effect of thin film growth conditions on the level of ordering in LNMO and consequently on magnetocaloric properties. The authors were able to control and adjust the shape and width of ΔS_{m} and get a temperature-independent magnetic entropy change over a wide temperature range, as large as 100 K, by changing the ratio of ordering in LNMO, taking advantage of the two magnetic transitions in the same sample and reproducing in a sense what is expected from a composite.

As other compounds, magnetic and magnetocaloric properties of manganites and double perovskites can be tuned in the hope of achieving a large and temperature independent magnetic entropy change. In order to attain a desirable magnetic entropy change close to room temperature, several routes have been widely explored such as doping with different elements and changing the growth conditions [13, 21, 22]. Another approach to control and tune the magnetocaloric properties of materials is to combine different materials in a composite structure [23–25]. In this case, materials with different transition temperatures are used to obtain a large magnetic entropy change over a wide temperature range [23, 24]. In this paper, we choose heterostructures mimicking composites to achieve a suitable magnetocaloric material at room temperature. For this purpose, we take advantage of the potential presence of tunable multiple magnetic transitions in LNMO and try to adjust them by subjecting each LNMO layer to different strain fields while combining it to LSMO showing a transition above room temperature. We grow and study the properties of bilayers and trilayers with the intention of tailoring the magnetic entropy change over a wide temperature range, while taking advantage of strain effects provoked by the lattice mismatches between the substrate and the materials included in different heterostructure layouts.

II. EXPERIMENTS AND METHODS

In this paper, two series of bilayers and trilayers of La_2NiMnO_6 (LNMO) and $La_{2/3}Sr_{1/3}MnO_3$ (LSMO) with different configurations are made on (001)-oriented LSAT substrates (Figure 1). The epitaxial bilayers and trilayers samples are grown by pulsed laser deposition (PLD) using a KrF excimer laser. The films are deposited at 800 °C, under an oxygen pressure of 200 mTorr. After the deposition, the PLD chamber is filled with oxygen up to 200 Torr, and then the films are cooled down to room temperature with a cooling rate of 10 °C/min. In the first type of bilayer samples (Fig. 1 (a)), a layer of LSMO is placed initially on the substrate and then a layer of LNMO is deposited on top: it is named B−SN. The other bilayer layout is simply the reverse (Fig. 1 (b)), with a first layer of LNMO on the substrate followed by a layer of LSMO on top (B−NS). These bilayers allow us to sort out the impact of strain on the magnetic properties caused by the lattice mismatch between the substrate and the films. Two different types of trilayer samples were also made. In the first trilayer samples shown in Fig. 1 (c), a layer of LNMO is sandwiched between two LSMO layers (T−SNS). Fig. 1 (d) shows the second type of trilayer samples with two LNMO layers and a middle LSMO layer (T−NSN). Each single layer of LSMO and LNMO has a thickness of 50 nm, implying that the bilayer and trilayer samples have a total thickness of 100 and 150 nm, respectively. 100 nm thick monolayers were also grown for comparison.

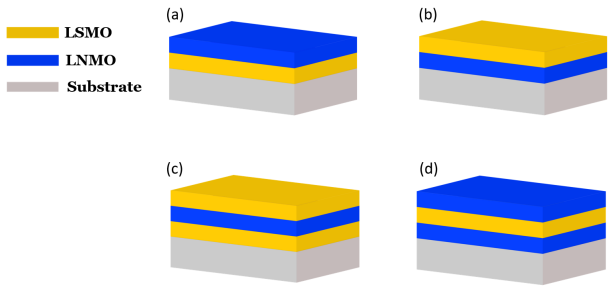

FIG. 1: Schematic illustration of all grown samples. (a) bilayer of LSMO-LNMO (B−SN), (b) bilayer of LNMO-LSMO (B−NS), (c) trilayer of LSMO-LNMO-LSMO (T−SNS) and (d) trilayer of LNMO-LSMO-LNMO (T−NSN).

Room temperature x-ray diffraction (XRD) was performed using a high-resolution Bruker AXS D8-diffractometer with $CuK_{\alpha 1}$ radiation in the $2\theta/\omega$ configuration. The measurement of the magnetic properties are carried out using a Magnetic Property Measurement System (MPMS) from Quantum Design. In order to detect the small magnetic signals from thin films, magnetization measurements were performed using the reciprocating sample option (RSO) with an external magnetic field applied parallel to the surface of the samples. In this work, in order to determine the Arrott plots and the isothermal magnetic entropy changes (ΔS_{m}), the isothermal magnetization curves as a function of the applied field up to 7 T in the temperature range of 50 to 370 K with a temperature interval of 10 K are measured for all the samples. Figure 2 shows an example of isothermal magnetization measurements for a B−NS sample. As one may notice, all the magnetization curves show a negative slope at large field (Fig. 2 (a)) which originates from the diamagnetism of the substrate and the sample holder. As shown in Fig. 2 (b), the magnetization of layers which saturate very rapidly at low field can be clearly seen by removing this negative background. It should also be mentioned that the mass of the multilayers were estimated using the theoretical density of LSMO and LNMO, as well as the volume of the layers.

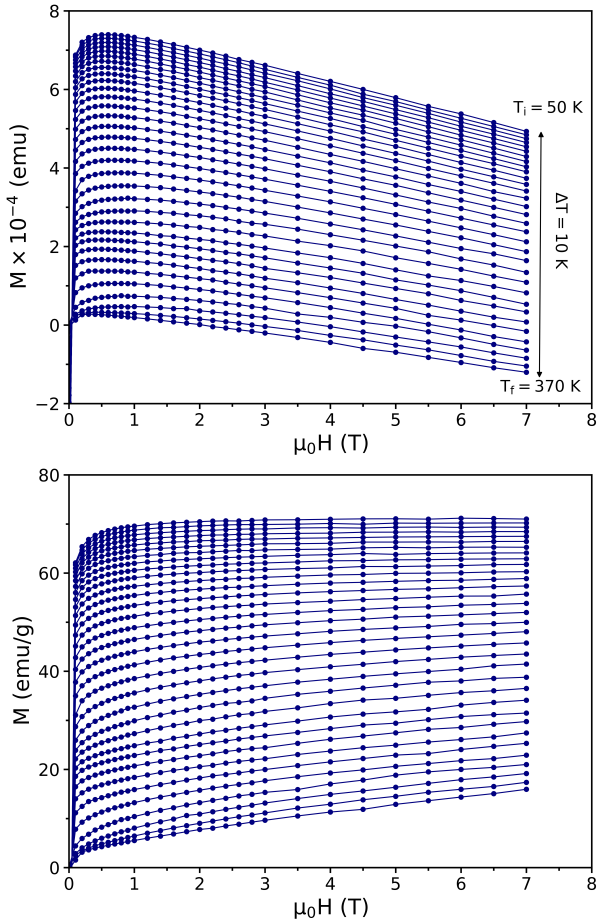

FIG. 2: Isothermal magnetization curves as a function of magnetic field in the temperature range from 50 to 370 K with the temperature interval of 10 K for B−NS sample; (a) Including the diamagnetic signal from the substrate and the sample holder (b) After removing the negative background.

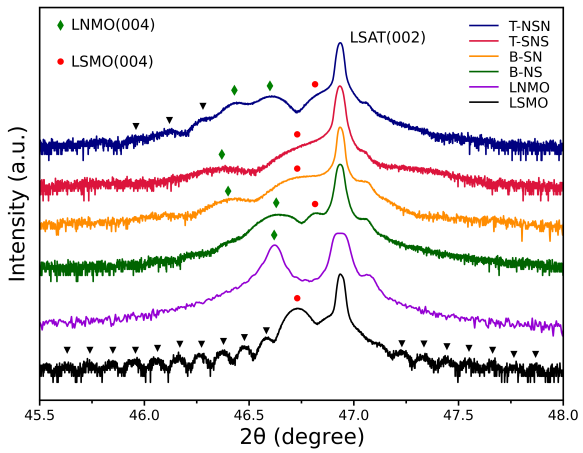

FIG. 3: X-ray diffraction patterns. From bottom to top: of the monolayers of LSMO and LNMO, two bilayers of B−SN and B−NS, as well as two trilayers of T−SNS and T−NSN. Laue oscillations are specified with (▼). The spectra have been moved vertically for clarity.

III. RESULTS AND DISCUSSION

Figure 3 shows the XRD patterns of all samples from 45° to 48° close to the substrate's (002) Bragg peak. The XRD patterns of 100 nm thick monolayers of LSMO and LNMO at the bottom of the figure show the proximity of their (004) diffraction peaks. In these individual spectra, the single layers of LSMO and LNMO exhibit a central peak at 46.73° and 46.62°, respectively. In both cases, their position is in part defined by the impact of strain due to their lattice mismatch with the substrate shifting their angular position with respect to the bulk [26, 27]. We are expecting strain to play also a role for thinner layers inserted in multilayers with additional shifts. Nevertheless, the growth conditions used for this work produce extremely smooth LSMO as revealed by the numerous Laue oscillations.

For the multilayers, all observed peaks can be assigned to the $(00l)$ crystallographic planes. It is confirming their out-of-plane orientation and a smooth cube-on-cube growth. For bilayers, the LNMO diffraction peak for B−SN sits at a lower value of 2θ than in B−NS as its top LNMO layer is affected by the compressive strain from the bottom LSMO layer. In the supplemental material, we show the spectra close to the substrate's (001) Bragg peak. In this case, we observe Laue oscillations coming from LSMO and/or LNMO layers. The presence of these oscillations confirms the good crystalline quality of our samples with a well-defined interface. The top two spectra in Fig. 3 present the data for T−NSN and T−SNS trilayers. We notice the presence of three distinct peaks in the spectrum for T−NSN, where the peaks for the top and the bottom layers of LNMO coexist in the sample: their separation is the result of different strain experienced by both layers. In this particular case, we conclude in fact that the top LNMO layer is affected by a stronger compressive strain than the bottom one consistent with expectations. Finally, the XRD spectrum for T−SNS shows only two diffraction peaks, one is associated to the middle LNMO layer, and two LSMO layers show a broad peak close to the substrate's peak.

Atomic force microscopy (AFM) data (see supplemental material) show that the surface roughness on top of the monolayers, bilayers and trilayers is on the order of 1–2 nm, 3–7 nm and 7–14 nm, respectively. In fact, variations of about 1–2 nm over lateral distances of the order of 1 μm for the monolayers indicate that the second and/or the third layers grow on top of a fairly smooth surface, resulting in well-defined interfaces between the layers.

In the next section the magnetic and magnetocaloric properties of bilayer and trilayer samples will be investigated in detail.

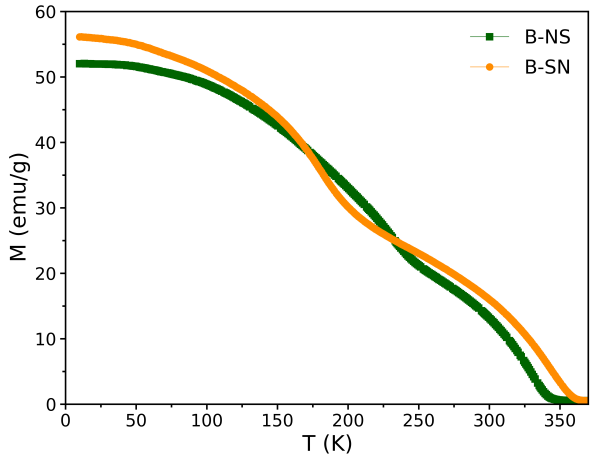

FIG. 4: Temperature dependence of the FC magnetization of the bilayer samples at a fixed magnetic field of 200 Oe in the temperature range between 10 to 370 K.

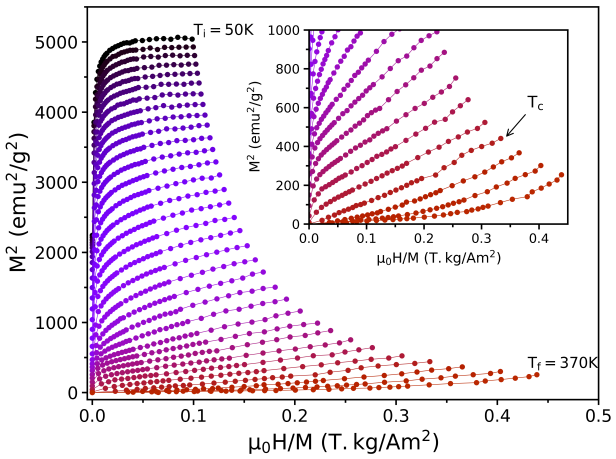

FIG. 5: Arrott plots in the temperature range from 50 to 370 K with a temperature interval of 10 K for B−NS sample. The inset of figure shows Arrott plots close to the transition temperature of the sample.

A. Bilayers

Figure 4 shows field-cooled (FC) magnetization measurements as a function of temperature at a fixed magnetic field of 200 Oe for bilayer samples. Both samples undergo two magnetic phase transitions from the ferromagnetic to the paramagnetic state. In the case of the B−NS sample, a first transition at roughly 230 K comes from the LNMO layer while the other at 330 K is related to the LSMO layer. The magnetic transition of LNMO at temperatures above 200 K confirms a high but incomplete level of cation ordering at the B/B′ sites in the LNMO layer sitting directly on the substrate. For B−SN layout, the magnetic transition of the LSMO layer shifts at 345 K, while the transition temperature of LNMO sitting on top of LSMO shifts down to 180 K. The lower transition temperature of the LNMO layer in this configuration indicates a lower level of cation ordering than in the previous bilayer [17]. This difference in cation ordering level for LNMO in both bilayers is likely driven by the different strain fields experienced by the LNMO layer [28, 29]. Even the slight difference in the transition temperature of the LSMO layer in different bilayer configurations with shifts from 330 K in B−NS to 345 K in B−SN can be also attributed to the effect of strain [30, 31].

This set of bilayers demonstrates that we can change easily the level of cation ordering in LNMO and control the magnetic properties of layers just by changing the layout of the layers in bilayers, but also in more complex heterostructures. This feature provides an interesting avenue to tailor the magnetocaloric behavior close to room temperature, which will be discussed in detail later.

As it is known, MCE strongly depends on the nature of the magnetic phase transition. It should be noted that materials with a first-order magnetic phase transition usually show a large magnetic entropy change in a very narrow temperature range while their magnetic transition is usually accompanied by large thermal and magnetic hysteresis which neither of them are favorable for magnetic cooling systems [10, 32]. On the other hand, the broad magnetic phase transition and the reversible nature in second-order phase transition materials make them better suited for magnetic cooling systems. So, in order to get a deeper understanding of the nature of magnetic phase transition in our samples, the Arrott plots for the bilayers are derived from isothermal magnetization curves which are measured in the temperature range between 50 to 370 K under to 0–7 T. According to Banerjee's criterion [33], the negative or positive slope of Arrott plots indicate whether the magnetic phase transition is first or second order, respectively. The Arrott plots of the B−NS bilayer sample is depicted in Figure 5 as an example, and it clearly shows a positive slope for the entire temperature range confirming the existence of a second-order magnetic phase transition in our sample. Moreover, the transition temperature of magnetic materials can be extracted using the same plots [34]. Based on the mean-field theory, Arrott plot curves near the transition temperature become straight lines crossing the origin. The inset of Fig. 5 shows the same Arrott plots near the highest transition temperature corresponding to LSMO for that B−NS sample. Similar plots can be found in the supplemental material for the other configurations. From this data, it was found that the highest transition temperature of B−NS and B−SN samples occur at 360 and 340 K, respectively. These transition temperatures from the LSMO layers are in close agreement with the M(T) measurements. Unfortunately, the lowest transition temperature of LNMO cannot be isolated out of these plots.

In order to determine $-\Delta S_{\mathrm{m}}$, Maxwell's relation linking the magnetic entropy change to the bulk magnetization (M), the temperature (T) and the external magnetic

field (B) can be used through the following equation [35]:

$$\left(\frac{\partial S}{\partial B}\right)_{P,T} = \left(\frac{\partial M}{\partial T}\right)_{P,B} \quad (1)$$

In both isothermal and isobaric conditions, the isothermal magnetic entropy change induced by a change in external magnetic field can then be written as:

$$\Delta S_{\mathrm{m}}(T, B_f \rightarrow B_i) = \int_{B_i}^{B_f} \left(\frac{\partial M}{\partial T}\right)_{P,B'} \mathrm{d}B' \quad (2)$$

Eq. 2 indicates that the magnetic entropy change is proportional to both the external field variation and the sharpness of a magnetic phase transition. Since magnetization measurements are usually made at discrete field and temperature intervals, $-\Delta S_{\mathrm{m}}$ can rather be computed using [10]:

$$\Delta S_{\mathrm{m}}(T, B) = \sum_i \frac{M_{i+1} - M_i}{T_{i+1} - T_i} \Delta B_i \quad (3)$$

where M_i and M_{i+1} are the magnetization value measured at temperatures T_i and T_{i+1}, under a magnetic field changing from 0 to B, respectively. Thus, Eq. 3 (and Eq. 2) evaluates the surface area between two isothermal magnetization curves measured at T_i and T_{i+1} (as presented in Fig. 2 (b)) with T being their average.

The main scope of this work is to tailor a large and temperature independent magnetic entropy change over a wide temperature range. In order to achieve this goal and make a desirable magnetocaloric material, composite-like bilayer and trilayer structures are chosen as the main route. On top of that, it uses LNMO as a magnetic material with a tunable magnetic transition and combines it within a composite-like structure in the hope of getting a unique magnetocaloric feature. As discussed earlier, the magnetic properties of bilayer samples such as T_{c} are affected by changing their layout. So, in this part we inspect to see how this change affects the magnetocaloric properties of bilayer samples.

The calculated isothermal magnetic entropy changes ($-\Delta S_{\mathrm{m}}$) as a function of temperature are shown in Figures 6 (a) and (b) for both bilayer samples under various magnetic field changes up to 7 T. Moreover, the magnetic entropy changes of the monolayers of LNMO and LSMO for $\mu_0 \Delta H =$ 5 T are displayed in the background of Fig. 6 with light blue and grey, respectively. As expected, both bilayer samples exhibit two broad maxima in $-\Delta S_{\mathrm{m}}$ curves approaching the transition temperatures of each layer. In the B−NS sample (Fig. 6 (a)), these two maxima seen at 235 and 335 K are related to the T_{c} of the cation ordered LNMO and the LSMO layers, respectively. The transition temperature of the LNMO layer almost coincides with that of the monolayer of LNMO with a T_{c} at 245 K, confirming that the level of cationic ordering in this layer is not very much affected by the strain from the top LSMO layer. In comparison to the monolayer of LSMO in which the T_{c} is at 365 K, the LSMO layer in the B−NS sample experiences a 30-K shift in transition. The difference could originate from the epitaxial strain caused by the bottom LNMO layer leading to a change in the bond length and bond angle of Mn−O−Mn bonds in the MnO_6 octahedra. The maximum magnetic entropy changes which are attributed to ordered LNMO and LSMO layers are 1.80 and 1.70 J kg^{-1} K^{-1} for a magnetic field change of 0–7 T. On the other hand, in the B−SN sample (Fig. 6 (b)), the maximum which is related to the transition of LNMO layer shifts down to 185 K, while the one related to the transition of LSMO increases to 345 K. The significant drop in the T_{c} of LNMO can be attributed to the reduction of the cationic ordering level due to the increased epitaxial strain on the LNMO layer, which is in agreement with the trend observed in the XRD data (Fig. 3). Also, $-\Delta S_{\mathrm{m}}$ reaches a maximum value of 1.76 and 1.42 J kg^{-1} K^{-1} for LNMO and LSMO layers under $\mu_0 \Delta H = 7$ T, respectively.

As noticed, both bilayer samples show a large magnetic entropy change which barely varies over a wide temperature range. The full width at half maximum is about 250 K for both samples (from ∼115 K to above room temperature at ∼365 K). Unlike the other approaches used to tune the magnetic properties and especially the MCE such as doping or changing the growth conditions, this composite-like approach allows one to widen the magnetic entropy change without sacrificing much of the ΔS_{m} magnitude. In the next section we show how ΔS_{m} can be further improved in terms of intensity and temperature span by adding another layer to the composites structure. Of course, we will show that strain can be used to our advantage as was done with bilayers.

B. Trilayers

As seen in the previous section, we can take advantage of the sensitivity of cation ordering to strain of LNMO in multilayer samples just by changing the stacking order of the layers. This effect originates from different lattice mismatches between the layers and the substrate. It provides an opportunity to control the magnetic and magnetocaloric properties of more complex heterostructures and tailor a large MCE over a wide temperature range. As a proof of concept, trilayer samples with LNMO−LSMO−LNMO and LSMO−LNMO−LSMO configurations are compared.

Figure 7 shows field-cooled (FC) magnetization as a function of temperature under a fixed magnetic field of 200 Oe for both trilayer samples. As expected, T−NSN sample exhibits three magnetic phase transitions at roughly 155, 230 and 335 K. This is confirmed in particular using the derivative $\mathrm{d}M/\mathrm{d}T$ as shown in the inset of Fig. 7. The first transition at 155 K comes from the top LNMO layer experiencing strain similar to that in the

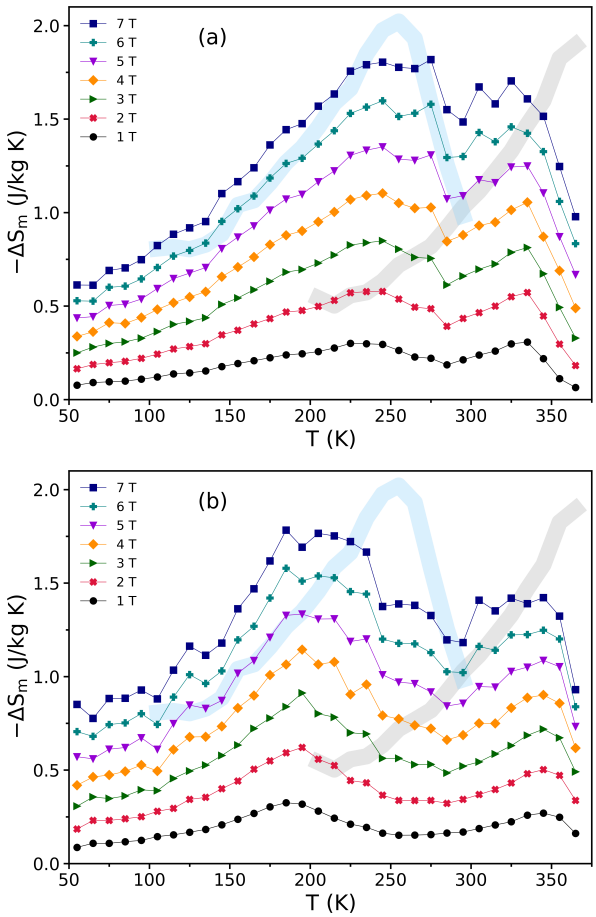

FIG. 6: The magnetic entropy change as a function of temperature for different magnetic field variations for (a) B−NS and (b) B−SN samples. The light blue and grey curves on the background show the $-\Delta S_m$ as a function of temperature at a magnetic field of 5 T for monolayers of LNMO and LSMO.

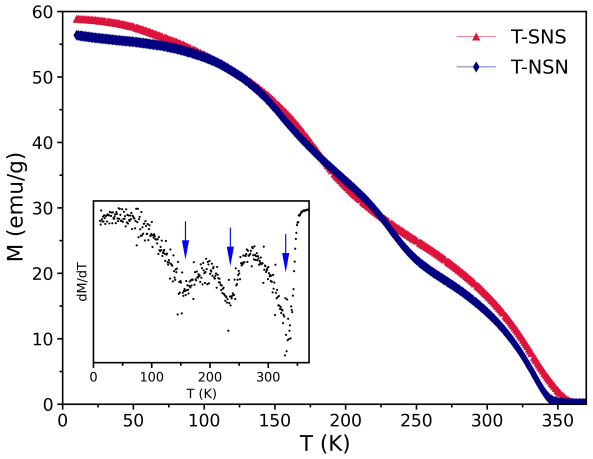

FIG. 7: Magnetization as a function of temperature under a magnetic field of 200 Oe for the trilayer samples. The inset shows the derivative of the magnetization with respect to the temperature for the T−NSN sample. The transitions are indicated with blue arrows.

B−SN sample. The second magnetic transition at 230 K comes from the bottom LNMO layer in direct contact with the substrate as was observed in the B−NS bilayer. Finally, the transition at 335 K is related to the LSMO layer sitting between two LNMO, consistent also with its T_c observed in the B−NS bilayer. In the other trilayer sample (T−SNS), we observe only two magnetic phase transitions in the M(T) curve at 180 and 340 K. The LSMO layers show a T_c at 340 K and the middle LNMO layer has a T_c at 180 K. This value of T_c ∼180 K indicates that it has almost the same level of cationic ordering as what we have observed for LNMO in B−SN sample.

In a trilayer sample with two LNMO layers, we can have both disordered and partially ordered LNMO phases simultaneously in the sample from the top and bottom layers experiencing different strain fields. As a result, trilayer samples with the T−NSN configuration gives three different transitions which covers quite a large temperature range starting from 155 to 335 K. With an appropriate choice of thicknesses for each layer, one could get a temperature-independent table-top magnetic entropy change over a wide temperature range close to room temperature.

As mentioned before, one of the biggest advantage of SOMT materials is their small thermal and magnetic hysteresis. In Figure 8 (a), the magnetization as a function of magnetic field was measured for a T−NSN sample at the transition temperature of each layer and at 10 K. The sample saturates very quickly at low magnetic field, and also it exhibits a very low coercive field of 160 Oe at 10 K and this value decreases to roughly 10 Oe at 335 K (Fig. 8 (b)). The same is observed for the T−SNS sample (see supplemental material).

Magnetic isotherms measurements are carried out in the temperature range going from 50 to 370 K to determine Arrott plots and magnetic entropy changes for both trilayer samples. Similar to bilayers, an example of Arrott plots measurements for trilayers is shown in Figure 9. All M^2 vs. H/M curves of the T−SNS sample show positive slopes in the entire temperature range which indicates that the sample undergoes a second-order magnetic phase transition. A similar trend can be observed in the Arrott plots of the other trilayer (T−NSN, see supplemental material). Furthermore, in order to determine the T_c of the samples, the Arrott plots close to the transition temperature of T−SNS multilayer is depicted in the inset of Fig. 9. It is found that the transition of T−SNS and T−NSN samples occur at 350 and 340 K, respectively. As we saw in the bilayer samples, these two transitions are those of the LSMO layers in agreement with the M(T) measurements in Fig. 7.

Magnetic entropy changes as a function of temperature taken at different magnetic fields for the two trilayer samples are plotted in Figures 10 (a) and (b). At the transition temperature of each layer, there is a broad

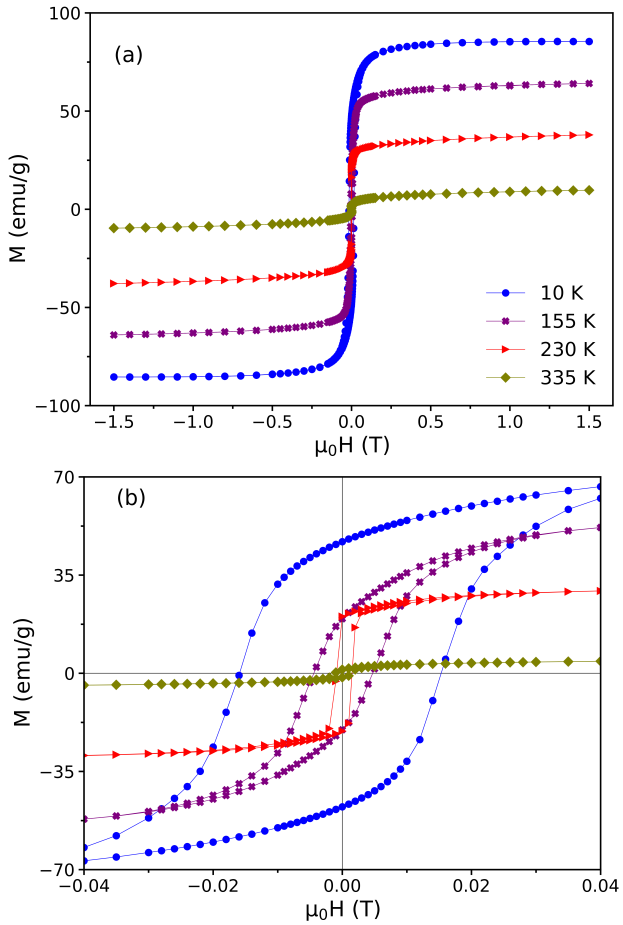

FIG. 8: (a) Magnetization as a function of magnetic field for a T−NSN sample at 10, 155, 230 and 335 K. (b) The hysteresis loops at low field showing the small coercive fields.

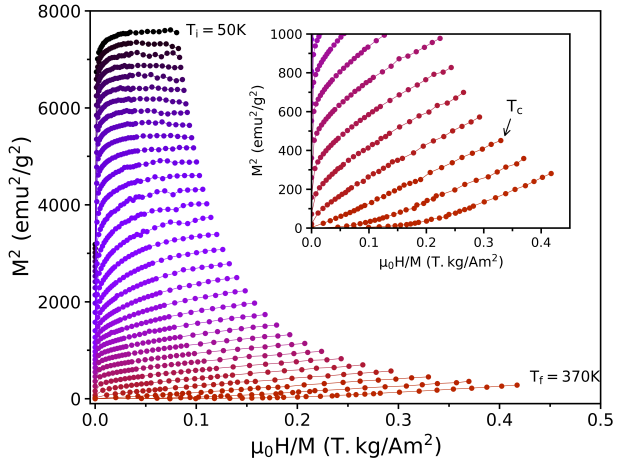

FIG. 9: Arrott plots of T−SNS sample in the temperature range between 50 and 370 K. The inset shows Arrott plots close to the T_c of the LSMO layer.

maximum in ΔS_m that comes from the magnetic phase transitions occurring at the transition temperatures of each layer. For instance, the T−SNS sample (Fig. 10 (a)) exhibits two peaks in ΔS_m curves at 185 and 335 K which correspond to the magnetic transition of LNMO and two LSMO layers, respectively. The maximum values of $-\Delta S_m$ corresponding to LNMO and LSMO layers are 1.56 and 2.03 J kg^{-1} K^{-1} for $\mu_0\Delta H = 7$ T. As shown in Fig. 10 (b), the other trilayer sample (T−NSN) shows three peaks in ΔS_m curves due to the existence of different magnetic phases in two LNMO layers. They can be better observed for low applied field (1 and 2 T). For this layer configuration, the peaks are located at 175, 245 and 345 K which are related to the transition of disordered LNMO layer (the top layer), the cation-ordered LNMO layer (the bottom layer) and the LSMO middle layer, respectively. For $\mu_0\Delta H = 7$ T, $-\Delta S_m$ shows a maximum of 2.21, 2.21 and 1.42 J kg^{-1} K^{-1} that correspond to disordered LNMO, ordered LNMO and LSMO layers, respectively.

It must be emphasized that the large magnetic entropy changes with a wide operating temperature range ($\delta T_{\rm FWHM} = 260$ K) which go slightly above room temperature would make these multilayer composites an interesting candidate for magnetic cooling systems at room temperature. In addition, both trilayer samples show a fairly flat and temperature-independent ΔS_m within the mid-range temperature which can extend over $\Delta T \sim 100$ K under $\mu_0\Delta H = 5$ T (Figs. 10). This temperature independent ΔS_m over a wide temperature window would make these two trilayer samples suitable candidates for AMR refrigeration [36]. Moreover, with an appropriate choice of thicknesses for each layer (for example a bit thicker for LSMO) one could likely generate a constant $-\Delta S_m$ from 175 to 335 K.

A useful tool which allows usually to compare the cooling performances of magnetocaloric materials is the relative cooling power (RCP). RCP is the amount of heat transfer between the cold and hot reservoirs in one refrigeration cycle and it is defined as:

$$RCP = -\Delta S_m(\max) \times \delta T_{\rm FWHM} \tag{4}$$

RCP is not only considering the amplitude of the magnetic entropy change $\Delta S_m(\max)$, but it also takes into account the working temperature range $\delta T_{\rm FWHM}$ which is a key parameter in magnetic cooling systems. RCP is mostly used for materials with a single transition which have a fairly symmetric peak in $\Delta S_m(T)$ curves. However, in the case of composites and materials with more than one transition, refrigerant capacity ($\mathcal{RC}$) is usually employed [21, 37]. $\mathcal{RC}$ is specified as the area under the curve of ΔS_m between the temperatures which correspond to half maximum [38]:

$$\mathcal{RC} = -\int_{T_C}^{T_H} \Delta S_m(T) \mathrm{d}T \tag{5}$$

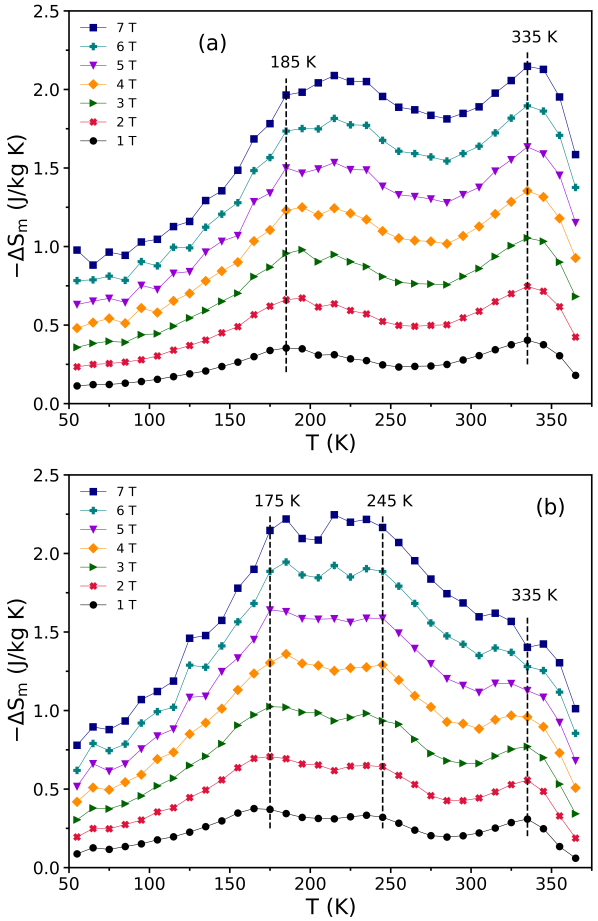

FIG. 10: Temperature dependence of the magnetic entropy change of (a) T−SNS and (b) T−NSN samples under various magnetic field changes.

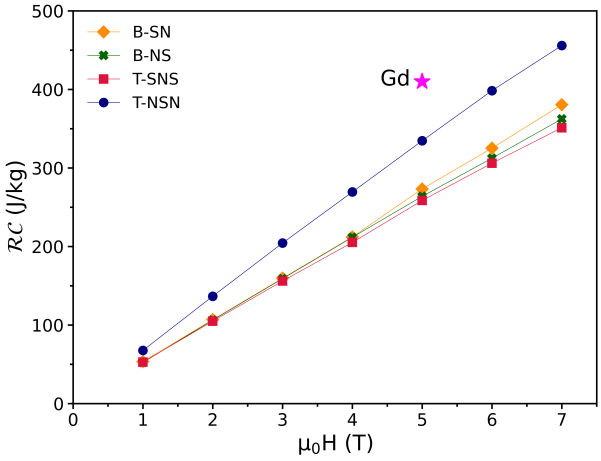

FIG. 11: Refrigerant capacity ($\mathcal{RC}$) as a function of magnetic field for all samples. $\mathcal{RC}$ of gadolinium is shown for comparison [39].

Figure 11 presents the $\mathcal{RC}$ values as a function of magnetic field for all four samples and also that of gadolinium as a reference to compare with our samples. All samples show a relatively large $\mathcal{RC}$ with an almost linear magnetic field dependence. The values of $\mathcal{RC}$ reach 273, 264, 259 and 335 J kg^{-1} for B−SN, B−NS, T−SNS and T−NSN under a magnetic field of 5 T, respectively. By comparing with Gadolinium as a reference [39], it can be seen that the value of $\mathcal{RC}$ for T−NSN sample is about 82 % of Gd for $\mu_0\Delta H = 5$ T. All the values of $\Delta S_{\rm m}$ and $\mathcal{RC}$ for our samples under different magnetic fields are listed in Table I. Among other families with comparable $\mathcal{RC}$ to Gd, such as La(FeSi)$_{13}$−based [40, 41] and Gd$_5$(SiGe)$_4$−based [42] compounds, our multilayer samples have additional advantages over other candidates such as wide working temperature range and a second order magnetic phase transition. Our results confirm that the composite approach combining 3*d* metals oxides such as manganites and double perovskites is a promising path to produce performant cooling devices based on the magnetocaloric effect.

IV. CONCLUSION

In this work, we obtain a large and almost temperature independent magnetocaloric effect extending from 175 K up to room temperature in multilayer composites of LNMO and LSMO. We take advantage of the sensitivity of cationic ordering to strain in LNMO layers to achieve multilayers with multiple magnetic transitions. For this purpose, two series of bilayer samples with different layouts of LSMO−LNMO and LNMO−LSMO, and two series of trilayer samples with layouts of LSMO−LNMO−LSMO and LNMO−LSMO−LNMO are prepared. All the samples show a large $\Delta S_{\rm m}$ over a wide temperature range, as large as 260 K, which extends above room temperature. The maximum value of $-\Delta S_{\rm m}$ in the trilayer samples is found to be 2.03 and 2.21 J kg^{-1} K^{-1} under a magnetic field change of 7 T in T−SNS and T−NSN samples, respectively. Moreover, the trilayer samples reveal an almost temperature independent magnetic entropy change that can extend over a large temperature range of $\Delta T \cong 100$ K. The refrigerant capacity ($\mathcal{RC}$) reaches a maximum value of 259 and 335 J kg^{-1} for $\mu_0\Delta H = 5$ T in T−SNS and T−NSN samples, respectively. These large values of $\mathcal{RC}$ in our multilayers are comparable to Gd and other reference materials demonstrating their potential in magnetic cooling systems.

ACKNOWLEDGMENT

The authors thank B. Rivard, S. Pelletier and M. Dion for technical support. The authors would also like to thank P. Brojabasi for preparing the initial samples. This work is supported by the Natural Sciences and Engineering Research Council of Canada (NSERC) under grant RGPIN-2018-06656, the Canada First Research Excel-

	$-\Delta S_{\mathrm{m}}$ (J kg^{-1} K^{-1})			$\mathcal{RC}$ (J kg^{-1})		
Sample	2 T	5 T	7 T	2 T	5 T	7 T
B – SN	0.62	1.33	1.76	106.82	273.23	380.62
B – NS	0.57	1.35	1.80	106.31	263.81	362.39
T – SNS	0.68	1.50	2.03	104.91	258.61	351.14
T – NSN	0.70	1.63	2.21	136.61	334.57	455.82

TABLE I: The values of $-\Delta S_{\mathrm{m}}$ and $\mathcal{RC}$ for all four multilayers under different magnetic fields.

lence Fund (CFREF), the Fonds de Recherche du Québec - Nature et Technologies (FRQNT) and the Université de Sherbrooke. M.B. acknowledges the financial support from the International University of Rabat.

[1] Balli, M., Jandl, S., Fournier, P., and Kedous-Lebouc, A. *Appl. Phys. Rev.* **4**(2), 021305 (2017).

[2] GschneidnerJr, K. A., Pecharsky, V., and Tsokol, A. *Rep. Prog. Phys.* **68**(6), 1479 (2005).

[3] Weiss, P. and Piccard, A. *J. Phys. Theor. Appl.* **7**(1), 103–109 (1917).

[4] Brown, G. *J. Appl. Phys.* **47**(8), 3673–3680 (1976).

[5] Pecharsky, V. K. and Gschneidner Jr, K. A. *Phys. Rev. Lett.* **78**(23), 4494 (1997).

[6] Xu, Z., Lin, G., and Chen, J. *J. Alloys Compd.* **639**, 520–525 (2015).

[7] Balli, M., Rosca, M., Fruchart, D., and Gignoux, D. *J. Magn. Magn. Mater.* **321**(2), 123–125 (2009).

[8] Fujieda, S., Fujita, A., and Fukamichi, K. *Appl. Phys. Lett.* **81**(7), 1276–1278 (2002).

[9] Tokura, Y. and Tomioka, Y. *J. Magn. Magn. Mater.* **200**(1-3), 1–23 (1999).

[10] Phan, M.-H. and Yu, S.-C. *J. Magn. Magn. Mater.* **308**(2), 325–340 (2007).

[11] Mira, J., Rivas, J., Hueso, L., Rivadulla, F., and Lopez Quintela, M. *J. Appl. Phys.* **91**(10), 8903–8905 (2002).

[12] Balli, M., Fournier, P., Jandl, S., Truong, K., and Gospodinov, M. *J. Appl. Phys.* **116**(7), 073907 (2014).

[13] Brahiti, N., Abbasi Eskandari, M., Balli, M., Gauvin-Ndiaye, C., Nourafkan, R., Tremblay, A.-M., and Fournier, P. *J. Appl. Phys.* **127**(11), 113905 (2020).

[14] Kobayashi, K.-I., Kimura, T., Sawada, H., Terakura, K., and Tokura, Y. *Nature* **395**(6703), 677–680 (1998).

[15] Anderson, P. W. *Solid State Phys.* **14**, 99–214 (1963).

[16] Kanamori, J. *J. Phys. Chem. Solids* **10**(2-3), 87–98 (1959).

[17] Singh, M., Truong, K., Jandl, S., and Fournier, P. *J. Appl. Phys.* **107**(9), 09D917 (2010).

[18] Iliev, M., Gospodinov, M., Singh, M., Meen, J., Truong, K., Fournier, P., and Jandl, S. *J. Appl. Phys.* **106**(2), 023515 (2009).

[19] Bull, C., Gleeson, D., and Knight, K. *J. Phys.: Condens. Matter* **15**(29), 4927 (2003).

[20] Truong, K., Singh, M., Jandl, S., and Fournier, P. *Phys. Rev. B* **80**(13), 134424 (2009).

[21] Matte, D., de Lafontaine, M., Ouellet, A., Balli, M., and Fournier, P. *Phys. Rev. Applied* **9**(5), 054042 (2018).

[22] Rebello, A., Naik, V., and Mahendiran, R. *J. Appl. Phys.* **110**(1), 013906 (2011).

[23] Zhong, X., Shen, X., Mo, H., Jiao, D., Liu, Z., Qiu, W., Zhang, H., and Ramanujan, R. *Mater. Today Commun.* **14**, 22–26 (2018).

[24] Zhang, Y., Yang, Y., Xu, X., Geng, S., Hou, L., Li, X., Ren, Z., and Wilde, G. *Sci. Rep.* **6**(1), 1–9 (2016).

[25] Tian, H., Zhong, X., Liu, Z., Zheng, Z., and Min, J. *Mater. Lett.* **138**, 64–66 (2015).

[26] Guo, Y., Shi, L., Zhou, S., Zhao, J., and Liu, W. *Appl. Phys. Lett.* **102**(22), 222401 (2013).

[27] Ettayfi, A., Moubah, R., Boutahar, A., Hlil, E., and Lassri, H. *J Supercond Nov Magn* **29**(1), 133–138 (2016).

[28] Wu, S.-Q., Cheng, S., Lu, L., Liu, M., Jin, X.-W., Cheng, S.-D., and Mi, S.-B. *Sci. Rep.* **8**(1), 1–9 (2018).

[29] Jin, X.-W., Lu, L., Mi, S.-B., Liu, M., and Jia, C.-L. *Appl. Phys. Lett.* **109**(3), 031904 (2016).

[30] Dey, P., Nath, T., and Taraphder, A. *Appl. Phys. Lett.* **91**(1), 012511 (2007).

[31] Wang, B., You, L., Ren, P., Yin, X., Peng, Y., Xia, B., Wang, L., Yu, X., Mui Poh, S., Yang, P., et al. *Nat. Commun.* **4**(1), 1–7 (2013).

[32] Smith, A., Bahl, C. R., Bjørk, R., Engelbrecht, K., Nielsen, K. K., and Pryds, N. *Adv. Energy Mater.* **2**(11), 1288–1318 (2012).

[33] Banerjee, B. *Physics Letters* **12**(1), 16–17 (1964).

[34] Arrott, A. *Phys. Rev.* **108**(6), 1394 (1957).

[35] Tishin, A. M. and Spichkin, Y. I. *The magnetocaloric effect and its applications*. CRC Press, (2016).

[36] Franco, V., Blázquez, J., Ipus, J., Law, J., Moreno-Ramírez, L., and Conde, A. *Prog. Mater. Sci.* **93**, 112–232 (2018).

[37] Zhou, L., Tang, Y., Chen, Y., Guo, H., Pang, W., and Zhao, X. *J. Rare Earths* **36**(6), 613–618 (2018).

[38] Gschneidner Jr, K., Pecharsky, V., Pecharsky, A., and Zimm, C. *Materials Science Forum* **315**, 69–76 (1999).

[39] Dan'Kov, S. Y., Tishin, A., Pecharsky, V., Gschneidner, K., et al. *Phys. Rev. B* **57**(6), 3478 (1998).

[40] Shamba, P., Zeng, R., Wang, J., Campbell, S., and Dou, S. *J. Magn. Magn. Mater.* **331**, 102–108 (2013).

[41] Shamba, P., Debnath, J., Zeng, R., Wang, J., Campbell, S. J., Kennedy, S., and Dou, S. *J. Appl. Phys.* **109**(7), 07A940 (2011).

[42] Provenzano, V., Shapiro, A. J., and Shull, R. D. *Nature* **429**(6994), 853–857 (2004).

Supplemental material

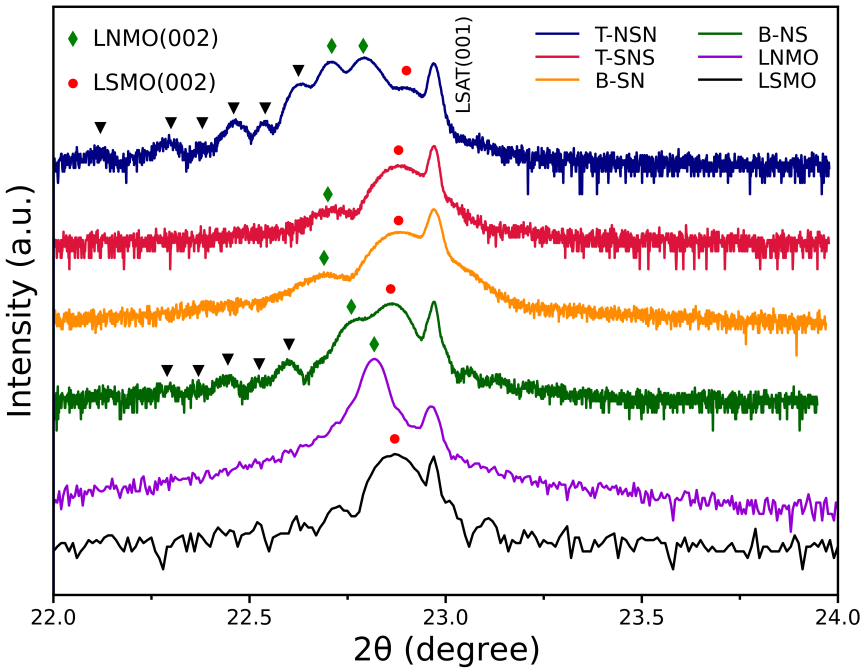

FIG. 12: X-ray diffraction patterns around the (001) Bragg peak of the substrate from $2\theta = 22°$ to $24°$. From bottom to top: the monolayers of LSMO and LNMO, bilayers of B−NS and B−SN, and trilayers of T−SNS and T−NSN. Laue oscillations are specified with (▼). Diamonds indicate the diffraction peaks of LNMO and solid circles for LSMO.

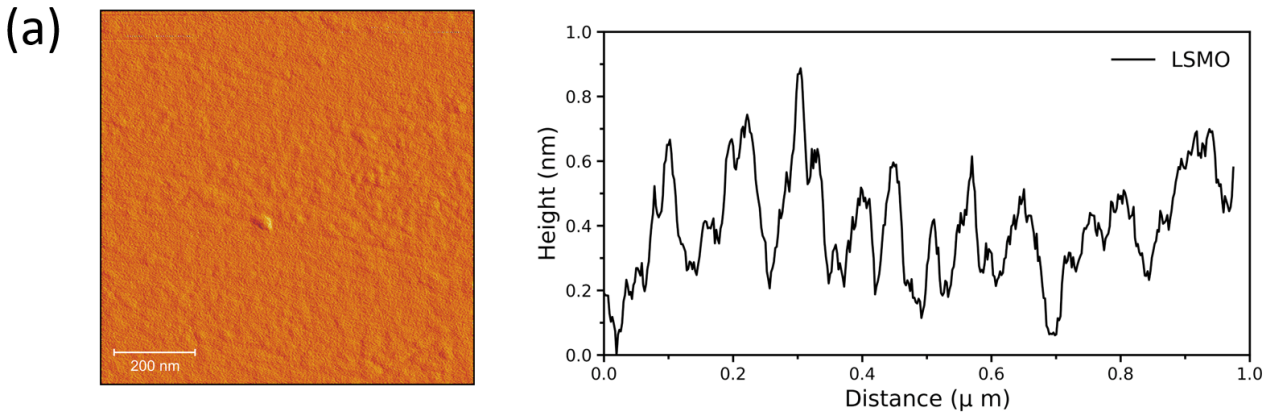

(b)

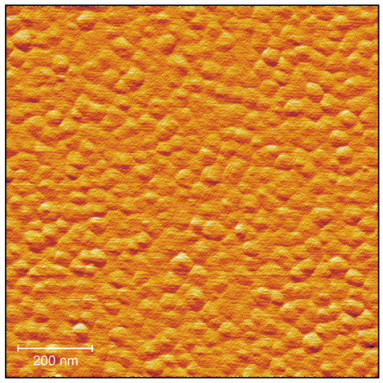
200 nm

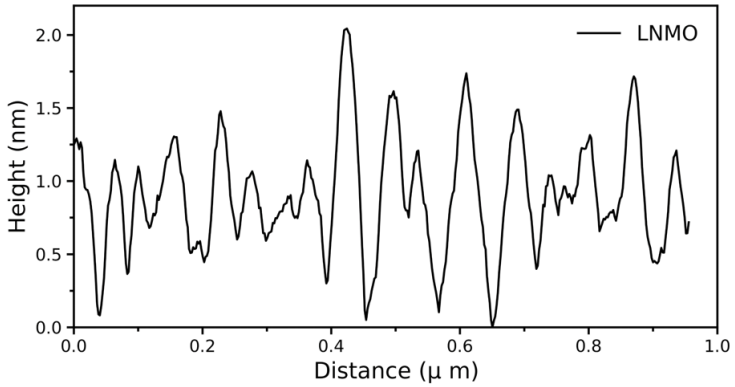
LNMO
Height (nm)
Distance (μ m)
0.0
0.5
1.0
1.5
2.0
0.0
0.2
0.4
0.6
0.8
1.0

(c)

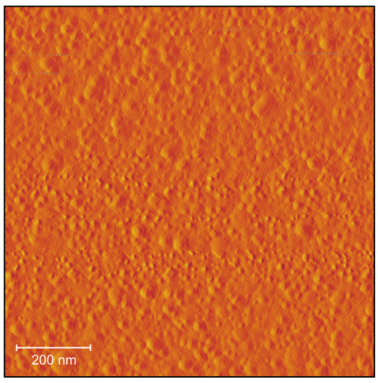
200 nm

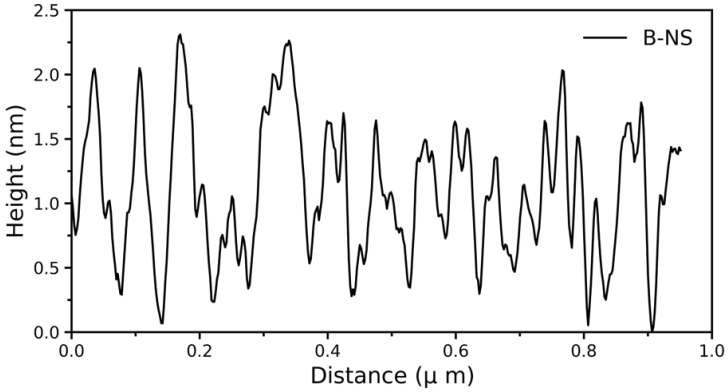
B-NS
Height (nm)
Distance (μ m)
0.0
0.5
1.0
1.5
2.0
2.5
0.0
0.2
0.4
0.6
0.8
1.0

(d)

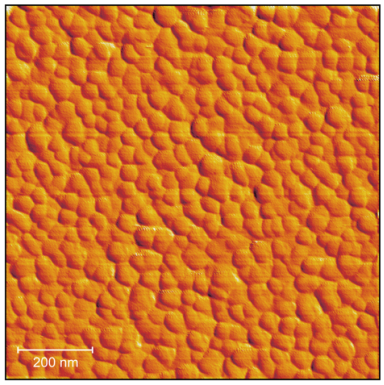
200 nm

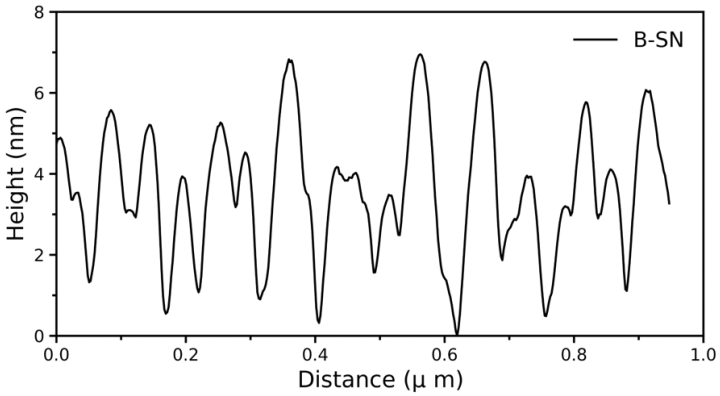
B-SN
Height (nm)
Distance (μ m)
0
2
4
6
8
0.0
0.2
0.4
0.6
0.8
1.0

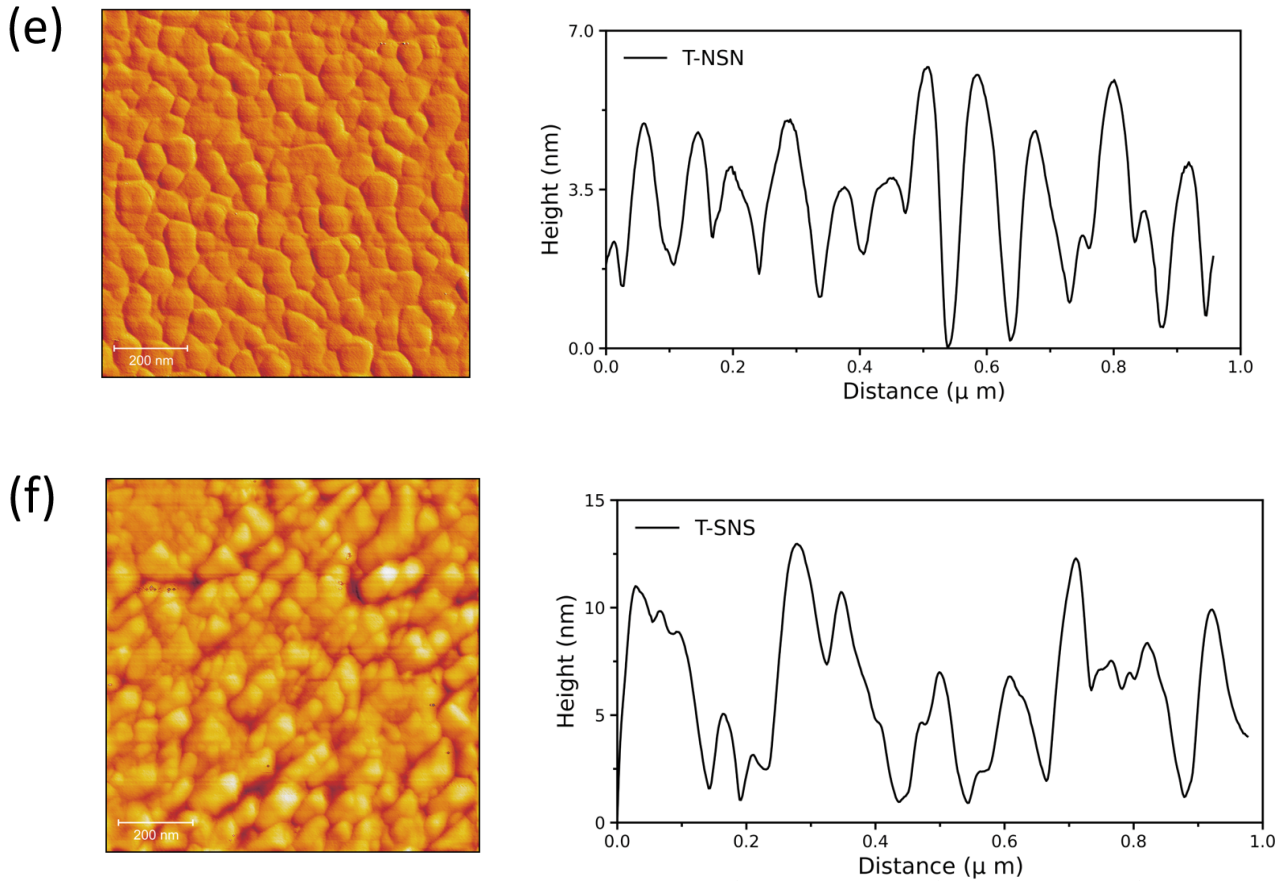

FIG. 13: AFM images (left) and height profiles (right) for a line drawn across the AFM images for (a) monolayer of LSMO, (b) monolayer of LNMO, (c) bilayer of B−NS, (d) bilayer of B−SN, (e) trilayer of T−NSN and (f) trilayer of T−SNS. The measurements were carried out using a Veeco Dimension Icon Atomic Force Microscope (AFM).

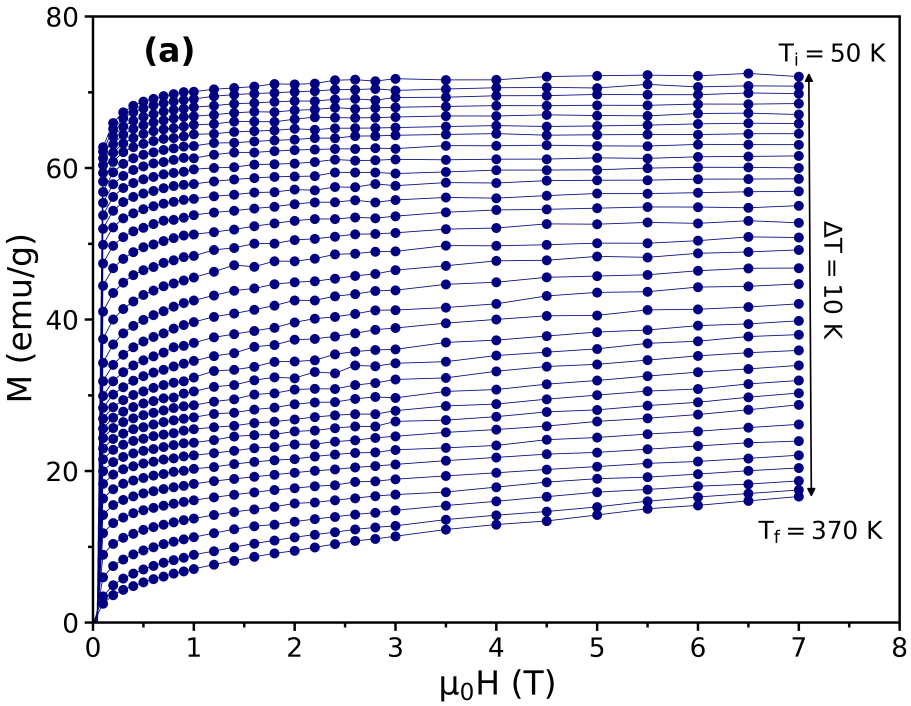

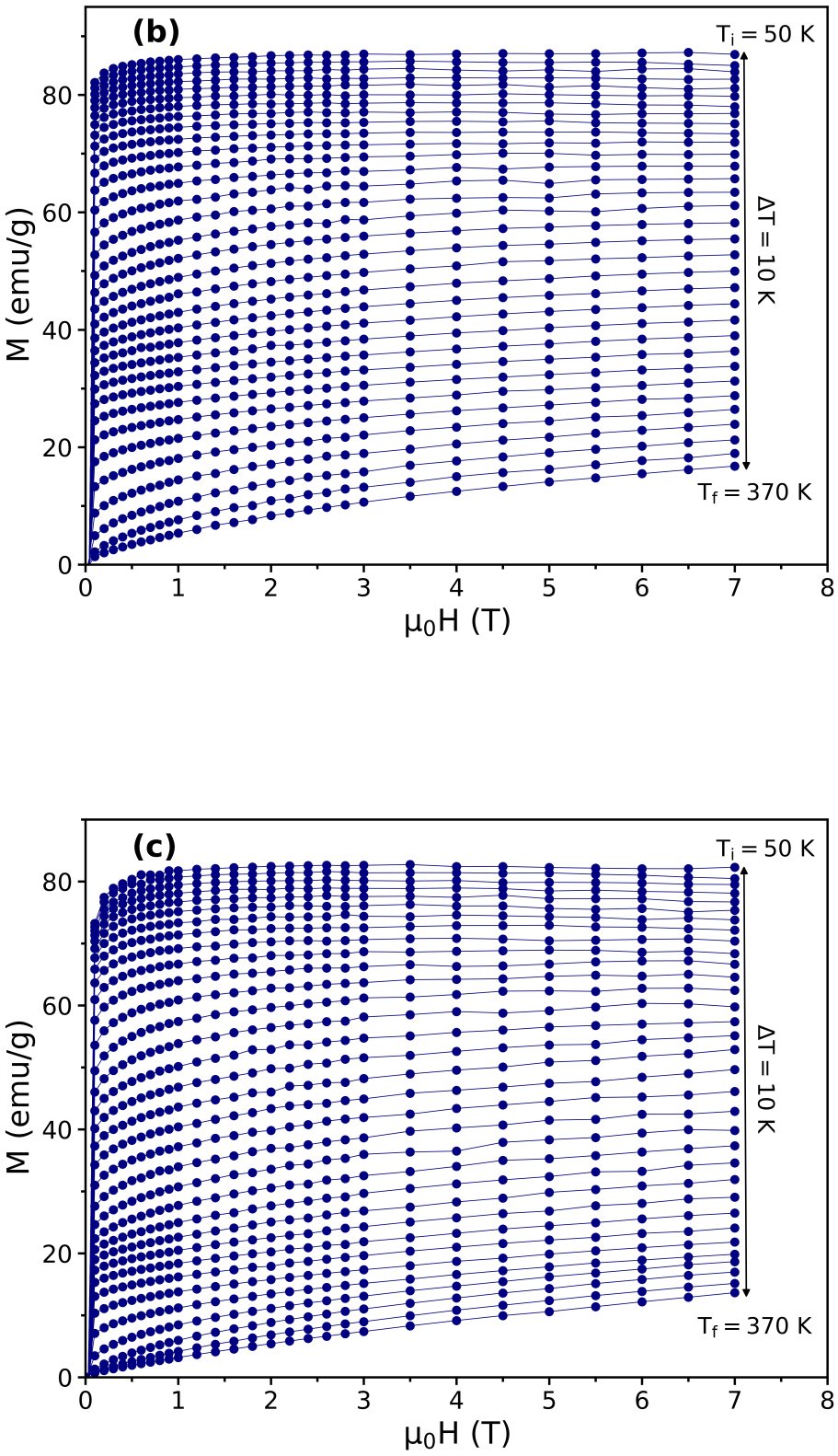

FIG. 14: Isothermal magnetization curves as a function of magnetic field in the temperature range from 50 to 370 K with a temperature interval of 10 K for (a) B–SN, (b) T–SNS and (c) T–NSN samples. These data are obtained after the subtraction of the diamagnetic background from the substrate and the sample holder.

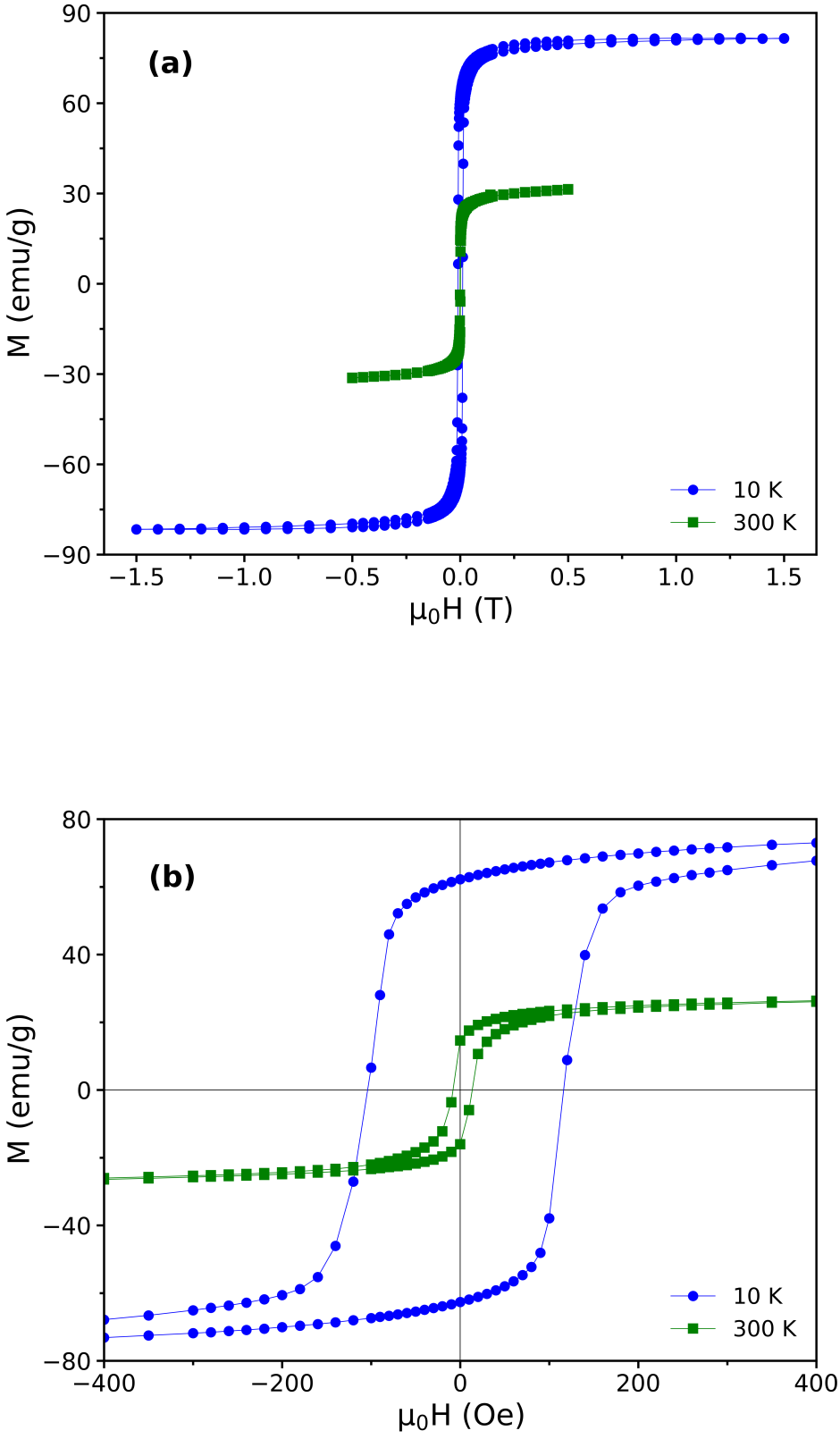

FIG. 15: (a) Magnetic hysteresis loops measured at 10 and 300 K for T−SNS sample. (b) Magnified view around zero field showing the coercive field and the remnant magnetization at 10 and 300 K.

2.3.3 Summary

In this work, we demonstrated that a large and temperature independent magnetocaloric effect can be obtained in composite-like heterostructures of LSMO and LNMO. We were able to switch between the two magnetic phases in LNMO by subjecting the layer to different values of epitaxial strain. This feature allowed us to tune and adjust the amplitude and the temperature span of ΔS_m in the heterostructures only by changing their layouts. As displayed in Figure 2.18, ΔS_m in all the multilayers reaches at least a maximum value of $1.4\,\mathrm{J\,kg^{-1}\,K^{-1}}$ for a magnetic field change of 0–5 T, while the magnetic entropy variation spreads over a wide temperature range, as large as 250 K. Furthermore, in LNMO/LSMO/LNMO trilayer samples where both cation-ordered and -disordered LNMO coexist, a temperature-independent and table-top-like magnetic entropy change is observed over a temperature range of $\Delta T = 100\,\mathrm{K}$, for $\mu_0 \Delta H = 5\,\mathrm{T}$. The value of refrigerant capacity ($\mathcal{RC}$) reaches $335\,\mathrm{J\,kg^{-1}}$ for LNMO/LSMO/LNMO sample under a magnetic field of 5 T which is comparable to Gd as a reference material. Our results indicate that the composite approach is a promising path to design new magnetocaloric materials for magnetic cooling systems with the specific oxides.

Aside from the fact that we are able to control the level of cationic ordering in the majority of the magnetic domains of LNMO layers in heterostructures and detect different magnetic phases in magnetization measurements, we are still wondering if there are other magnetic domains in LNMO layers with different magnetic properties (higher or lower transition temperature) which contribute to the magnetic entropy change but cannot be revealed in magnetization measurements due to their small volume. It is also worth noticing that the bilayers of B−SN show a small peak in the MCE measurements above 200 K indicating the presence of some domains with cation-ordered phase in the LNMO layer, whereas, this layer is considered to be fully disordered. In contrast to the MCE measurements, there is no trace of these domains in the M(T) measurements nor in the trilayers of T−SNS with a similar arrangement. In order to answer this question and clarify if these domains also exist in the T−SNS samples, in the following chapter, we introduce LNMO as a ferromagnetic insulating barrier in magnetic tunnel junctions and explore the tunneling through it, in order to extract information about two magnetic

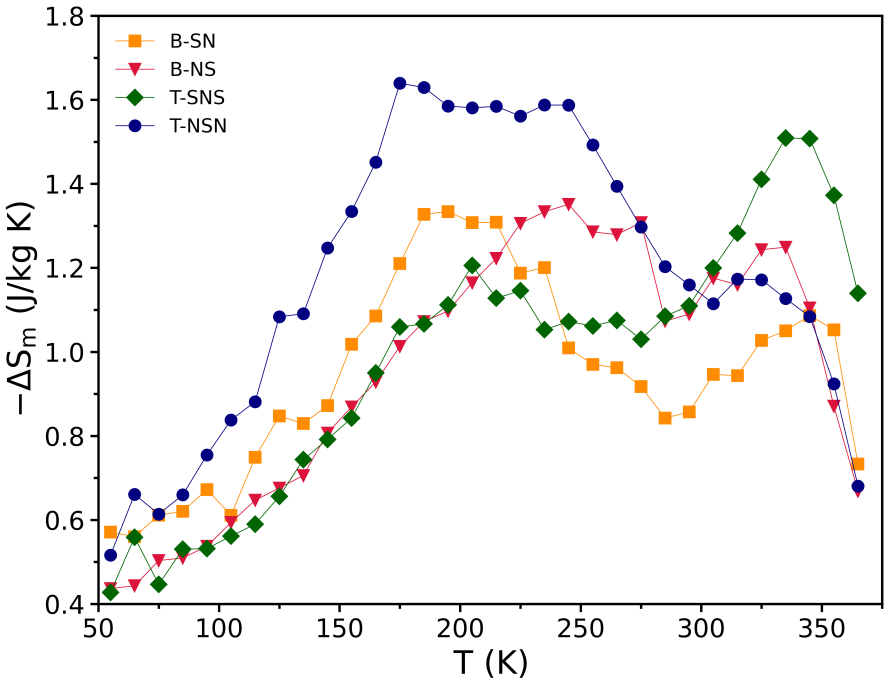

Figure 2.18: Comparison of ΔS_{m} in all multilayer samples for $\mu_0 \Delta H = 5\,\mathrm{T}$.

phases (ordered and disordered) and their distribution in LNMO layer. It is likely that the tunneling of spin polarized electrons through a magnetic barrier is strongly dependent on its magnetization and it could reveal its magnetic properties.

Chapter 3

Tunnel magnetoresistance in oxide magnetic tunnel junctions

3.1 Theoretical concepts

Spintronics is a rapidly evolving field of technology that uses the electron spin degrees of freedom to manipulate the electron transport or to store information. The phenomenon of spin-dependent electron transport was first discovered in 1970 by Meservy and Tedrow, leading to a revolution in the data storage and magnetic sensing technology. Following that in 1975, the French physicist Jullière [25] discovered the tunnel magnetoresistance (TMR) effect which received little attention as the MR ratio was only attainable at low temperature. Then, the discovery of giant magnetoresistance (GMR) effect at room temperature in 1988 by Peter Grunberg and Albert Fert [131], that resulted in the Nobel Prize in Physics in 2007, opened a new research domain on spin-dependent transport, known as "spintronics". Many applications have been developed using this phenomenon such as highly sensitive magnetic sensors, non-volatile magnetic units in magnetic random access memory (MRAM), logic gates in spin current driven logic devices and read heads in the hard disk drives.

Magnetic tunnel junctions (MTJ) are a class of spin-based devices which consists of two ferromagnetic metal layers separated by a thin insulating barrier layer.

Electrons can tunnel through this thin insulating barrier when a bias voltage is applied between the two electrodes across the barrier. Based on a classical physics point of view that electrons are not allowed to flow across an insulating barrier, this would require electrons to pass through a classically forbidden region. On the other hand, with a quantum mechanical interpretation, an electron wave function penetrates and exponentially decays into an insulator, so it allows electrons to tunnel across the barrier if it is sufficiently thin. The tunneling resistance in MTJs strongly depends on the relative orientation of the magnetic moments in the two ferromagnetic electrodes. As schematically illustrated in Figure 3.1, when the magnetic moments of the two FM layers are aligned, the junction has its lowest resistance, whereas the anti-parallel alignment gives the highest resistance. This spin-dependent tunneling in MTJs is known as the tunnel magnetoresistance effect.

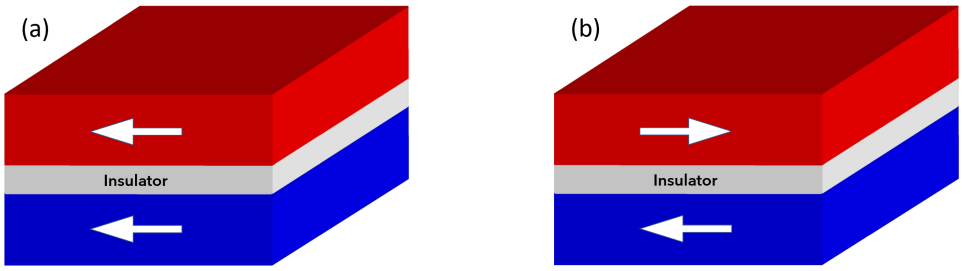

Figure 3.1: Schematic of spin-dependent tunneling in a MTJ structure for the (a) low-resistance parallel and (b) high-resistance anti-parallel alignment.

The TMR ratio is defined as:

$$TMR = \frac{R_{AP} - R_P}{R_P} = \frac{G_P - G_{AP}}{G_{AP}} \tag{3.1}$$

where R_P and G_P are the resistance and the conductance in the parallel configuration, R_{AP} and G_{AP} are the resistance and the conductance in the antiparallel configuration.

3.1.1 Jullière's model

The first observation of TMR in a MTJ structure was made by Jullière where he used Co and Fe as metallic electrodes and Ge as an insulator. He observed a TMR

ratio of about 14 % at 4.2 K [25]. He also proposed the first simple model of TMR in MTJs based on the spin polarizations of ferromagnets. Jullière has quantified the TMR phenomenon under two main assumptions:

1. Spin conservation during tunneling: this assumption implies that the electron spin is conserved during the tunneling process, namely no spin flip occurs. That means, tunneling of spin-up and spin-down electrons are two independent processes and occur via two separate channels. According to this assumption, electrons originating from one spin state of the first FM layer can reach only unoccupied states of the same spin polarization of the second FM layer. When the two FM layers are aligned in the parallel configuration, the majority spins tunnel to the majority states and the minority spins tunnel to the minority states. In this scenario, the density of occupied states at the Fermi level in the first FM layer perfectly matches the number of vacant states just above the Fermi level in the second FM layer. Thus, the conductance is high in this configuration. In the opposite scenario, when the two FM layers are magnetized in the antiparallel configuration, the majority spins from one FM layer tunnel to the minority states of the other FM layer and vice versa. The conductance is much lower in this configuration. The spin transfer process in a MTJ with two spin transfer channels is depicted in Figure 3.2.

2. The conductance of each magnetic configuration is proportional to the product of the effective density of states of the two magnetic layers. The conductance for the parallel (G_{P}) and antiparallel (G_{AP}) alignments can be defined as follows:

$$G_{\mathrm{P}} \propto \rho_1^{\uparrow}\rho_2^{\uparrow} + \rho_1^{\downarrow}\rho_2^{\downarrow} \tag{3.2}$$

$$G_{\mathrm{AP}} \propto \rho_1^{\uparrow}\rho_2^{\downarrow} + \rho_1^{\downarrow}\rho_2^{\uparrow} \tag{3.3}$$

where $\rho_i^{\uparrow}$ and $\rho_i^{\downarrow}$ are the density of states of spin-up and spin-down electrons for each FM layer ($i = 1, 2$). Using Eq. 3.2 and 3.3, the TMR ratio can be defined in term of spin polarization (P_i) of the two ferromagnetic layers:

$$TMR = \frac{R_{\mathrm{AP}} - R_{\mathrm{P}}}{R_{\mathrm{P}}} = \frac{G_{\mathrm{P}} - G_{\mathrm{AP}}}{G_{\mathrm{AP}}} = \frac{2P_1P_2}{1 - P_1P_2} \tag{3.4}$$

where P_i is:

$$P_i = \frac{\rho_i^{\uparrow} - \rho_i^{\downarrow}}{\rho_i^{\uparrow} + \rho_i^{\downarrow}} \tag{3.5}$$

Using the known values of the spin polarization for Co and Fe, Jullière calculated a TMR value of 26 % which was higher than the maximum measured value of 14 %. He explained the discrepancy by magnetic coupling between the ferromagnetic electrodes and spin-flip scattering.

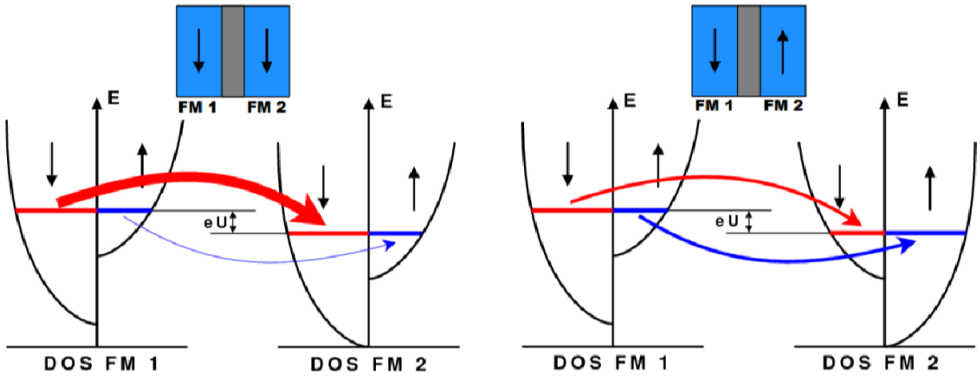

Figure 3.2: Electronic tunneling process for a MTJ with parallel (left) and antiparallel (right) configurations. The thick and thin lines in the parallel configuration indicate the major and minor conduction channels, respectively.

The Jullière's model is an oversimplified model because it does not take into account the details in the electronic structure of the FM materials and the properties of the tunnel barrier. It also fails to explain higher TMR ratio observed in junctions with crystalline barriers such as MgO [132, 133].

3.1.2 Slonczewski's model

The first accurate theoretical model of TMR which considers the effect of the angle of the magnetization orientations in FM layers and the height of the barrier was proposed by Slonczewski in 1989 [134]. He first assumed that only the delocalized electrons contribute to the conduction. He also considered a rectangular barrier

with a finite height separating the two FM layers which can be characterized by parabolic bands of free electrons whose momentum is conserved when flowing across the barrier. Having imposed perfect translational symmetry of the tunnel junction along the layers and matched the wave functions of electrons across the junction, he solved the Schrödinger equation and determined the conductance as a function of the relative magnetization alignment of the two FM electrodes. In the limit of a thick barrier, he found that the conductance is a linear function of the cosine of angle θ between the magnetic moments of the electrodes:

$$G(\theta) = G_0 \left(1 + P_{eff}^2 \cos\theta\right) \tag{3.6}$$

where the effective spin polarization of the ferromagnetic electrodes is:

$$P_{eff} = \left(\frac{k_\uparrow - k_\downarrow}{k_\uparrow + k_\downarrow}\right)\left(\frac{k^2 - k_\uparrow k_\downarrow}{k^2 + k_\uparrow k_\downarrow}\right) \tag{3.7}$$

where $k_\uparrow$ and $k_\downarrow$ represent the wave numbers of electrons in the majority- and minority spin bands, and k is the decay coefficient in the barrier region which is determined by the potential barrier height U, $k = \sqrt{\left(2m/\hbar^2\right)(U - E_\mathrm{F})}$. In Slonczewski's model, TMR depends on both the spin polarization of the two FM electrodes as well as the barrier potential height. In addition, this model incorporates the energy dependence of the electronic structure of materials. However, it only provides a qualitative (or at best a semi-quantitative) explanation of TMR.

3.1.3 Magnetic field dependence

Observation of TMR requires both parallel and antiparallel magnetization alignments in a MTJ. This can simply be achieved by using two ferromagnetic layers with different coercive fields. Once the field sweeps through zero and reaches values between the coercive fields of the electrodes, an antiparallel alignment is formed and the resistance reaches its maximum values. Increasing the magnetic field will bring

the FM layers back into parallel alignment which lowers the resistance. The typical behavior of TMR versus magnetic field is shown in Figure. 3.3.

Moodera and Kindder's experiments [135] confirmed Slonczewski's model in which he states that the TMR ratio depends on the relative orientation of the magnetic moments in two FM electrodes with respect to each other. They measured the angular dependence of the magnetoresistance which varied nearly as the cosine of the relative angle of the electrodes, as predicted.

3.1.4 Temperature dependence

Temperature dependence of the TMR ratio became a topic of considerable interest after the first observation of the large TMR ratio. In general, the TMR in MTJs decreases with increasing temperature and disappears at a critical temperature T^*, which is well below the Curie temperature of the electrodes. Shang *et al* [136] have proposed a model to explain the temperature dependence of TMR. Based on their model, the tunneling spin polarization and the interface magnetization decrease with increasing temperature due to spin-wave excitations. The tunneling spin polarization (P) and the interface magnetization (M) follow the same temperature dependence, as the Bloch $T^{3/2}$ law.

$$P(T) = P_0\left(1 - \alpha T^{3/2}\right) \tag{3.8}$$

$$M(T) = M_0\left(1 - \alpha T^{3/2}\right) \tag{3.9}$$

where α is a fitting parameter. This model successfully described the experimental data obtained from $Co/Al_2O_3/Co/Ni$ and $Co/Al_2O_3/Ni_{80}Fe_{20}$ MTJs [136]. Furthermore, the spin-independent two-step tunneling model [137] could also explain the temperature dependence of TMR. Based on this model, electrons from localized defect states in the barrier can be also activated thermally and make these states available for two-step tunneling. Additionally, magnetic impurities in the barrier can also cause spin-flip scattering resulting in the decrease of TMR with temperature. Vedyayev *et al* [138] investigated the TMR of a MTJ in the presence of mag-

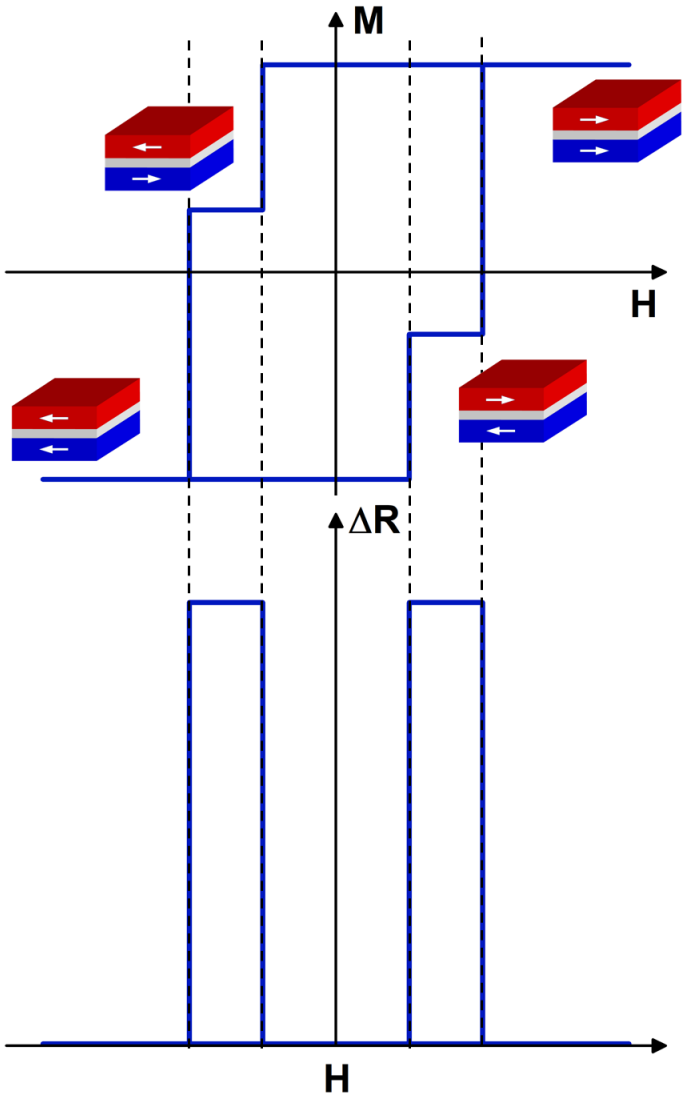

Figure 3.3: Schematic drawings of TMR behavior as a function of magnetic field for a MTJ consisting of two ferromagnetic materials with different coercive fields. (Top) magnetization, (Bottom) resistance. The resistance of the MTJ reaches its maximum value when the FM electrodes are aligned in opposite directions.

netic impurities within the barrier. They assumed that magnetic couplings exist both between the spin of the impurity and the bulk magnetization of the neighboring magnetic electrode, and between the spin of the impurity and the spin of the tunneling electron. It was found that an increase in temperature leads to a decrease in the TMR amplitude due to the excitation of spin-flip processes resulting in the mixing of spin-up and spin-down channels. In the presence of spin-flip scattering, TMR is reported to vary as $\exp\left(-k_{\mathrm{B}}T/E_{\mathrm{mr}}\right)$, where E_{mr} is the energy associated with spin-flip scattering. Therefore, the key to improving the MR and minimizing the voltage and temperature dependence is high quality barriers with low defect state density.

3.1.5 Barrier dependence

3.1.5.1 Amorphous barriers

Amorphous AlO_x was the most studied type of barrier in the early research of high tunneling magnetoresistance in MTJs. Two decades after the discovery of TMR at low temperature, it was shown that a higher TMR ratio can be obtained with an amorphous AlO_x barrier at room temperature, the TMR ratio could reach 15 % for CoFe/AlO_x/Co tunnel junctions [139]. Afterwards, extensive efforts have been made on finding ferromagnetic electrodes with higher spin polarization in order to gain a larger TMR in AlO_x based tunnel junctions. So far, the largest TMR ratio of AlO_x based tunnel junction was observed in CoFeB/AlO_x/CoFeB MTJs, where it reaches 81 % at room temperature [140]. Amorphous AlO_x is a favorable barrier due to its advantages such as the ease in fabrication of ultrathin, pinhole-free AlO_x layers and spin conservation demonstrated across AlO_x barriers. However, from a theoretical perspective, it is difficult to understand the physics of spin-dependent tunneling through an amorphous insulating barrier since there is no crystallographic symmetry in amorphous layers. Bloch states with various symmetries in the ferromagnetic electrodes would couple with evanescent states in the AlO_x barrier, resulting in finite tunneling probabilities called incoherent tunneling. Each Bloch state has different tunneling probability depending on its symmetry. According to Jullière's model, the TMR ratio only depends on the spin polarization

of the two ferromagnetic electrodes. This model only provides a good approximation for explaining TMR in MTJs where incoherence tunneling occurs, like AlO_x based tunnel junctions. Nevertheless, there are other important factors that need to be taken into account, such as the crystallographic orientation of individual layers as well as the thickness, quality, specific materials used as tunnel barriers and for the ferromagnetic electrodes.

3.1.5.2 Crystalline barriers

Crystalline MgO was used as a barrier in MTJs for the first time in 1997, where it was grown by dc magnetron sputtering with thicknesses in the range of 2 to 30 nm between two magnetic transition metals [141]. A large TMR on the order of 20 % at 77 K has been observed in MgO-based MTJs due to spin-polarized tunneling effect . Soon after that, the theoretical calculations showed that the TMR ratio could exceed 1000 % for an epitaxial $Fe/MgO/Fe(001)$ tunnel junction [132]. The main reason of such a high TMR ratio is a small lattice mismatch of about 3.5 % between the Fe – Fe and O – O (in MgO) in-plane distances, which can be absorbed by lattice distortions in the Fe and MgO layers and/or by the formation of dislocations at the interface [142]. Afterwards, MgO has been widely explored in the hope of getting a large TMR close to room temperature. The first MgO-based tunnel junctions which could overcome the performance of AlO_x based tunnel junctions at room temperature, were made by Parkin *et al* in 2004 [143]. In such junctions, the TMR ratio reaches values of up to 220 % at room temperature and 300 % at low temperature. Until now, the largest TMR was observed in $Ta/Co_{20}Fe_{60}B_{20}/MgO/Co_{20}Fe_{60}B_{20}/Ta$ pseudo-spin-valve magnetic tunnel junction where TMR ratio exceeds 600 % at room temperature [144]. Moreover, the highest TMR ratio observed at 5 K was 1144 % which is in close agreement with the theoretical predictions. Hence, the performance of the MgO based tunnel junctions has become extremely attractive to magnetic random access memory applications. Figure 3.4 illustrates how TMR ratio has evolved over time for magnetic tunnel junctions based on AlO_x and MgO.

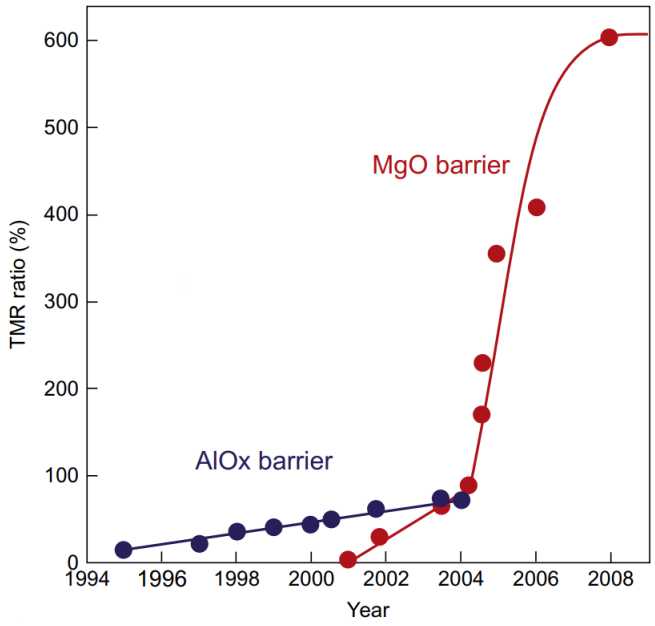

Figure 3.4: Time evolution of the TMR ratio for magnetic tunnel junctions based on AlO_x and MgO [145].

3.1.5.3 Magnetic barriers

Due to the rarity of magnetic insulating materials, this type of barriers have not been explored extensively in MTJs. A few studies have investigated the effect of magnetic barriers in MTJs [146] and spin-filter junctions [147–149]. Hueso *et al* [146] have studied the transport properties of a trilayer this film consisting of two $La_{0.7}Ca_{0.3}MnO_3$ electrodes separated by a $La_{0.59}Ca_{0.41}MnO_3$ layer. The *MR* measurements as a function of magnetic field indicate that there is a sharp switching from the low to high resistance states arising from the antiparallel alignment of the top and bottom electrodes. Unlike other MTJs, the low resistance state is not recovered when the magnetization of top and bottom layers reverse to yield the parallel alignment again. Instead, the transition from high to low resistance states mimics the magnetic change in the middle layer. This behavior is attributed to the formation of domain walls at the interfaces which have high electrical resistance due to mesoscopic phase separation.

Spin-filter junctions are another way to obtain spin-dependent tunneling effect in which the spin polarization of the current tunneling from a nonmagnetic

electrode through a ferromagnetic tunnel barrier can be analyzed either with a superconductor, or with a ferromagnetic counterelectrode [150]. The concept was reported by Moodera *et al* with EuS, EuSe and EuO tunnel barriers and superconducting Al counterelectrodes [150]. Up to recently, spin-filter junctions have relied on the use of Eu-based magnetic semiconductors as the tunnel barrier but the low T_c and poor chemical compatibility of these compounds have hindered their use for practical applications.

The progress in the growth of oxide thin films is now making it possible to integrate nanometric layers of complex insulating ferromagnetic oxides into epitaxial heterostructures. For instance, the effect of ferromagnetic insulator $BiMnO_3$ with a Curie temperature of $T_c = 150\,K$ has been investigated as a magnetic barrier in spin-filter junctions consisting of a LSMO counterelectrode [148]. It was demonstrated that a TMR of up to 50 % can be obtained at 3 K whether the magnetization of BMO and LSMO are parallel or opposite. This effect corresponds to a spin-filtering efficiency of up to 22 %. The TMR decreases rapidly with temperature and vanishes below the transition temperature of BMO. This may indicate that the T_c of BMO ultrathin layers is suppressed compared to its bulk value. Further investigations of ferromagnetic insulators such as $NiFe_2O_4$ and $La_{0.1}Bi_{0.9}MnO_3$ indicate that spin-filter junctions usually operate at low temperature and TMR vanishes way below the T_c of the ferromagnetic barrier [147, 148].

3.1.6 TMR in oxides

It has been shown that half-metallic materials that possess only one spin direction at their Fermi level can produce a very large TMR ratio due to their large spin polarization [26]. Among the materials that have been predicted to be half-metals, manganites are considered as a popular choice for ferromagnetic electrodes in MTJs due to their large spin polarization and tunable transition temperature which can be used to design electronic devices to meet specific functional requirements. $La_{1-x}Sr_xMnO_3$ with $x = 0.2$–0.4 has been a popular choice as a magnetic electrode in MTJs due to its half-metallic character with nearly 100 % spin polarization. LSMO was used in MTJs for the first time in 1996 [151, 152], where two $La_{2/3}S_{1/3}MO_3$ electrodes were separated by a 3–6 nm thick STO barrier. A com-

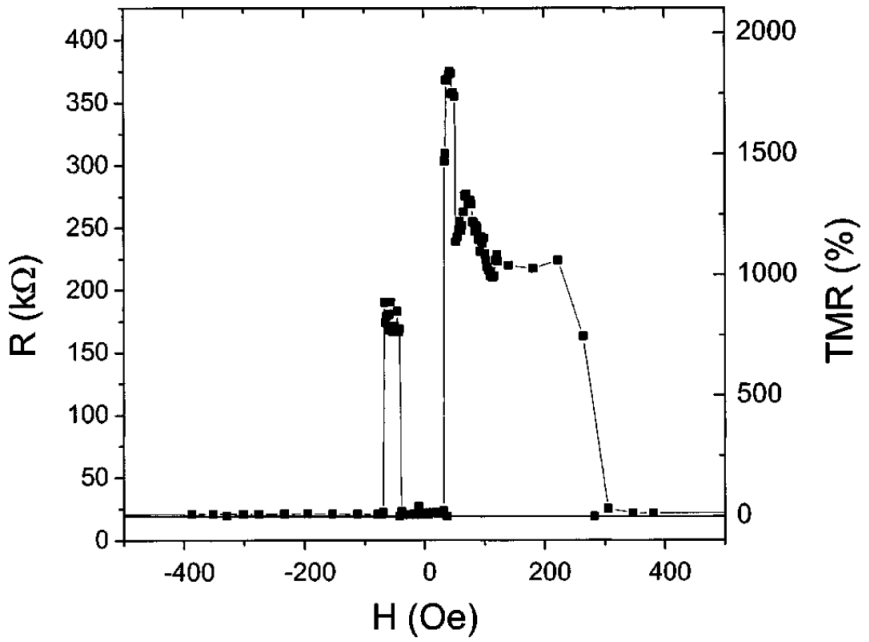

Figure 3.5: TMR as a function of magnetic field for a LSMO/STO/LSMO tunnel junction structure at 4.2 K [28]

bination of self-aligned lithographic and ion-beam etching were used to fabricate this device. It showed a TMR ratio of 83 % in small external fields at 4 K. This corresponds to 54 % spin polarization in LSMO using the spin-polarized tunneling model. A few years later, a considerably larger TMR ratio was reported in LSMO-based tunnel junctions [28]. As illustrated in Figure 3.5, the epitaxial trilayer $La_{2/3}Sr_{1/3}MnO_3/SrTiO_3/La_{2/3}Sr_{1/3}MnO_3$ structure shows a TMR ratio of 1850 % at 4.2 K, where an average spin polarization of at least 95 % was observed for LSMO at the interface with STO. The TMR decreases upon increasing the temperature and reaches 30 % and 12 % at 250 K and 270 K, respectively. It vanishes only at above 280 K.

Despite these promising results, LSMO electrodes also come with some disadvantages. For instance, there is a strong temperature dependence of TMR in LSMO-based tunnel junctions. Garcia *et al* [153] have investigated the TMR of LSMO-based MTJs with various barrier materials including $SrTiO_3$, TiO_2 and $LaAlO_3$. They have reported that the TMR tends to decrease sharply with temperature and vanishes in the vicinity of 285 K for all three barriers (Figure 3.6 (a)) well below

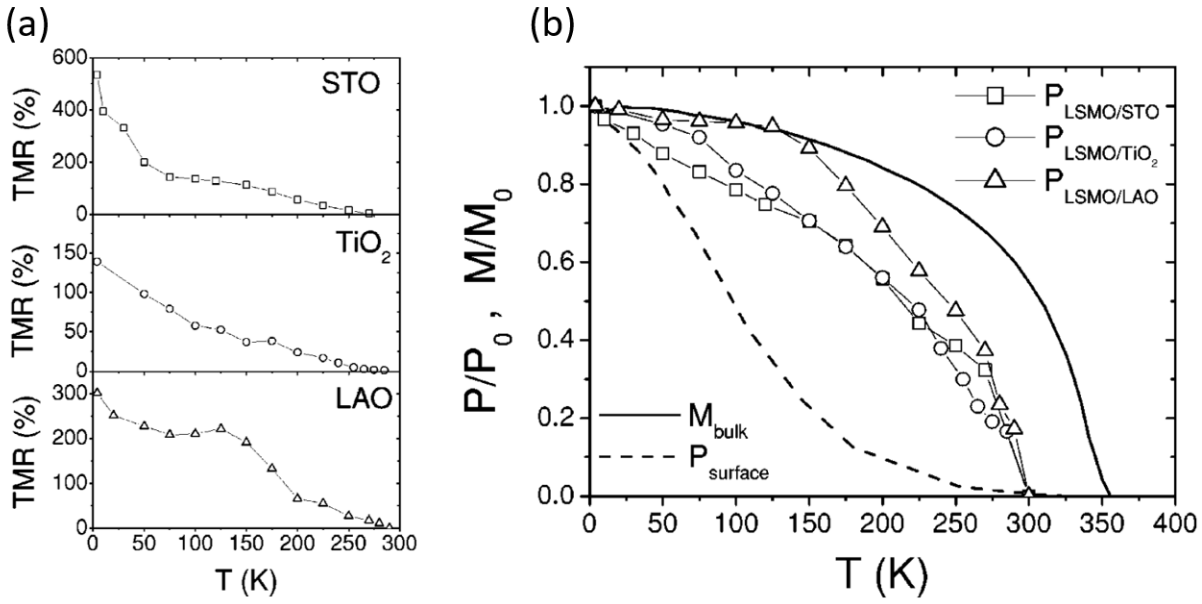

Figure 3.6: (a) Temperature dependence of the TMR for LSMO-based MTJs with STO, TiO_2 and LAO barriers. (b) Temperature dependence of the normalized spin polarization at the interface between LSMO and the three different barriers as well as the spin polarization of a free LSMO surface and the bulk magnetization of a LSMO/LAO/LSMO trilayer [153].

T_c ∼370 K of LSMO. Moreover, the spin polarization was deduced from the TMR measurements by means of the Jullière formula. Figure 3.6 (b) shows the comparison of the temperature dependence of spin polarization at the interface between LSMO and the different barriers as well as the spin polarization of a free LSMO surface and the bulk magnetization of LSMO/LAO/LSMO trilayer sample. Interestingly, the spin polarization versus temperature for the three interfaces shows a very different temperature-dependent behavior when compared to that of a free surface, and resembles that of the magnetization of the trilayer, but with a lower transition temperature. This similarity is particularly clear in the case of the LSMO/LAO interface. The faster decay in the spin polarization at the surface of LSMO is attributed to the discontinuation of oxygen bonds at the interface. These results indicate that free surfaces and interfaces have very different properties in manganites and also the magnetism of LSMO interfaces can indeed be as robust as that of transition metals.

Another family of perovskite oxides which has commonly been used as elec-

trode in MTJs is $La_{1-x}Ca_xMnO_3$ (LCMO). Similar to LSMO, LCMO is a half-metallic manganite where the relatively narrow spin up and down conduction bands are completely separated leading to 100 % spin polarization at low temperature. In 2000, Jo *et al* [154] fabricated spin polarized tunneling devices consisting of two $La_{0.67}Ca_{0.33}MnO_3$ electrodes separated by $NdGaO_3$ as the barrier material with different surface areas. As depicted in Figure 3.7, all the devices show very large TMR up to 86 % at low temperatures, with extremely sharp switching between the high and low resistance states which are attributed to antiparallel and parallel alignment of the magnetic moments of the two LCMO electrodes resulting from different coercive fields between the two electrodes. The maximum polarization of the LCMO electrodes was calculated to be 86 % at 77 K. This value is even higher than that of 78–80 % in $La_{0.7}Sr_{0.3}MnO_3$ measured directly by Andreev reflection at 4.2 K [155, 156]. It was proposed that a better lattice mismatch between the electrodes and the barrier could dramatically improve the properties of MTJs.

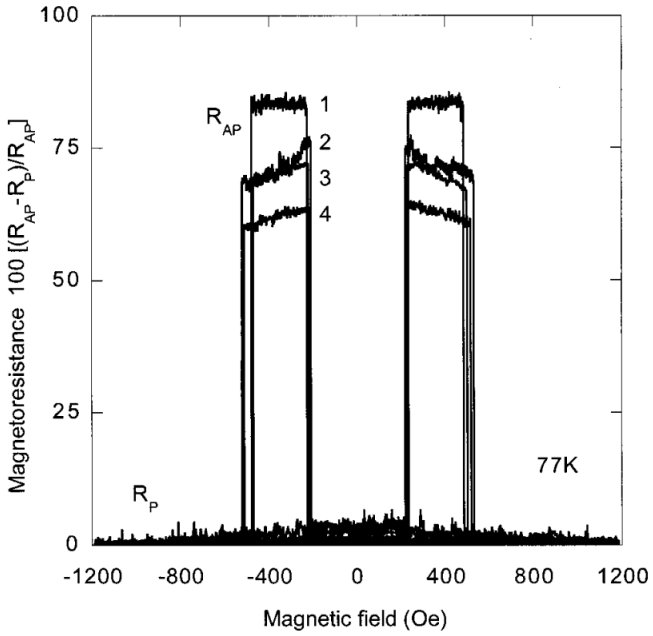

Figure 3.7: Resistance versus magnetic field for four LCMO/$NdGaO_3$/LCMO junctions measured at 77 K [154]. Junction areas (1) 6.6 μm^2, (2) 8.8 μm^2, (3) 8.16 μm^2 and (4) 20.30 μm^2.

3.1.7 Oxide-based magnetic barrier

Some oxides offer the possibility to explore further the properties of MTJs when the barrier is made of a ferromagnetic insulator such as La_2NiMnO_6 double perovskite. Apart from the fact that it provides an opportunity to study the effect of a ferromagnetic barrier on TMR, the dependence of the tunneling on the magnetization of the barrier also allows one to use these junctions as a probe to detect different magnetic phases in the barrier (LNMO).

3.2 Experimental techniques

In this section, the methods and techniques we have used to fabricate and characterize the MTJ devices will be described. The epitaxial thin films were deposited using the PLD technique which was previously explained in section 2.2.1.

3.2.1 Photolithography

Photolithography is a fabrication technique in which patterns of geometric shapes are transferred onto a surface covered with the resist sensitive to the irradiation (UV photons). We have used this technique to fabricate our MTJ devices by defining a mid-section strip on top of a LSMO monolayer.

In order to do that, first the surface of the sample is cleaned by immersing it in isopropyl alcohol and drying it with a jet of nitrogen. Once the sample is cleaned, it is fixed by the suction of a spin coater machine (Laurell model WS 400A-6NPP/LITE/IND). A drop of photoresist AZ1512 is deposited on the surface of the sample. Then, the spinner is rotated with the speed of 4000 rpm for 30 s to spread the resin uniformly all over the sample. The sample is then heated up to 115 °C for 60 s to evaporate the solvent from the resin and harden it. Afterwards, the sample is placed inside the mask-less photolithography machine (SF-100 XPress) and the pattern (strip) is aligned on the middle of the sample. Now, the sample is exposed

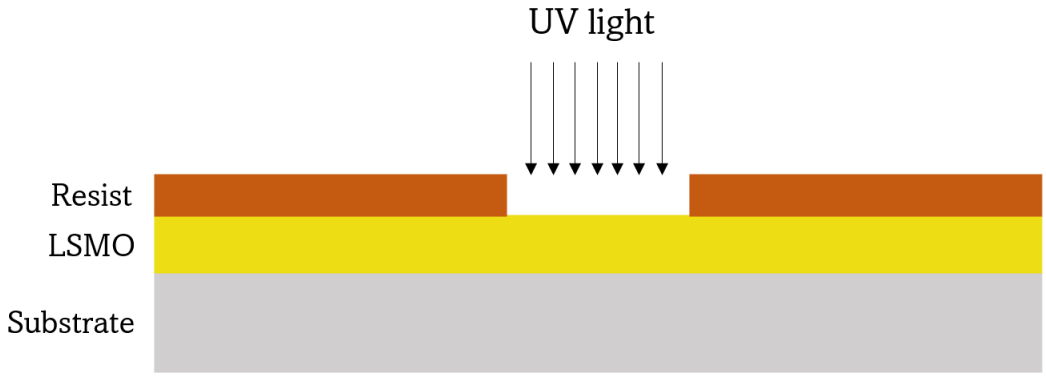

Figure 3.8: Defining a narrow strip on a LSMO monolayer using the photolithography technique.

to UV light with an exposure time of 1.65 s. Finally, the sample is immersed in developer (MF-319) for 60 s and then water for 30 s with rotational movements. A schematic drawing of a patterned sample is shown in Figure 3.11.

Following the amorphous layer deposition which will be explained in the next section, the resin needs to be removed. To do this, the sample is immersed in the MICROPOSIT REMOVER 1165 solution and is kept in an ultrasonic bath for at least 3 min to dissolve the mask. Then, the sample is rinsed with isopropyl alcohol and dried with a nitrogen jet. Depending on the circumstances, it may be necessary to repeat these steps several times before the sample is clean.

3.2.2 Sputtering

Sputtering is a physical vapor deposition technique where energetic ions knock off surface atoms of a selected target in order for the ejected particles to deposit on a substrate. A sputtering system consists of a chamber which isolates the deposition environment from the atmosphere, vacuum pumps, gas lines and power generators. The mechanism of sputtering is explained with the help of Figure 3.9. Initially, the chamber is pumped down to very low pressure ($\leq 5 \times 10^{-6}$ Torr), then it is backfilled with a sputtering gas to the desired pressure which normally is in the range of 1–40 mTorr. Argon is the most commonly used process gas due to its

inertness. The process initiates by applying a large negative potential to the target. The target behaves as a cathode and electrons will be emitted from its surface. The ejected electrons accelerate away from the target due to the negative potential and get a very high kinetic energy. They collide with the Ar atoms and ionize them. The positive Ar ions accelerate towards the cathode (target) and collide with its surface. Part of their kinetic energy is transferred to the target particles and eventually they get enough energy to leave the surface of the target. The collision also extracts more electrons from the surface which then are accelerated from the target and ionize more Ar atoms that will sputter the target and so on. Finally, the sputtered atoms travel across the plasma to deposit onto the substrate. There are two types of sputtering modes, DC and RF.

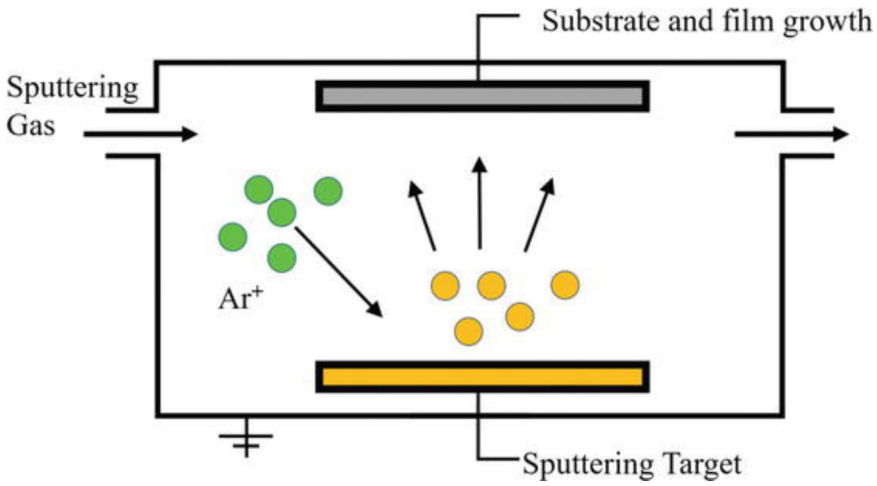

Figure 3.9: Schematic representation of the sputtering deposition process [157]. The yellow circles are the sputtered atoms from the target.

3.2.2.1 DC sputtering

The deposition process described previously is for DC sputtering in which the target and the substrate are always cathode and anode, respectively. In this case, the voltage source is in direct current (DC) mode. DC sputtering is only used to deposit conducting materials. It is impossible to sputter insulating and semiconducting materials with this technique due to the accumulation of positive charged ions

on the target surface which repels the positive Ar ions. In need for sputtering insulating materials, RF sputtering comes into play.

3.2.2.2 RF sputtering

Radio frequency (RF) sputtering is a technique that can be used to deposit either insulating and conducting materials. In this process, a high frequency alternating signal is generated by an alternating current source at radio frequencies. Similar to DC sputtering, a negative potential is generated at the target and consequently, it will be bombarded by positive Ar ions. Since the target is insulating, these positive ions stick to the surface of the target. Later during the positive half of the cycle, electrons are attracted to the target resulting in the neutralization of these accumulated Ar^+ ions on the target. Due to the higher mobility of electrons compared to heavy ions, more electrons will reach the target surface during the positive half cycle than the positive ions during the negative half cycle, hence the target will remain negatively self-biased. The permanent negative surface repels electrons near the target and creates a cloud of positive ions in the vicinity of the target. These ions will continue bombarding the target and a continuous sputtering can be achieved without any decay in the process.

3.2.2.3 Magnetron sputtering

In conventional sputtering, some electrons are lost due to recombination with the wall and other ions in the chamber resulting in the glow discharge diminishing down. In order to avoid this problem, magnetron sputtering has been developed, where a magnetic field is applied perpendicular to the electric field between the cathode and anode. Due to the superimposition of the electric and magnetic field, electrons no longer move parallel to the electric field lines, but are deflected onto a spiral path which is perpendicular to both fields. This motion traps electrons close to the target where the magnetic field is applied parallel to the target surface. The accumulation of electrons will cause a significant increase in the probability of electron-Argon collision in the vicinity of the target, which increases the deposition rate. The biggest disadvantage of this method is that the non-uniform removal

of particles from the target causes the poor utilization of targets. Moreover, the deposition of magnetic materials is more difficult.

3.2.2.4 Reactive sputtering

Reactive sputtering is a deposition technique in which materials are sputtered on a substrate in the presence of a reactive gas. Oxygen and nitrogen are two common reactive gases which can be mixed with Argon as the sputtering gas. This results in the formation of a thin film consisting of the target material and the reactive gas. With reactive sputtering, the chemical composition of the film can be adjusted and the deposition rate can be increased, as well. The most common compounds that are grown by reactive sputtering with oxygen as the reactive gas are: Al_2O_3, SiO_2, In_2O_3, SnO_2 and Ta_2O_5.

The problem with reactive sputtering is that reactive gases usually react with the target material and form their compounds on the surface resulting in a low deposition rate. In extreme cases, this problem will result in instabilities such as sparks or extinguishing of the plasma.

3.2.2.5 RF sputtering deposition conditions

For this project, magnetron sputtering with a RF generator 300 W at 13.56 MHz with automatic matching network designed by Plasmionique has been employed to grow amorphous layers of Al_2O_3 and SiO_2. Figure 3.10 is a picture of the pulsed laser deposition chamber and RF sputtering load lock chamber used to grow epitaxial thin films and amorphous layers.

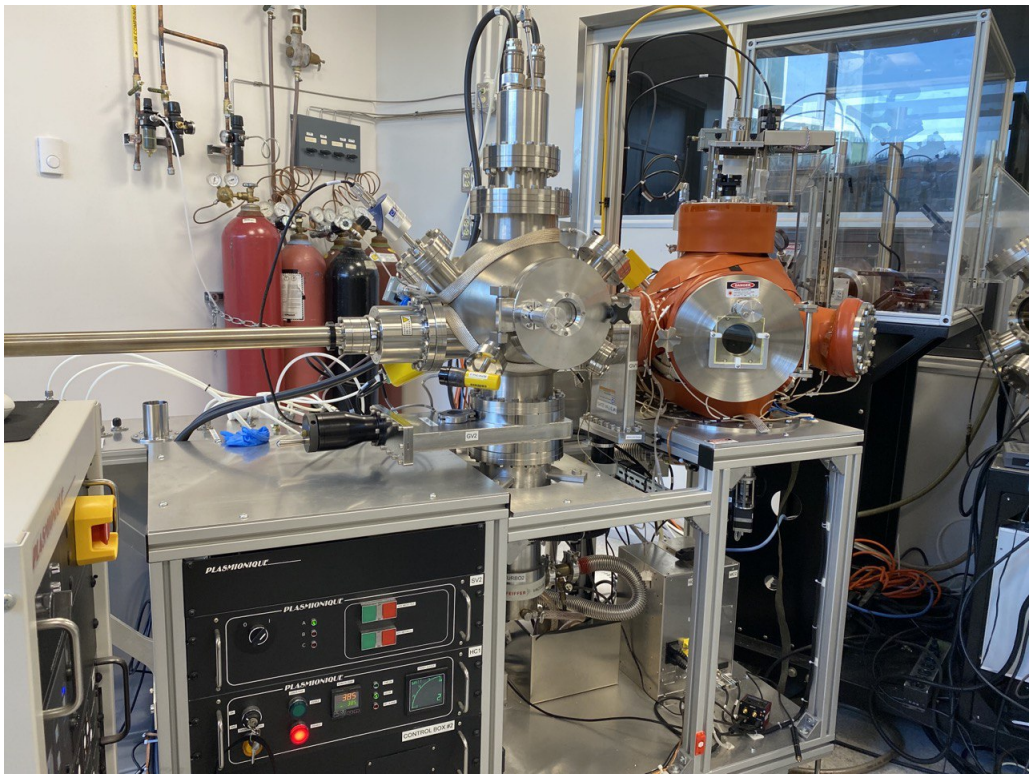

Figure 3.10: Pulsed laser deposition chamber (in orange) with load lock RF sputtering equipment (chamber to the right) used for this project.

Deposition of amorphous Al_2O_3

Reactive RF sputtering technique was used to grow amorphous layers of Al_2O_3 at room temperature. For this purpose, a high purity 99.999 % Al target with a diameter of two inches was used as the sputtering target. Initially, the chamber was pumped down to a base pressure of approximately $\sim 5 \times 10^{-6}$ Torr. Then, 18 sccm Ar and 2 sccm O_2 were introduced to the chamber and the pressure is stabilized at 5 mTorr by adjusting the gate valve slowly. Once the pressure is stabilized, the power is increased to 130 W. Sometimes low pressure can make it difficult for gas to break down and initiate the plasma, so to start a magnetron discharge, it can be helpful to use a gas "puff" by closing the gas shutoff valve for a few seconds and reopening it while RF power is on. When the plasma appears, the target is "trained" for at least 30 min before the final deposition. Then, the shutter is removed and the deposition begins. The thickness of amorphous Al_2O_3 layers is measured using the

profilometer and it is found to be around 150 nm for a 30 min deposition, which gives the deposition rate of 5 nm/min for the given conditions.

Deposition of amorphous SiO_2

Unlike Al_2O_3, amorphous layers of SiO_2 were deposited with direct sputtering technique with the use of a SiO_2 target where only the sputtering gas (Ar) was present in the chamber during the deposition runs. In this case, the chamber is pumped down to low pressures ($\sim 5 \times 10^{-6}$ Torr). Then, 20 sccm Ar is injected slowly to the chamber and the pressure is kept at 5 mTorr by adjusting the gate valve. Following this, the power is increased to 70 W with a slow rate of 10 W/min in order to prevent the fragile SiO_2 target from cracking. A gas puff is usually needed to ignite the plasma. Similar to Al_2O_3, a 30 min preablation is done while the shutter is closed to "train" the target. Figure 3.11 shows an example of a strip of amorphous SiO_2 deposited on a LSMO layer using RF sputtering. According to the profilometer measurements, these strips of SiO_2 have a thickness and a width of 150 nm and 0.7 mm, respectively (Figure 3.12). The thickness measurements indicate that the deposition rate of amorphous SiO_2 is around 3–4 nm/min for the conditions mentioned above.

To complete the fabrication of MTJ devices, layers of LNMO and LSMO need to be grown after depositing a SiO_2 strip on the samples. In order to have a clean and smooth interface between the bottom electrode (LSMO) and the barrier (LNMO), first a thin layer of LSMO is deposited on top of the electrode, then it is followed by the deposition of LNMO and LSMO layers, respectively. It has to be mentioned that due to the presence of an amorphous layer (either SiO_2 or Al_2O_3) in these samples, they were heated up from room temperature to the growth temperature in 50 mTorr oxygen to prevent degradation and transformation of the amorphous layer.

3.2.3 Physical property measurement system

The Physical Property Measurement System (PPMS) is able to perform a variety of measurements like specific heat, magnetic AC and DC susceptibility and both

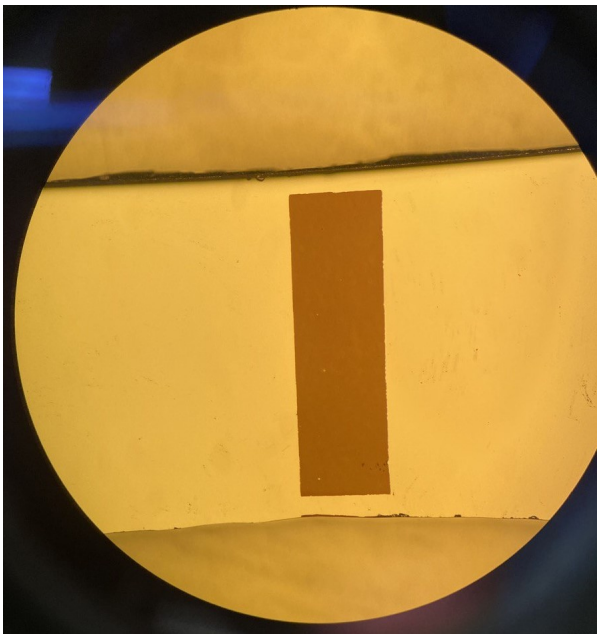

Figure 3.11: A picture of an amorphous SiO_2 strip (dark brown) deposited on a LSMO layer.

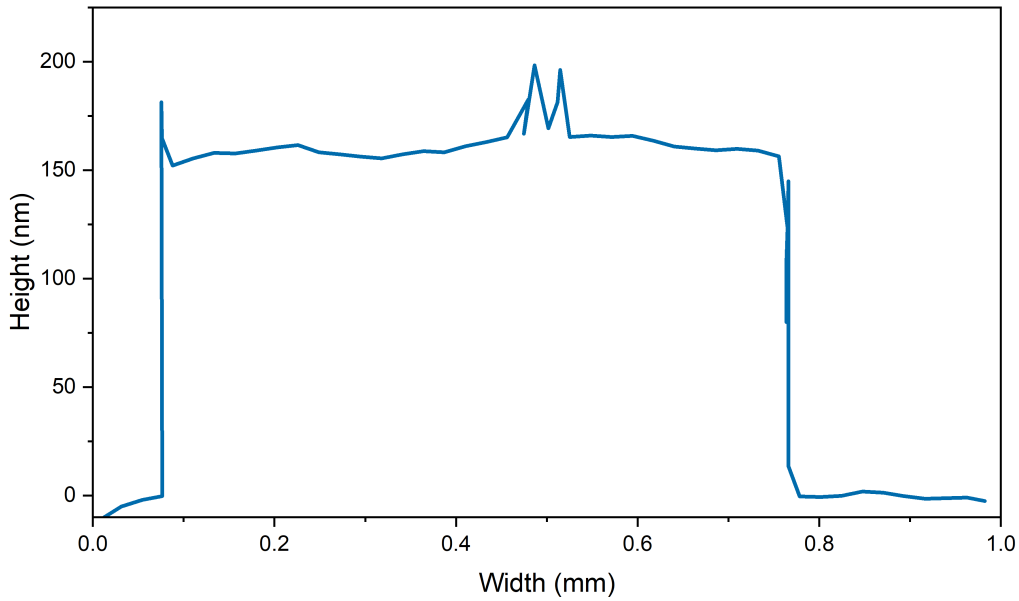

Figure 3.12: The thickness and the width of an amorphous SiO_2 strip measured using the profilometer.

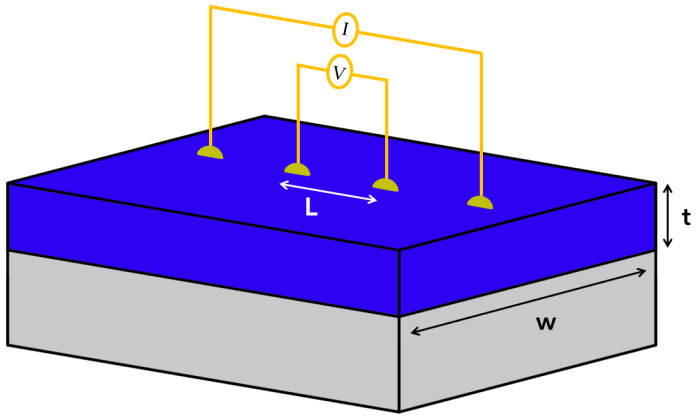

Figure 3.13: Schematic of the four probes method on a thin film layer where the two outer contacts are used to inject current and the two inner ones are voltage probes.

electrical and thermal transport properties such as the Hall effect and thermoelectric effect. In this project, the Quantum Design PPMS was used to carry out all the electrical transport measurements in the temperature range of 2–350 K and the magnetic field of 0–9 T.

3.2.3.1 Resistivity measurements

We have conducted all transport measurements using the four probe technique which is a widely used method to measure the resistivity of materials. The experimental setup consists of four contacts arranged linearly in a straight line, two probes are for electric current and the two other ones measure the voltage drop over a length (L) in the sample. A constant electric current is passed along the sample through the two outermost contacts and the voltage drop across the middle two probes is measured (Figure 3.13).

The resistance of a conductor is directly proportional to its length (L) and inversely proportional to its cross-sectional area (A):

$$R = \rho \frac{L}{A} \tag{3.10}$$

where ρ is the resistivity of the conductor. As indicated in Figure 3.13, for a thin film layer, L is the distance between the two voltage contacts, and A is the cross sectional area, $A = t \times w$.

3.2.3.2 MTJs measurement setup

Figure 3.14 shows a drawing picture of the fabricated MTJ devices and the position of the contacts for resistivity measurements. As specified in this schematic, the electrical current is forced to flow through the barrier due to the non-epitaxial growth of LNMO and LSMO layers on top of the SiO_2 strip.

The Quantum Design horizontal rotator option for the PPMS is employed to measure the tunnel magnetoresistance of the magnetic tunnel junction devices. It allows us to rotate the samples around an axis that is perpendicular to the magnetic field. The range of rotation is from -10° to 370°. In this measurement setup, the samples were mounted on a sample holder board, which is then attached to the rotator platform circuit board. The sample holder makes thermal contact with a thermometer on the rotator platform, allowing close monitoring of the sample temperature. It consists of 3 channels with one of them connected to the thermometer. Samples were wired to the contact pads using gold wires and indium tips soldered onto the sample at high temperature. A picture of the horizontal rotator and different types of sample holder boards as well as a mounted sample on the sample holder are shown in Figure 3.15.

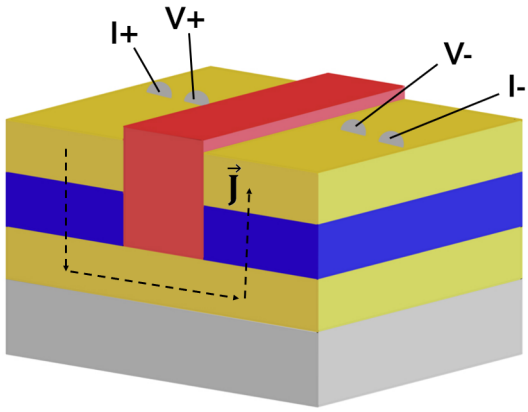

Figure 3.14: Schematic of the MTJ device consisting of two LSMO electrodes (yellow) separated by a LNMO barrier (blue). The middle slab (red) separating two devices is made of an amorphous layer of SiO_2. The dashed line shows the direction of the electrical current in the sample.

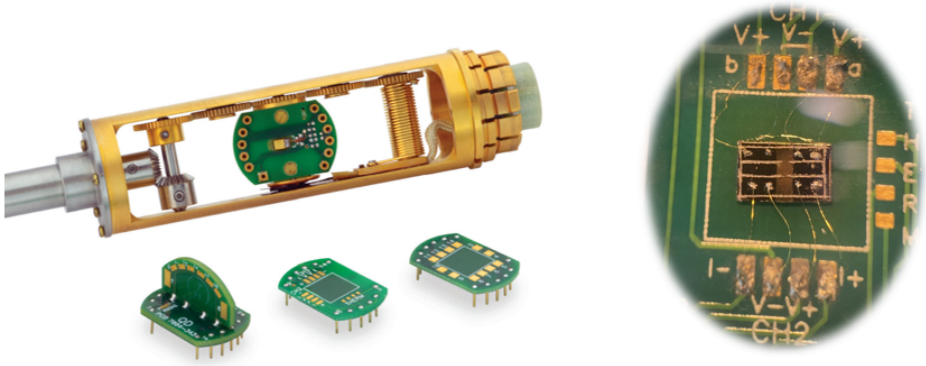

Figure 3.15: Horizontal rotator with different sample-mounting platforms (left) [158]. A mounted sample on the sample holder board (right). It shows that two separate devices can be measured at the same time. The surface area of each junction is about 0.5 mm^2.

3.3 Results and discussion

3.3.1 Motivation

Magnetic tunnel junctions are usually fabricated using non-magnetic amorphous or crystalline barriers. Therefore, the tunnel magnetoresistance depends only on the relative orientation of the magnetic moments in the two ferromagnetic electrodes with respect to each other. Due to the rarity of magnetic insulating materials, this type of barriers have not been explored extensively. In this work, we intend to study the effect of a ferromagnetic barrier on the tunnel magnetoresistance in MTJs. We investigate how TMR occurs through a magnetic barrier when its magnetic moments are oriented differently with respect to two FM electrodes. Furthermore, the sensitivity of the tunneling process to the magnetization of the barrier could be used as a probe to explore and detect all the magnetic phases in the LNMO barrier. It may help to explain the wide magnetic entropy change seen in the heterostructures (see Chapter 2) and identify phases (domains) that are hardly observable using magnetization measurements.

For this purpose, we used LNMO double perovskites as the ferromagnetic insulating barrier to fabricate MTJ devices. We have also chosen half-metallic ferromagnetic LSMO manganites as the electrodes due to its large spin polarization at low temperature and its magnetic transition above room temperature. Trilayers of LSMO/LNMO/LSMO have been fabricated using the PLD method in combination with RF sputtering and photolithography techniques on $SrTiO_3$ (001) substrates. It should be mentioned that some preliminary tests were performed on the single layers of LSMO and LNMO which are shown in the supplemental material of the paper (below) and also in appendix A. The results of this work are summarized in the following paper submitted to Physical Review B on Dec 5, 2022.

The authors confirm contribution to the paper as follows: **M. Abbasi Eskandari:** Conceptualization, Samples preparation, Investigation, Visualization, Writing – original draft. **S. Ghotb:** Samples preparation, Investigation. **P. Fournier:** Conceptualization, Writing – review & editing, Supervision, Project administration, Funding acquisition.

3.3.2 Paper

Impact of a ferromagnetic insulating barrier in perovskite-based magnetic tunnel junctions

M. Abbasi Eskandari, S. Ghotb, and P. Fournier
Institut quantique, Regroupement québécois sur les matériaux de pointe et Département de physique, Université de Sherbrooke, Sherbrooke, J1K 2R1, Québec, Canada

We investigate spin-dependent conductance across a magnetic tunnel junction (MTJ) including a ferromagnetic insulating barrier. The MTJ consists of two half-metallic ferromagnetic $La_{2/3}Sr_{1/3}MnO_3$ (LSMO) manganites as electrodes and La_2NiMnO_6 (LNMO) double perovskite as a ferromagnetic insulating barrier. The resistance of the junction is strongly dependent not only on the orientation of the magnetic moments in LSMO electrodes, but also on the direction of the magnetization of the LNMO barrier with respect to that of LSMO. The ratio of tunnel magnetoresistance reaches a maximum value of 24 % at 10 K, and it decreases with temperature until it completely disappears above 280 K, close to the maximum critical temperature of cation-ordered LNMO. The tunneling process is described using a mechanism which involves both empty and filled e_g states of the LNMO barrier acting as a spin-filter. A magnetic insulating barrier is an interesting path for achieving room temperature magnetoresistance in oxide-based heterostructures.

I. INTRODUCTION

Spintronics uses the electron spin degrees of freedom to manipulate the electron transport or to store information. An entirely new generation of electronic devices has emerged with spintronics featuring non-volatile storage, ultra-fast switching, reduced energy consumption and increased integration density [1, 2]. Tunnel magnetoresistance (TMR), one of the most important phenomena in spintronics, was first discovered by Jullière in 1975 in magnetic tunnel junctions (MTJs) [3]. Since then, MTJs have generated considerable interest due to their potential applications in spin-electronic devices such as magnetic sensors and magnetic random-access memories (MRAMs) [4]. MTJs consist of two ferromagnetic metallic layers separated by a thin insulating barrier. In MTJs, the ratio of TMR depends on the relative orientation of the magnetization in the two ferromagnetic layers on each side of the barrier, which can be controlled by an external magnetic field. The tunnel magnetoresistance can be expressed in term of the junction resistances when the magnetic moments of two ferromagnets are parallel (R_{P}) and antiparallel (R_{AP}), as follows:

$$TMR = (R_{\mathrm{AP}} - R_{\mathrm{P}})/R_{\mathrm{P}} \times 100$$

It has been shown that half-metallic materials that possess only one spin polarization at the Fermi level can produce a very large TMR ratio due to their large spin polarization [5]. Among the materials that are half-metals, manganites are considered as popular choices for ferromagnetic electrodes in MTJs due to their large spin polarization and tunable transition temperature that can be used to design electronic devices to meet specific functional requirements. The best results on manganite-based MTJs have been reported with optimally-doped $La_{2/3}Sr_{1/3}MnO_3$ (LSMO) manganite [6–8], particularly it showed a TMR as high as 1850 % in a LSMO/$SrTiO_3$/LSMO MTJ, corresponding to a spin polarization of 95 % for LSMO at low temperature [9].

Two types of barrier have been extensively studied in MTJs including amorphous and crystalline insulating barriers. Amorphous barriers such as AlO_x were a common choice in the first generation of MTJs due to their ease of fabrication process, spin conservation across the barrier and pinhole-free layers [10, 11]. MTJs with amorphous barrier never showed TMR larger than 81 % at room temperature which were in close agreement with Jullière's model prediction [12]. The most remarkable results were obtained using crystalline insulating compounds such as MgO as the tunnel barrier, leading to a large TMR of up to 600 % at room temperature due to coherent tunneling through the barrier [13, 14]. Since then, crystalline insulating barriers have been the focus of MTJs' studies.

Due to the rarity of ferromagnetic insulators, this type of barriers has not been explored extensively. Only a few studies have investigated the effect of magnetic barriers on TMR in spin-filter junctions [15–17]. For instance, Gajek *et al* [15] have demonstrated that a TMR of up to 50 % can be obtained in Au/$BiMnO_3$/LSMO junctions according to whether the magnetization of BMO and LSMO are parallel or opposite. It should also be noted that spin-filter junctions usually operates at low temperature and the TMR decays very fast with temperature.

In the present work, we use La_2NiMnO_6 (LNMO) double perovskite to explore the impact of a ferromagnetic barrier on the TMR of MTJs. The insulating nature of LNMO provides the tunneling conditions in the entire temperature range of operation, combined with a ferromagnetic order with a transition temperature ranging from 180 to 285 K depending on the level of cationic ordering in the sample [18]. In the case of cation-disordered LNMO with the lowest magnetic transition, Mn^{4+} and Ni^{2+} cations position randomly at the $3d$ metal sites. In ordered LNMO, Mn^{4+} cations are surrounded by six Ni^{2+} ions and vice versa, giving rise to the highest pos-

sible magnetic transition temperature in this compound. We also employ half-metallic LSMO manganite as the electrodes to maximize spin polarization. We explore how the tunneling occurs through the magnetic barrier and propose a mechanism involving empty and filled e_g states around the Fermi level in the barrier. It is also shown that the device can be operated up to 280 K, close to the maximum magnetic phase transition temperature of the LNMO barrier.

II. EXPERIMENTS AND METHODS

The MTJ devices consist of a ferromagnetic insulating LNMO barrier sandwiched between two half-metallic LSMO layers as the electrodes. Pulsed laser deposition (PLD) technique has been used to grow epitaxial layers of LSMO and LNMO on (001)-oriented $SrTiO_3$ substrates. A schematic illustration of the final device is displayed in Figure 1. In order to fabricate a MTJ device, first a layer of LSMO is deposited on the substrate, followed by patterning a resin layer using photographically technique defining a strip of exposed LSMO in the middle of the layer. Then, a 100 nm-thick amorphous SiO_2 layer is deposited using RF magnetron sputtering. Following a lift-off that removes the resin covered by the amorphous layer and leaves a strip of SiO_2 on top of LSMO, a LNMO layer and then a LSMO layer are deposited. The amorphous strip of SiO_2 prevents the epitaxial growth of LNMO and LSMO layers on top of it, imposing a current flow through the barrier with the contact configuration shown in Fig. 1. The bottom and top LSMO electrodes are 50 nm thick, while the thickness of LNMO barrier is chosen at 40 nm after a few trials. The surface area of each junction is around 0.5 mm^2. Structural characterization were performed using a Bruker AXS D8-diffractometer with $CuK_{\alpha 1}$ radiation in $2\theta/\omega$ configuration. Further surface investigations have been performed using a Veeco Dimension Icon Atomic Force Microscope (AFM). A physical properties measurement system (PPMS) from Quantum Design was employed to carry out the transport measurements with the help of a horizontal rotator option allowing to apply magnetic field in different directions with respect to the interfaces of the sample, in the temperature range of 10 K to 300 K. Finally, the magnetization measurements were performed using the reciprocating sample option (RSO) of a 7 T SQUID magnetometer from Quantum Design.

III. RESULTS AND DISCUSSION

The XRD $2\theta/\omega$ scan of the epitaxial part of the sample in the range from 10° to 80° (see supplemental material) confirms the absence of impurity or secondary phases in the samples by assigning all the peaks to LSMO and LNMO layers. A magnified view of a XRD pattern around the (002) peak from the substrate is displayed

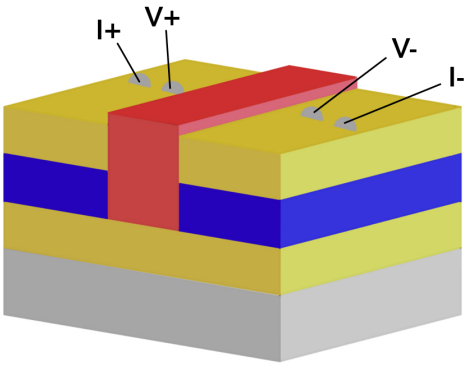

FIG. 1: Schematic of the MTJ device consisting of two $La_{2/3}Sr_{1/3}MnO_3$ electrodes (yellow) separated by a La_2NiMnO_6 barrier (blue). The middle slab (red) separating two devices is made of an amorphous layer of SiO_2 deposited on the bottom layer of epitaxial LSMO. This slab includes also an insulating non-epitaxial LNMO/LSMO cover.

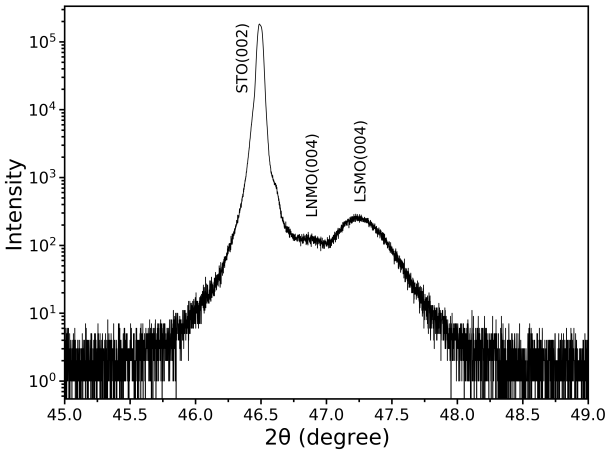

FIG. 2: X-ray diffraction (XRD) pattern of a trilayer MTJ device consisting of two LSMO layers and one LNMO layer on a STO substrate.

in Figure 2 where the (004) reflections from the LSMO and LNMO layers can be clearly seen, indicating the out-of-plane growth of these epitaxial layers. AFM measurements on the surface of the bottom LSMO layer before completing the device show a surface roughness less than 1 nm over lateral distances of 5 μm for a 50 nm-thick LSMO layer. In addition, AFM images of the top LSMO layer indicate a pinhole-free growth of the two top layers with roughness of the order of 10 nm (see supplemental material). These two separate AFM checks confirm well-defined interfaces between the layers with roughness of only a few nanometers over lateral distances of the order of 5 μm.

Field-cooled magnetization of a MTJ device was measured as a function of temperature at a fixed magnetic field of 200 Oe in the temperature range from 10 to 370 K. As depicted in Figure 3, the sample clearly goes through

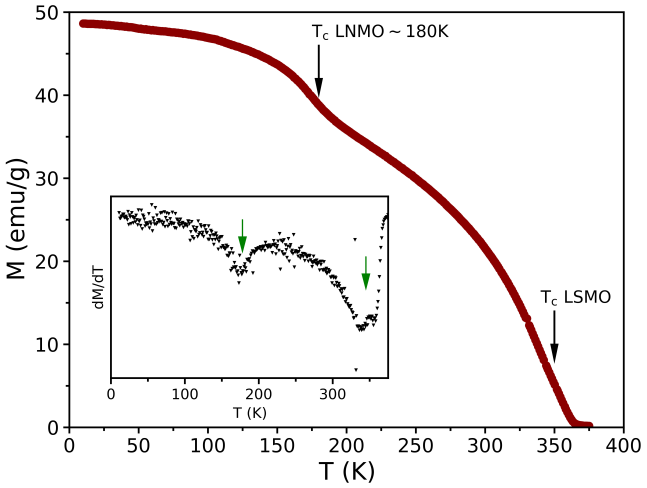

FIG. 3: Field-cooled magnetization as a function of temperature under a magnetic field of 200 Oe for a LSMO/LNMO/LSMO MTJ device. The inset shows the derivative of the magnetization versus temperature.

two magnetic phase transitions at approximately 180 and 350 K, corresponding to the ferromagnetic-paramagnetic transitions of LNMO and LSMO layers, respectively. The transition temperatures were determined from the minimum in the derivative of the magnetization with respect to temperature (inset of Fig. 3). The low transition temperature of the LNMO layer compared to its maximum T_c of 280 K–285 K [19] is ascribed to a low cation-ordering level in the system, where Mn^{4+} and Ni^{2+} ions occupy the 3*d* metal sites randomly with partial ordering.

Figure 4 (a) shows the temperature dependence of the junction resistance measured at low bias under zero and 0.2 T magnetic field applied parallel to the surface of a trilayer device. In addition, Figure 4 (b) displays the conductance as a function of voltage at 10 and 300 K. The non-linear behavior of the conductance implies that a direct tunneling channel through the barrier exists in our device, and that it persists up to room temperature. The presence of parallel diffusive channels cannot be ruled out in our devices and evidences of them are actually observed in the MR measurements below. Similar to typical oxide-based MTJs, the resistance of our devices exhibits different temperature dependence in different temperature regions in Fig. 4 (a). From 185 to 300 K, the junction shows a semiconducting-like behavior where the resistance increases with decreasing temperature consistent with the conductance signature of direct tunneling transport in the junction at 300 K in Fig. 4 (b) [20]. This is a common characteristic feature in all MTJs, regardless of their compositions [7, 13, 21]. The non-metallic behavior is also consistent with the insulating resistivity for LNMO [22]. However, below 185 K, the junction enters a low temperature region in which the zero-field resistance decreases with decreasing temperature which is incompatible with the non-metallic behavior of LNMO. There have only been a few oxide-based MTJs that exhibit this unusual metallic-like resistance. Its origin has not yet been determined, but it was proposed that it may be the result of oxygen deficiencies at the interface when the barrier is an insulator [7, 8, 23]. In our case, this anomaly in our MTJ devices could instead be attributed to the onset of magnetic order around 200 K in most of the LNMO barrier as confirmed by the magnetization in Fig. 3. The decreasing resistance would then imply an increase of the tunneling probability through the LNMO barrier as its magnetization grows.

The application of 0.2 T magnetic field lowers further the junction resistance in the same temperature range below 200 K. In fact, the observed magnetoresistance goes to zero at 275 K as shown in the inset of Fig. 4. This onset temperature is very close to the maximum T_c of 285 K observed for cation-ordered LNMO [19]. Although we cannot really observe a magnetic transition around 275 K–285 K in the M(T) curve in Fig. 3, we cannot rule out the presence of domains with a high degree of cationic ordering with such high T_c. Moreover, in contrast with the typical behavior of colossal magnetoresistance in manganites which usually shows a shift in the resistance peak to higher temperatures under an applied magnetic field [24], the position of the peak in the R(T) measurements of our devices does not change with magnetic field, indicating clearly that the magnetoresistance does not originate from the LSMO layers [23]. Thus, the high-field MR is likely from a parallel diffusive channel in LNMO. Altogether, the conductance of these devices is controlled mostly by the magnetic polarization of the barrier with respect to the metallic and ferromagnetic electrodes for one channel and a background MR of LNMO.

Figures 5 (a) and (b) present the magnetic field dependence of the MTJ resistance at 10 K and 250 K with the magnetic field applied parallel to the surface of the film. The junction shows a symmetric magnetoresistance hysteresis loop with low and high resistance states defined by the parallel and antiparallel alignment of the magnetic moments in LSMO and LNMO layers with respect to each other. This trend persists up to 280 K (Fig. 5 (b) and also shown in supplemental material). As schematically illustrated in Fig. 5 (a), switching between the low and high resistance states is governed by the magnetization direction in the LNMO barrier. In general, we have observed that LNMO thin films present larger coercive fields ($\sim$ 500 Oe–1000 Oe) than LSMO films ($\sim$ 50 Oe–300 Oe): see supplemental material. While LSMO films show usually sharp polarization switches at their coercive field, LNMO films tend to have broader polarity transitions (see supplemental material). In a sufficiently high magnetic field, the magnetic moments of all three layers are aligned and the junction stays in the lowest resistance state. With decreasing magnetic field, the magnetic moments of the LNMO layer start flipping gradually and orient antiparallel to those of the LSMO elec-

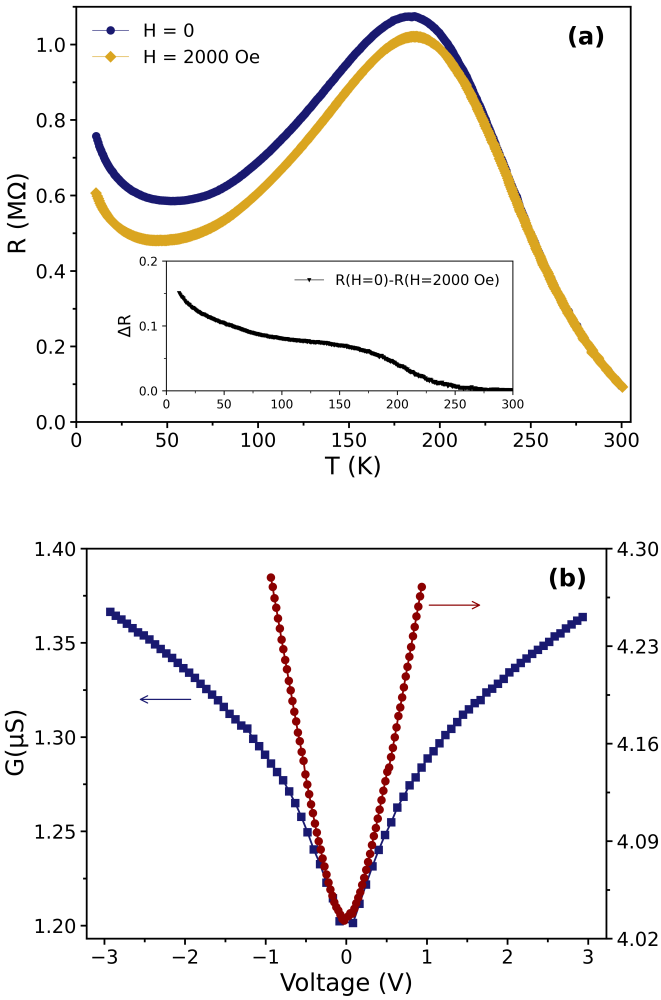

FIG. 4: (a) Temperature dependence of the junction resistance at zero and 0.2 T magnetic field. Inset displays the difference between the two curves (magnetoresistance) which goes to zero at 275 K. (b) Conductance as a function of voltage for MTJ devices. Dark blue squares and dark red circles indicate the conductance at 10 and 300 K, respectively.

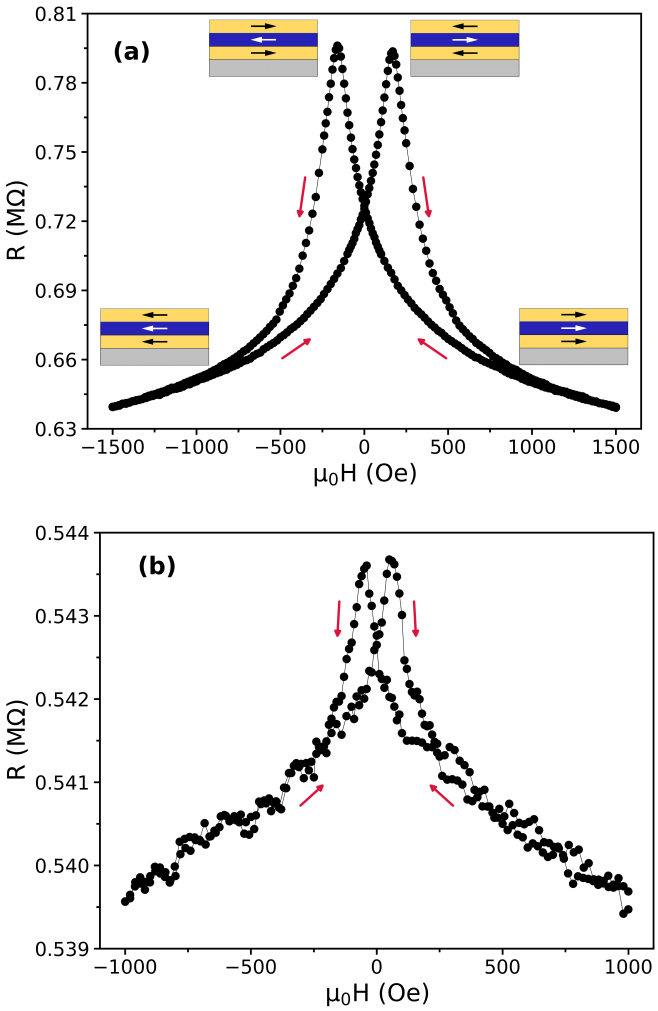

FIG. 5: TMR versus applied magnetic field at (a) 10 K and (b) 250 K. Fig. (b) demonstrates that the tunneling process persists even above the apparent transition temperature of the LNMO barrier at 180 K.

trodes. This antiparallel configuration in some areas of the junction blocks the low-resistance conduction paths and consequently conduction occurs via another channel with higher resistance. The gradual increase of resistance continues as more magnetic domains flip in the LNMO layer, until the magnetic field reaches the coercive field of LSMO. At this point, the junction reaches its maximum resistance at ±160 Oe, where a large proportion of the magnetic domains in the LNMO barrier are aligned in opposite direction with respect to those of the LSMO electrodes. This magnetic field is very close to the coercive field of LSMO (see supplemental material) and far from the coercive field of the device (see Fig. 7 and discussion below). From 160 Oe, further increasing the magnetic field flips rapidly the magnetic moments of both LSMO electrodes. If we assume that the top and bottom LSMO electrodes in our devices have identical coercive fields, this rapid flip of both LSMO electrodes results again in the all-parallel configuration and reestablishes the high conduction paths. Consequently, the resistance decreases with field above 160 Oe. Unlike typical MTJs with a sharp switching between two resistance states at the different coercive fields of the ferromagnetic electrodes [25, 26], the rounded shape of the MR peak in our device can be attributed to the presence of a magnetic spacer with a gradual switching of its magnetic moments.

The difference in resistance between the two magnetic configurations in our MTJ devices originates from the contribution of different direct tunneling processes taking into account the location in energy of the spin-polarized occupied and unoccupied levels in LNMO. Based on band structure calculations [27], these levels in LNMO can be positioned roughly according to the schematic

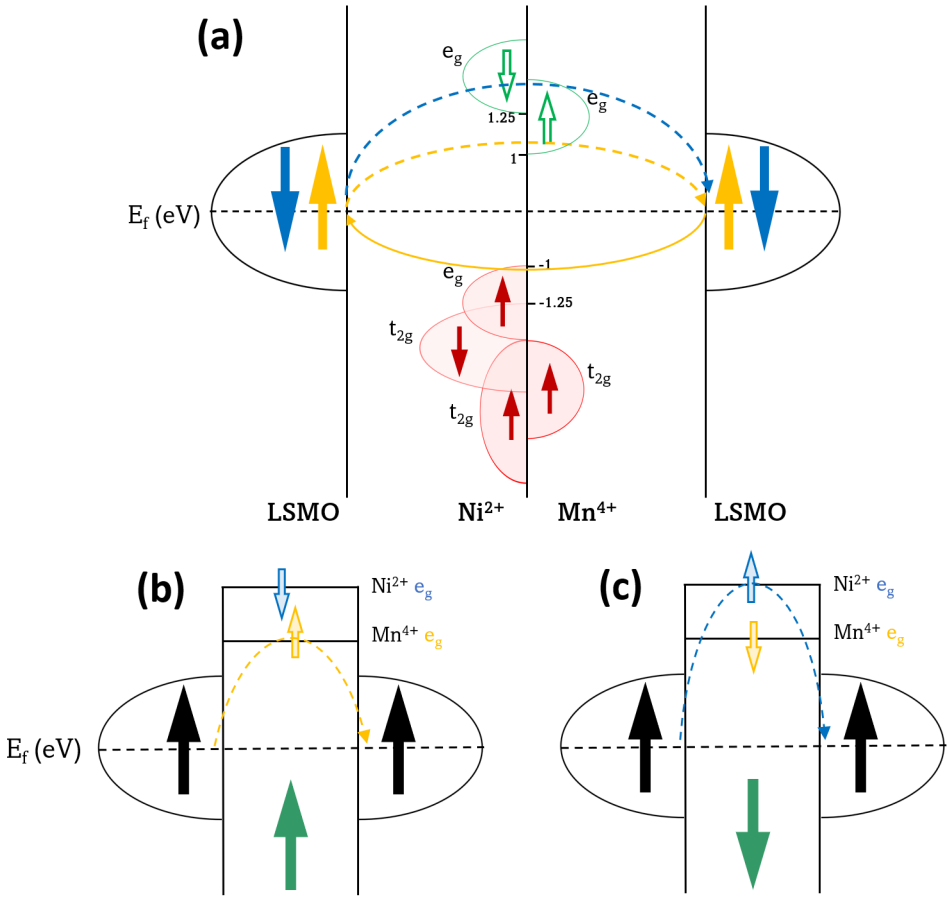

FIG. 6: (a) Schematic of the conduction mechanism including the electron and hole channels in our devices in parallel and antiparallel configurations. Oxygen levels have been left out intentionally as they are not affecting the final outcome. The electron and hole channels are represented with the dashed and solid lines, respectively. Simplified schemes of the conduction mechanism excluding the hole channels for (b) parallel and (c) antiparallel configurations.

presented in Figure 6 (a) assuming that the Fermi energy (E_F) of insulating LNMO is sitting in the middle of its gap. Tunneling can take place through several channels in which the height of the barrier is defined by the spin polarization of empty and filled e_g states. The first type of channels involves electrons in LSMO e_g levels tunneling through the barrier defined by the bottom of the band corresponding to the empty e_g levels above the Fermi energy of LNMO. The second type of channels involves instead hole tunneling through the occupied states of LNMO below the Fermi energy. In this mechanism, we assumed that electrons can only tunnel between bands carrying the same symmetry explaining the absence of a hole channel in the anti-parallel configuration. If tunneling does not require that the wavefunction symmetry must be preserved but only the spin, an additional hole channel through the occupied t_{2g} levels should also be considered. However, since it is further away from E_F than the occupied e_g levels for the hole channel of the parallel configuration in Fig. 6 (a), it would lead also to a higher resistance. It should be underlined that doping due to off-stoichiometry, for example oxygen vacancies which is a common scenario in oxides, will likely shift E_F in the gap of LNMO towards the empty e_g states. This shift only changes the magnitude of the barrier heights for the electron and hole channels but their role in the tunneling processes remains unchanged. For this reason, the contribution from the hole channels will be neglected in the following due to possible higher barrier heights induces by a E_F shift. This assumption will also simplify the description of the direct tunneling below.

Since the electron spin polarization should be preserved during these different tunneling processes, the magnetic polarization of the barrier will select specific channels. The energy barrier height will then be set by the energy position of these empty e_g states of LNMO relative to E_F. Fig. 6 (b) shows a schematic of the all-parallel configuration in which the hole channel is not included for simplicity. In this arrangement, the empty e_g levels of Mn^{4+} contribute to the tunneling current defining a barrier height of roughly 1 eV for this channel. When both LSMO electrodes are anti-parallel with

respect to that of LNMO as in Fig. 6 (c), the tunneling occurs through the empty e_g levels of Ni^{2+} implying a barrier height of roughly 1.25 eV. This higher barrier explains the higher resistance when the polarizations of LNMO and the LSMO electrodes are opposite.

As mentioned previously, the presence of some diffusive conduction channels alongside the tunneling channels cannot be ruled out. These channels may contribute to the conductance of our junctions by providing the background magnetoresistance that we observe in all our data in Fig. 5 (and also in supplemental material), which is commonly observed in LNMO double perovskites [22]. Nevertheless, the direct tunneling is confirmed by the G(V) measurements (Fig. 4 (b)) which is also causing the irreversibility in our R(H) measurements.

Figure 7 displays the magnetic hysteresis loops of the MTJ device at 10 and 300 K with the magnetic field applied parallel to the surface of the sample. Magnetization at 10 K reaches saturation at magnetic fields of the order of 1000 Oe, matching closely the field required to reach resistance reversibility in the R(H) measurements at the same temperature. It confirms that the magnetic moments of LNMO layer saturate and completely align with those of the LSMO electrodes at high field. Moreover, the coercive field (H_c) of the devices is found to be 210 Oe which is closer to the coercive field of a LNMO monolayer (240 Oe) than that of a LSMO monolayer with $H_c \sim$ 140 Oe (see supplemental material). In fact, this confirms that the switching field of 160 Oe observed in the R(H) data in Fig. 5 (a) is related to the polarization switching of LSMO. Also, the M(H) loop at 300 K shows a sharp polarization switching confirming that the device is still magnetic at room temperature and its magnetization originates only from the LSMO electrodes. Generally, MTJs made with a regular insulator have the same coercive and switching fields. In our case, the higher coercive field in the magnetization measurements originates from the contribution of the LNMO layer, whereas the switching field (the peaks) observed in the R(H) measurements is mostly a signature of the coercive field of the LSMO layers. These findings are consistent with the behavior observed in a spin-filter device containing $BiMnO_3$ as a ferromagnetic insulating barrier [15], where a coercive field of 460 Oe was measured from magnetization measurements while the switching field was as low as 100 Oe, corresponding to the coercive field of the LSMO electrode.

The ratio of TMR is extracted from the R(H) data collected for different temperatures up to 300 K (see supplemental material) and is displayed in Figure 8. The maximum TMR ratio is 24 % at 10 K, while it drops rapidly to 0.1 % at 280 K. No irreversibility is observed above this temperature even though the LSMO layers remain ferromagnetic. Typically, the critical temperature of MTJs is associated with spin polarization at the interface of the ferromagnetic electrodes and the barrier, which usually decays much faster with temperature than the bulk magnetization. For instance, the critical temperature for LSMO-based junctions with non-magnetic barriers such as $SrTiO_3$, $LaAlO_3$ and TiO_2 are found to be 260, 280 and 300 K, respectively, while LSMO electrodes are magnetic up to 350 K [28]. Unlike MTJs with non-magnetic barriers, this temperature of our devices is not only controlled by the magnetic properties of the electrodes at their interfaces, it also depends on the magnetization in the barrier. Nevertheless, the effect of non-optimal magnetic properties due to oxygen vacancies at electrode/barrier interfaces on TMR cannot be ruled out [8].

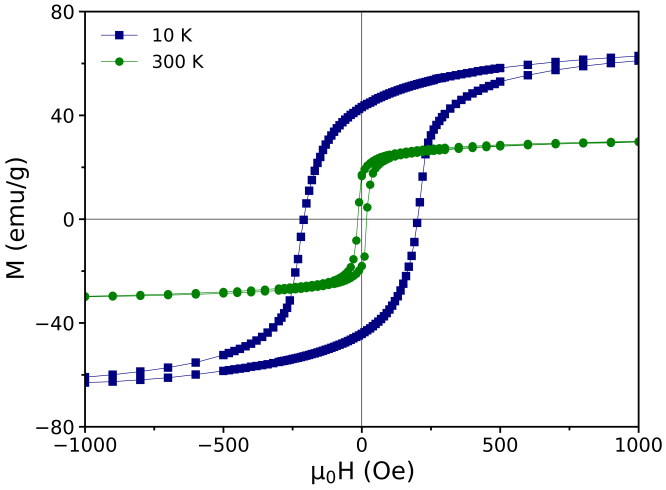

FIG. 7: Magnetic hysteresis loops of the MTJ device with magnetic field applied parallel to the surface of the sample at 10 and 300 K. The M(H) loop at 300 K indicates that the LSMO electrodes are still ferromagnetic at room temperature.

Furthermore, contrary to expectations, the TMR does not disappear above the apparent transition temperature of the LNMO barrier at 180 K observed by magnetization in Fig. 3. In fact, we notice that the R(H) loops become noisy and show a small TMR above this temperature (see Fig. 5(b)). The observation of the TMR above the apparent T_c of LNMO can be ascribed to the presence of some persisting magnetic domains in the LNMO layer with a higher transition temperature, up to ∼280 K. These domains are probably originating from regions of the LNMO film with a high level of cationic ordering [18]. These magnetic domains form only a small fraction of the volume of the LNMO layer, so they could not be detected in the M(T) measurements dominated by the LSMO transition above 200 K but can be noticed in the R(H) data. Finally, the switching field that approaches closely the coercive field of LSMO electrodes is also plotted as a function of temperature in Fig. 8, as well. One can see that it follows almost the same trend as the TMR and that it cannot be detected above 280 K, emphasizing the absence of TMR above the ferromagnetic to paramagnetic transition temperature of LNMO.

Our results indicate that the use of LNMO double per-

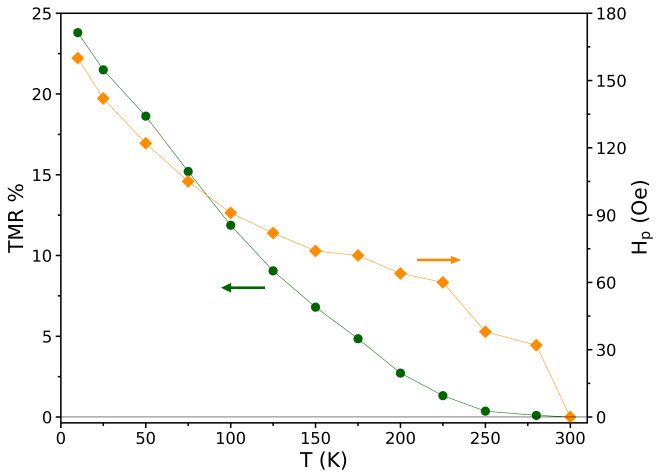

FIG. 8: left axis) The ratio of TMR in LSMO/LNMO/LSMO junctions as a function of temperature. (right axis) The switching (peak) field that corresponds to the coercive field of LSMO layers as a function of temperature.

ovskite as the barrier in MTJs can improve the operating temperature range of tunnel junctions containing a magnetic insulating barrier. Better performances might be expected if one can improve the ratio of cationic ordering in LNMO.

CONCLUSION

In summary, we have presented a study of oxide-based magnetic tunnel junctions including a La_2NiMnO_6 (LNMO) double perovskite as a ferromagnetic insulating barrier. The temperature dependence of the junction resistance shows a similar behavior to that of other oxide-based junctions with a maximum in the mid-temperature range. We have measured a tunnel magnetoresistance of up to 24 % at low temperature with a gradual switching between high and low resistance states. We demonstrate that the TMR depends on the direction of the relative polarity of the magnetization of both LSMO electrodes and the LNMO barrier with a mechanism involving the difference in barrier height driven by the location of the spin polarized empty and filled e_g states in LNMO around its Fermi energy. The junctions exhibit a TMR up to 280 K, offering an improvement over existing spin-filtering junctions. A magnetic insulating barrier is an interesting path for achieving room temperature magnetoresistance in oxide-based heterostructures.

ACKNOWLEDGMENT

The authors thank B. Rivard, S. Pelletier and M. Dion for technical support. The authors also gratefully acknowledge Prof. I. Garate for the helpful discussions. This work is supported by the Natural Sciences and Engineering Research Council of Canada (NSERC) under grant RGPIN-2018-06656, the Canada First Research Excellence Fund (CFREF), the Fonds de Recherche du Québec - Nature et Technologies (FRQNT) and the Université de Sherbrooke.

[1] Wolf, S., Awschalom, D., Buhrman, R., Daughton, J., von Molnár, v. S., Roukes, M., Chtchelkanova, A. Y., and Treger, D. *Science* **294**(5546), 1488–1495 (2001).
[2] Bratkovsky, A. *Rep. Prog. Phys.* **71**(2), 026502 (2008).
[3] Julliere, M. *Phys. lett., A* **54**(3), 225–226 (1975).
[4] Maekawa, S. and Shinjo, T. *Spin dependent transport in magnetic nanostructures*. CRC press, (2002).
[5] Bratkovsky, A. *Phys. Rev. B* **56**(5), 2344 (1997).
[6] Lu, Y., Li, X., Gong, G., Xiao, G., Gupta, A., Lecoeur, P., Sun, J., Wang, Y., and Dravid, V. *Phys. Rev. B* **54**(12), R8357 (1996).
[7] Sun, J., Krusin-Elbaum, L., Duncombe, P., Gupta, A., and Laibowitz, R. *Appl. Phys. Lett.* **70**(13), 1769–1771 (1997).
[8] Viret, M., Drouet, M., Nassar, J., Contour, J., Fermon, C., and Fert, A. *EPL* **39**(5), 545 (1997).
[9] Bowen, M., Bibes, M., Barthélémy, A., Contour, J.-P., Anane, A., Lemaitre, Y., and Fert, A. *Appl. Phys. Lett.* **82**(2), 233–235 (2003).
[10] Meservey, R. and Tedrow, P. *Phys. Rep.* **238**(4), 173–243 (1994).
[11] Moodera, J. S., Kinder, L. R., Wong, T. M., and Meservey, R. *Phys. Rev. Lett.* **74**(16), 3273 (1995).
[12] Wei, H., Qin, Q., Ma, M., Sharif, R., and Han, X. *J. Appl. Phys.* **101**(9), 09B501 (2007).
[13] Bowen, M., Cros, V., Petroff, F., Fert, A., Martinez Boubeta, C., Costa-Krämer, J. L., Anguita, J. V., Cebollada, A., Briones, F., De Teresa, J., et al. *Appl. Phys. Lett.* **79**(11), 1655–1657 (2001).
[14] Ikeda, S., Hayakawa, J., Ashizawa, Y., Lee, Y., Miura, K., Hasegawa, H., Tsunoda, M., Matsukura, F., and Ohno, H. *Appl. Phys. Lett.* **93**(8), 082508 (2008).
[15] Gajek, M., Bibes, M., Barthélémy, A., Bouzehouane, K., Fusil, S., Varela, M., Fontcuberta, J., and Fert, A. *Phys. Rev. B* **72**(2), 020406 (2005).
[16] Lüders, U., Bibes, M., Bouzehouane, K., Jacquet, E., Contour, J.-P., Fusil, S., Bobo, J.-F., Fontcuberta, J., Barthélémy, A., and Fert, A. *Appl. Phys. Lett.* **88**(8), 082505 (2006).
[17] LeClair, P., Ha, J., Swagten, H., Kohlhepp, J., Van de Vin, C., and De Jonge, W. *Appl. Phys. Lett.* **80**(4), 625–627 (2002).

[18] Singh, M., Truong, K., Jandl, S., and Fournier, P. *J. Appl. Phys.* **107**(9), 09D917 (2010).
[19] Kitamura, M., Ohkubo, I., Kubota, M., Matsumoto, Y., Koinuma, H., and Oshima, M. *Appl. Phys. Lett.* **94**(13), 132506 (2009).
[20] Jönsson-Åkerman, B., Escudero, R., Leighton, C., Kim, S., Schuller, I. K., and Rabson, D. *Appl. Phys. Lett.* **77**(12), 1870–1872 (2000).
[21] Xia, H., Zhang, S., Li, H., Li, T., Liu, F., Zhang, W., Guo, W., Miao, T., Hu, W., Shen, J., et al. *Results Phys.* **22**, 103963 (2021).
[22] Guo, Y., Shi, L., Zhou, S., Zhao, J., and Liu, W. *Appl. Phys. Lett.* **102**(22), 222401 (2013).
[23] Galceran, R., Balcells, L., Pomar, A., Konstantinović, Z., Bagués, N., Sandiumenge, F., and Martínez, B. *AIP Advances* **6**(4), 045305 (2016).
[24] Tokura, Y. *Rep. Prog. Phys.* **69**(3), 797 (2006).
[25] Jo, M.-H., Mathur, N., Todd, N., and Blamire, M. *Phys. Rev. B* **61**(22), R14905 (2000).
[26] Ishii, Y., Yamada, H., Sato, H., Akoh, H., Ogawa, Y., Kawasaki, M., and Tokura, Y. *Appl. Phys. Lett.* **89**(4), 042509 (2006).
[27] Gauvin-Ndiaye, C., Baker, T., Karan, P., Massé, É., Balli, M., Brahiti, N., Eskandari, M., Fournier, P., Tremblay, A.-M., and Nourafkan, R. *Phys. Rev. B* **98**(12), 125132 (2018).
[28] Garcia, V., Bibes, M., Barthélémy, A., Bowen, M., Jacquet, E., Contour, J.-P., and Fert, A. *Phys. Rev. B* **69**(5), 052403 (2004).

Supplemental material

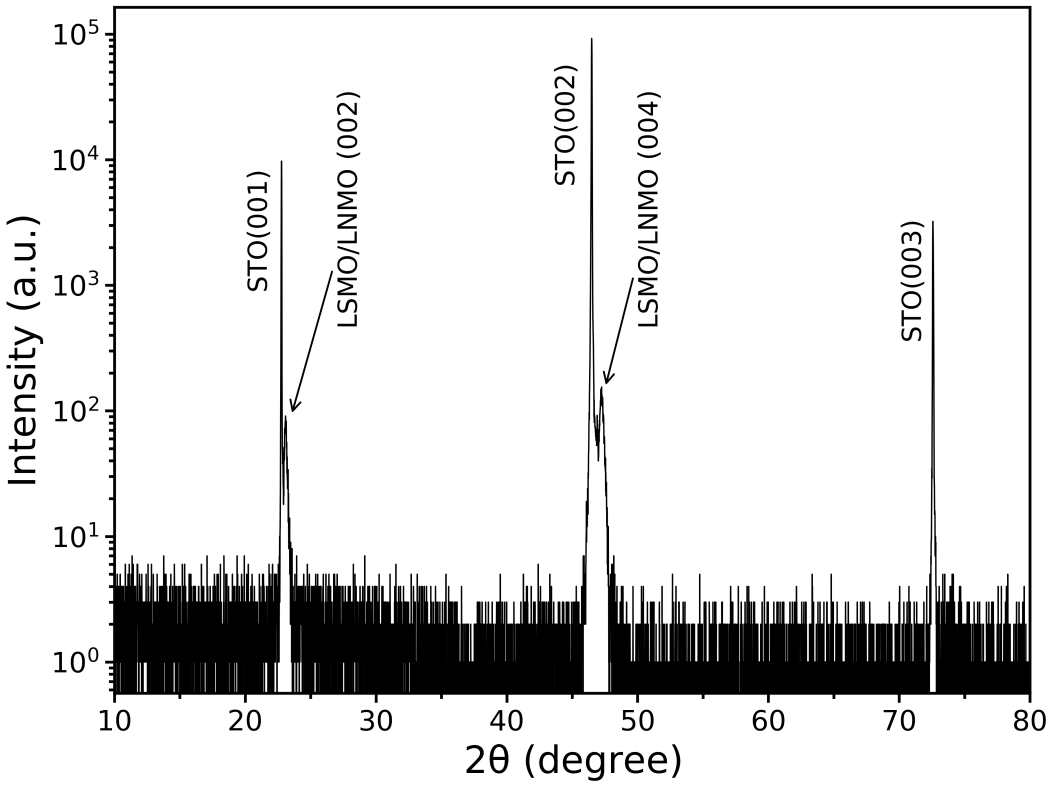

FIG. 9: X-ray diffraction pattern of a LSMO/LNMO/LSMO MTJ from 10° to 80°. All peaks are assigned to the substrate, LSMO and LNMO layers.

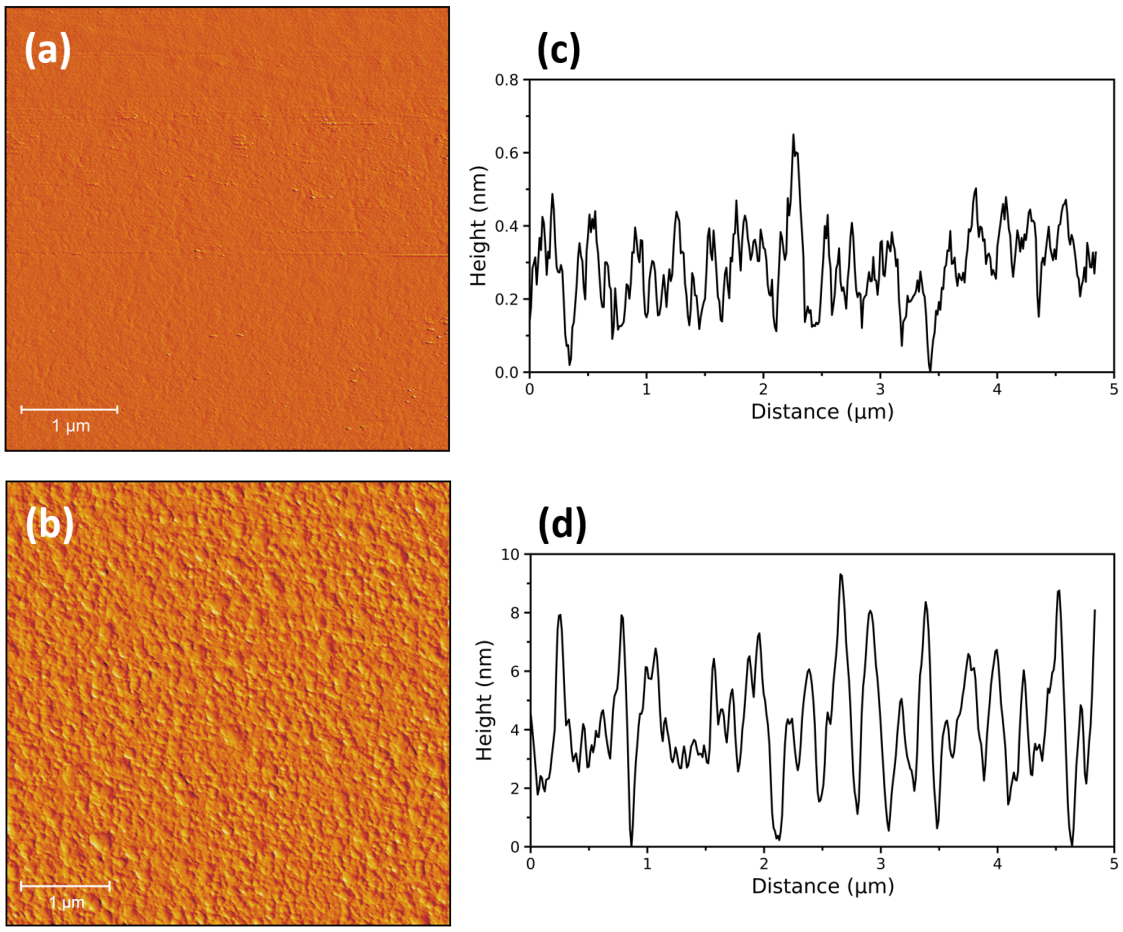

FIG. 10: AFM images of the surface of (a) the bottom LSMO layer before completing the device fabrication and (b) the top LSMO layer after completing the device. (c) and (d) Profile along a typical line indicating the surface roughness of each layer. The surface roughness extracted from the right panels using Gwyddion is less than 1 and 10 nm for the bottom and top LSMO, respectively, with no pinholes.

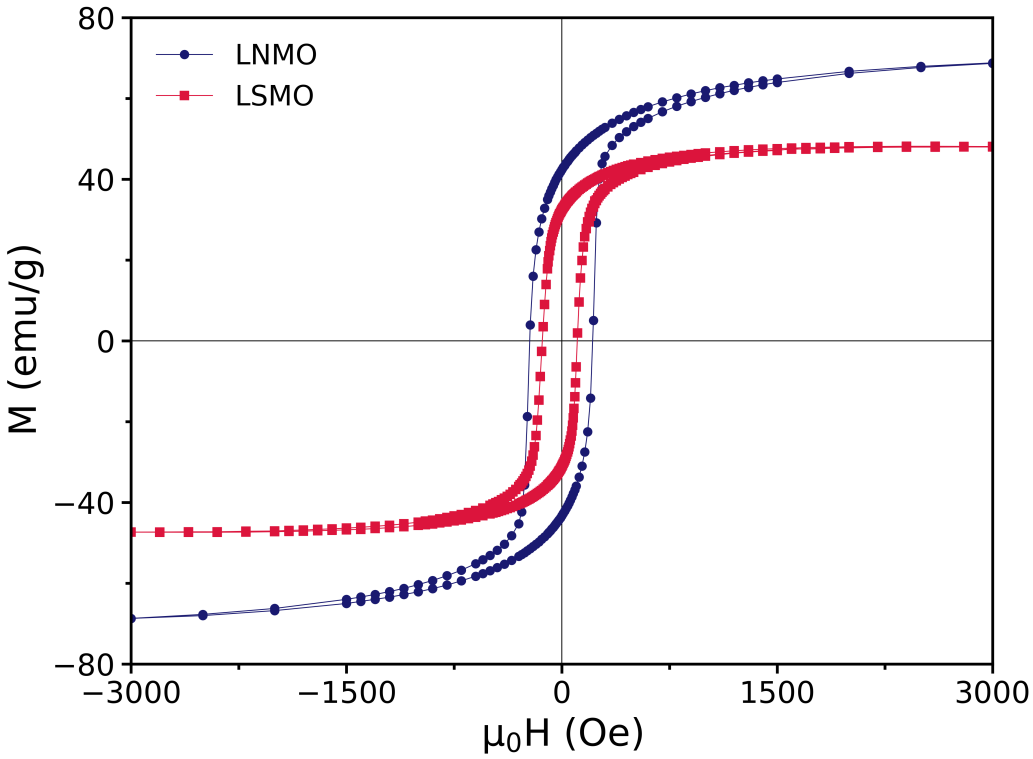

FIG. 11: Magnetic hysteresis loops of the LSMO and LNMO monolayers at 10 K. As noticed, the LSMO layer shows sharper polarization switches than the LNMO layer and a lower coercive field (H_c is ±140 Oe for LSMO and ±230 K for LNMO).

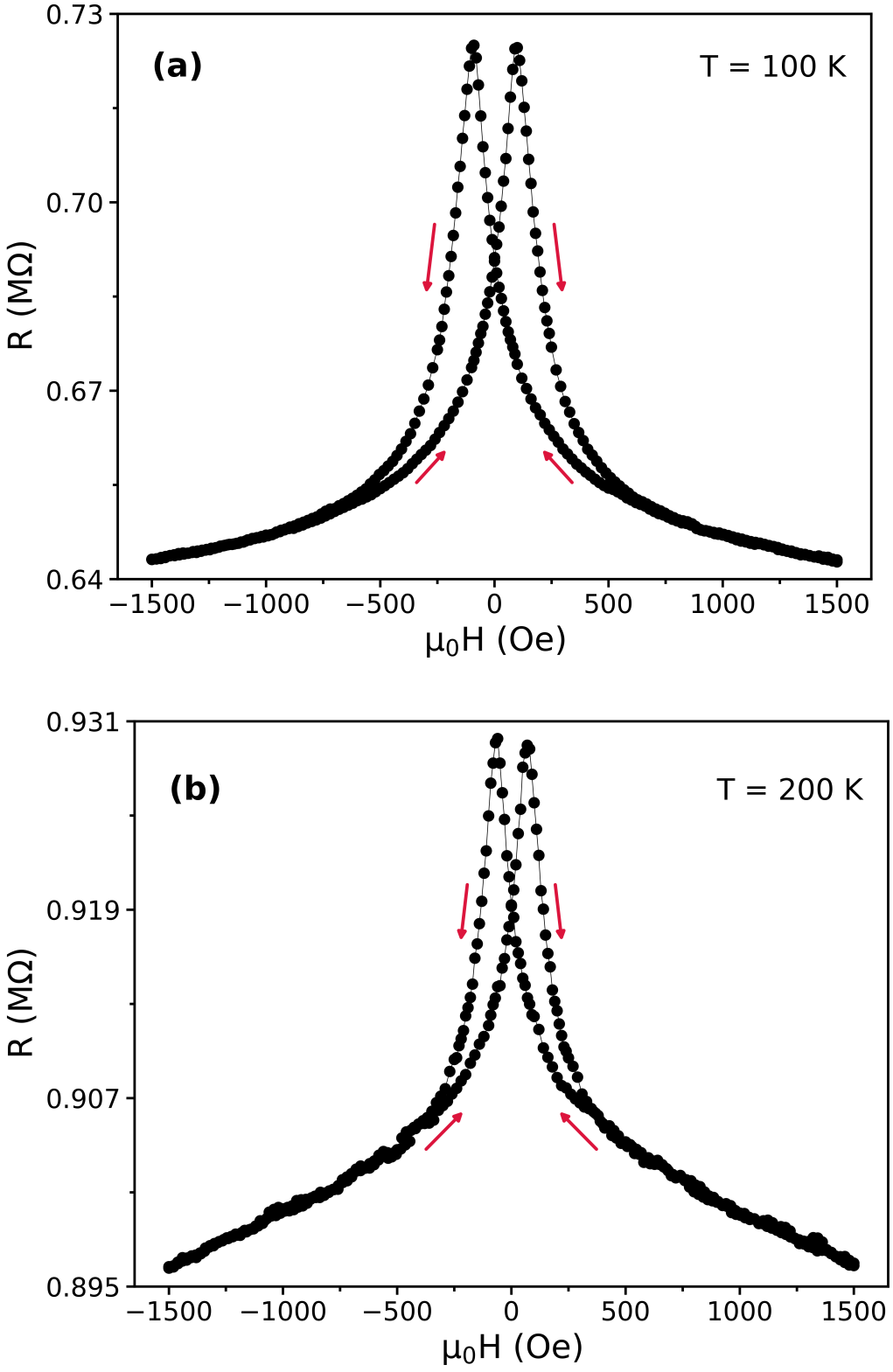

FIG. 12: Magnetic field dependence of the junction resistance at a) 100 K and b) 200 K.

3.3.3 Summary

To summarize, we have studied the impact of LNMO double perovskite as a ferromagnetic insulating barrier on the tunnel magnetoresistance (TMR) in magnetic tunnel junctions (MTJs). There is a gradual switching between the high and low resistance states indicating that the junction resistance is strongly correlated with the relative orientation of the magnetic moments in the LNMO with respect to those of the LSMO electrodes. In order to explain the conduction of the devices, a mechanism was proposed based on the empty and filled e_g states around the Fermi level in the LNMO barrier. In this mechanism, the conduction occurs via the electron and hole channels depending on the orientation of the magnetic moments in the electrodes and the barrier. The TMR reaches its maximum value of 24 % at 10 K and it decreases with temperature until it reaches zero at 280 K. The observation of the TMR above the apparent transition temperature of the LNMO barrier ($\sim$180 K) is ascribed to the presence of some magnetic domains with a high level of cationic ordering in LNMO. These magnetic domains which were not detected by the magnetization measurements can have a transition temperature up to 285 K, corresponding to the critical temperature of the MTJs. The presence of this minor phase keeps the TMR up to 280 K.

Chapter 4

Conclusion

In this thesis, we focused on oxide-based heterostructures and their potential in the field of magnetic cooling technology and spintronics. We have used La_2NiMnO_6 double perovskite with magnetic phase transitions at 170 and 285 K, and $La_{2/3}Sr_{1/3}MnO_3$ manganite with T_c at 370 K to fabricate bilayers and trilayers heterostructures meant to simulate the behaviors of composite materials. We have demonstrated that these multilayer samples present promising properties as magnetic refrigerants. The magnitude and the temperature span of their magnetic entropy change can be easily tuned and adjusted. We have also used these multilayers as magnetic tunnel junctions (MTJs) where LNMO acts as a magnetic barrier. It allowed us to measure the tunnel magnetoresistance through a magnetic insulating barrier for the first time. Moreover, these MTJs can act as a probe to detect different magnetic domains with different transition temperature in the barrier.

In the first part of the thesis, we aimed to tailor a large and almost temperature independent magnetic entropy change over a wide range of temperature using composite-like heterostructures. We exploited the sensitivity of cationic ordering to strain in LNMO to tune its magnetic properties. For this purpose, two series of bilayers with configurations of LSMO/LNMO and LNMO/LSMO as well as two series of trilayers with layouts of LSMO/LNMO/LSMO and LNMO/LSMO/LNMO were fabricated and compared. We observed that the level of cationic ordering in LNMO can be decreased by subjecting it to a larger epitaxial strain. It results in a

shift in T_c from 240 to 170 K when it is placed directly onto the substrate and on top of a LSMO layer, respectively. We were able to alternate between two magnetic phases in LNMO simply by switching the stacking order of the layers. In order to take advantage of this feature, trilayers of LNMO/LSMO/LNMO were fabricated in which both LNMO magnetic phases coexist. Magnetic entropy measurements indicated that all four types of samples show a large magnetic entropy change over a wide temperature range, as wide as 260 K, covering room temperature. The maximum value of $-\Delta S_m$ was calculated to be around 1.80 J kg^{-1} K^{-1} and 2.20 J kg^{-1} K^{-1} for bilayer and trilayer samples, under a magnetic field change of 7 T, respectively. Furthermore, a fairly flat and table-top-like magnetic entropy change was observed in both trilayer samples in a temperature span of $\Delta T = 100$ K, starting at 175 K. This temperature independent entropy change over a wide temperature window makes these two trilayer samples suitable candidates for active magnetic regenerator (AMR) refrigeration. Furthermore, all multilayer samples show a pretty large refrigerant capacity with a linear magnetic field dependence. For instance, trilayers of LNMO/LSMO/LNMO exhibit the largest refrigerant capacity among multilayers, where it reaches a maximum value of 335 J kg^{-1} for $\Delta H = 5$ T which is 82 % of Gd, the reference material. The $\mathcal{RC}$ values in our samples are also comparable to other families with giant MCE such as $La(Fe,Si)_{13}$ and $Gd_5(SiGe)_4$. It should be emphasized that the materials with giant MCE usually operate below or in some cases close to room temperature, whereas the MCE in our composite-like multilayers goes beyond room temperature, up to 370 K.

In the second part of the thesis, we have used the LSMO/LNMO/LSMO trilayer samples to study the tunnel magnetoresistance in magnetic tunnel junctions in which LNMO behaves as a ferromagnetic insulating barrier. We demonstrated that the tunneling occurs through the LNMO barrier via a spin selective process. In this mechanism, the conduction takes place through two separate spin-polarized conduction bands above the Fermi level in LNMO. The tunneling depends not only on the relative orientation of the magnetic moments in two FM LSMO electrodes as in conventional MTJs, but also on the magnetization direction of the LNMO barrier with respect to those of LSMO electrodes. In contrast to typical MTJs with a sharp switching between two resistance states, the gradual switching between the

low and high resistance states in our device is driven by the magnetization direction in the LNMO barrier. The junction shows a maximum TMR ratio of 24 % at 10 K, which decreases with temperature until it completely disappears above a critical temperature at 280 K. This critical temperature of our junctions corresponds to the magnetic phase transition of cation-ordered LNMO. It is also observed that the TMR becomes small and noisy above 180 K which corresponds to the T_c of cation-disordered phase in LNMO. According to the results obtained from the TMR and magnetization measurements, it is concluded that the dominant magnetic phase in LNMO barrier is cation-disordered phase with a T_c at 180 K, however cation-ordered phase exists in a small fraction of the sample with a transition temperature at 280 K. This phase is hardly observed by magnetization but reveals itself through tunneling which becomes a sensitive probe of the magnetic properties of the barrier. The absence of tunneling above the critical temperature of LNMO indicates that the tunneling process through the LNMO barrier depends on the magnetic order in it. The results demonstrate an improvement over spin-filter junctions containing magnetic insulating barrier towards room temperature magnetoresistance. Also, the presence of some domains with a higher magnetic transition in LNMO layer could explain the wide magnetic entropy change we have seen in the heterostructures. It indicates that despite their small proportion, they can still play a role in the magnetic properties of the samples.

Appendix A

MCE in monolayers

A.1 $La_{2/3}Sr_{1/3}MnO_3$ monolayer

The monolayers of LSMO were grown on LSAT substrates using the PLD technique under the conditions explained in section 2.2.1.4. A high-resolution X-ray diffractometer has been employed to characterize the structural properties of the samples. Figure A.1 (a) shows the $2\theta/\omega$ XRD pattern of a LSMO thin film in the range from 10° to 80°. A single set of LSMO diffraction peaks along with peaks from the substrate are observed, revealing the epitaxial growth and the absence of any secondary phases. In addition, a higher resolution measurement with the step of 0.001° was performed around the (002) peak from the substrate (Figure A.1 (b)). Laue oscillations can be seen on both sides of the LSMO diffraction peak indicating the good film crystallinity with a uniform thickness and smooth interfaces. Moreover, Laue oscillations can be used to estimate the thickness of epitaxial film using the following equation:

$$t = \frac{\lambda(i-j)}{2\left(\sin\theta_i - \sin\theta_j\right)} \tag{A.1}$$

where θ_i and θ_j represent the positions of the i^{th} and j^{th} peaks, and λ is the wavelength of the X-rays. The thickness of LSMO layer was calculated to be around 25–30 nm for 5000 laser shots, leading to a deposition rate of 0.05 to 0.06 Å/shot.

The temperature dependence of the field-cooled (FC) magnetization of the

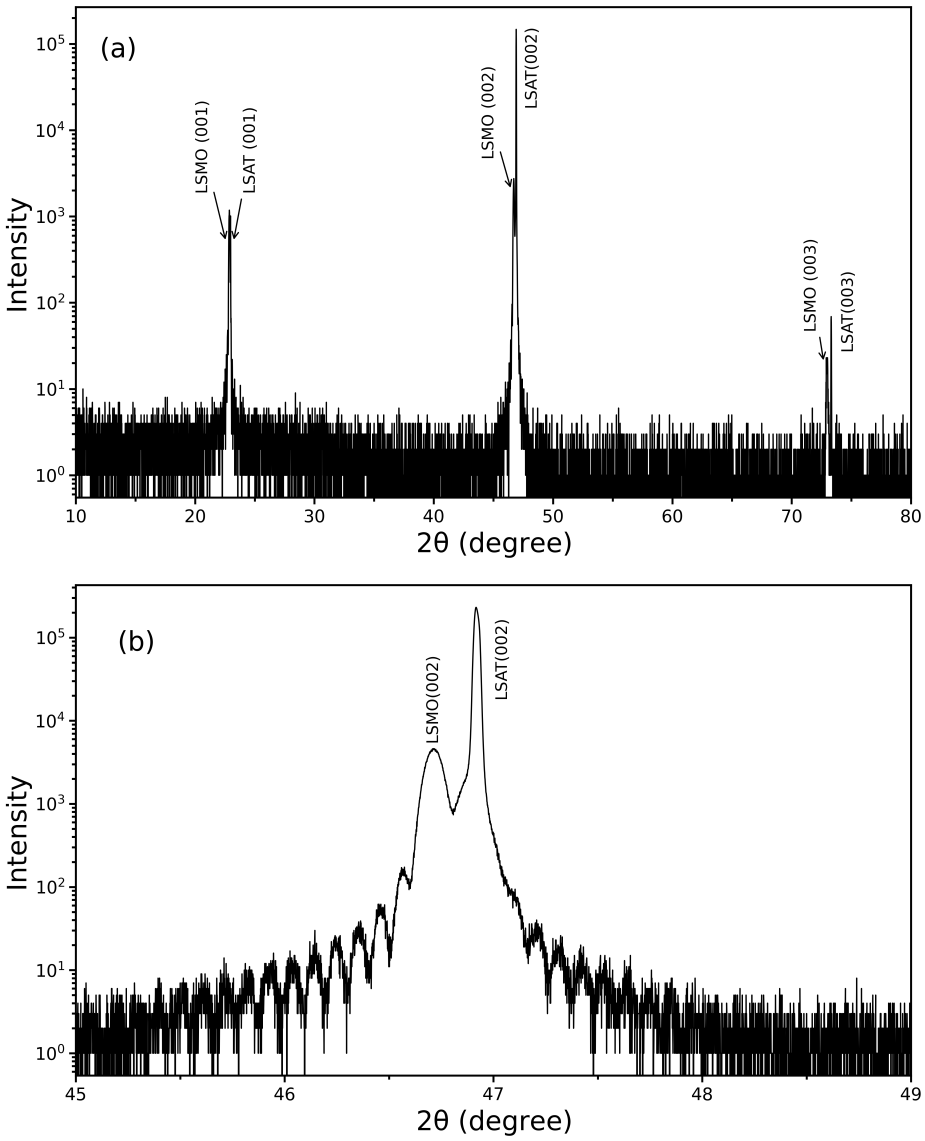

Figure A.1: (a) Full-scale X-ray diffraction pattern of LSMO layer deposited on a LSAT (001) substrate. (b) Data around the (002) peak from the substrate with higher resolution showing the Laue oscillations.

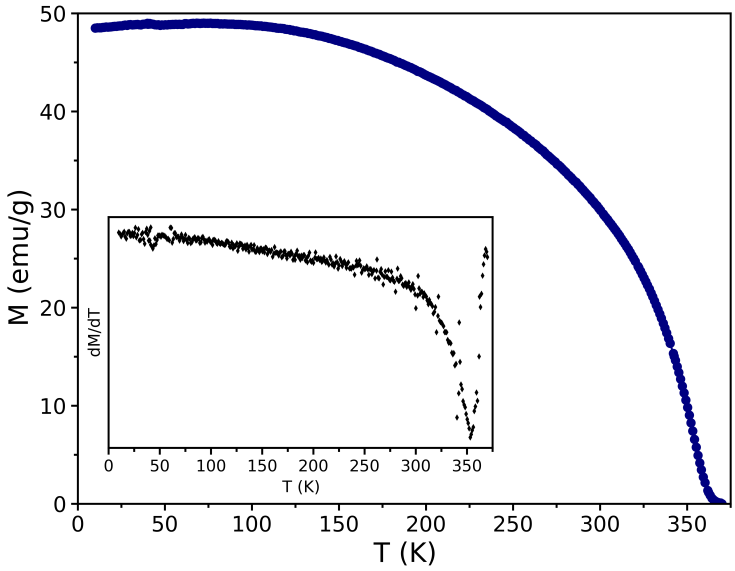

Figure A.2: FC magnetization as a function of temperature under a magnetic field of 200 Oe for the LSMO thin film. The inset shows the derivative of the magnetization with respect to the temperature.

LSMO thin film at a fixed magnetic field of 200 Oe applied parallel to the surface of the sample is displayed in Figure A.2. The sample undergoes a paramagnetic to ferromagnetic transition at 358 K which is very close to the maximum $T_c \sim 370$ K ever reported for this material [17, 159]. The transition temperature is defined where the dM/dT vs. temperature reaches its minimum. The derivative of the magnetization is shown in the inset of Figure A.2.

The measurements of magnetic hysteresis loops with a magnetic field applied parallel to the surface of the film were performed at 10 and 300 K. As displayed in Figure A.3, the magnetization saturates very rapidly at low magnetic fields and reaches its maximum value of 2.87 μ_B/Mn and 1.89 μ_B/Mn, at 10 K and 300 K, respectively. These values are in close agreement with the other reported values for LSMO [160]. The low-temperature saturation magnetization M_s approaches the maximum theoretical value of 3.67 μ_B/Mn expected for fully aligned spins in LSMO at low temperature. Furthermore, the coercive field decreases from 140 to 20 Oe by increasing the temperature from 10 to 300 K.

The isothermal magnetization was measured under an applied magnetic field up to 7 T in the temperature range from 200 to 370 K with a temperature interval

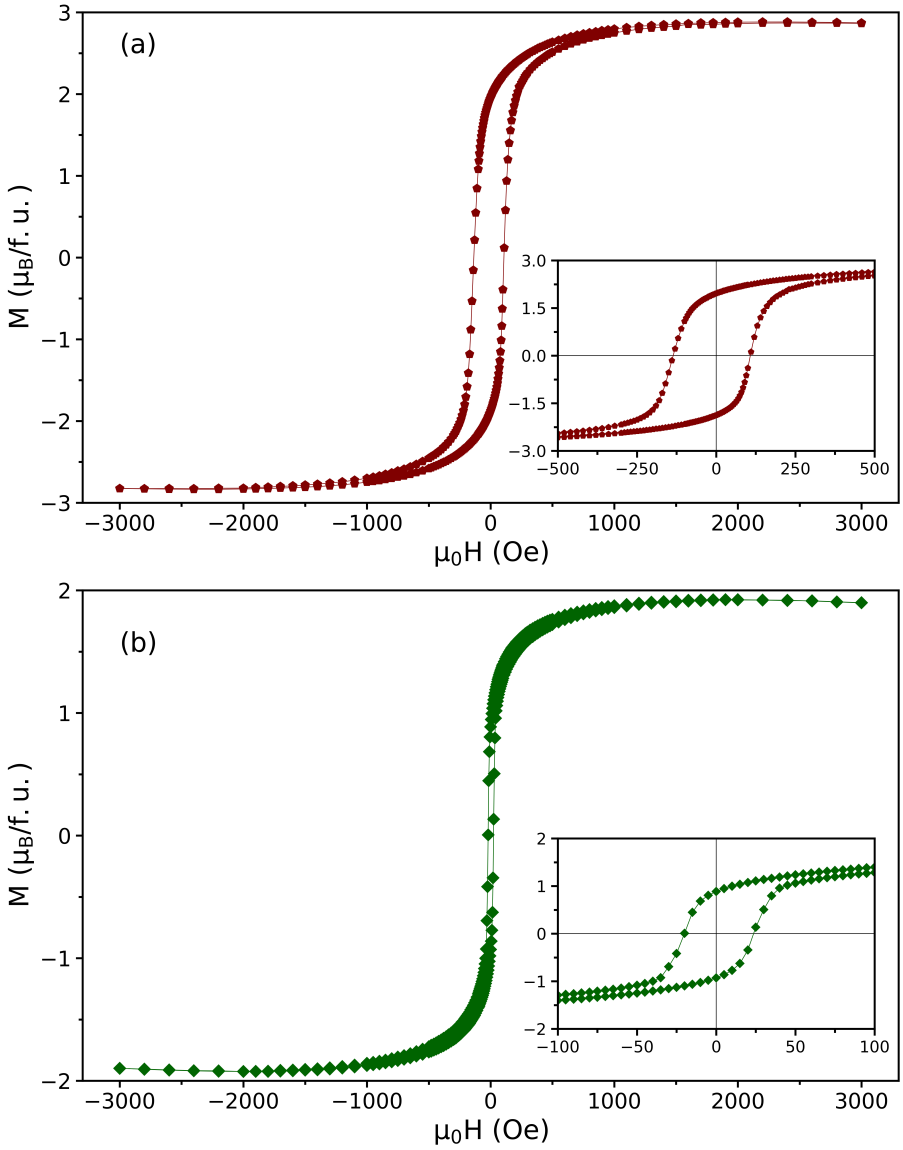

Figure A.3: Magnetic hysteresis loops of the LSMO thin film with in-plane applied magnetic field at (a) 10 K and (b) 300 K. Insets show the enlarged magnetic hysteresis loops at low magnetic fields.

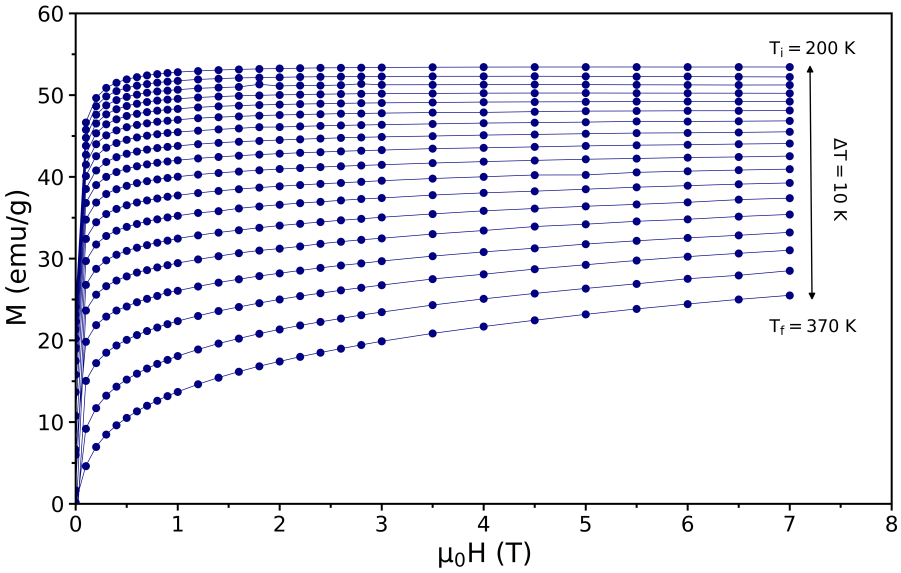

Figure A.4: Isothermal magnetization curves of the LSMO thin film up to a magnetic field of 7 T in the temperature range from 200 to 370 K with a temperature interval of 10 K.

of 10 K (Figure A.4). It should be noted that all the magnetic isotherms showed a negative background at high magnetic field arising from the diamagnetic contribution of the sample holder and the substrate. The magnetization of the layer can be observed after removing this background. These magnetic isotherms were used to calculate the Arrott plots and the isothermal magnetic entropy change (ΔS_m).

The nature of a magnetic phase transition can be explored using the Arrott plots. Based on Banerjee's criterion, the positive or negative slope of Arrott plots indicates weather the magnetic phase transition is second or first order, respectively. The Arrott plots of the LSMO thin film in the temperature range of 200–370 K are displayed in Figure A.5. As it can be clearly seen, all the curves have positive slope in the entire temperature range indicating the existence of a second-order magnetic transition in the LSMO sample. Moreover, the transition temperature can be extracted from the Arrott plots using the mean field theory [161]. It has been shown that, near the transition temperature, the Arrott plot curve becomes a straight line passing through the origin. Using this method, it is estimated that the transition temperature of LSMO layer would be around 370 K which is in close agreement with the M(T) measurements in Fig. A.2.

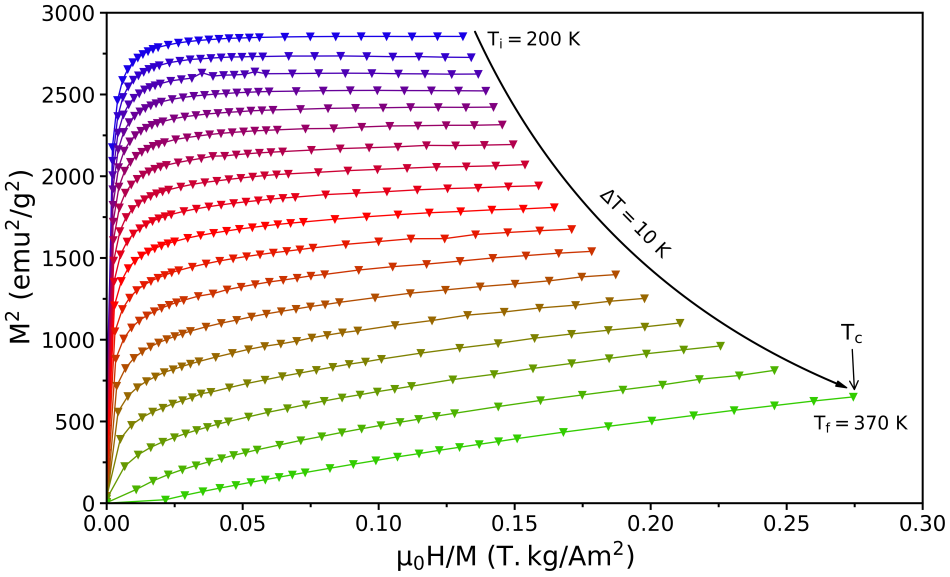

Figure A.5: The Arrott plots of LSMO thin film in the temperature range between 200 to 370 K. The transition temperature is determined to be at 370 K using the mean field theory based on Banerjee's criterion.

The isothermal magnetic entropy change (ΔS_m) is calculated from the isothermal magnetization measurements using the Maxwell relation (Eq. 2.12). The temperature dependence of ΔS_m under various applied magnetic field changes up to 7 T is illustrated in Figure A.6. As expected, the maximum of ΔS_m occurs around the FM-PM transition where dM/dT is maximum, and it also strongly depends on the magnitude of the applied magnetic field. ΔS_m reaches a maximum value of 0.87, 1.58 and 2.50 J kg^{-1} K^{-1}, for the magnetic field changes of 0–2 T, 0–5 T, and 0–7 T, respectively. Due to the instrumental limitations, we were not able to cover the entire ΔS_m peak. So, we could not extract additional information such as the relative cooling power or the refrigerant capacity.

Our findings are in close agreement with the results previously reported on LSMO thin films [11, 102]. For instance, Kumar *et al* have reported that the LSMO thin films grown on LSAT substrates show a maximum magnetic entropy change of 1.47 J kg^{-1} K^{-1} for $\mu_0 \Delta H = 1.5$ T around their transition at 321 K [11]. On the other hand, a higher transition temperature was reported for LSMO films on $LaAlO_3$ substrates where the T_c reaches 350 K, while ΔS_m drops to 1.65 J kg^{-1} K^{-1} for $\mu_0 \Delta H$ =5 T [102]. In comparison to these results, our samples show an im-

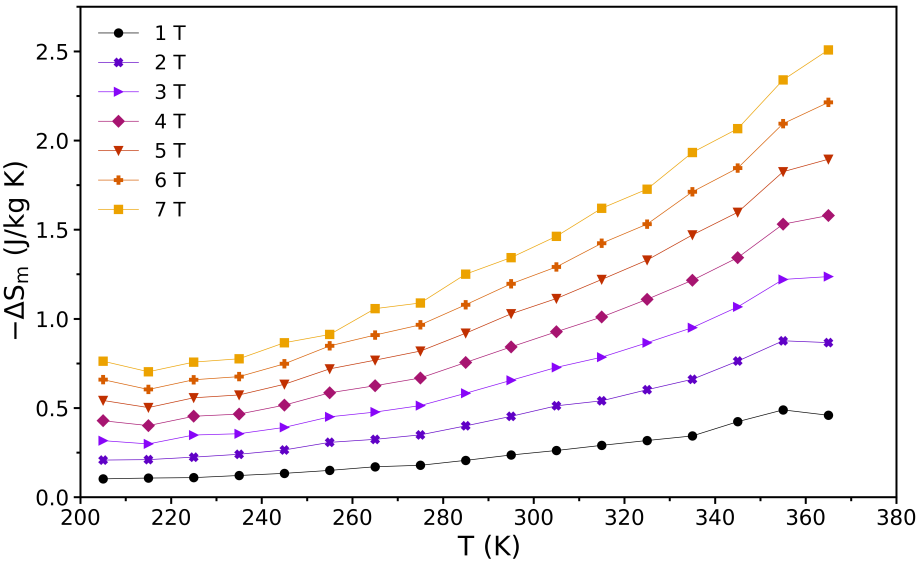

Figure A.6: Isothermal magnetic entropy change as a function of temperature in various magnetic fields for LSMO thin film.

provement in the T_c while ΔS_m still remain relatively large.

A.2 La_2NiMnO_6 monolayer

La_2NiMnO_6 (LNMO) double perovskite has been considered as an interesting candidate for magnetic cooling systems below room temperature due to its ferromagnetic insulating nature as well as the potential presence of multiple magnetic phase transitions. In this work, monolayers of LNMO were grown using the PLD technique on (001)-oriented LSAT substrates. The structural, magnetic and magnetocaloric properties of LNMO thin films have been investigated and the results are presented in this section.

The X-ray diffraction pattern of LNMO layer on a LSAT substrate is shown in Figure A.7 (a). The $\theta - 2\theta$ pattern from 10° to 80° reveals the diffraction peaks from the LNMO layer and the LSAT substrate indicating the epitaxial growth of LNMO layer with no trace of impurity. Moreover, the thickness of the film was estimated to be 25–30 nm for 5000 laser shots very similar to LSMO, using the thickness fringes around the (002) peak of LNMO (Figure A.7 (b)).

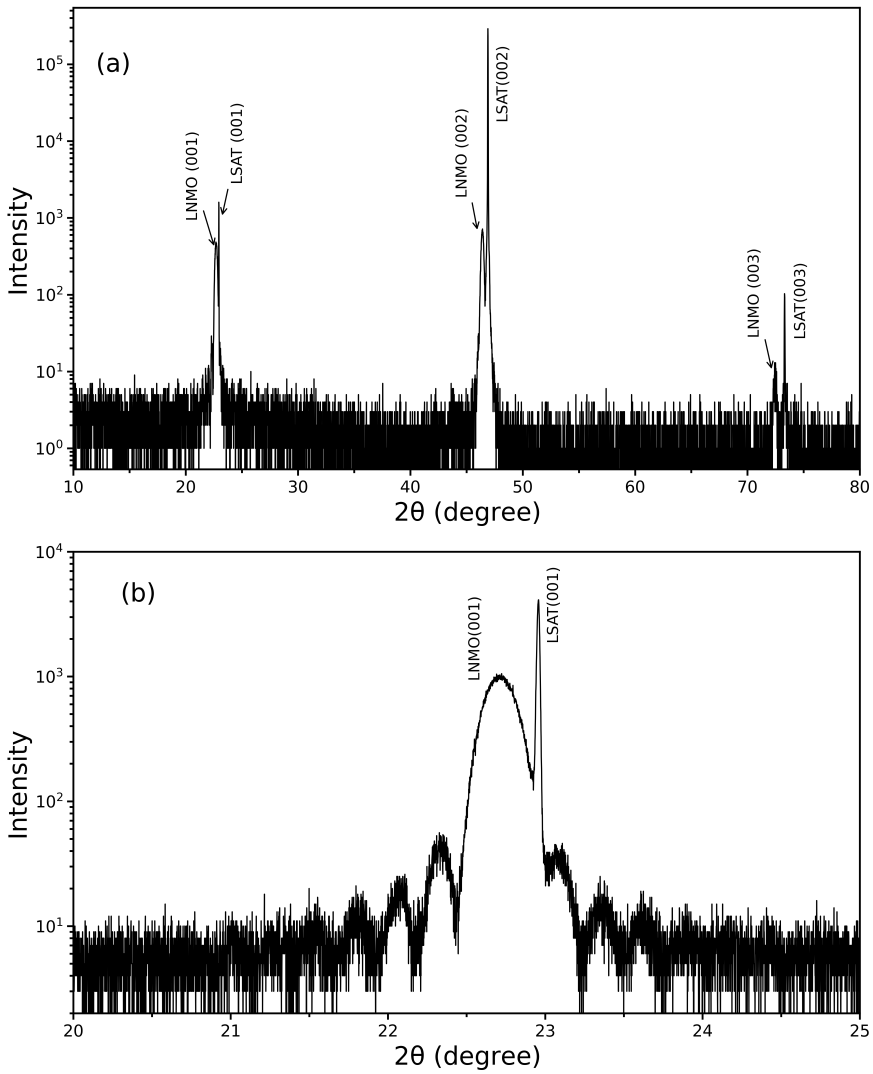

Figure A.7: (a) XRD $\theta - 2\theta$ scan of the LNMO film grown on LSAT (001) substrate. (b) Enlarged view of the LNMO (001) diffraction peak.

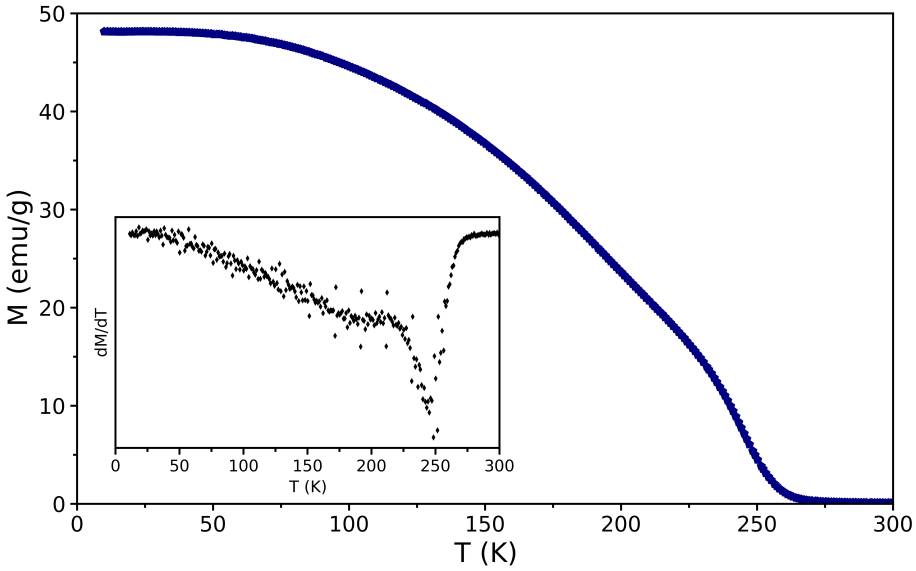

Figure A.8: Magnetization as a function of temperature of LNMO monolayer under an applied magnetic field of 200 Oe. The inset shows the derivative of the magnetization with respect to the temperature.

Figure A.8 shows the temperature dependence of the FC magnetization in a fixed magnetic field of 200 Oe applied parallel to the surface of the film. A magnetic transition from ferromagnetic to paramagnetic state is observed at 250 K which was defined from the derivative of the magnetization with respect to the temperature (inset of Figure A.8). The transition temperature of this LNMO layer is close to the maximum possible T_c (285 K) for this double perovskite. Relatively high transition temperature indicates the presence of long-range cation ordering in LNMO where Mn^{4+} and Ni^{2+} cations alternatively occupy the B and B′ sites, leading to the formation of ferromagnetic $Mn^{4+}-O-Ni^{2+}$ bonds. Moreover, its M(T) curve shows a small anomaly at 175 K indicating the presence of secondary phase in the sample. It corresponds to the cation-disordered phase which contains only a small portion of the sample. In regions with the cation-disordered phase, antiferromagnetic interactions between $Mn^{4+}-O-Mn^{4+}$ and $Ni^{2+}-O-Ni^{2+}$ are contributing, resulting in a lower transition at 175 K.

One of the biggest advantages of LNMO double perovskites which makes them an interesting candidate for magnetic cooling systems is their low magnetic and thermal hysteresis. In order to demonstrate that, magnetization as a function of

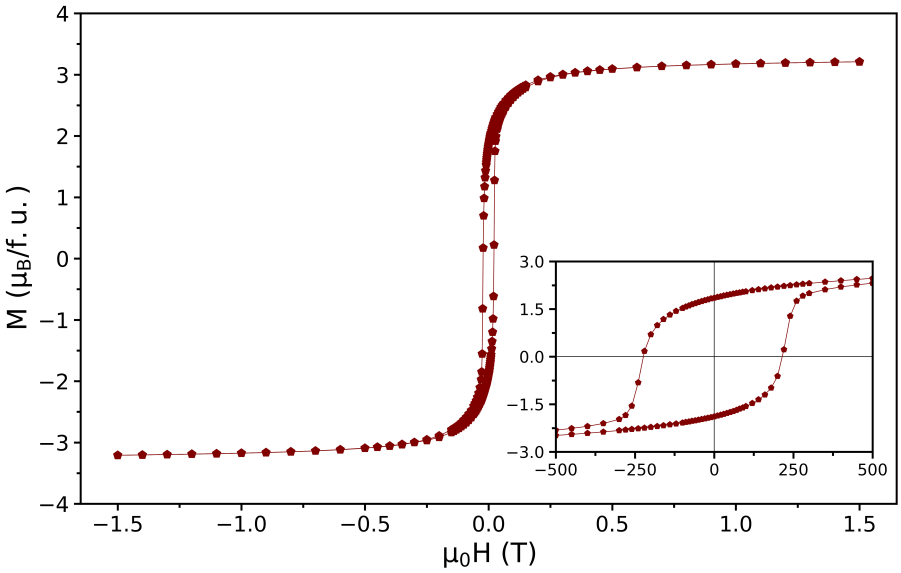

Figure A.9: Magnetic hysteresis loop of the LNMO layer at 10 K. Inset represents the enlarged view of M(H) at low magnetic fields.

magnetic field was measured in increasing and decreasing magnetic field between −1.5 to 1.5 T at 10 K. As depicted in Figure A.9, LNMO layer saturates at a low magnetic field of 500 Oe and reaches a maximum value of 3.20 μ_B/f.u. which is lower than the maximum theoretical value of 5 μ_B/f.u. predicted for fully ordered LNMO [73]. The lower saturation magnetization can be attributed to the partial formation of the disordered phase in the sample. The coercive field H_c was determined to be 220 Oe at 10 K which is considerably low compared to other magnetocaloric materials with giant MCE such as intermetallic alloys [162].

The measurement of magnetic isotherms was performed in the temperature range from 100 to 300 K with a temperature interval of 10 K up to 7 T to determine the Arrott plots and also to calculate the isothermal magnetic entropy change (Figure A.10). As displayed in Figure A.11, all curves have positive slope in the entire temperature range indicating the presence of a second-order magnetic transition in the sample. Moreover, the T_c was determined to be at 270 K using the mean-field theory which is consistent with the results obtained from the M(T) measurements.

Figure A.12 displays the isothermal magnetic entropy change of the LNMO sample in various applied magnetic field changes. ΔS_m remains negative in the entire temperature range and shows a peak at the T_c where dM/dT is maximum.

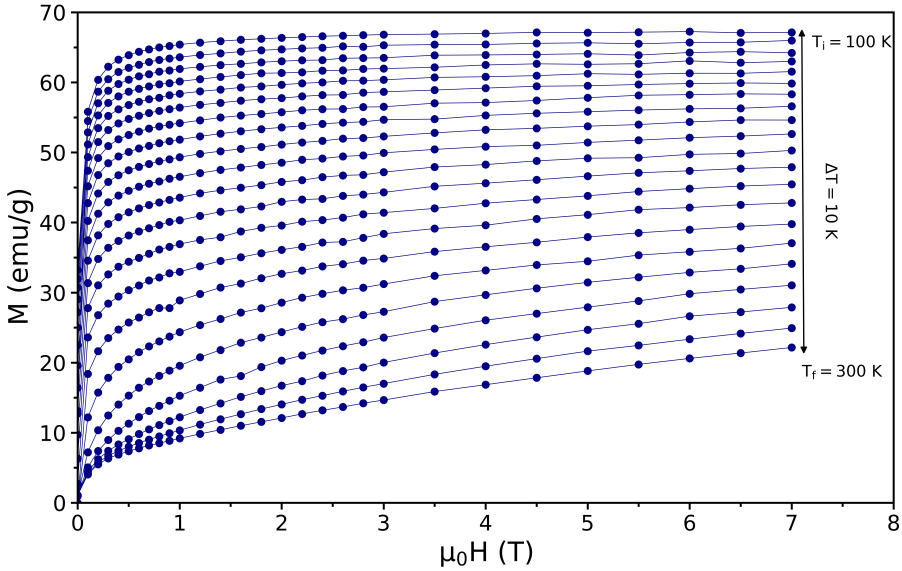

Figure A.10: Isothermal magnetization of the La_2NiMnO_6 layer in the temperature range from 100 to 300 K up to 7 T with a temperature interval of 10 K.

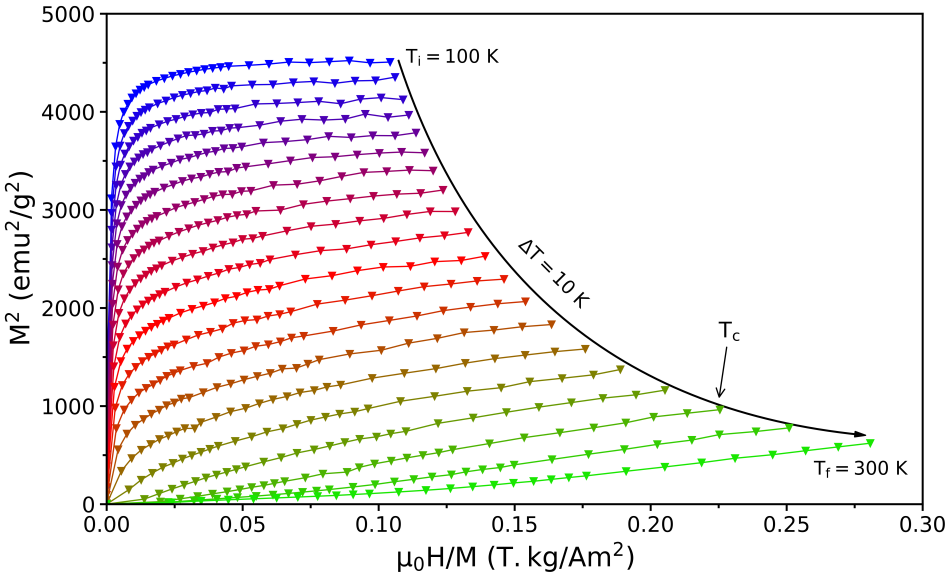

Figure A.11: The Arrott plots of the LNMO thin film calculated from the isothermal magnetization measurements.

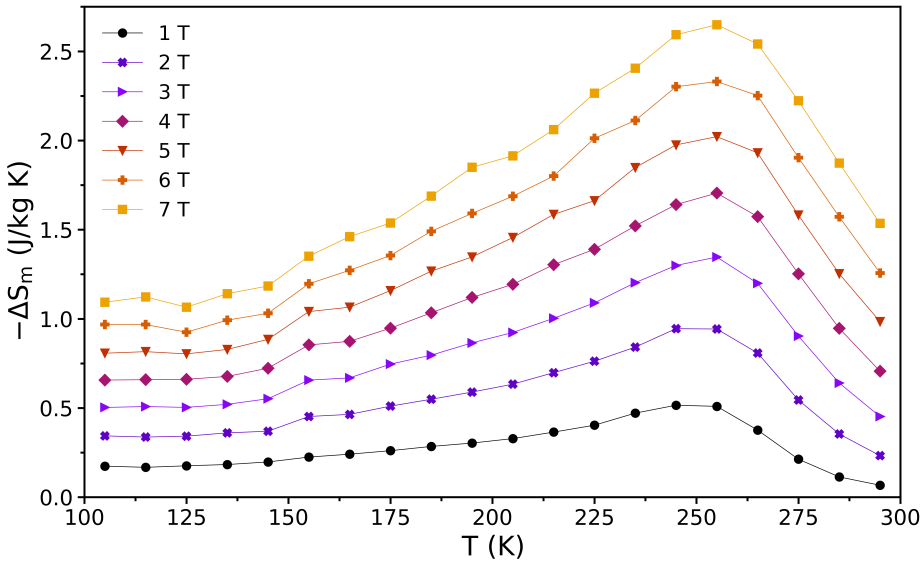

Figure A.12: Temperature dependence of the isothermal magnetic entropy change of the La_2NiMnO_6 double perovskite thin film under different magnetic field changes.

ΔS_m reaches a maximum value of 0.95, 2.03 and 2.65 J kg^{-1} K^{-1} for $\mu_0\Delta H = 2, 5$ and 7 T, respectively. These values closely match with the results reported by Matte *et al* [7] for LNMO thin films where ΔS_m reaches a maximum value of 2 J kg^{-1} K^{-1} for $\mu_0\Delta H = 7$ T. Moreover, it should be noted that the position of the ΔS_m peak does not change much with the magnetic field while the width increases which is a signature of SOMT materials.

Refrigerant capacity ($\mathcal{RC}$) was calculated as another evaluation tool to compare the efficiency of our sample to other magnetocaloric materials. As discussed in section 2.1.5, it takes into account both the magnitude of entropy change and the full-width at half-maximum (δT_{FWHM}) known as the operating temperature range. δT_{FWHM} and $\mathcal{RC}$ were found to be 114, 139 and 151 K and 80.30, 211.87 and 290.68 J kg^{-1} for $\Delta H = 2, 5$ and 7 T, respectively. The monolayer of LNMO exhibits an interesting level of refrigerant capacity reaching about 85 % of that presented by the materials with giant MCE such as $Gd_5Si_2Ge_2$ under the same variation of the magnetic field ($\Delta H = 5$ T).

Appendix B

Magnetization data of LSMO/LNMO/LSMO MTJs

In this section, we display the additional measurements that we have performed on the magnetic tunnel junction devices. Figure B.1 shows the magnetic hysteresis loops measured at different temperatures to determine the coercive field of the devices and compare them to the switching field determined by the R(H) measurements.

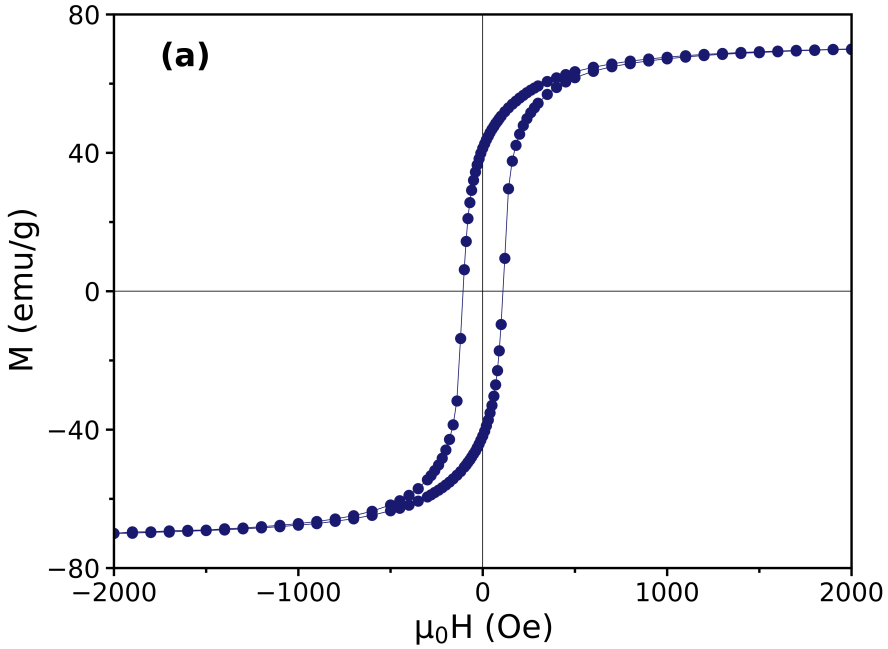
(a)
M (emu/g)
μ0H (Oe)
80
40
0
−40
−80
−2000
−1000
0
1000
2000

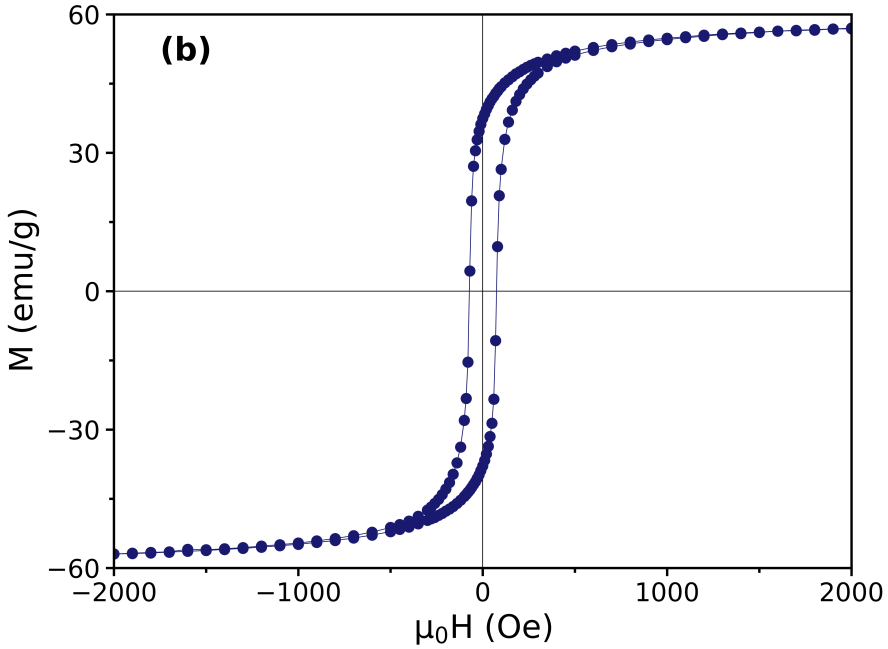
(b)
M (emu/g)
μ0H (Oe)
60
30
0
−30
−60
−2000
−1000
0
1000
2000

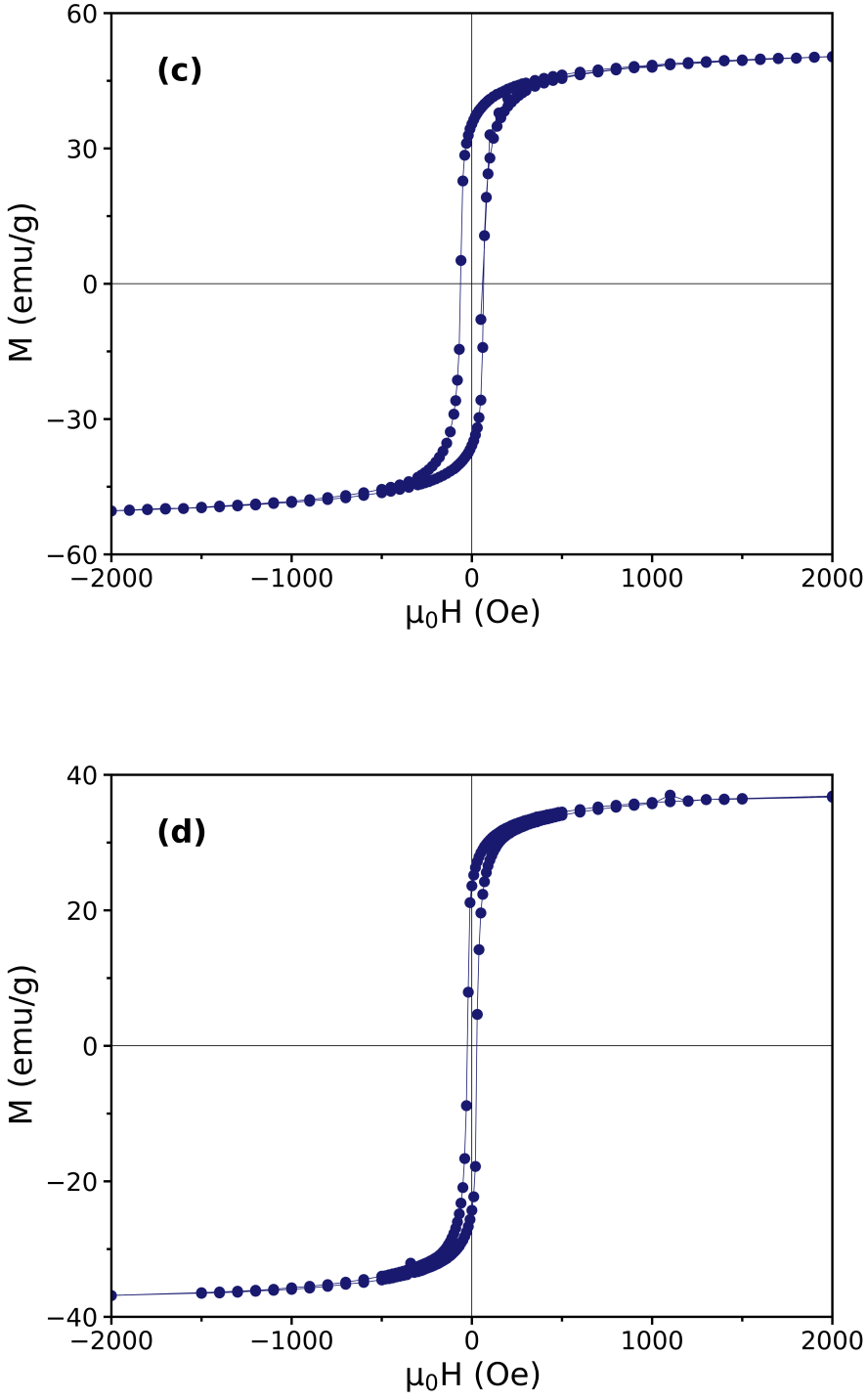

Figure B.1: Magnetic hysteresis loop for a LSMO/LNMO/LSMO MTJ device at (a) 100 K, (b) 175 K, (c) 200 K and (d) 270 K.

Bibliography

1. Tokura, Y. & Tomioka, Y. Colossal magnetoresistive manganites. *J. Magn. Magn. Mater.* **200,** 1–23 (1999).
2. Phan, M.-H. & Yu, S.-C. Review of the magnetocaloric effect in manganite materials. *J. Magn. Magn. Mater.* **308,** 325–340 (2007).
3. Park, S., Hur, N., Guha, S. & Cheong, S.-W. Percolative conduction in the half-metallic-ferromagnetic and ferroelectric mixture of $(La, Lu, Sr)MnO_3$. *Phys. Rev. Lett.* **92,** 167206 (2004).
4. Majumdar, S. & van Dijken, S. Pulsed laser deposition of $La_{1-x}Sr_xMnO_3$: thin-film properties and spintronic applications. *J. Phys. D: Appl. Phys.* **47,** 034010 (2013).
5. Singh, M., Truong, K., Jandl, S. & Fournier, P. Multiferroic double perovskites: Opportunities, issues, and challenges. *J. Appl. Phys.* **107,** 09D917 (2010).
6. King, G. & Woodward, P. M. Cation ordering in perovskites. *J. Mater. Chem.* **20,** 5785–5796 (2010).
7. Matte, D., de Lafontaine, M., Ouellet, A., Balli, M. & Fournier, P. Tailoring the magnetocaloric effect in La_2NiMnO_6 thin films. *Phys. Rev. Applied* **9,** 054042 (2018).
8. Brahiti, N. *et al.* Analysis of the magnetic and magnetocaloric properties of $ALaFeMnO_6$ (A= Sr, Ba, and Ca) double perovskites. *J. Appl. Phys.* **127,** 113905 (2020).
9. Zhang, Y. *et al.* Tunable magnetocaloric effect near room temperature in $La_{0.7-x}Pr_xSr_{0.3}MnO_3$ ($0.02 \leq x \leq 0.30$) manganites. *J. Appl. Phys.* **111,** 063918 (2012).

10. Wu, S.-Q. *et al.* B-site ordering and strain-induced phase transition in double-perovskite La_2NiMnO_6 films. *Sci. Rep.* **8,** 1–9 (2018).

11. Kumar, V. S., Chukka, R., Chen, Z., Yang, P. & Chen, L. Strain dependent magnetocaloric effect in $La_{0.67}Sr_{0.33}MnO_3$ thin-films. *Aip Advances* **3,** 052127 (2013).

12. European Commission Energy Efficiency, B. `http://ec.europa.eu/energy/en/topics/energy-efficiency/buildings`.

13. Balli, M., Jandl, S., Fournier, P. & Kedous-Lebouc, A. Advanced materials for magnetic cooling: Fundamentals and practical aspects. *Appl. Phys. Rev.* **4,** 021305 (2017).

14. Pecharsky, V. K. & Gschneidner Jr, K. A. Giant magnetocaloric effect in $Gd_5(Si_2Ge_2)$. *Phys. Rev. Lett.* **78,** 4494 (1997).

15. Fujieda, S., Fujita, A. & Fukamichi, K. Large magnetocaloric effect in $La(Fe_xSi_{1-x})_{13}$ itinerant-electron metamagnetic compounds. *Appl. Phys. Lett.* **81,** 1276–1278 (2002).

16. Sharma, V. *et al.* Magnetocaloric effect in Heusler alloys $Ni_{50}Mn_{34}In_{16}$ and $Ni_{50}Mn_{34}Sn_{16}$. *J. Phys.: Condens. Matter* **19,** 496207 (2007).

17. Rostamnejadi, A., Venkatesan, M., Kameli, P., Salamati, H. & Coey, J. Magnetocaloric effect in $La_{0.67}Sr_{0.33}MnO_3$ manganite above room temperature. *J. Magn. Magn. Mater.* **323,** 2214–2218 (2011).

18. Balli, M., Fournier, P., Jandl, S. & Gospodinov, M. A study of the phase transition and magnetocaloric effect in multiferroic La_2MnNiO_6 single crystals. *J. Appl. Phys.* **115,** 173904 (2014).

19. Rebello, A., Naik, V. & Mahendiran, R. Large reversible magnetocaloric effect in $La_{0.7-x}Pr_xCa_{0.3}MnO_3$. *J. Appl. Phys.* **110,** 013906 (2011).

20. Zhang, Y. *et al.* Excellent magnetocaloric properties in RE_2Cu_2Cd (RE= Dy and Tm) compounds and its composite materials. *Sci. Rep.* **6,** 1–9 (2016).

21. Tian, H., Zhong, X., Liu, Z., Zheng, Z. & Min, J. Achieving table-like magnetocaloric effect and large refrigerant capacity around room temperature in $Fe_{78-x}Ce_xSi_4Nb_5B_{12}Cu_1$ ($x = 0 - -10$) composite materials. *Mater. Lett.* **138,** 64–66 (2015).

22. Zhong, X. *et al.* Table-like magnetocaloric effect and large refrigerant capacity in $Gd_{65}Mn_{25}Si_{10}$ – Gd composite materials for near room temperature refrigeration. *Mater. Today Commun.* **14,** 22–26 (2018).

23. Wolf, S. *et al.* Spintronics: a spin-based electronics vision for the future. *Science* **294,** 1488–1495 (2001).

24. Bratkovsky, A. Spintronic effects in metallic, semiconductor, metal–oxide and metal–semiconductor heterostructures. *Rep. Prog. Phys.* **71,** 026502 (2008).

25. Julliere, M. Tunneling between ferromagnetic films. *Phys. lett., A* **54,** 225–226 (1975).

26. Bratkovsky, A. Tunneling of electrons in conventional and half-metallic systems: Towards very large magnetoresistance. *Phys. Rev. B* **56,** 2344 (1997).

27. Bibes, M. & Barthelemy, A. Oxide spintronics. *IEEE transactions on electron devices* **54,** 1003–1023 (2007).

28. Bowen, M. *et al.* Nearly total spin polarization in $La_{2/3}Sr_{1/3}MnO_3$ from tunneling experiments. *Appl. Phys. Lett.* **82,** 233–235 (2003).

29. Jonker, G. & Van Santen, J. Ferromagnetic compounds of manganese with perovskite structure. *Physica* **16,** 337–349 (1950).

30. Von Helmolt, R., Wecker, J., Holzapfel, B., Schultz, L. & Samwer, K. Giant negative magnetoresistance in perovskitelike $La_{2/3}Ba_{1/3}MnO_x$ ferromagnetic films. *Phys. Rev. Lett.* **71,** 2331 (1993).

31. Coey, J., Viret, M. & Von Molnar, S. Mixed-valence manganites. *Adv. Phys.* **48,** 167–293 (1999).

32. Nielsen, M. B. *et al.* Phase stability of the $SrMnO_3$ hexagonal perovskite system at high pressure and temperature. *Phys. Rev. B* **90,** 214101 (2014).

33. Jahn, H. A. & Teller, E. Stability of polyatomic molecules in degenerate electronic states-I—Orbital degeneracy. *Proc. R. Soc. Lond. A* **161,** 220–235 (1937).

34. Goodenough, J. B. Theory of the role of covalence in the perovskite-type manganites $[La, M(II)]MnO_3$. *Phys. Rev.* **100,** 564 (1955).

35. Kanamori, J. Superexchange interaction and symmetry properties of electron orbitals. *J. Phys. Chem. Solids* **10,** 87–98 (1959).

36. Anderson, P. W. in *Solid State Phys.* 99–214 (Elsevier, 1963).

37. Coey, J. M. *Magnetism and magnetic materials* (Cambridge university press, 2010).

38. Zener, C. Interaction between the d-shells in the transition metals. II. Ferromagnetic compounds of manganese with perovskite structure. *Phys. Rev.* **82,** 403 (1951).

39. Anderson, P. W. & Hasegawa, H. Considerations on double exchange. *Phys. Rev.* **100,** 675 (1955).

40. De Gennes, P.-G. Effects of double exchange in magnetic crystals. *Phys. Rev.* **118,** 141 (1960).

41. Park, J.-H. *et al.* Direct evidence for a half-metallic ferromagnet. *Nature* **392,** 794–796 (1998).

42. Yu, X. *et al.* High room-temperature TCR and MR of $La_{1-x}Sr_xMnO_3$ thin films for advanced uncooled infrared bolometers and magnetic sensors. *Appl. Surf. Sci.* **570,** 151221 (2021).

43. Fujishiro, H., Fukase, T. & Ikebe, M. Charge ordering and sound velocity anomaly in $La_{1-x}Sr_xMnO_3$ ($x \geqslant 0.5$). *J. Phys. Soc. Jpn.* **67,** 2582–2585 (1998).

44. Hwang, H., Cheong, S., Radaelli, P., Marezio, M. & Batlogg, B. Lattice Effects on the Magnetoresistance in Doped $LaMnO_3$. *Phys. Rev. Lett.* **75,** 914 (1995).

45. Millis, A. J., Littlewood, P. B. & Shraiman, B. I. Double exchange alone does not explain the resistivity of $La_{1-x}Sr_xMnO_3$. *Phys. Rev. Lett.* **74,** 5144 (1995).

46. Millis, A. Lattice effects in magnetoresistive manganese perovskites. *Nature* **392,** 147–150 (1998).

47. Röder, H., Zang, J. & Bishop, A. R. Lattice effects in the colossal-magnetoresistance manganites. *Phys. Rev. Lett.* **76,** 1356 (1996).

48. Millis, A., Shraiman, B. I. & Mueller, R. Dynamic Jahn-Teller effect and colossal magnetoresistance in $La_{1-x}Sr_xMnO_3$. *Phys. Rev. Lett.* **77,** 175 (1996).

49. Tsui, F., Smoak, M., Nath, T. & Eom, C. Strain-dependent magnetic phase diagram of epitaxial $La_{0.67}Sr_{0.33}MnO_3$ thin films. *Appl. Phys. Lett.* **76,** 2421–2423 (2000).

50. Konishi, Y. *et al.* Orbital-state-mediated phase-control of manganites. *J. Phys. Soc. Jpn* **68,** 3790–3793 (1999).

51. Dey, P., Nath, T. & Taraphder, A. Effect of substrate-induced strain on transport and magnetic properties of epitaxial $La_{0.66}Sr_{0.33}MnO_3$ thin films. *Appl. Phys. Lett.* **91,** 012511 (2007).

52. Dho, J., Kim, Y., Hwang, Y., Kim, J. & Hur, N. Strain-induced magnetic stripe domains in $La_{0.7}Sr_{0.3}MnO_3$ thin films. *Appl. Phys. Lett.* **82,** 1434–1436 (2003).

53. Wang, K. *et al.* Epitaxial growth and magnetic/transport properties of $La_{0.7}Sr_{0.3}MnO_3$ thin films grown on $SrTiO_3$ with optimized growth conditions. *RSC Advances* **7,** 31327–31332 (2017).

54. Kumari, S. *et al.* Effects of oxygen modification on the structural and magnetic properties of highly epitaxial $La_{0.7}Sr_{0.3}MnO_3$ (LSMO) thin films. *Sci. Rep.* **10,** 1–11 (2020).

55. Liu, J.-M. *et al.* Low-field magnetoresistive property of partially crystallized $La_{0.5}Sr_{0.5}MnO_3$ thin films by pulsed laser deposition. *J. Appl. Phys.* **88,** 2791–2798 (2000).

56. Longo, J. & Ward, R. Magnetic compounds of hexavalent rhenium with the perovskite-type structure. *J. Am. Chem. Soc.* **83,** 2816–2818 (1961).

57. Kobayashi, K.-I., Kimura, T., Sawada, H., Terakura, K. & Tokura, Y. Room-temperature magnetoresistance in an oxide material with an ordered double-perovskite structure. *Nature* **395,** 677–680 (1998).

58. Anderson, M. T., Greenwood, K. B., Taylor, G. A. & Poeppelmeier, K. R. B-cation arrangements in double perovskites. *Prog. Solid. State Ch.* **22,** 197–233 (1993).

59. Chandrasekhar, K. D., Das, A., Mitra, C. & Venimadhav, A. The extrinsic origin of the magnetodielectric effect in the double perovskite La_2NiMnO_6. *J. Phys.: Condens. Matter* **24,** 495901 (2012).

60. Hernández, J. *et al.* Bivalent nature of Fe and W ions in the antiferromagnetic Sr_2FeWO_6 material produced by the combustion technique. *arXiv* (2019).

61. Pradheesh, R. *et al.* Observation of spin glass state in weakly ferromagnetic Sr_2FeCoO_6 double perovskite. *J. Appl. Phys.* **111,** 053905 (2012).

62. De Vries, M. A., Mclaughlin, A. & Bos, J.-W. Valence bond glass on an fcc lattice in the double perovskite Ba_2YMoO_6. *Phys. Rev. Lett.* **104,** 177202 (2010).

63. Choudhury, D. *et al.* Near-room-temperature colossal magnetodielectricity and multiglass properties in partially disordered La_2NiMnO_6. *Phys. Rev. Lett.* **108,** 127201 (2012).

64. Luo, X. *et al.* The magnetic entropy change in the double perovskite La_2NiMnO_6 with strong spin–phonon coupling. *Solid State Commun* **149,** 810–813 (2009).

65. Zhu, M. *et al.* Electronic and magnetic properties of La_2NiMnO_6 and La_2CoMnO_6 with cationic ordering. *Appl. Phys. Lett.* **100,** 062406 (2012).

66. Rogado, N. S., Li, J., Sleight, A. W. & Subramanian, M. A. Magnetocapacitance and magnetoresistance near room temperature in a ferromagnetic semiconductor: La_2NiMnO_6. *Adv. Mater.* **17,** 2225–2227 (2005).

67. Blasco, J. *et al.* Synthesis and structural study of $LaNi_{1-x}Mn_xO_{3+\delta}$ perovskites. *J. Phys. Chem. Solids* **63,** 781–792 (2002).

68. Bull, C., Gleeson, D. & Knight, K. Determination of B-site ordering and structural transformations in the mixed transition metal perovskites La_2CoMnO_6 and La_2NiMnO_6. *J. Phys.: Condens. Matter* **15,** 4927 (2003).

69. Dass, R., Yan, J.-Q. & Goodenough, J. Oxygen stoichiometry, ferromagnetism, and transport properties of $La_{2-x}NiMnO_{6+\delta}$. *Phys. Rev. B* **68,** 064415 (2003).

70. Joly, V. J., Joy, P., Date, S. & Gopinath, C. Two ferromagnetic phases with different spin states of Mn and Ni in $LaMn_{0.5}Ni_{0.5}O_3$. *Phys. Rev. B* **65,** 184416 (2002).

71. Jin, X.-W., Lu, L., Mi, S.-B., Liu, M. & Jia, C.-L. Phase stability and B-site ordering in La_2NiMnO_6 thin films. *Appl. Phys. Lett.* **109,** 031904 (2016).

72. Lan, C. *et al.* Investigation on structures, band gaps, and electronic structures of lead free La_2NiMnO_6 double perovskite materials for potential application of solar cell. *J. Alloys Compd.* **655,** 208–214 (2016).

73. Guo, Y., Shi, L., Zhou, S., Zhao, J. & Liu, W. Near room-temperature magnetoresistance effect in double perovskite La_2NiMnO_6. *Appl. Phys. Lett.* **102,** 222401 (2013).

74. Chandrasekhar, K. D., Das, A. & Venimadhav, A. Spin glass behaviour and extrinsic origin of magnetodielectric effect in non-multiferroic La_2NiMnO_6 nanoparticles. *J. Phys.: Condens. Matter* **24,** 376003 (2012).

75. Weiss, P. & Piccard, A. Sur un nouveau phénomène magnétocalorique. *Comptes Rendus* **166,** 352–354 (1918).

76. Giauque, W. A thermodynamic treatment of certain magnetic effects. A proposed method of producing temperatures considerably below 1 absolute. *J. Am. Chem. Soc.* **49,** 1864–1870 (1927).

77. Giauque, W. & MacDougall, D. Attainment of Temperatures Below 1 Absolute by Demagnetization of $Gd_2(SO_4)_3 \cdot 8\,H_2O$. *Phys. Rev.* **43,** 768 (1933).

78. Brown, G. Magnetic heat pumping near room temperature. *J. Appl. Phys.* **47,** 3673–3680 (1976).

79. Steyert, W. Stirling-cycle rotating magnetic refrigerators and heat engines for use near room temperature. *J. Appl. Phys.* **49,** 1216–1226 (1978).

80. Gschneidner Jr, K. & Pecharsky, V. K. Magnetocaloric materials. *Annual Review of Materials Science* **30,** 387–429 (2000).

81. Szewczyk, A., Gutowska, M., Piotrowski, K. & Dąbrowski, B. Direct and specific heat study of magnetocaloric effect in $La_{0.845}Sr_{0.155}MnO_3$. *J. Appl. Phys.* **94,** 1873–1876 (2003).

82. Pecharsky, V., Gschneidner Jr, K., Pecharsky, A. & Tishin, A. Thermodynamics of the magnetocaloric effect. *Phys. Rev. B* **64,** 144406 (2001).

83. Amaral, J. & Amaral, V. On estimating the magnetocaloric effect from magnetization measurements. *J. Magn. Magn. Mater.* **322,** 1552–1557 (2010).

84. Swamy, N. K. *et al.* Specific heat and magnetocaloric effect studies in multiferroic $YMnO_3$. *J Therm Anal Calorim* **119,** 1191–1198 (2015).

85. Zhou, L. *et al.* Table-like magnetocaloric effect and large refrigerant capacity of composite magnetic refrigerants based on $LaFe_{11.6}Si_{1.4}Hy$ alloys. *J. Rare Earths* **36,** 613–618 (2018).

86. Gschneidner Jr, K., Pecharsky, V., Pecharsky, A. & Zimm, C. *Recent developments in magnetic refrigeration* in *Materials Science Forum* **315** (1999), 69–76.

87. Dan'Kov, S. Y., Tishin, A., Pecharsky, V., Gschneidner, K., *et al.* Magnetic phase transitions and the magnetothermal properties of gadolinium. *Phys. Rev. B* **57,** 3478 (1998).

88. Smaıli, A. & Chahine, R. Thermodynamic investigations of optimum active magnetic regenerators. *Cryogenics* **38,** 247–252 (1998).

89. Balli, M. *et al.* $Gd_{1-x}Tb_x$ alloys for Ericsson-like magnetic refrigeration cycles. *J. Alloys Compd.* **442,** 129–131 (2007).

90. Pecharsky, V. K. & Gschneidner Jr, K. A. Tunable magnetic regenerator alloys with a giant magnetocaloric effect for magnetic refrigeration from 20 to 290 K. *Appl. Phys. Lett.* **70,** 3299–3301 (1997).

91. Podmiljsak, B., J McGuiness, P. & Kobe, S. Complex Metallic Alloys for Applications in Magnetic Refrigeration. *Recent Pat. Mater. Sci.* **8,** 129–154 (2015).

92. Sun, J., Hu, F. & Shen, B. Comment on "Direct Measurement of the-Giant'Adiabatic Temperature Change in $Gd_5Si_2Ge_2$". *Phys. Rev. Lett.* **85,** 4191 (2000).

93. Palstra, T., Mydosh, J., Nieuwenhuys, G., Van der Kraan, A. & Buschow, K. Study of the critical behaviour of the magnetization and electrical resistivity in cubic $La(Fe,Si)_{13}$ compounds. *J. Magn. Magn. Mater.* **36,** 290–296 (1983).

94. Jia, L. *et al.* Magnetocaloric effects in the $La(Fe,Si)_{13}$ intermetallics doped by different elements. *J. Appl. Phys.* **105,** 07A924 (2009).

95. Shen, B., Sun, J., Hu, F., Zhang, H. & Cheng, Z. Recent progress in exploring magnetocaloric materials. *Adv. Mater.* **21,** 4545–4564 (2009).

96. Hu, F.-x. *et al.* Influence of negative lattice expansion and metamagnetic transition on magnetic entropy change in the compound $LaFe_{11.4}Si_{1.6}$. *Appl. Phys. Lett.* **78,** 3675–3677 (2001).

97. Wen, G. *et al.* Magnetic entropy change in $LaFe_{13-x}Si_x$ intermetallic compounds. *J. Appl. Phys.* **91,** 8537–8539 (2002).

98. Nascimento, F. C., Santos, A. O. d., Campos, A. d., Gama, S. & Cardoso, L. P. Structural and magnetic study of the MnAs magnetocaloric compound. *Mater. Res.* **9,** 111–114 (2006).

99. Wada, H. & Tanabe, Y. Giant magnetocaloric effect of $MnAs_{1-x}Sb_x$. *Appl. Phys. Lett.* **79,** 3302–3304 (2001).

100. Wada, H., Taniguchi, K. & Tanabe, Y. Extremely large magnetic entropy change of $MnAs_{1-x}Sb_x$ near room temperature. *Materials Transactions* **43,** 73–77 (2002).

101. Wada, H. *et al.* Giant magnetocaloric effect of $MnAs_{1-x}Sb_x$ in the vicinity of first-order magnetic transition. *Physica B Condens. Matter* **328,** 114–116 (2003).

102. Morelli, D. T., Mance, A. M., Mantese, J. V. & Micheli, A. L. Magnetocaloric properties of doped lanthanum manganite films. *J. Appl. Phys* **79,** 373–375 (1996).

103. Guo, Z. *et al.* Large magnetic entropy change in perovskite-type manganese oxides. *Phys. Rev. Lett.* **78,** 1142 (1997).

104. Guo, Z., Zhang, J., Huang, H., Ding, W. & Du, Y. Large magnetic entropy change in $La_{0.75}Ca_{0.25}MnO_3$. *Appl. Phys. Lett.* **70,** 904–905 (1997).

105. Zhang, X. *et al.* Magnetocaloric effect in $La_{0.67}Ca_{0.33}MnO_6$ and $La_{0.60}Y_{0.07}Ca_{0.33}MnO_6$ bulk materials. *Appl. Phys. Lett* **69,** 3596 (1996).

106. Szewczyk, A. *et al.* Magnetocaloric effect in $La_{1-x}Sr_xMnO_3$ for x= 0.13 and 0.16. *Appl. Phys. Lett.* **77,** 1026–1028 (2000).

107. Szewczyk, A. *et al.* Specific heat anomalies in $La_{1-x}Sr_xMnO_3$ ($0.12 < x < 0.2$). *Phys. Rev. B* **71,** 224432 (2005).

108. Jeong, Y. S., Anwar, M., Ahmed, F., Lee, S. R. & Koo, B. H. Study of Magnetic Transition and Magnetocaloric Effect in $La_{1-x}Sr_xMnO_3$ ($0.20 \leqslant x \leqslant 0.35$) Compounds. *Applied Mechanics and Materials* **378,** 225–229 (2013).

109. Ehsani, M., Kameli, P., Ghazi, M., Razavi, F. & Taheri, M. Tunable magnetic and magnetocaloric properties of $La_{0.6}Sr_{0.4}MnO_3$ nanoparticles. *J. Appl. Phys.* **114,** 223907 (2013).

110. Hazzez, M., Ihzaz, N., Boudard, M. & Oumezzine, M. The structural, magnetic and above room temperature magnetocaloric properties of $La_{0.5}Sr_{0.5}MnO_3$ compound. *Eur. Phys. J. Plus* **130,** 1–8 (2015).

111. Kallel, N., Kallel, S., Hagaza, A. & Oumezzine, M. Magnetocaloric properties in the Cr-doped $La_{0.7}Sr_{0.3}MnO_3$ manganites. *Physica B Condens. Matter* **404,** 285–288 (2009).

112. Guo, Z., Yang, W., Shen, Y. & Du, Y. Magnetic entropy change in $La_{0.75}Ca_{0.25-x}Sr_xMnO_3$ perovskites. *Solid State Commun* **105,** 89–92 (1998).

113. Lu, W., Luo, X., Hao, C., Song, W. & Sun, Y. Magnetocaloric effect and Griffiths-like phase in $La_{0.67}Sr_{0.33}MnO_3$ nanoparticles. *J. Appl. Phys.* **104,** 113908 (2008).

114. Tadout, M. *et al.* Magnetic Properties and Magnetocaloric Effect in $Gd_{100-x}Co_x$ Thin Films. *Crystals* **9,** 278 (2019).

115. Recarte, V., Pérez-Landazábal, J., Sánchez-Alárcos, V., Chernenko, V. & Ohtsuka, M. Magnetocaloric effect linked to the martensitic transformation in sputter-deposited Ni−Mn−Ga thin films. *Appl. Phys. Lett.* **95,** 141908 (2009).

116. Giri, S. *et al.* Strain induced extrinsic magnetocaloric effects in $La_{0.67}Sr_{0.33}MnO_3$ thin films, controlled by magnetic field. *J. Phys. D: Appl. Phys.* **52,** 165302 (2019).

117. Passanante, S. *et al.* Magnetocaloric effect in $La_{0.88}Sr_{0.12}MnO_3$ films. *Mater. Today: Proc* **14,** 104–108 (2019).

118. Moon, J., Kim, M., Choi, Y. J. & Lee, N. Giant anisotropic magnetocaloric effect in double-perovskite Gd_2CoMnO_6 single crystals. *Sci. Rep.* **7,** 1–10 (2017).

119. Yang, Z., Ge, J.-Y., Ruan, S., Cui, H. & Zeng, Y.-J. Cryogenic magnetocaloric effect in distorted double-perovskite Gd_2ZnTiO_6. *J. Mater. Chem. C* **9,** 6754–6759 (2021).

120. Balli, M., Fournier, P., Jandl, S., Truong, K. & Gospodinov, M. Analysis of the phase transition and magneto-thermal properties in La_2CoMnO_6 single crystals. *J. Appl. Phys.* **116,** 073907 (2014).

121. Hashimoto, T. *et al.* New application of complex magnetic materials to the magnetic refrigerant in an Ericsson magnetic refrigerator. *J. Appl. Phys.* **62,** 3873–3878 (1987).

122. Balli, M., Fruchart, D. & Gignoux, D. The $LaFe_{11.2}Co_{0.7}Si_{1.1}C_x$ carbides for magnetic refrigeration close to room temperature. *Appl. Phys. Lett.* **92,** 232505 (2008).

123. Balli, M., Fruchart, D. & Gignoux, D. Optimization of $La(Fe,Co)_{13-x}Si_x$ based compounds for magnetic refrigeration. *J. Phys.: Condens. Matter* **19,** 236230 (2007).

124. Zhang, Q. *et al.* Magnetocaloric effect and improved relative cooling power in $(La_{0.7}Sr_{0.3}MnO_3/SrRuO_3)$ superlattices. *J. Phys.: Condens. Matter* **23,** 052201 (2011).

125. Mukherjee, T., Sahoo, S., Skomski, R., Sellmyer, D. J. & Binek, C. Magnetocaloric properties of Co/Cr superlattices. *Phys. Rev. B* **79,** 144406 (2009).

126. Miller, C. W., Williams, D., Bingham, N. & Srikanth, H. Magnetocaloric effect in Gd/W thin film heterostructures. *J. Appl. Phys.* **107,** 09A903 (2010).

127. Smith, H. M. & Turner, A. Vacuum deposited thin films using a ruby laser. *Appl. Opt.* **4,** 147–148 (1965).

128. Dijkkamp, D. *et al.* Preparation of Y–Ba–Cu oxide superconductor thin films using pulsed laser evaporation from high T_c bulk material. *Appl. Phys. Lett.* **51,** 619–621 (1987).

129. Bragg, W. L. The structure of some crystals as indicated by their diffraction of X-rays. *The Royal Society* **89,** 248–277 (1913).

130. Harrington, G. F. & Santiso, J. Back-to-Basics tutorial: X-ray diffraction of thin films. *J Electroceram*, 1–23 (2021).

131. Baibich, M. N. *et al.* Giant magnetoresistance of (001) Fe/(001) Cr magnetic superlattices. *Phys. Rev. Lett.* **61,** 2472 (1988).

132. Mathon, J. & Umerski, A. Theory of tunneling magnetoresistance of an epitaxial Fe/MgO/Fe (001) junction. *Phys. Rev. B* **63,** 220403 (2001).

133. Yuasa, S., Nagahama, T., Fukushima, A., Suzuki, Y. & Ando, K. Giant room-temperature magnetoresistance in single-crystal Fe/MgO/Fe magnetic tunnel junctions. *Nature Mater* **3,** 868–871 (2004).

134. Slonczewski, J. C. Conductance and exchange coupling of two ferromagnets separated by a tunneling barrier. *Phys. Rev. B* **39,** 6995 (1989).

135. Moodera, J. S. & Kinder, L. R. Ferromagnetic–insulator–ferromagnetic tunneling: Spin-dependent tunneling and large magnetoresistance in trilayer junctions. *J. Appl. Phys.* **79,** 4724–4729 (1996).

136. Shang, C. H., Nowak, J., Jansen, R. & Moodera, J. S. Temperature dependence of magnetoresistance and surface magnetization in ferromagnetic tunnel junctions. *Phys. Rev. B* **58,** R2917 (1998).

137. Zhang, J. & White, R. Voltage dependence of magnetoresistance in spin dependent tunneling junctions. *J. Appl. Phys.* **83,** 6512–6514 (1998).

138. Vedyayev, A., Bagrets, D., Bagrets, A. & Dieny, B. Resonant spin-dependent tunneling in spin-valve junctions in the presence of paramagnetic impurities. *Phys. Rev. B* **63,** 064429 (2001).

139. Moodera, J. S., Kinder, L. R., Wong, T. M. & Meservey, R. Large magnetoresistance at room temperature in ferromagnetic thin film tunnel junctions. *Phys. Rev. Lett.* **74,** 3273 (1995).

140. Wei, H., Qin, Q., Ma, M., Sharif, R. & Han, X. 80% tunneling magnetoresistance at room temperature for thin Al−O barrier magnetic tunnel junction with CoFeB as free and reference layers. *J. Appl. Phys.* **101,** 09B501 (2007).

141. Platt, C., Dieny, B. & Berkowitz, A. Spin polarized tunneling in reactively sputtered tunnel junctions. *J. Appl. Phys.* **81,** 5523–5525 (1997).

142. Yuasa, S. & Djayaprawira, D. Giant tunnel magnetoresistance in magnetic tunnel junctions with a crystalline MgO (0 0 1) barrier. *J. Phys. D: Appl. Phys.* **40,** R337 (2007).

143. Parkin, S. S. *et al.* Giant tunnelling magnetoresistance at room temperature with MgO (100) tunnel barriers. *Nature Mater* **3,** 862–867 (2004).

144. Ikeda, S. *et al.* Tunnel magnetoresistance of 604% at 300 K by suppression of Ta diffusion in CoFeB/MgO/CoFeB pseudo-spin-valves annealed at high temperature. *Appl. Phys. Lett.* **93,** 082508 (2008).

145. Radu, F. & Sánchez-Barriga, J. in *Novel Magnetic Nanostructures* 267–331 (Elsevier, 2018).

146. Hueso, L., Granja, L., Levy, P. & Mathur, N. Spintronic investigation of the phase separated manganite $(La, Ca)MnO_3$. *J. Appl. Phys.* **100,** 023903 (2006).

147. Gajek, M. *et al.* Spin filtering through ferromagnetic $BiMnO_3$ tunnel barriers. *Phys. Rev. B* **72,** 020406 (2005).

148. Luders, U. *et al.* Spin filtering through ferrimagnetic $NiFe_2O_4$ tunnel barriers. *Appl. Phys. Lett.* **88,** 082505 (2006).

149. LeClair, P. *et al.* Large magnetoresistance using hybrid spin filter devices. *Appl. Phys. Lett.* **80,** 625–627 (2002).

150. Moodera, J., Hao, X., Gibson, G. & Meservey, R. Electron-spin polarization in tunnel junctions in zero applied field with ferromagnetic EuS barriers. *Phys. Rev. Lett.* **61,** 637 (1988).

151. Lu, Y. *et al.* Large magnetotunneling effect at low magnetic fields in micrometer-scale epitaxial $La_{0.67}Sr_{0.33}MnO_3$ tunnel junctions. *Phys. Rev. B* **54,** R8357 (1996).

152. Sun, J. *et al.* Observation of large low-field magnetoresistance in trilayer perpendicular transport devices made using doped manganate perovskites. *Appl. Phys. Lett.* **69,** 3266–3268 (1996).

153. Garcia, V. *et al.* Temperature dependence of the interfacial spin polarization of $La_{2/3}Sr_{1/3}MnO_3$. *Phys. Rev. B* **69,** 052403 (2004).

154. Jo, M.-H., Mathur, N., Todd, N. & Blamire, M. Very large magnetoresistance and coherent switching in half-metallic manganite tunnel junctions. *Phys. Rev. B* **61,** R14905 (2000).

155. Soulen Jr, R. *et al.* Measuring the spin polarization of a metal with a superconducting point contact. *Science* **282,** 85–88 (1998).

156. Osofsky, M. *et al.* Measurement of the spin polarization of LaSrMnO. *J. Appl. Phys.* **85,** 5567–5569 (1999).

157. Shi, F. in *Magnetron Sputtering* (IntechOpen, 2018).

158. Quantum-Design. *Physical Property Measurement System, Horizontal Rotator* `https://www.qdusa.com/products/ppms.html`.

159. Mira, J., Rivas, J., Hueso, L., Rivadulla, F. & Lopez Quintela, M. Drop of magnetocaloric effect related to the change from first-to second-order magnetic phase transition in $La_{2/3}(Ca_{1-x}Sr_x)_{1/3}MnO_3$. *J. Appl. Phys.* **91,** 8903–8905 (2002).

160. Lu, Z. *et al.* Synthesis of single-crystal $La_{0.67}Sr_{0.33}MnO_3$ freestanding films with different crystal-orientation. *APL Materials* **8,** 051105 (2020).

161. Arrott, A. Criterion for ferromagnetism from observations of magnetic isotherms. *Phys. Rev.* **108,** 1394 (1957).

162. Li, Y. *et al.* Successive magnetic transitions and magnetocaloric effect in Dy_3Al_2 compound. *J. Alloys Compd.* **651,** 278–282 (2015).